



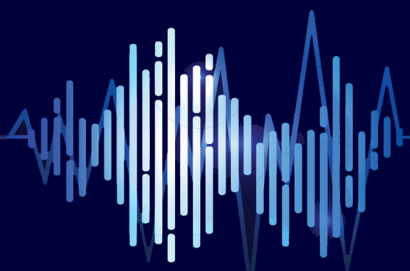
Iranian Association of Electrical
and Electronics Engineers



Shahid Chamran
University of Ahvaz

Journal of Applied Research in Electrical Engineering

Vol. 3, No. 2, Summer and Autumn 2024



PUBLISHER: SHAHID CHAMRAN UNIVERSITY OF AHVAZ

E-ISSN: 2783-2864

P-ISSN: 2717-414X



Journal of Applied Research in Electrical Engineering

E-ISSN: 2783-2864
P-ISSN: 2717-414X



**Journal of Applied Research in Electrical Engineering (JAREE),
Volume 3, Number 2, Summer and Autumn 2024**

Publisher: Shahid Chamran University of Ahvaz, Iran

This magazine is the result of a formal partnership of **Shahid Chamran University of Ahvaz** and **Iranian Association of Electrical and Electronics Engineers**

Website: <https://jaree.scu.ac.ir>

E-mails: jaree@scu.ac.ir; jaree.scu@gmail.com












Address: Department of Electrical Engineering, Faculty of Engineering, Shahid Chamran University of Ahvaz, Golestan Street, Ahvaz, Iran

P.O. Box: 61357-85311

















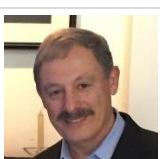

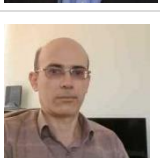
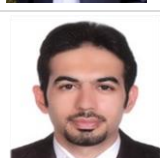
Tel: +986133226782, +989122876375

Fax: +986133226597

Managing Committee and Staff

| | | | |
|---|---|--|--|
|  | <p>Editor-in-Chief</p> <p>Prof. Mahmood Joorabian Shahid Chamran University of Ahvaz, Ahvaz, Iran</p> <p><i>Power System Planning, Renewable Energy and Smart Grid, FACTS Devices</i> mjoorabian@scu.ac.ir</p> |  | <p>Director-in-Charge</p> <p>Prof. Seyed Ghodratoollah Seifossadat Shahid Chamran University of Ahvaz, Ahvaz, Iran</p> <p><i>Power System Protection, Power Electronics, Power Quality</i> seifossadat@yahoo.com</p> |
|  | <p>Managing Editor</p> <p>Dr. Alireza Saffarian (Associate Professor) Shahid Chamran University of Ahvaz, Ahvaz, Iran</p> <p><i>Power System Protection, Power System Stability, Power Quality, Distribution Systems</i> a.saffarian@scu.ac.ir</p> |  | <p>Executive Assistant</p> <p>Dr. Mohammad Nabipour (Associate Professor) Shahid Chamran University of Ahvaz, Ahvaz, Iran</p> <p><i>Reliability of Power Systems, Microgrids and Distributed Energy Sources, Smart Grids</i> farzin@scu.ac.ir</p> |
|  | <p>Associate Editor (Electronics and Telecommunications)</p> <p>Prof. Yousef Seifi Kavian Shahid Chamran University of Ahvaz, Ahvaz, Iran</p> <p><i>Digital Circuits and Systems, Communication Networks and Distributed Systems</i> y.s.kavian@scu.ac.ir</p> |  | <p>Associate Editor (Power and Control)</p> <p>Dr. Mohsen Saniei (Associate Professor) Shahid Chamran University of Ahvaz, Ahvaz, Iran</p> <p><i>Power System Dynamics, High Voltage Engineering, Electricity Market, Microgrid</i> m.saniei@scu.ac.ir</p> |
|  | <p>Language Editor</p> <p>Majid Sadeghzadeh Hemayati English Language Editing</p> <p>m_s_hemayati@yahoo.com</p> |  | <p>Page Designer</p> <p>Mehdi Mohammadian Mehr Shahid Chamran University of Ahvaz, Ahvaz, Iran</p> <p>eng.mohammadianmehr@gmail.com</p> |
|  | <p>Executive Director</p> <p>Masoomeh Shaygan Shahid Chamran University of Ahvaz, Ahvaz, Iran</p> <p>masoomeh.shaygan@gmail.com</p> | | |

Editorial Board

| | |
|--|--|
|  <p>Prof. Mahmood Joorabian Shahid Chamran University of Ahvaz, Ahvaz, Iran</p> <p><i>Power System Planning, Renewable Energy and Smart Grid, FACTS Devices</i> mjoorabian@scu.ac.ir</p> |  <p>Prof. Seyed Ghodratoollah Seifossadat Shahid Chamran University of Ahvaz, Ahvaz, Iran</p> <p><i>Power System Protection, Power Electronics, Power Quality</i> seifossadat@yahoo.com</p> |
|  <p>Prof. Saeedallah Mortazavi Shahid Chamran University of Ahvaz, Ahvaz, Iran</p> <p><i>Intelligent Control Systems, Power System Control, Automation, Fuzzy Logic, Neural Networks</i> mortazavi_s@scu.ac.ir</p> |  <p>Prof. Abdolnabi Kosarian Shahid Chamran University of Ahvaz, Ahvaz, Iran</p> <p><i>Solid State Electronic Devices, Solar Cell Fabrication Technology</i> a.kosarian@scu.ac.ir</p> |
|  <p>Prof. Ebrahim Farshidi Shahid Chamran University of Ahvaz, Ahvaz, Iran</p> <p><i>Analog and Digital Integrated Circuits, Data Converters, Microelectronics</i> farshidi@scu.ac.ir</p> |  <p>Prof. Naser Pariz Ferdowsi University of Mashhad, Mashhad, Iran</p> <p><i>Nonlinear Control, Hybrid Systems, Aeronautics, Industrial Control, Applied Mathematics</i> n-pariz@um.ac.ir</p> |
|  <p>Prof. Yousef Seifi Kavian Shahid Chamran University of Ahvaz, Ahvaz, Iran</p> <p><i>Digital Circuits and Systems, Communication Networks and Distributed Systems</i> y.s.kavian@scu.ac.ir</p> |  <p>Dr. Mohsen Saniei (Associate Professor) Shahid Chamran University of Ahvaz, Ahvaz, Iran</p> <p><i>Power System Dynamics, High Voltage Engineering, Electricity Market, Microgrid</i> m.saniei@scu.ac.ir</p> |
|  <p>Prof. Reza Ghaderi Shahid Baheshti University, Tehran, Iran</p> <p><i>Control Theory, System Identification, Control Systems, Fuzzy Engineering</i> r_ghaderi@sbu.ac.ir</p> |  <p>Dr. Edris Pouresmaeil (Associate Professor) Aalto University, Espoo, Finland</p> <p><i>Integration of Renewable Energies into the Power Grid</i> edris.pouresmaeil@aalto.fi</p> |
|  <p>Prof. Abbas Zarifkar Shiraz University, Shiraz, Iran</p> <p><i>Optical Electronics</i> zarifkar@shirazu.ac.ir</p> |  <p>Prof. Fushuan Wen Tallinn University of Technology, Tallinn, Estonia</p> <p><i>Power Systems and Power Economics</i> fushuan.wen@taltech.ee</p> |
|  <p>Prof. Majid Sanaye-pasand University of Tehran, Tehran, Iran</p> <p><i>Power Systems Protection, Digital Protective Relays, Power Systems Automation, Power System Transients</i> msanaye@ut.ac.ir</p> |  <p>Prof. Zabih (Fary) Ghassemlooy North Umbria University, Newcastle upon Tyne, United Kingdom</p> <p><i>Optical Communications, Visible Light, Communication Systems</i> z.ghassemlooy@northumbria.ac.uk</p> |
|  <p>Prof. Mahdi Tavakoli University of Alberta, Alberta, Canada</p> <p><i>Robotics and Telerobotics, Haptics and Teleoperation Control, Surgical and Therapeutic Robotics, Image-Guided Surgery</i> mahdi.tavakoli@ualberta.ca</p> |  <p>Prof. Mohamad Hassan Modir Shanechi Illinois Institute of Technology, Chicago, USA</p> <p><i>Nonlinear and intelligent systems, Power system dynamics and security, Power system planning and maintenance scheduling</i> shanechi@iit.edu</p> |
|  <p>Prof. Mohammad Shahidehpour Illinois Institute of Technology, Chicago, USA</p> <p><i>Power Systems, Microgrids, Power System Operation, Power System Planning</i> ms@iit.edu</p> |  <p>Prof. Gholamreza Akbarizadeh Shahid Chamran University of Ahvaz, Ahvaz, Iran</p> <p><i>Image Processing, Machine Vision, SAR Satellite Imaging Systems and Remote Sensing, Machine Learning and Deep Learning</i> g.akbari@scu.ac.ir</p> |
|  <p>Prof. Mohammad Soroosh Shahid Chamran University of Ahvaz, Ahvaz, Iran</p> <p><i>Photonic Crystals, Optoelectronics, Plasmonic Devices, Graphene, Photodetectors</i> m.soroosh@scu.ac.ir</p> |  <p>Dr. Alireza Saffarian (Associate Professor) Shahid Chamran University of Ahvaz, Ahvaz, Iran</p> <p><i>Power System Protection, Power System Stability, Power Quality, Distribution Systems</i> a.saffarian@scu.ac.ir</p> |

About Journal

Journal of Applied Research in Electrical Engineering (J. Appl. Res. Electr. Eng.) is a single-blind peer-reviewed, **open access** and **free of charge** international journal published by Shahid Chamran University of Ahvaz in cooperation with Iranian Association of Electrical and Electronics Engineers (IAEEE). The JAREE is a medium for global academics to exchange and spread the latest discoveries and advances in their applied research in electrical engineering. The JAREE aims at presenting important results of analytical, computational and experimental works within all specialized fields of electrical engineering (electronics, power, control and telecommunications). It welcomes high quality original research papers from contributors throughout the world. All papers are subject to a peer reviewing procedure. Submission, processing and publication of the papers in JAREE is **free of charge**.

Types of accepted papers include:

- Research articles
- Review articles
- Applied articles

Research papers are expected to present innovative solutions, novel concepts, or creative ideas that can help to address existing or emerging technical challenges in electrical engineering.

Application papers are expected to share valuable industry experiences on dealing with challenging technical issues, developing/adopting new standards, applying new technologies or solving complex problems. JAREE welcomes application papers that can have a significant impact on industry practices in the coming years.

Review papers are expected to provide insightful and expert reviews, tutorials, or study cases on an important, timely and widely-interested topic in electrical engineering.

All researchers in the fields of electrical science are invited to publish their scientific and research achievements in this journal. Interested authors can submit their manuscripts in the journal's website. More information is available in the website on how to prepare and submit the manuscripts.

Amis and Scope

The *Journal of Applied Research in Electrical Engineering* aims to provide a medium for dissemination of innovative and consequential papers that present analytical, computational and experimental works within all specialized fields of electrical engineering (electronics, power, control and telecommunications). The scope of the journal includes, but is not limited to, the following topic areas:

Electronics:

- Optical electronics, photonics and solar cells
- Integrated analog circuits and mixed signals
- Integrated radio frequency circuits
- Digital electronics (VLSI)
- Semiconductor devices
- Sensor technology

Power:

- Dynamics and stability of the power systems
- Power system protection
- Electric power quality
- Operation and planning of the power systems
- High voltage insulation technology
- Flexible AC Transmission Systems (FACTS)
- Electric power distribution systems
- Smart grids, micro-grids, renewable energies and distributed generation
- Reliability of electrical energy systems
- Energy management and electricity market
- Electric machines and transformers
- Power electronic and electric drives

Control:

- Linear and non-linear control systems
- Adaptive, optimal and stochastic control
- Fuzzy systems, neural networks and intelligent control
- Robotic and mechatronic
- Modeling, Identification and optimization of systems
- Guidance and navigation systems
- Automation, industrial control and instrumentation

Telecommunications:

- Signal and image processing
- Wireless and cellular communication systems
- Telecommunication networks
- Radar and sonar
- Information theory and coding
- Cognitive radio
- Antenna design
- Microwave devices
- Wave propagation and electromagnetic compatibility

Indexing Databases and Social Networks

| | |
|---|---|
|  | Scopus: JAREE was accepted to be indexed in Scopus. JAREE articles are being indexed in Scopus. https://www.scopus.com/results/results.uri?st1=2783-2864&st2=&s=ISSN%282783-2864%29&limit=10&origin=searchbasic&sort=plf&src=s&sot=b&sdt=b&sessionSearchId=c250309f5b53a538326bd4219cbf8ffb |
|  | Islamic World Science Citation Center (ISC): https://mj1.isc.ac/Searchresult.aspx?Cond=2&SrchTxt=27832864 |
|  | Iran Ministry of Science, Research and Technology Scientific Journals: (Journal Rank: International) https://journals.msrt.ir/home/detail/16058/ |
|  | Directory of Open Access Journals (DOAJ): https://doaj.org/toc/2783-2864 |
|  | Google Scholar: https://scholar.google.com/citations?user=F7KOPtYAAAAJ&hl=en&authuser=1 |
|  | Directory of Open Access Scholarly Resources (ROAD): https://portal.issn.org/resource/ISSN/2783-2864 |
|  | Elton B. Stephens Company (EBSCO): https://jaree.scu.ac.ir/news?newsCode=204 |
|  | CIVILICA: https://en.civilica.com/I/140583/ |
|  | National Publications Information Bank (magiran): https://www.magiran.com/magazine/8471 |
|  | Digital Object Identifier (DOI): https://www.doi.org/ |
|  | LinkedIn: https://www.linkedin.com/in/journal-of-applied-research-in-electrical-engineering-jaree-7540871b2/ |
|  | Academia: https://shahidchamranahwaz.academia.edu/JournalAppliedResearchinElectricalEngineering |
|  | Mendeley: https://www.mendeley.com/profiles/journal-of-applied-res-in-electrical-engineer/ |
|  | Twitter: https://twitter.com/jaree_scu |
|  | Facebook: https://www.facebook.com/jaree.scu |
|  | Researchgate: https://www.researchgate.net/profile/Jaree_Engineering |
|  | Telegram: https://t.me/jareescu |

Indexing Databases and Social Networks (Continued)

| | |
|---|--|
|  | Instagram: https://www.instagram.com/jaree.scu/ |
|  | Journal homepage: https://jaree.scu.ac.ir |

Guide for Authors

How to submit a manuscript

For the initial submission, the authors have to just send the main manuscript file and the signed [Copyright Form](#) of the journal. While preparing manuscripts for initial submission, authors are kindly requested to follow the guidelines, described below:

- The manuscript should be written in a Microsoft Word file (.doc or .docx).
- The file should include text (preferably in 10 points, “Times New Roman” font) and all figures (figures can be placed within the text at the appropriate point or at the end of the text).
- The manuscript pages should be prepared either using a double-column single-line spacing layout or a single-column double-line spacing layout. A margin of at least 1.5 cm on each side is required.
- All papers should be composed of Title, Author Name, Affiliation, Corresponding author email, Abstract, Keywords, Body, and References.
- The manuscript should be written in good English. It should have been carefully checked for clarity, conciseness, the correctness of grammar, and typographical errors.
- The corresponding author should sign the journal copyright form on behalf of any and all co-authors and upload it to the Journal’s Submission System when submitting the manuscript. The journal copyright form can be downloaded from [here](#).
- The corresponding author can use the [JAREE Template for Cover Letter](#) as a default text for the cover letter when submitting the manuscript.
- It is recommended that the title of the paper does not contain abbreviations or formulae.
- The abbreviations used in the abstract should be introduced both in the abstract and again on first use in the body.
- References should be numbered in the order they are mentioned in the text.

Manuscript Submission

Submission to this journal proceeds totally online and you will be guided stepwise through the creation and uploading of your files. All correspondence, including notification of the Editor's decision and requests for revision, takes place by e-mail. To submit your manuscript, click on the [Submit Manuscript](#) link on the journal's homepage. Then, click on [Register](#) to create an author account. A message is sent to your email address containing your username and password. Then, login to the Journal’s Submission System at the [User's login](#) page using the username and password to submit your new manuscript. Once you have logged in, you can change your password by clicking on the My Home link at the top menu.

Copyright and Open Access License

An author submitting a paper should ensure that he or she has the right to publish the paper and that it contains nothing defamatory. The JAREE will assume that all co-authors have agreed to the submission of any paper received. The corresponding author should sign the journal copyright form on behalf of any and all co-authors and upload it to the Journal’s Submission System when submitting the manuscript.

Contents

| Article Title and Authors | Page No. |
|---|----------|
| Wide Area Robust Controller Design for SSSC to Improve the Oscillations Caused by the Time Delay of Remote Signals Babak Keshavarz Zahed, Mohammad Hassan Moradi | 120 |
| Network Virtualization Utilizing Blockchain: A Review Patikiri Arachchige Don Shehan Nilmantha Wijesekara | 136 |
| Voltage Regulation in Low Voltage Distribution Networks Using Reactive Power Capability of Photovoltaic Inverters (PV) and PID Consensus Algorithm Iman Ali Hassanvand, Javad Ebrahimi, Mahyar Abasi | 159 |
| Optimization of PSS and UPFC Controllers to Enhance Stability by Using a Combination of Fuzzy Algorithm and Shuffled Frog Leaping Algorithm Mohammad Abedini, Mahyar Abasi | 168 |
| Economic Analysis of Photovoltaic Systems During Peak Load of the Electric Power Distribution System in the Presence of Electric Vehicles Musa Khosravi, Saeed Hasanvand, Mahyar Abasi, Mohammad Esmaeil Hassanzadeh | 177 |
| Improving Power Quality Using a Fuzzy Inference System-Based Variable Forgetting Factor Recursive Least Error Square Control Scheme of DSTATCOM Arash Rohani, Javad Ebrahimi, Shirin Besati | 185 |
| Comparative Analysis of Lithium-ion Battery for Long and Short Pulse Discharge Experiments in State-of-Charge Estimation with Extended Kalman Filter Behnam Ersi Alambaz, Mohsen Ghalehnoie, Hamid Reza Moazami | 200 |
| Investigating the Flashover Probability of Transmission Network Insulators During Dust Storms Yasaman Abbasi Chahardah Cheriki, Hossein Farzin, Elaheh Mashhour | 207 |
| Improving the Performance Characteristics of Conventional Linear Switched Reluctance Motor by Eliminating Translator Yoke and Embedding Permanent Magnets in Stator Yoke Milad Golzarzadeh, Hashem Oraee, Babak Ganji | 222 |
| Investigating Robust Tracking of Type 1 Diabetes Control Using Model-Free Controllers Peyman Vafadoost Sabzevar, Ahmad Hajipour, Hamidreza Tavakoli | 232 |
| IRS-Assisted Visible Light Communication for Improved Monitoring of Patient Vital Signals in Hospital Environment Babak Sadeghi, Seyed Mohammad Sajad Sadough | 240 |
| Reliability Modelling of Central Receiver Power Plants Amir Ghaedi, Mehrdad Mahmoudian | 250 |

Copyrights

© 2024 Licensee Shahid Chamran University of Ahvaz, Ahvaz, Iran. This article is an open-access article distributed under the terms and conditions of the Creative Commons Attribution –Non-Commercial 4.0 International (CC BY-NC 4.0) License (<http://creativecommons.org/licenses/by-nc/4.0/>).





Research Article

Wide Area Robust Controller Design for SSSC to Improve the Oscillations Caused by the Time Delay of Remote Signals

Babak Keshavarz Zahed , and Mohammad Hassan Moradi 

Department of Electrical Engineering, Faculty of Engineering, Bu-Ali Sina University, Hamedan, Iran

* Corresponding Author: mhmoradi@basu.ac.ir

Abstract: The penetration of double-fed induction generators (DFIG) as renewable energy sources (RES) in power systems leads to fluctuations caused by wind energy. Therefore, based on this challenge, a wide area damping controller (WADC) has been designed to compensate the oscillatory modes by a static synchronous series compensator (SSSC). In addition to the design of WADC for SSSC, a parallel compensator in the form of a supercapacitor energy storage system (CESS) has been used in the DC link of the wind unit so that DFIG can be used optimally to supply the power system. The design method for compensating time delays in WADC is based on free weight matrices (FWM). First, based on the theory of robust control based on delay-dependent feedback, a set of constraints related to linear matrix inequality (LMI) is formulated. In the following, the free weight matrix (FWM) has been used to solve the delay-dependent time problem. The purpose of applying FWM is to extract the most optimal gain for the controller in the presence of the time delay. The proposed FWM matrix tries to find the most optimal gain in the controller with the help of an iterative algorithm based on the linearization of the conical complement. The simulation results have been implemented in the MATLAB software environment after obtaining the critical modes in the nonlinear time domain on the power system of 16 improved machines. Based on the simulation results, the robustness of the proposed controller under various uncertainties is clearly shown in this paper.

Keywords: Power system, linear matrix inequality, WAMS, SSSC, DFIG, stability.

Article history

Received 28 February 2024; Revised 26 April 2024; Accepted 24 June 2024; Published online 23 October 2024.

© 2024 Published by Shahid Chamran University of Ahvaz & Iranian Association of Electrical and Electronics Engineers (IAEEE)

How to cite this article

B. Keshavarz Zahed, and M. H. Moradi, "Wide area robust controller design for SSSC to improve the oscillations caused by the time delay of remote signals," *J. Appl. Res. Electr. Eng.*, vol. 3, no. 2, pp. 120-135, 2024.

DOI: [10.22055/jaree.2024.45909.1103](https://doi.org/10.22055/jaree.2024.45909.1103)



NOMENCLATURE

Synchronous Generator (SG) Variables

| | |
|------------------|--|
| E'_{qi} (p.u.) | The field voltage of the SG in the q-axis |
| E'_{di} (p.u.) | The field voltage of the SG in the d-axis |
| I_{di} | The current of the SG in the d-axis |
| I_{qi} | The current of the SG in the q-axis |
| E_{fdi} | The SG excitation field voltage |
| K_{Ei} | Excitation system controller gain |
| S_{Ei} | Saturation component of excitation field in SG |
| V_{Ri} | SG terminal voltage |

| | |
|-------------|--|
| ω_i | SG rotor angular velocity |
| ω_s | SG synchronous speed |
| δ_i | Rotor angle in SG |
| D_i | Damping coefficient in SG model |
| L'_{qi} | Transient inductance in the q-axis |
| L'_{di} | Transient inductance in the d-axis |
| T_{mi} | Mechanical torque in SG |
| τ_{ji} | Time constant between generators i and j |
| X_d | d-axis steady state reactance |
| X'_d | d-axis transient state reactance |

| | |
|-----------------------|--|
| X_q | q-axis steady state reactance |
| X'_q | q-axis transient state reactance |
| $T'_{doi}(s)$ | The time constant of the d-axis |
| $T'_{qoi}(s)$ | The time constant of the q-axis |
| $H(s)$ | Inertia constant in SG |
| DFIG Variables | |
| i_{dsw} | Stator current SG in d-axis |
| i_{qsw} | Stator current SG in q-axis |
| i_{drw} | Rotor current SG in d-axis |
| i_{qrw} | Stator current SG in q-axis |
| H | Inertia constant in DFIG |
| R_s | Stator winding resistance |
| L_{rr} | Rotor internal inductance |
| L_{mm} | Field self-inductance |
| L_{ss} | Stator self-inductance |
| V_{drw} | DFIG rotor voltage in d-axis |
| V_{qrw} | DFIG rotor voltage in q-axis |
| R_r | Rotor winding resistance |
| V_{qsw} | DFIG stator voltage in d-axis |
| V_{dsw} | DFIG stator voltage in q-axis |
| ω_s | Synchronous speed of induction generator |
| ω_r | Rotor speed of induction generator |

| | |
|-----------------------------|-------------------------------------|
| SCESS-SSSC Variables | |
| i_{sc} | Storage current |
| L_s | Circuit inductance SCESS |
| f_s | SCESS switching frequency |
| V_{DC} | DC voltage |
| C_{SC} | SCESS orbital capacity |
| V_{CSC} | Capacitor voltage in SCESS |
| R_{psc} | Parallel branch resistance in SCESS |
| v_{ds} | SSSC voltage on d-axis |
| v_{qs} | SSSC voltage on d-axis |
| m_c | Modulation index in SSSC inverter |
| Z_{inv} | Inverter filter impedance in SSSC |
| V_{dc_sssc} | DC voltage in SSSC |
| α_{se} | SSSC inverter fire angle |
| C_{dc} | Capacitance of the dc link in SSSC |
| i_d | SSSC current in d-axis |
| i_q | SSSC current in q-axis |
| R_{dc} | DC link resistance in SSSC |

1. INTRODUCTION

1.1. Background and Motivation

One of the most popular RES to produce electrical energy is the use of wind energy. But due to wind speed fluctuations, the use of these units in the power system leads to additional fluctuations. Therefore, controlling fluctuations caused by variable speed wind units is essential and important from the point of view of stability in the power system [1-2]. For this purpose, the presence of energy storage systems (ESS) along with flexible alternating current transmission systems (FACTS) in the power system leads to increased damping of fluctuations and reliable utilization [3-4].

One of the most popular types of variable speed wind turbines is DFIG. The use of these generators is more common than other wind units because of the direct control of active and reactive powers and the type of protection in the way of connecting the converters to each other [5]. In the DFIG structure, a back-to-back two-way converter is used as a grid-side converter (GSC), a rotor-side converter (RSC) and a control loop for the DC link capacitor to connect the two converters [6]. The use of SCESS in the DC link of a DFIG leads to soft start-up and, as a result, reduces fluctuations caused by wind [7].

1.2. Literature Review

In the studies of low frequency oscillations (LFO) of the power system to identify local modes (frequency range 0.9 to 2 Hz) and inter-area (frequency range 0.2 to 0.9 Hz) design of power system stabilizers (PSS) and power oscillation dampers (POD) is considered useful for synchronous generators (SG) and FACTS devices[8]. In the family of

FACTS devices, the SSSC compensator is placed in series in the transmission line and controls the power flow in the transmission line [9]. Among the useful methods for SSSC controller design are non-linear robust control in damping local fluctuations and improving transient stability [10], methods based on intelligence for optimal selection of controller parameters in PSS-SSSC coordinated design [11, 12], model predictive control (MPC) and sliding mode control (SMC).

Due to the expansion of the dimensions of power systems, it is not possible to control inter-area fluctuations through the identification of local modes. Therefore, to control the inter-area modes, it is necessary to use the wide area measurement system (WAMS), in which the signals caused by the inter-area modes can be measured and sent by phasor measurement units (PMU) at different points of the power system. [13]. In this type of operation, the feedback signal (containing information about inter-regional modes) is applied to the input of WADC controllers [13]. However, the information resulting from the feedback signal due to the use of telecommunications equipment and sending from a remote area is associated with time delays that must be considered in the design of WADC [14]. In various researches for time delay compensation, methods such as Padé approximation [15], MPC method [16], loop shaping [17], H2/H ∞ robust control [18, 19], reinforcement learning method [20], Linear quadratic estimator (LQE) is proposed in [21] and robust controller by solving Lyapunov function (LF) problem [22, 23]. The state estimation method is one of the methods that require high accuracy to determine the characteristics of the power system. Therefore, as the dimensions of the power system increase, extensive measurement is required, which leads to a high order of system states [24, 25].

The hybrid particle swarm optimization method is a simple yet practical method that has been used to optimize WADC controller parameters in the presence of time delays in various researches [26]. Among other optimization methods, we can refer to the reinforcement learning method based on policy gradient using neural networks [27]. However, in this method, because the system model is not available, a very extensive discretization operation is needed to identify it. Analysis of dynamic modes based on an online model is a method introduced in the measurement of WADC signals in [28]. The basis of this method is based on singular value decomposition (SVD). This depends on the accurate low-order model in the dynamics of the power system. Using SVD to reduce the order of power system and design with discrete linear quadratic regulator (LQR) for WADC controller is a method introduced without considering time delay in [28]. Network Predictive Control (NPC) is another online model identification method that is introduced in the WADC design for the rotor side converter (RSC) of a wind farm [29]. One of the important advantages of NPC is considering the physical constraints of the system in the online optimization process. However, in order for the prediction of system outputs to be valid, it is necessary to be very careful in identifying the online model of the plant. In WADC design, it is very important to try to increase the delay margin to compensate for the time delay. Based on this, in [30], the delay margin has been designed for second-order oscillatory modes with respect to fixed delays, square wave and gamma distribution. In this design method, a probability distribution function is used in order to be able to consider the special values of the oscillatory modes in the presence of random delays. However, no method is considered for the distribution of the probability function.

1.3. Research Gap and Contribution

The use of Lyapunov functions is another problem solving method in order to prove stability, which can be effectively useful in WADC design. With the help of the LMI criterion, the stability of the Lyapunov function can be obtained, which can be proved by its negative derivative. The application of LMI in wide area systems is to obtain the gain of controllers in the presence of time delays. In other words, it can be said that through LMI, matrices with large dimensions are solved faster, and therefore the imbalance of the system due to the existence of time delays is avoided [31]. However, the big disadvantage of LMI is its high degree of conservatism, which through the LF; we are looking for solutions that can achieve this degree of conservatism along with the desired stability. Therefore, the design of a suitable LF should include variables that, in addition to maintaining the degree of conservatism of LMI, also have the necessary stability. In [32], Pad approximation is used as delay modeling in LMI for WADC design where only fixed delays are controlled. In [33], the problem of solving time-varying delays based on feedback signals by LMI is investigated. However, additional variables and cross terms are not used in the LF structure. Therefore, the analysis of LMI has been done in a very simple way, so that the long-range delay is easily replaced by its boundaries, and as a result, it is not possible to accurately track it.

In [23], the design of the robust damper controller for the power system is transformed into a general H_∞ problem and solved by the LMI method, but the selection of the optimal

weight parameters for the H_∞ controller is difficult. Based on the above studies, in this paper, an improved optimal control method based on the FWM approach is used to design the WADC, which has the ability to effectively compensate for time delays. Therefore, the main purpose of the damping controller in this paper is to be able to damp the inter-area modes through the WADC in the SSSC converter. Based on this, first the remote signals are determined by the visibility and controllability index and then it enters the FWM design process as a $u(t - \tau) = Kx(t - \tau)$ signal. Finally, based on the response obtained from the design method, damping signals can be applied to the SCESS control loop along with time delay compensation.

Briefly, the innovations of this paper are presented under the following comments:

- New FWM design to compensate for the uncertainty caused by continuous and disruptive time delays.
- Adapting the FWM method to the LMI in the form of an optimization problem.
- Combined modeling of energy storage system with RES in large-scale power system.

The written structure of this paper is as described in the second part of the supplementary explanations related to WADC design. This section includes subsections related to FWM modeling, observer-based state feedback. The third part is related to the modified 16-machine power system model, the dynamic equations of the synchronous generator and DFIG along with the block diagram of the controllers. In the fourth part, the simulation results have been analyzed and in the fifth part, the conclusion of the proposed method has been reported.

2. THE WADC DESIGN

The use of small signal analysis is a practical method in obtaining the critical modes of the power system for designing optimal gains in damping controllers. Therefore, when using WAMS, the problem of variable time delay should be considered. For this purpose, in this work, Pade's first-order approximation along with the use of low-pass and high-pass filters have been used to model the time delay. In addition to compensating the time delay, the K gain related to the state feedback control matrix has been optimally extracted using FWM. On the other hand, the gain matrix K is for state variables, and therefore, these states cannot be easily measured in systems with large dimensions. Therefore, in this work, the state observer $O_b(s)$ has been introduced to observe the state variables based on pole placement, so that a more accurate response can be made from the controller design.

2.1. FWM method

Delay-dependent and delay-independent criteria are two methods in the design of delay controllers. Considering that the delay-dependent measure uses delay size information, but the delay-independent stability measure does not need this information; Therefore, the delay-dependent criterion usually has a lower degree of conservatism than the delay-independent criterion, and it becomes more prominent when the time delays are small. The Lyapunov method is a main method for deriving the delay-dependent criterion, in which the discretized Lyapunov is one of the most efficient methods, but combining this method with the control system is very difficult and complicated. Another method is to transform the

fixed model, one of the most effective and practical of which is the combined method of Park's and Moon's inequalities, whose preliminary model is presented in reference [34, 35]. However, extensive research in this field continues. Therefore, the FWM method is proposed as a new method to solve the stability problem in many delayed systems. In the present work, the degree of conservatism of the controller is reduced compared to the fixed model transformation methods. In the fixed model transformation, when the LF derivative is calculated, the upper bound estimate of Park's and Moon's inequality methods should be used. In contrast, the FWM method does not require bounding techniques for some cross terms. To illustrate this, a common stability problem for a delayed system is considered as follows (1):

$$\begin{cases} \dot{x}(t) = \bar{A}x(t) + \bar{B}x(t_1) + \bar{C}u(t) \\ t_1 = t - \tau \end{cases} \quad (1)$$

In (1), \bar{A} , \bar{B} , and \bar{C} represent fixed real matrices with suitable dimensions. τ is used to represent the time delay and $u(t)$ is used to introduce the input control signal. In this paper, to introduce the Lyapunov function, we describe (2) [31]:

$$\begin{aligned} \bar{V}(t, x_t) = & x^T(t) \bar{P} x(t) + \int_{t_1}^t x^T(s) \bar{Q} x(s) ds \\ & + \int_{-\tau}^0 \int_{t+\theta}^t \dot{x}^T(s) \bar{Z} \dot{x}(s) ds d\theta \end{aligned} \quad (2)$$

In (2), the first and second parts of LF are considered as potential kinetic energy quantities in mechanical systems, and the third term is used for the derivative. $\bar{P} = \bar{P}^T$, $\bar{Q} = \bar{Q}^T$, $\bar{Z} = \bar{Z}^T$ expressions should be determined and then the derivative of the LF should be calculated as (3) [31]:

$$\begin{aligned} \dot{V}(x_t) = & \dot{x}^T(t) \bar{P} x(t) + x^T(t) \bar{P} \dot{x}(t) + x^T(t) \bar{Q} \dot{x}(t) \\ & - x^T(t_1) \bar{Q} x(t_1) + \tau \dot{x}^T(t) \bar{Z} \dot{x}(t) \\ & - \int_{t_1}^t \dot{x}^T(s) \bar{Z} \dot{x}(s) ds \end{aligned} \quad (3)$$

In order to provide the LMI-based stability criterion, using the conventional stationary model transformation and LF, the right-hand side of (4) is usually added to the $V(t, x_t)$ derivative in (3). Based on this, we will have (4) [31]:

$$0 = 2x^T(t) \bar{P} \bar{B} \left[x(t) - x(t_1) - \int_{t_1}^t \dot{x}(s) ds \right] \quad (4)$$

In (4), \bar{B} is the matrix of coefficients and \bar{P} is the Lyapunov matrix.

It is clear that for conventional solutions such as time-constant model transformation, inequalities must be solved to satisfy the $\dot{V}(x_t) < 0$ condition; therefore, determining \bar{B} and \bar{P} matrices is a serious limitation in solving classical methods that cannot be obtained freely. For this purpose, in the proposed method to reduce the degree of conservatism of LMI, the derivative of the LF is used in such a way that the matrices M and N are placed as auxiliary links in the New Leibniz problem instead of \bar{B} and \bar{P} . Therefore, calculating the derivative of (3) is equivalent to adding the right side of (5) to $\dot{V}(x_t) < 0$. Then we can provide some LMI inequalities to satisfy the condition. Based on this, we will have:

$$0 = [x^T(t) \bar{M} + \dot{x}^T(t) \bar{N}] \left[x(t) - x(t_1) - \int_{t_1-\tau}^t \dot{x}(s) ds \right] \quad (5)$$

So, as seen in the FWM method, there is no need to choose \bar{B} and \bar{P} , and it is enough to optimize \bar{M} and \bar{N} by solving the LMIs, so the FWM method reduces the degree of conservatism of the controller for the time delay system.

2.2. Mathematical Modeling for WADC Design Based on FWM Method

This section has been investigated using the modeling of power system components including synchronous machines, wind turbines and loads in the form of state space. In the analysis of the state space matrix, BESS supplementary signal is used as input and WAMS signals are used as output in the design. Furthermore, when the time delay is used as the transmission delay for the WADC controller input, the linearized system model is expressed as (6):

$$\begin{cases} \dot{x}(t) = \bar{A}x(t) + \bar{B}u(t_1) \\ y(t) = \bar{C}x(t) \end{cases} \quad (6)$$

In (6), vectors \bar{A} and \bar{B} , and \bar{C} correspond to the state, input, and output matrices, respectively. The state feedback controller can be expressed as (7):

$$u(t_1) = Kx(t_1) \quad (7)$$

According to (5) for the open loop system and also (6) for the expression of the controller, the closed loop system can be described as (8):

$$\begin{cases} \dot{x}(t) = \bar{A}x(t) + \bar{B}Ku(t_1) \\ y(t) = \bar{C}x(t) \end{cases} \quad (8)$$

The purpose of this section is to provide a delay-dependent stability criterion in the new model to optimally provide the controller gain in the presence of time delay, so that the closed-loop system of (8) remains stable. Therefore, with the definition of Lemma 1, we will have:

Lemma 1 (Schur's complement [36]): According to the definition of Schur's complement, in order to make the matrix $(\bar{S} = \bar{S}^T = \begin{bmatrix} \bar{S}_{11} & \bar{S}_{12} \\ \bar{S}_{21} & \bar{S}_{22} \end{bmatrix} (\bar{S}_{11} \in \mathbb{R}^{r \times r}))$ symmetric, the following three conditions must be met:

1. $\bar{S} < 0$
2. $\bar{S}_{11} < 0, \bar{S}_{22} - \bar{S}_{12}^T \bar{S}_{11}^{-1} \bar{S}_{12} < 0$
3. $\bar{S}_{22} < 0, \bar{S}_{11} - \bar{S}_{12}^T \bar{S}_{22}^{-1} \bar{S}_{12} < 0$

Theorem 1: In a certain scalar such as h , a feedback controller such as (7) can exist for which the closed loop system (8) remains stable, provided there are $Y = \begin{bmatrix} Y_{11} & Y_{12} \\ Y_{21} & Y_{22} \end{bmatrix} \geq 0, \bar{L} = \bar{L}^T > 0, \bar{Q}_1 = \bar{Q}_1^T > 0, \bar{R} = \bar{R}^T > 0$ and matrices \bar{M}_1, \bar{M}_2 . Also, \bar{V} is used in such a way that matrix inequalities (9) and (10) are satisfied [31]:

$$\begin{aligned} & \bar{\Phi} \\ & = \begin{bmatrix} \bar{A}\bar{L} + \bar{L}\bar{A}^T + \bar{M}_1 + \bar{M}_1^T + \bar{Q}_1 + h\bar{Y}_{11} & \bar{B}\bar{V} - \bar{M}_1 & h\bar{L}\bar{A}^T \\ * & -\bar{M}_2 - \bar{M}_2^T & h\bar{V}^T \bar{B}^T \\ * & * & -h\bar{R} \end{bmatrix} \quad (9) \\ & < 0 \end{aligned}$$

$$\bar{\Psi} = \begin{bmatrix} Y_{11} & Y_{12} & \bar{M}_1 \\ * & * & -\bar{M}_2 \\ * & * & \bar{L}\bar{R}^{-1}\bar{L} \end{bmatrix} > 0 \quad (10)$$

where the sign * indicates the symmetry of the matrix and $K = \bar{V}\bar{L}^{-1}$ the gain of the feedback controller.

Proof: According to the Newton-Leibniz formula, we have (11):

$$x(t) - x(t_1) - \int_{t_1}^t \dot{x}(s)ds = 0 \quad (11)$$

According to (10), for every matrix with appropriate dimensions \bar{N}_1 and \bar{N}_2 , equation (12) is satisfied:

$$0 = 2(x^T(t)\bar{N}_1 + x^T(t_1)\bar{N}_2) \times \left[x(t) - x(t_1) - \int_{t_1}^t \dot{x}(s)ds \right] \quad (12)$$

In the definition of any semi-positive definite matrix such as $Y = \begin{bmatrix} X_{11} & X_{12} \\ X_{12}^T & X_{22} \end{bmatrix} \geq 0$, equation (13) can be satisfied [31]:

$$\bar{h}\bar{\xi}^T(t)X\bar{\xi}(t) - \int_{t_1}^t \bar{\xi}^T(s)X\bar{\xi}(s)ds > 0 \quad (13)$$

where $\bar{\xi}(t) = [x^T(t), x^T(t_1)]^T$.

Now, by constructing the candidate LF, we will have equation (14) [31]:

$$V(x_t) = x^T(t)\bar{P}x(t) + \int_{t_1}^t x^T(s)\bar{Q}x(s)ds + \int_{-\bar{h}}^0 \int_{t+\theta}^t \dot{x}^T(s)\bar{Z}\dot{x}(s)dsd\theta \quad (14)$$

where $\bar{P} = \bar{P}^T > 0, \bar{Q} = \bar{Q}^T > 0, \bar{Z} = \bar{Z}^T > 0$ should be determined.

Then, by calculating the derivative of $V(x_t)$ in (14) for system (8), we will have (15):

$$\begin{aligned} \dot{V}(x_t) &= \dot{x}^T(t)\bar{P}x(t) + x^T(t)\bar{P}\dot{x}(t) + x^T(t)\bar{Q}\dot{x}(t) \\ &\quad - x^T(t_1)\bar{Q}x(t_1) + \bar{h}\dot{x}^T(t)\bar{Z}\dot{x}(t) \\ &\quad - \int_{t_1}^t \dot{x}^T(s)\bar{Z}\dot{x}(s)ds \\ &= x^T(t)[\bar{P}\bar{A} + \bar{A}^T\bar{P}]x(t) + 2x^T(t)\bar{P}\bar{B}\bar{K}x(t_1) \\ &\quad + x^T\bar{Q}x(t) - x^T(t_1)\bar{Q}x(t_1) \\ &\quad + \bar{h}[\bar{A}x(t) + \bar{B}\bar{K}x(t_1)]^T\bar{Z}[\bar{A}x(t) + \bar{B}\bar{K}x(t_1)] \\ &\quad - \int_{t-h}^t \dot{x}^T(s)\bar{Z}\dot{x}(s)ds \end{aligned} \quad (15)$$

The next, by adding the right-hand side of (12) and (13) to $\dot{V}(x_t)$, equation (16) is derived (Appendix 3).

We also define (17) and (18):

$$\bar{\Xi} = \begin{bmatrix} \bar{P}\bar{A} + \bar{A}^T\bar{P} + \bar{Q} + \bar{h}X_{11} & \bar{P}\bar{B}\bar{K} - \bar{N}_1 + \bar{N}_2^T \\ +\bar{N}_1 + \bar{N}_1^T + \bar{h}\bar{A}^T\bar{Z}\bar{B}\bar{K} & -\bar{N}_2 + \bar{N}_2^T - \bar{Q} \\ * & +\bar{h}\bar{K}^T\bar{B}^T\bar{Z}\bar{B}\bar{K} \end{bmatrix} \quad (17)$$

$$\bar{\Psi} = \begin{bmatrix} X_{11} & X_{12} & \bar{N}_1 \\ * & X_{22} & \bar{N}_2 \\ * & * & \bar{Z} \end{bmatrix} \quad (18)$$

It can be seen from (16) that if it is $\Xi < 0, \Psi > 0$, then it is $\dot{V}(x_t) < 0$ and this means that the closed loop system of (8) is stable. The next, based on Lemma 1, $\Xi < 0$ can be easily provided in (19) (Appendix 3).

To obtain the K gain of the controller, it is necessary to use the following definitions:

$$\begin{aligned} \bar{L} &= \bar{P}^{-1}, \bar{M}_1 = \bar{P}^{-1}\bar{N}_1\bar{P}^{-1}, \bar{M}_2 = \bar{P}^{-1}\bar{N}_2\bar{P}^{-1}, \bar{R} = \bar{Z}^{-1}, \bar{V} \\ &= \bar{K}\bar{P}^{-1}, \bar{Q}_1 = \bar{P}^{-1}\bar{Q}\bar{P}^{-1}, Y \\ &= \text{diag}\{\bar{P}^{-1}, \bar{P}^{-1}\}X\text{diag}\{\bar{P}^{-1}, \bar{P}^{-1}\} \end{aligned}$$

By multiplying the right-hand and left-hand sides of (19) by $\text{diag}\{\bar{P}^{-1}, \bar{P}^{-1}, \bar{Z}^{-1}\}$, equation (20) is extracted (Appendix 3).

Obviously, equation (19) becomes equivalent to (9). Similarly, by multiplying the sides of (18) by $\text{diag}\{\bar{P}^{-1}, \bar{P}^{-1}, \bar{P}^{-1}\}$, equation (18) becomes equivalent to (10). Therefore, the proof of theorem 1 is completely finished.

According to the definition of Theorem 1, equation (10) can no longer be called an LMI due to the nonlinear conditions of $\bar{L}\bar{R}^{-1}\bar{L}$, therefore, it is not possible to use the convex optimization algorithm to search for the minimum value. For this reason, this paper uses cone complementarity linearization algorithm so that this algorithm is able to solve LMI [37]. Based on this, we can define the nonlinear optimization problem and its related constraints as (21) (Appendix 3).

In the following, according to the mentioned non-linear optimization process, the optimal gain matrix of the controller as well as the maximum value of the $\bar{h} = \max(\tau)$ delay margin can be searched using the iterative algorithm proposed below.

Algorithm solution process:

Step 1: First, a small initial value for the delay margin should be chosen so that it can satisfy the feasibility region for (9) and (21).

Step 2: First, a set of possible matrix variable values should be set for $(\bar{L}', \bar{L}_1', \bar{V}', \bar{M}_1', \bar{M}_2', \bar{F}', \bar{F}_1', \bar{Q}', \bar{R}', \bar{R}_1', \bar{Y}')$, so that it satisfies (9) and (21), and then $k = 0$ is set.

Step 3: Solving the aforementioned nonlinear optimization problem with the constraints of LMIs in (9) and (21) and then setting:

$$\begin{aligned} \bar{F}_{k+1} &= \bar{F}, \bar{F}_{1,k+1} = \bar{F}_1, \bar{L}_{k+1} = \bar{L}, \bar{L}_{1,k+1} = \bar{L}_1, \bar{R}_{k+1} \\ &= \bar{R}, \bar{R}_{1,k+1} = \bar{R}_1. \end{aligned}$$

Step 4: If the inequality (10) is possible, increase the scalar value h to a small amount and then return to step 2. Stop if inequality (10) is not feasible in a certain number of iterations. And otherwise, set step $k = k + 1$ and go to step 3.

Therefore, according to theorem 1 and the aforementioned algorithm, we will be able to obtain the optimal benefit of the feedback controller along with the maximum delay margin.

2.3. Observer-based state feedback design

In practical power systems, because the working state variables are not fully observed, it is usually preferred to use a feedback controller with measurable variables. Therefore, the state observer $Ob(s)$ has been used to observe the state

variables unavailable for WAMS. In the present work, the mode observer based on normal pole placement is used in the design process [38]. In Fig. 1, the structure of the state observer in the WADC design is shown. In this case, the design process is done in two stages:

Step 1: determining a state feedback gain matrix for the desired poles of the system.

Step 2: determination of an observer's gain matrix for optimal placement of the observer's poles.

By combining the state space equations of the system and the observer equations and by defining the $e(t)$ error signal (difference between the actual and estimated signal), we will have (22):

$$\begin{bmatrix} \dot{x}(t) \\ \dot{e}(t) \end{bmatrix} = \begin{bmatrix} \bar{A} - \bar{B}\bar{K} & -\bar{B}\bar{K} \\ 0 & s\bar{I} - \bar{A} - \bar{L}\bar{C} \end{bmatrix} \quad (22)$$

Equation (22) describes the dynamics of a closed loop system with a state feedback controller and an observer. Therefore, the characteristic equation of the closed loop system is (23):

$$\begin{bmatrix} \bar{A} - \bar{B}\bar{K} & -\bar{B}\bar{K} \\ 0 & s\bar{I} - \bar{A} - \bar{L}\bar{C} \end{bmatrix} = 0 \quad (23)$$

And as a result we will have (24):

$$|s\bar{I} - \bar{A} + \bar{B}\bar{K}||s\bar{I} - \bar{A} - \bar{L}\bar{C}| \quad (24)$$

Therefore, the closed loop poles of the state feedback control system with the observer are formed from the sum of the poles resulting from the state feedback design and the observer design. This means that the design of the observer and the positioning of the pole with mode feedback are done separately and independently from each other.

The desired poles of the closed loop (caused by the state feedback) are determined in such a way that the performance characteristics of the closed loop system are met. The poles of the observer are also determined in such a way that the response of the observer is much faster than the response of the system. A rule of thumb for determining the location of observer poles is to choose them in such a way that the response of the observer is 2 to 10 times faster than the response of the system. Therefore, in this paper, by forming state and observability matrices in MATLAB software, it is possible to obtain the sum of closed loop poles with state and observer feedback. Therefore, first, the closed loop poles of the system are extracted using the command $\bar{P} = \text{eig}(A)$ in MATLAB software, and considering that we need the dynamics of the observer to be faster than the system itself, the poles of the observer must be at least 3 times farther from be the dominant poles of the system. Therefore, after obtaining the dominant poles of the system as $P = \text{eig}(A)$ and placing these poles with a factor of 3 times farther from \bar{P} as \bar{P}_1 , the gain of the observer can be extracted using the $\bar{L} = \text{place}(\bar{A}', \bar{C}', \bar{P}_1)$ command.

In this paper, for gain K , we will have feedback according to the proposed controller and for gain L , we will have an observer in MATLAB software (Appendix 3).

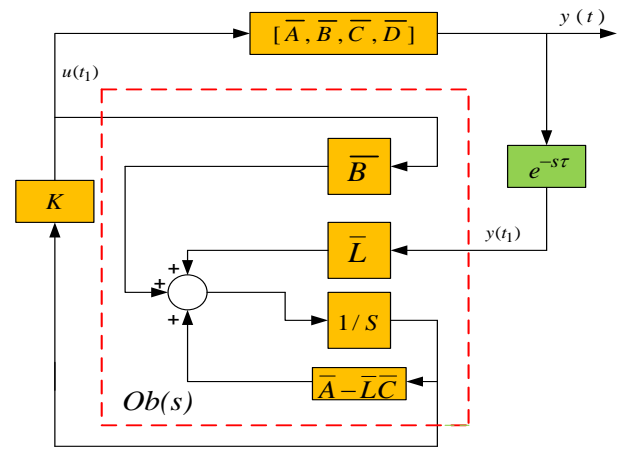


Fig. 1: Structure of state observer in WADC design for closed loop system.

3. THE SYSTEM UNDER OPERATION

According to Fig. 2, in this paper, the improved power system of 16 machines and 68 buses is used as a large-scale network for the performance of the proposed controller. For this purpose, the power system is connected to a DFIG-based wind farm equipped with SCESS through the SSSC compensator. The information of this network in connection with the parameters of transmission lines of synchronous generators and excitation system is reported in [38]. In the improved power system, the wind farm has a power of 100 MW, and in order to reduce wind fluctuations, a SCESS with a bidirectional converter is used in the DC link. According to the results of modal analysis in the power grid, between machines 10 and 14 there is an inter-area oscillatory mode with a frequency of 0.56 Hz and a damping ratio of 0.0165. For such LFO, WADC-based supplementary controller strategy for SSSC is better than injecting local signals. However, it should be noted that for effective application of WADC, appropriate wide feedback signals should be selected first. In this regard, based on the index JCOI [39], the power changes of P1-48 lines have a higher observability than the active power of other lines, so it has been used as a candidate for the stabilizing feedback signal to the WADC input. It should be noted that all synchronous generators are modeled with 5th order dynamic model, wind unit with 4th order model, SCESS unit with 2nd order and SSSC modeled with 2nd order. By specifying the input vector $U = [\Delta V_R, \Delta X_F]$ and the output vector $Y = [\Delta E_{fd}, \Delta \alpha_{se}]$, the system model can be reduced to order 13 using the *schmr* reduction model. For this purpose, the *schmr* function in the Robust MATLAB Simulink toolbox was used [36]. It is worth mentioning that local PSS is installed on generators (G₁, G₄, G₈, G₉, G₁₂, G₁₃, G₁₄, G₁₅, G₁₆) by default. For the purpose of comparison, in addition to the design of the WADC controller, the classical power oscillation damping (CPOD) controller with PL input (specified in Fig. 2) has been used as a local signal in the SSSC. This controller has no time delay because it is fed through the local signal.

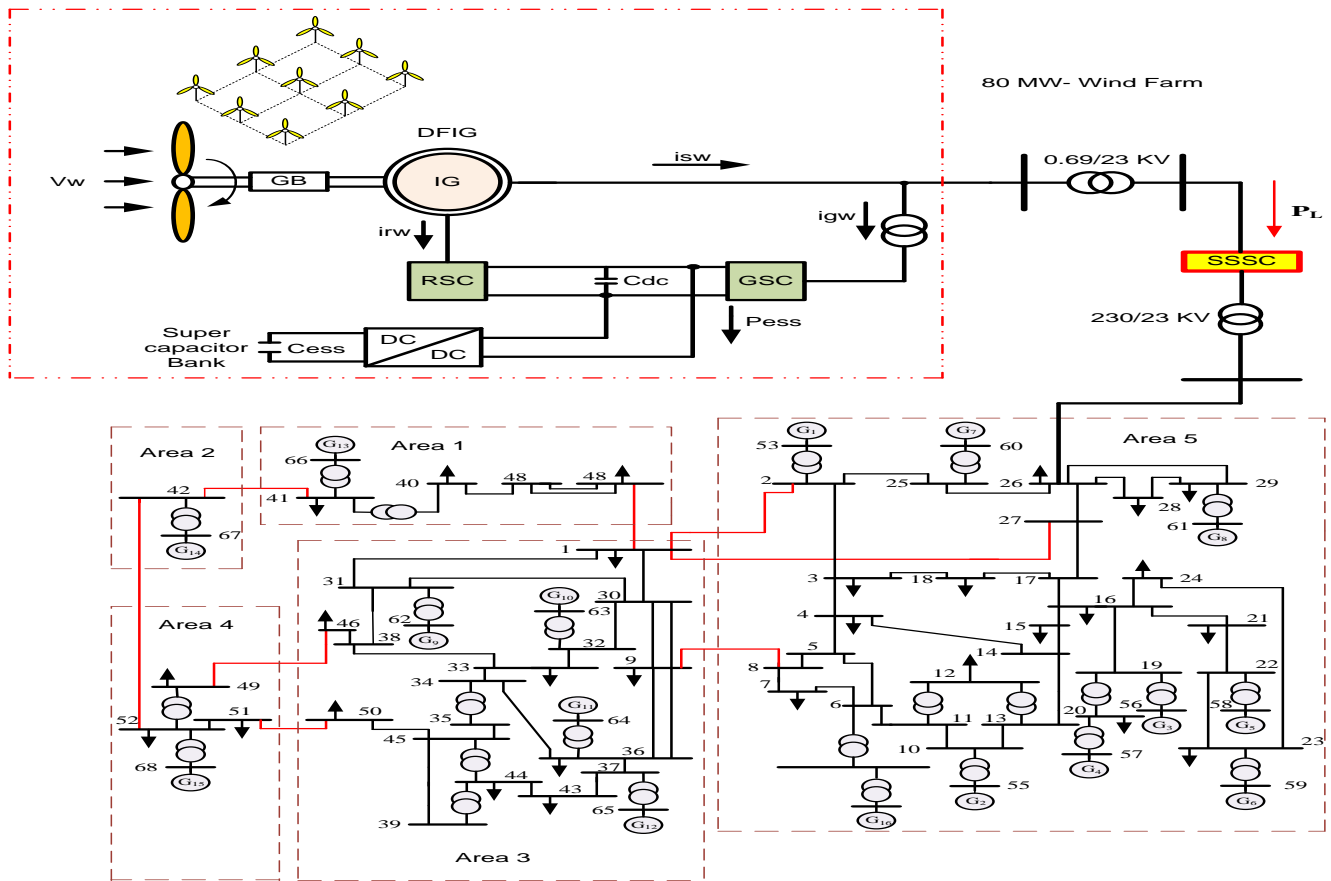


Fig. 2: Single-line diagram of the power system under study.

3.1. Modeling of the Elements Related to the Power System Under Study

3.1.1. Synchronous generator model

In this part, in order to analyze the dynamic equations of SG, the two-axis model is used [40]. In this model, the effects of sub-transient reactances are ignored and only the transient reactances of the synchronous generator are used in the modeling. Based on this, the dynamic equations of the biaxial model for the i -th SG can be expressed as (25):

$$\begin{cases} \frac{dE'_{qi}}{dt} = \frac{1}{T'_{doi}} [-E'_{qi} + E_{fdi} + (X_{di} - X'_{di})I_{di}] \\ \frac{dE'_{di}}{dt} = \frac{1}{T'_{dqi}} [-E'_{di} - (X_{qi} - X'_{qi})I_{qi}] \\ \frac{dE_{fdi}}{dt} = \frac{-1}{T_{Ei}} [E_{fdi}(K_{Ei} + S_{Ei}(E_{fdi})) - V_{Ri}] \\ \frac{d\omega_i}{dt} = \frac{1}{\tau_{ji}} \times \\ [T_{mi} - [I_{di}E'_{di} + I_{qi}E'_{qi} - (L'_{qi} - L'_{di})I_{di}I_{qi} + D_i\omega_i] \\ \frac{d\delta_i}{dt} = \omega_i - \omega_s \end{cases} \quad (25)$$

3.1.2. DFIG descriptive model

As can be seen from Fig. 3, the DFIG unit connects the RSC and GSC converters back to back through the dc link, and its task is to maintain the power balance between the converters. In the present work, vector method is used for DFIG dynamic modeling [40]. Based on the equations of

voltage and leakage flux in the induction generator, the state equations for the rotor and stator currents in the d-q reference frame can be described as (26) (Appendix 3).

$$\text{In (26) it is } H = \omega_b \cdot (L_{mm}^2 - L_{ss} \cdot L_{rr})^{-1}.$$

3.1.3. SCESS converter controller

In this pipe, a SCEES has been used in order to fully ensure that the DC link voltage is maintained in the air unit. The circuit structure of SCESS is shown in Fig. 4. The SCESS structure includes a capacitor bank and a two-switch DC/DC converter that is connected to the DFIG through a DC link. DC/DC converter can be used in BOOST and BUCK modes depending on S_1 and S_2 switches.

It can be seen from Fig. 4 that the SCESS converter has two switches S_1 and S_2 along with an inductor and energy storage [32].

According to the average value of the dynamic model, the output current of this converter is equal to (27):

$$\begin{cases} \frac{di_{sc}}{dt} = \frac{1}{L_s} (V_{sc} - f_s V_{DC} - R s i_{sc}) \\ i_{sc,DC} = f_s i_{sc} \end{cases} \quad (27)$$

In which, if it is $f_s = D_s$, the converter will work in Buck mode, and if it is $f_s = 1 - D_s$, the converter will work in Boost mode. According to the equivalent circuit in Fig.4, the dc link voltage is equal to (28):

$$\begin{cases} \frac{dV_{Csc}}{dt} = \frac{1}{C_{sc}} (-i_{sc} - \frac{V_{Csc}}{R_{psc}}) \\ V_{sc} = V_{Csc} - R_{sc} i_{sc} \end{cases} \quad (28)$$

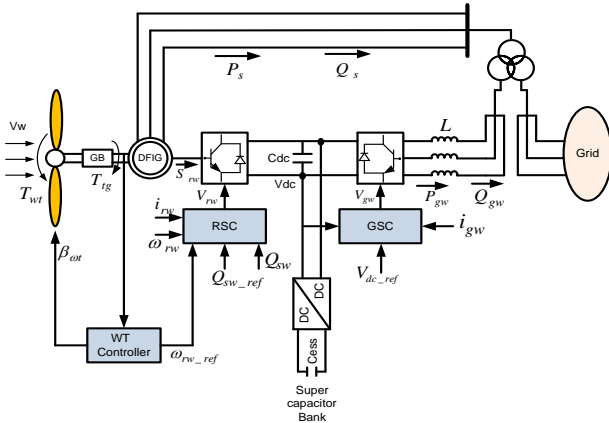


Fig. 3: Diagram of DFIG-based wind turbine.

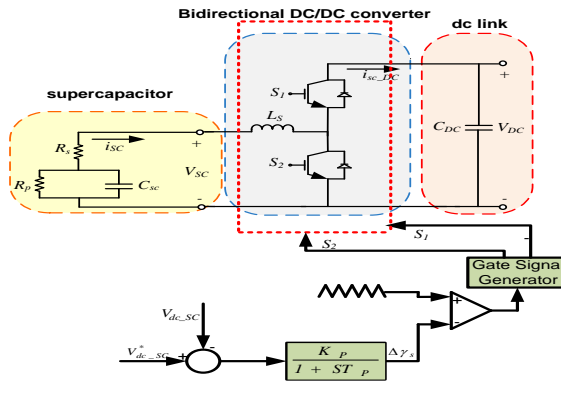


Fig. 4: Control block diagram for SCESS.

3.1.4. SSSC Mathematical Model

The SSSC is used as a voltage source converter (VSC) in both inductive and capacitive modes for compensating reactive power in the transmission line. The circuit structure of this type of FACTS is shown in Fig. 5. In SSSC circuit structure, a VSC, a series transformer, a capacitor with C_{dc} capacity and a controller are used. Using the synchronous reference frame, the series injection voltage in SSSC can be described by (29) in the d-q axis [41]:

$$\begin{cases} v_{ds} = m_c Z_{inv} V_{dc_SSSC} \cos(\alpha_{se}) \\ v_{qs} = m_c Z_{inv} V_{dc_SSSC} \sin(\alpha_{se}) \end{cases} \quad (29)$$

In (29), α_{se} is the phase angle of the injection voltage, m_c is the conversion ratio of the coupling transformer and Z_{inv} is the constant of the inverter, which is related to the voltage of the dc side over the line-phase voltage of the ac side. The dynamic equation of the DC link capacitor in order to maintain the power balance on the dc and ac sides is expressed by (30):

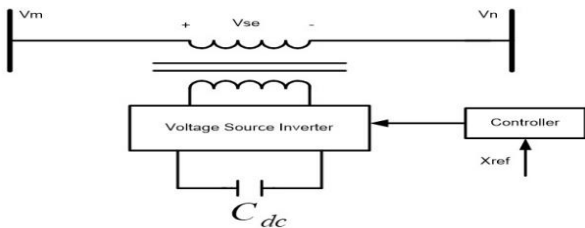


Fig. 5: One-line diagram of a SSSC.

$$\frac{dV_{dc_SSSC}}{dt} = \frac{1}{C_{dc}} [m_c Z_{inv} (i_d \cos \alpha_{se} + i_q \sin \alpha_{se})] - \frac{V_{dc_SSSC}}{C_{dc} R_{dc}} \quad (30)$$

The control block diagram of SSSC for the capacitor mode along with the damping controller is shown in Fig. 6. In this structure, by adding a control signal based on X_{F3} , inter-area fluctuations in the power system can be damped through WADC or CPOD.

4. SIMULATION RESULTS

The structure of the closed loop system for simulations is shown in Fig. 7. In this structure, the loops related to the controllers and how they are related to the power system is specified. All the control loops including the SSSC converter control loop along with the damping control loop, the SCESS converter control loop and the DFIG control loops in the RSC and the GSC are connected to each other through the DC link. The simulation results have been evaluated in the form of four scenarios, so that in this evaluation, the wind pattern for all four scenarios is according to Fig. 8. The SG excitation system is IEEE-1 type, the details of which are reported in [42].

4.1. First scenario

In this scenario, we apply a three-phase short-circuit fault temporarily for 0.1 second near bus 11 (between lines 11-12). Accordingly, in Figs. 9a and 9b, respectively, the changes in the output power of the wind unit and the response of the active power of line 1-48 are shown by applying a time delay of 100ms in sending remote signals to the WADC. It can be seen from the results of this response, even if there is a time delay, the WADC controller provides better stability than the CPOD method. Also, in Figs. 9c and 9d, the DC voltage of SSSC and the reactive power changes of the inter-area line 1-27 per time delay of 100ms are shown, respectively. From the results of this scenario, it can be seen that the proposed controller for damping power fluctuations has a favorable performance against uncertainties caused by time delay and three-phase fault. This improvement is clearly seen both in the settling time and in overshoot and undershoots.

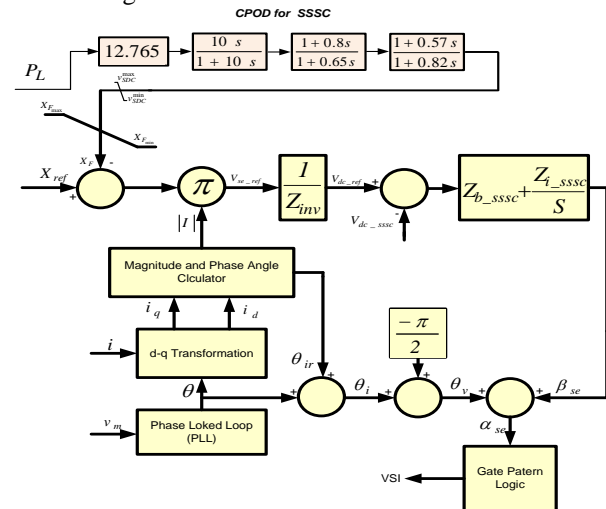


Fig. 6: The proposed damping controller structure for a SSSC.

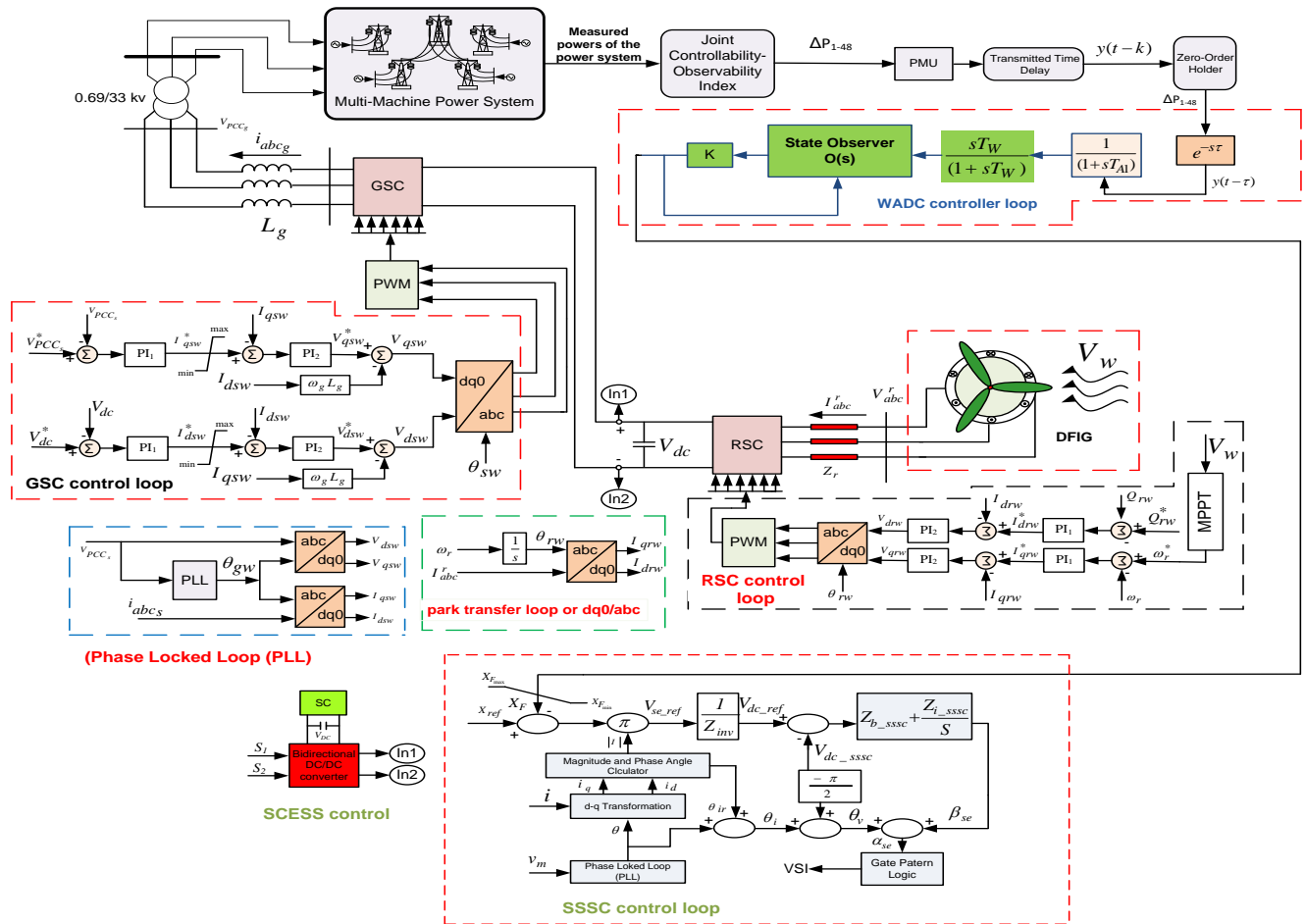


Fig. 7: The closed loop system of the proposed controller along with all the control loops of the converters.

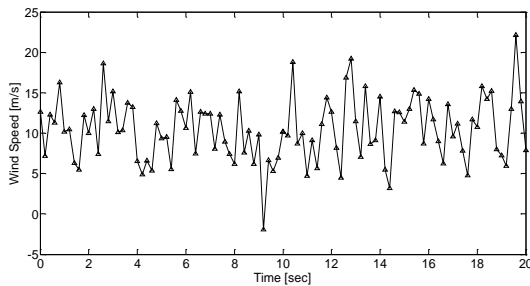


Fig. 8: Wind variation for DFIG unit.

4.2. Second scenario

In this scenario, a three-phase fault occurred permanently near bus 31 (between line 31 and 38) within 2 seconds, and because the fault was not resolved after 0.1 second, line 31-38 was outage. In addition, by changing the input mechanical power of the generators (G_1 , G_4 , G_8 , G_{10} , G_{12}) by +10% and considering the wind pattern as in the first scenario, the simulation results have been evaluated. Based on this, the speed deviation of generators 6-14 in Fig.10 (a), the power changes of line 14-15 in Fig.10 (b), the SSSC output power in Fig.10(c), as well as the power changes of line 8-9 in Fig.10 (d) is shown for time delays of 300ms. From these results of this scenario, it is clearly seen that the proposed controller is optimal under any conditions and provides the desired stability for the system. If in the case without a controller, the oscillations caused by uncertainties are not well damped and the stability of the system decreases with the passage of time.

4.3. Third scenario

In this scenario, in order to operate with greater uncertainty, step changes have been made on the load connected to bus 26 of the power system. Thus: in 5 seconds, the amount of load increased from 3.5 to 4.82, and in 12 seconds, it decreased from 3.82 to 2.22, and again in 25 seconds, it increased from 2.22 to 5.3. The details of these changes are shown in Fig. 11a. It should be noted that the wind speed for the wind farm increases from 11 m/s to 12 m/s with increasing load and decreases from 12 m/s to 11 m/s with decreasing load. In addition, a time delay of 200 milliseconds in 5 seconds is considered for WADC. Figs. 11b and 11c show the speed deviation response of G9-10 and G6-8 for load changes. So that WADC has been able to control and dampen the deviations well at different moments with its accurate performance during load change. The response of changes in active power between buses 41-42 is shown in Fig. 11d, as well as changes in reactive power of the wind unit in Fig. 11e. In this figure, with load reduction in 5 seconds, first the power between lines increased, and with load increase in 12 seconds, the amount of power between lines decreased, and then with load reduction in 25 seconds, the amount of power flow in lines increased. Also, the input attenuation signal for SSSC by the proposed controller is shown in Fig. 11f. According to the results obtained in this scenario, the robustness of the proposed controller under rapid changes in power compared to the CPOD controller has been well demonstrated.

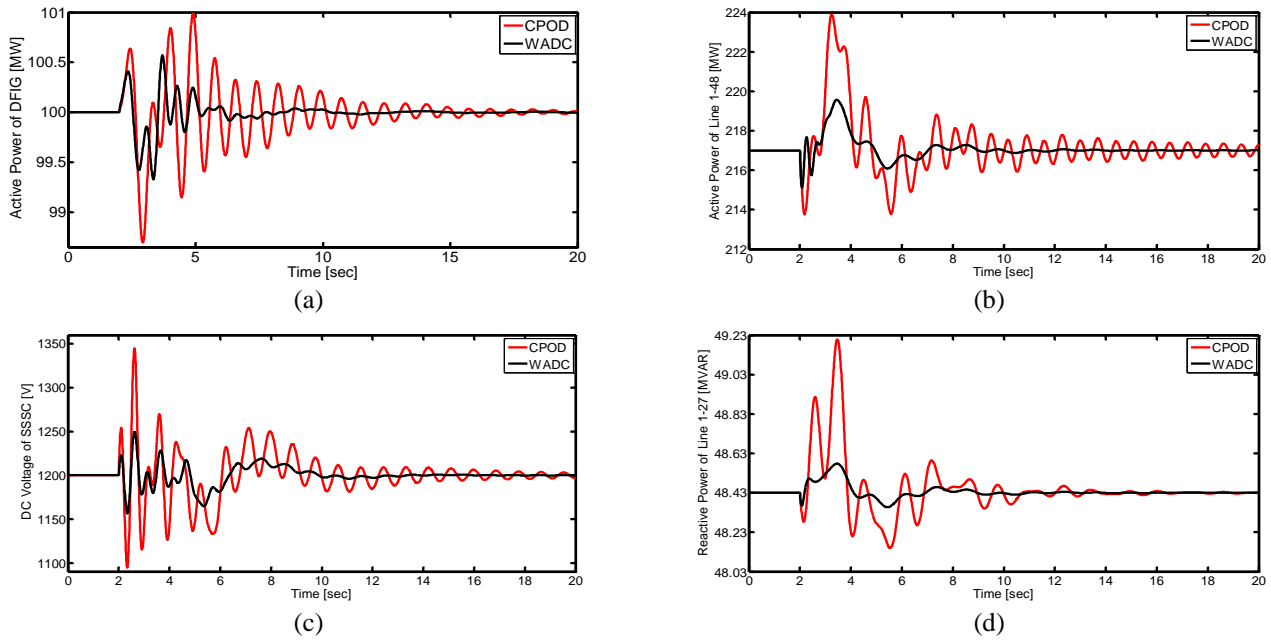


Fig. 9: Response results related to scenario 1.

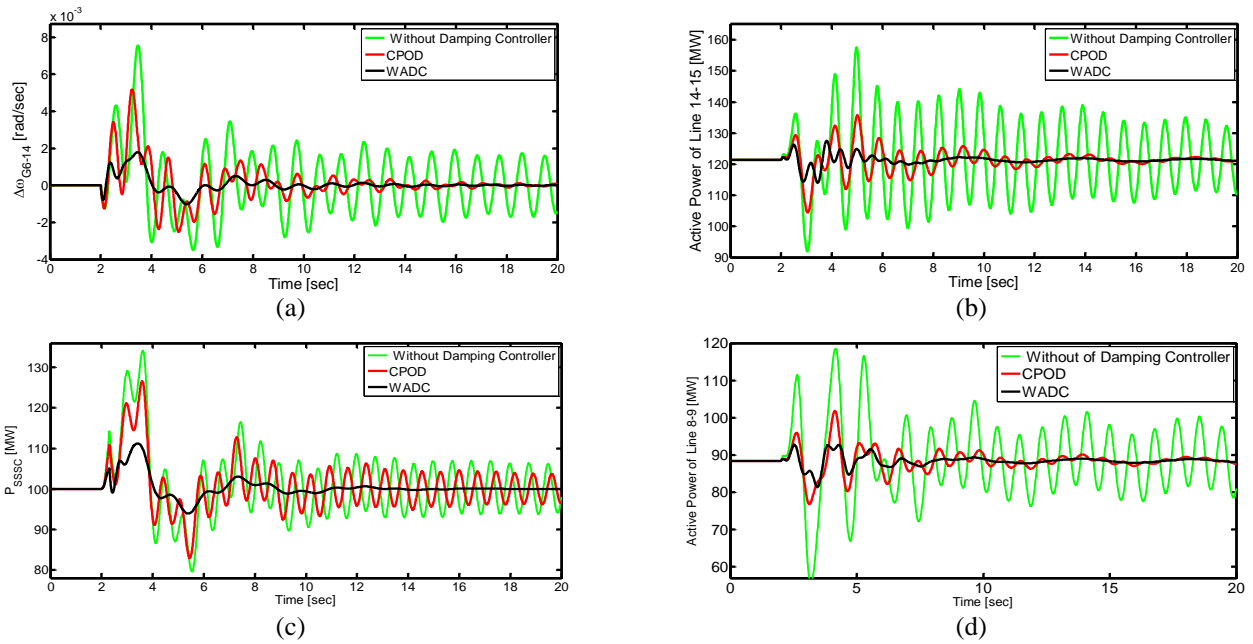


Fig. 10: Response results related to scenario 2.

4.4. Fourth scenario: Case comparison with other methods and discussion and analysis

In this section, in order to show the better performance of the proposed controller compared to references [22, 23], the simulation results have been analyzed. Therefore, by applying a permanent three-phase short-circuit fault in 2 seconds near bus 2 (between line 2 and 3), line 2-3 is outage after 0.1 second due to the fault not being resolved. The pattern of wind blowing and solar radiation is the same as the first scenario and the change in the input mechanical power of the generators (G_1 , G_5 , G_{11} , G_{40}) is considered to be +15%. Based on this, Figs. 12a and 12b show the changes of active power between line 42-52 and DC voltage of SCESS per time delay of 300ms, respectively. From these figs, it can be seen that the improvement of oscillation damping in the proposed

method is much more favorable and faster than the other two references, which has led to the reduction of settling time, overshooting and undershooting. Figs. 12c and 12d show the changes in the active power of the wind unit for the presence and absence of SSSC and SCESS units, respectively. From these figures, it can be seen that due to the outage, each unit is affected by the power grid, wind farm power and SSSC power, which leads to a decrease in the stability of the power system. This is despite the fact that in the presence of SSSC and SCESS units, even if there are time delays of 300 milliseconds at the WADC input, a much more favorable damping is provided than without them. Therefore, the effect of SSSC and SCESS in connecting to the power system and DC link is very important, so that the power fluctuations of renewable units can be improved through these units. In Figs. 12a and 12b, it can be seen that the presence of a fault leads

to changes in the active power and DC voltage of the storage system to more than 5%, which by applying a time delay of 300 milliseconds, the amplitude and cycle of oscillations for the proposed method, reference [22] and [23] is about 8.2, 14.7 and 16.6. It can be seen in Figs. 12c and 12d that if SSSC and SCESS are used alone to compensate the network stability, the existence of fluctuations caused by delay and disturbances lasts for more than 15 seconds. Therefore, the

overshoot and undershoot will be more than 5%, which will not be a good number to maintain optimal stability. But with the optimal design of SSSC together with SCESS, it is possible to reduce the amount of overshoot and undershoot to below 5%, after which the average settling time is reduced to less than 8.476 seconds.

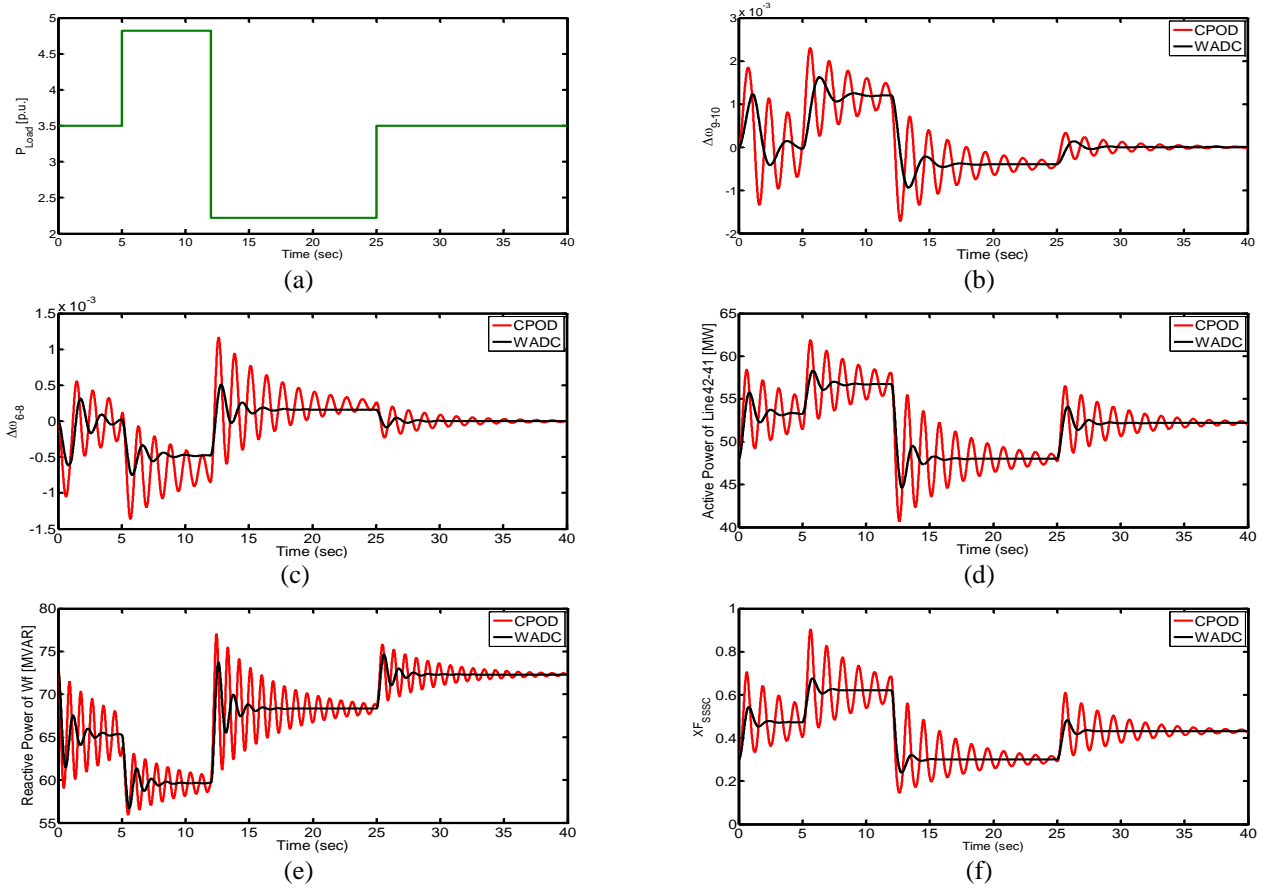


Fig. 11: Response results related to scenario 3.

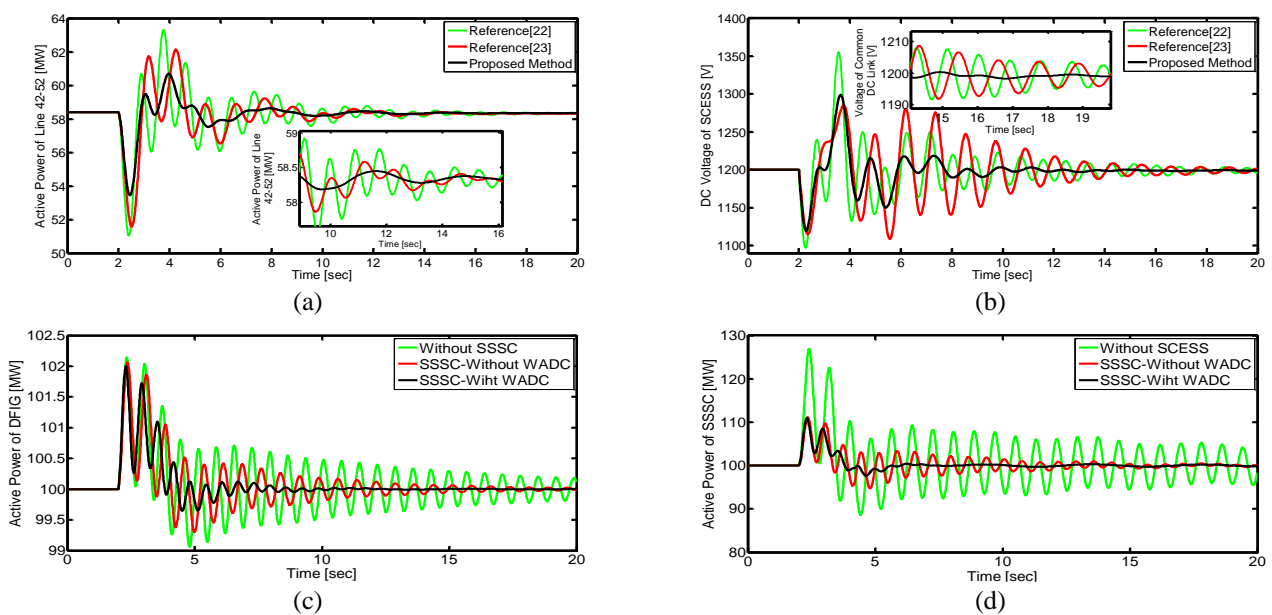


Fig. 12: Response results related to scenario 4.

5. CONCLUSION

In this paper, with the design of the WADC controller, the stability of the power system was evaluated using the FWM method under different scenarios. The FWM design method is solved by introducing a set of nonlinear matrix inequality constraints based on LMI constraints in the form of an optimization problem. In this method, by introducing the non-linear optimization algorithm, it can be used to search for the most optimal gain matrix and the maximum delay margin of the control signal. This design process is able to avoid the destructive effect of large amplitude time delays on the performance of the power system. Finally, the damping signal of the WADC controller was applied using the proposed method as a supplementary signal to the SSSC converter to reduce low frequency oscillations. The simulation results were tested on the improved power system of 16 -machines using MATLAB software. From the results of this simulation, it is clearly seen that in the proposed method, in addition to improving the stability of the power system, the changes caused by time delays in sending signals from far away can be well controlled.

In summary, it can be said that in the proposed method, the average settling time for scenarios 1 and 2 is 8.2 and 8.8 seconds, respectively. Meanwhile, in these scenarios, the average sitting time for the classic CPOD method is equal to 18.5 and 19.65 seconds, respectively. In scenario 3, the overshoot and undershoot values for the proposed method and CPOD are equal to (2.567% and 1.996%) and (5.765% and 4.873%) respectively. In the same way, in scenario 4, the average settling time, overshoot and undershoot compared to the methods in [22] and [23] are equal to (8.476 seconds, 2.328% and 2.096%), respectively (14.532 seconds and 4.842% and 3.559%) and (16.956 seconds and 4.389% and 3.994%) have been obtained. Based on this, it can be seen that the proposed method has been of great help in improving of the settling time, overshoot and undershoot of fluctuations.

APPENDICES

Appendix 1. Adapting the proposed method to the studied power system

This part of matching the proposed controller with the dynamic model of the system includes: synchronous machines [40], wind power plant [40], BESS [42] and SSSC [41]. Therefore, for the closed loop system of (6), X is the state vector of the system, U is the input vector, and Y is the output state vector, which are defined in this paper as follows:

$$\begin{cases} X = [\Delta i_{dsw}, \Delta i_{qsw}, \Delta i_{drw}, \Delta i_{qrw}, \Delta E'_d, \Delta E'_q, \Delta E_{fd}, \Delta \delta, \\ \Delta \omega, \Delta i_{SC}, \Delta V_{CSC}, \Delta \alpha_{se}, \Delta V_{dc_sssc}]^T \\ U = [\Delta V_R, \Delta X_F] \\ Y = [\Delta E_{fd}, \Delta \alpha_{se}] \end{cases}$$

For the above vectors we will have:

$\Delta i_{dsw}, \Delta i_{qsw}, \Delta i_{drw}, \Delta i_{qrw}$: Corresponding to the stator and rotor currents of the wind unit in d and q axes, respectively.

$\Delta E'_d, \Delta E'_q$: Corresponding to the electromotive force voltage of synchronous generators in d and q axes, respectively.

$\Delta E_{fd}, \Delta \delta, \Delta \omega, \Delta V_R$: Respectively related to excitation field voltage, rotor angle, rotor speed and supplementary signal of PSS controller in synchronous generators [43].

$\Delta i_{SC}, \Delta V_{CSC}, \Delta \alpha_{se}$: Respectively related to the current, voltage and switching signal of the PWM converter in the BESS control loop.

ΔV_{dc_sssc} : SSSC compensator dc voltage.

ΔX_F : Supplementary damping controller signal sent through WADC to SSSC.

The values of matrices A, B and C are equal to:

$$A = \begin{bmatrix} 1.2435 & 0.5671 & 0.1256 & 0.9801 & 0.3451 & 1.7654 & 0.4056 & 0.5674 & 0.7658 & 0.2345 & 0.6547 & 1.2087 & 0.5187 \\ 0.4062 & 0.6134 & 1.8964 & 0.9380 & 0.5438 & 0.3275 & 0.5610 & 0.7403 & 1.5021 & 0.6581 & 0.8055 & 0.4328 & 0.6004 \\ 0.7630 & 0.6543 & 0.6754 & 1.4571 & 1.5430 & 0.5611 & 0.1134 & 1.3267 & 1.2278 & 0.1087 & 1.5670 & 0.4328 & 0.5611 \\ 1.3335 & 1.6533 & 0.7641 & 0.8904 & 1.8601 & 1.7773 & 0.8765 & 0.7653 & 0.4455 & 0.7655 & 0.6531 & 0.7004 & 0.7432 \\ 0.4033 & 0.5427 & 1.6187 & 1.5890 & 0.9403 & 0.8126 & 1.2864 & 0.4243 & 0.5679 & 0.5428 & 0.6541 & 0.6507 & 1.4506 \\ 0.6643 & 0.6782 & 0.8439 & 0.7901 & 1.8404 & 0.8175 & 0.5602 & 1.7632 & 0.8922 & 0.9027 & 0.8900 & 0.9764 & 0.9654 \\ 0.8765 & 0.5431 & 1.7654 & 1.8612 & 0.4428 & 0.5670 & 1.4321 & 1.6643 & 0.8754 & 1.6540 & 0.6543 & 1.4328 & 0.7654 \\ 0.5432 & 0.6704 & 0.4328 & 0.8953 & 1.7654 & 0.2109 & 0.5130 & 0.1986 & 0.2687 & 0.4356 & 1.7521 & 0.6705 & 1.7608 \\ 0.5631 & 0.1778 & 0.5899 & 0.4332 & 0.6477 & 0.6728 & 0.8769 & 0.6654 & 1.1345 & 0.2876 & 0.5431 & 0.7567 & 0.8876 \\ 0.4332 & 0.6088 & 1.4328 & 0.8601 & 0.7754 & 0.8658 & 1.4458 & 1.7765 & 0.3322 & 0.5548 & 0.8876 & 1.6654 & 1.8904 \\ 0.6367 & 1.8654 & 0.6784 & 1.0876 & 0.5567 & 0.7439 & 0.8992 & 0.9701 & 1.0677 & 0.9978 & 0.3379 & 0.5543 & 0.8327 \\ 1.0408 & 0.6648 & 0.3972 & 0.6520 & 1.1390 & 0.7694 & 0.4861 & 0.3863 & 0.8129 & 0.9411 & 0.6034 & 1.4561 & 0.8750 \\ 0.6276 & 0.5399 & 0.6499 & 0.6781 & 0.7892 & 0.8904 & 0.7432 & 0.7894 & 0.6432 & 0.8902 & 1.432 & 1.167 & 0.6571 \end{bmatrix}$$

$$B = \begin{bmatrix} 0 & 0 & 0 & 0 & 0 & 0 & 0.9765 & 0 & 0 & 0 & 0 & 0 & 0 \\ 0 & 0 & 0 & 0 & 0 & 0 & 0 & 0 & 0 & 0 & 0 & 0.8765 & 0 \end{bmatrix}$$

$$C = \begin{bmatrix} 0 & 0 & 0 & 0 & 0 & 0 & 0.6543 & 0 & 0 & 0 & 0 & 0 & 0 \\ 0 & 0 & 0 & 0 & 0 & 0 & 0 & 0 & 0 & 0 & 0 & 0.9501 & 0 \end{bmatrix}$$

Appendix 2. The information related to the controller parameters is reported in Table 1.

Table 1: Information about controllers and parameters related to them.

| Information about the BESS along with the controllers related to it | | | |
|---|-------------------------------|---|---|
| $R_s=0.1 \ \Omega$ | $R_p=0.04 \ \Omega$ | $L_s=4.5 \ \text{mH}$ | $C_{sc}=75\mu\text{f}$ |
| $T_w=10$ | $T_{A1}=2.45$ | $K_{pf}=6.65$ | $K_{if}=3.15$ |
| $K_{pg}=6.65$ | $K_{ig}=6.65$ | <i>(switching frequency) $f=5 \ \text{KH}$</i> | |
| Information about DFIG controllers | | | |
| $PI1:K_{p1}=4.65,K_{i1}=1.51$ | $PI2:K_{p2}=6.43,K_{i2}=2.32$ | $R_g+j\omega L_g=0.86+j0.054\omega\Omega$ | $R_g+j\omega L_g=0.22+j.0.18\omega\Omega$ |

Appendix 3. Equations (16), (19), (20), (21), (26) and gain K and gain L , which were used in this paper are defined as follows:

$$\begin{aligned} \dot{V}(x_t) = & x^T(t)[\bar{P}\bar{A} + \bar{A}^T\bar{P}]x(t) + 2x^T(t)\bar{P}\bar{B}Kx(t_1) + x^T\bar{Q}x(t) - x^T(t_1)\bar{Q}x(t_1) + h[\bar{A}x(t) + \bar{B}Kx(t_1)]^T \\ & \bar{Z}[\bar{A}x(t) + \bar{B}Kx(t - \tau)] + \bar{h}\xi^T(t)X\xi(t) + 2(x^T(t)\bar{N}_1 + x^T(t_1)\bar{N}_2)[x(t) - x(t_1)] - \int_{t_1}^t \dot{x}^T(s)\bar{Z}\dot{x}(s)ds \\ & - \int_{t_1}^t \xi^T(t)X\xi(t)ds - 2[x^T(t)\bar{N}_1 + x^T(t_1)\bar{N}_2] \int_{t_1}^t \dot{x}(s)ds = x^T(t)[\bar{P}\bar{A} + \bar{A}^T\bar{P} + \bar{h}\bar{A}^T\bar{Z}\bar{A} + \bar{Q} + \bar{h}X_{11} + \bar{N}_1 + \bar{N}_1^T]x(t) \\ & + x^T(t)[\bar{P}\bar{B}K + \bar{h}\bar{A}^T\bar{Z}\bar{B}K - \bar{N}_1 + \bar{N}_2^T + \bar{h}X_{12}]^T x(t_1) + x^T(t_1)[\bar{P}\bar{B}K + \bar{h}\bar{A}^T\bar{Z}\bar{B}K - \bar{N}_1 + \bar{N}_2^T + \bar{h}X_{12}]^T x(t) \\ & + x^T(t_1)[-\bar{N}_2 - \bar{N}_2^T - \bar{Q} + \bar{h}X_{22} + \bar{h}K^T\bar{B}^T\bar{Z}\bar{B}KX_{12}]x(t_1) \\ & - \int_{t_1}^t [\dot{x}^T\bar{Z}\dot{x}(s) + \xi^T(t)X\xi(t) + 2(x^T(t)\bar{N}_1 + x^T(t_1)\bar{N}_2)\dot{x}(s)] ds = \end{aligned} \quad (16)$$

$$\begin{aligned} & \begin{bmatrix} x(t) \\ x(t - \tau) \end{bmatrix}^T \begin{bmatrix} \bar{P}\bar{A} + \bar{A}^T\bar{P} + \bar{Q} + \bar{h}X_{11} & \bar{P}\bar{B}K - \bar{N}_1 + \bar{N}_2^T \\ +\bar{N}_1 + \bar{N}_1^T + \bar{h}\bar{A}^T\bar{Z}\bar{A} & +\bar{h}X_{12} + \bar{h}\bar{A}^T\bar{Z}\bar{B}K \\ * & -\bar{N}_2 + \bar{N}_2^T - \bar{Q} \\ * & +\bar{h}K^T\bar{B}^T\bar{Z}\bar{B}K \end{bmatrix} \times \begin{bmatrix} x(t) \\ x(t_1) \end{bmatrix} \\ & \int_{t_1}^t \begin{bmatrix} x(t) \\ x(t_1) \\ \dot{x}(s) \end{bmatrix}^T \times \begin{bmatrix} X_{11} & X_{12} & \bar{N}_1 \\ * & X_{22} & \bar{N}_2 \\ * & * & \bar{Z} \end{bmatrix} \begin{bmatrix} x(t) \\ x(t_1) \\ \dot{x}(s) \end{bmatrix} ds \\ & \bar{\Xi} = \begin{bmatrix} \bar{P}\bar{A} + \bar{A}^T\bar{P} + \bar{Q} + \bar{h}X_{11} + \bar{N}_1 + \bar{N}_1^T & \bar{P}\bar{B}K - \bar{N}_1 + \bar{N}_2^T + \bar{h}X_{12} & \bar{h}\bar{A}^T\bar{Z} \\ * & -\bar{N}_1 + \bar{N}_2^T - \bar{Q} + \bar{h}X_{22} & \bar{h}K^T\bar{B}^T\bar{Z} \\ * & * & -\bar{h}\bar{Z} \end{bmatrix} < 0 \end{aligned} \quad (19)$$

$$\begin{aligned} \Xi = & \begin{bmatrix} \bar{P}^{-1} & 0 & 0 \\ 0 & \bar{P}^{-1} & 0 \\ 0 & 0 & \bar{Z}^{-1} \end{bmatrix} \begin{bmatrix} \bar{P}\bar{A} + \bar{A}^T\bar{P} + \bar{Q} + \bar{h}X_{11} + \bar{N}_1 + \bar{N}_1^T & \bar{P}\bar{B}K - \bar{N}_1 + \bar{N}_2^T + \bar{h}X_{12} & \bar{h}\bar{A}^T\bar{Z} \\ * & -\bar{N}_1 + \bar{N}_2^T - \bar{Q} + \bar{h}X_{22} & \bar{h}K^T\bar{B}^T\bar{Z} \\ * & * & -\bar{h}\bar{Z} \end{bmatrix} \\ & \times \begin{bmatrix} \bar{P}^{-1} & 0 & 0 \\ 0 & \bar{P}^{-1} & 0 \\ 0 & 0 & \bar{Z}^{-1} \end{bmatrix} = \begin{bmatrix} \bar{A}\bar{L} + \bar{L}\bar{A}^T + \bar{Q}_1 + \bar{h}Y_{11} + \bar{M}_1 + \bar{M}_1^T & \bar{B}\bar{V} - \bar{M}_1 + \bar{M}_2^T + \bar{h}Y_{12} & \bar{h}\bar{L}\bar{A}^T \\ * & -\bar{M}_2 - \bar{M}_2^T - \bar{Q}_1 + \bar{h}Y_{22} & \bar{h}\bar{V}^T\bar{B}^T \\ * & * & -\bar{h}\bar{R} \end{bmatrix} < 0 \end{aligned} \quad (20)$$

Minimize $tr\{\bar{F}\bar{F}_1 + \bar{L}\bar{L}_1 + \bar{R}\bar{R}_1\}$

Subject to:

$$\begin{aligned} & \begin{bmatrix} \bar{A}\bar{L} + \bar{L}\bar{A}^T + \bar{Q}_1 + \bar{h}Y_{11} + \bar{M}_1 + \bar{M}_1^T & \bar{B}\bar{V} - \bar{M}_1 + \bar{M}_2^T + \bar{h}Y_{12} & \bar{h}\bar{L}\bar{A}^T \\ * & -\bar{M}_2 - \bar{M}_2^T - \bar{Q}_1 + \bar{h}Y_{22} & \bar{h}\bar{V}^T\bar{B}^T \\ * & * & -\bar{h}\bar{R} \end{bmatrix} < 0 \\ & \begin{bmatrix} Y_{11} & Y_{12} & \bar{M}_1 \\ * & Y_{22} & \bar{M}_2 \\ * & * & \bar{F} \end{bmatrix} > 0 \\ & \begin{bmatrix} \bar{F} & \bar{I} \\ \bar{I} & \bar{F}_1 \end{bmatrix} > 0, \begin{bmatrix} \bar{F}_1 & \bar{L}_1 \\ \bar{L}_1 & \bar{R}_1 \end{bmatrix} > 0 \\ & \bar{L} > 0, \bar{F} > 0, \bar{R} > 0 \end{aligned} \quad (21)$$

$$\begin{cases} \frac{di_{dsw}}{dt} = H[R_s L_{rr} i_{dsw} + ((\omega_s - \omega_r).L_{mm}^2 - \omega_s L_{rr} L_{ss})i_{qsw} - R_r L_{mm} i_{drw} - \omega_r L_{rr} L_{mm} i_{qrw} + L_{mm} V_{drw} - L_{rr} V_{dsw}] \\ \frac{di_{qsw}}{dt} = H[(-\omega_s - \omega_r).L_{mm}^2 + \omega_s L_{rr} L_{ss})i_{dsw} + R_s L_{rr} i_{qsw} + \omega_r L_{rr} L_{mm} i_{drw} - R_r L_{mm} i_{qrw} + L_{mm} V_{qrw} - L_{rr} V_{qsw}] \\ \frac{di_{drw}}{dt} = H[-R_s L_{mm} i_{dsw} + \omega_r L_{ss} L_{mm} i_{qsw} + R_r L_{ss} i_{drw} + (\omega_s L_{mm}^2 - (\omega_s - \omega_r).L_{ss} L_{rr})i_{qrw} - L_{ss} V_{drw} + L_{mm} V_{dsw}] \\ \frac{di_{qrw}}{dt} = H[-\omega_r L_{ss} L_{mm} i_{dsw} - R_s L_{mm} i_{qsw} + (-\omega_s L_{mm}^2 + (\omega_s - \omega_r).L_{ss} L_{rr})i_{drw} + R_r L_{ss} i_{qrw} - L_{ss} V_{qrw} + L_{mm} V_{qsw}] \end{cases} \quad (26)$$

$$K = \begin{bmatrix} -0.6578 & 1.3214 & -7.2346 & 5.1104 & 0.5467 & 2.3791 & 4.3639 & -3.6218 & 0.6435 & 0.1654 & -0.5672 & 3.4562 & -2.4567 \\ -0.7891 & 1.0678 & 5.3211 & -0.9875 & -1.8976 & 1.7654 & -5.6784 & -4.4566 & 1.3211 & 0.8745 & 0.5678 & -1.4567 & -1.0678 \end{bmatrix}^T$$

$$L = \begin{bmatrix} -2.4501 & -1.5647 & -2.7716 & -1.6557 & -3.8121 & -2.3116 & -0.7891 & -2.3456 & -0.9876 & -1.1245 & -2.1456 & -1.5431 & -0.5671 \\ -1.9123 & -1.5671 & -2.0677 & -1.9544 & -2.7891 & -1.766 & -1.7654 & -0.5456 & -2.5671 & -2.5673 & -1.7893 & -3.456 & -1.0543 \end{bmatrix}^T$$

CREDIT AUTHORSHIP CONTRIBUTION STATEMENT

Babak Keshavarz Zahed: Conceptualization, Data curation, Formal analysis, Funding acquisition, Investigation, Methodology, Resources, Software, Visualization, Writing - review & editing. **Mohammad Hossan Moradi:** Project administration, Supervision, Validation, Writing - original draft, Writing - review & editing.

DECLARATION OF COMPETING INTEREST

The authors declare that they have no known competing financial interests or personal relationships that could have appeared to influence the work reported in this paper. The ethical issues; including plagiarism, informed consent, misconduct, data fabrication and/or falsification, double publication and/or submission, redundancy has been completely observed by the authors.

REFERENCES

- [1] R. Arjmandzadeh, M. Banejad, and A. Akbarzadeh Kalat, "Improving the performance of a vsg in the distorted grid using third-order generalized integrator," *Journal of Applied Research in Electrical Engineering*, vol. 3, no. 1, pp. 1-8, 2024.
- [2] M. Darabian, A. Bagheri, and S. Yousefi, "Design of a new robust controller for voltage regulation of DC link in wind-farm-side converter integrated with a hybrid AC and DC large-scale power system," *IET Generation, Transmission & Distribution*, vol. 17, no. 7, pp. 1674-1685, 2023.
- [3] S. Aminzadeh, M. Tarafdar Hagh, and H. Seyedi, "Reactive power coordination between solid oxide fuel cell and battery for microgrid frequency control," *Journal of Applied Research in Electrical Engineering*, vol. 1, no. 3, pp. 121-130, 2022.
- [4] M. Zolfaghari, G. B. Gharehpetian, and A. Anvari-Moghaddam, "Quasi-Luenberger observer-based robust DC link control of UIPC for flexible power exchange control in hybrid microgrids," *IEEE Systems Journal*, vol. 15, no. 2, pp. 2845-2854, 2020.
- [5] J. Ma et al., "A low frequency oscillation suppression method for grid-connected DFIG with virtual inertia," *International Journal of Electrical Power & Energy Systems*, vol. 144, p. 108531, 2023.
- [6] M. Darabian, and A. Bagheri, "Stability improvement of large-scale power systems including offshore wind farms and MTDC grid aiming at compensation of time delay in sending robust damping signals," *International Journal of Electrical Power & Energy Systems*, vol. 143, p. 108491, 2022.
- [7] L. Xiong et al., "Optimal allocation of energy storage system in DFIG wind farms for frequency support considering wake effect," *IEEE Transactions on Power Systems*, vol. 37, no. 3, pp. 2097-2112, 2021.
- [8] C. Olivieri et al., "Application of an integrated RNN-ensemble method for the short-term forecast of inter-area oscillations modal parameters," *Electric Power Systems Research*, vol. 225, p. 109790, 2023.
- [9] S. Galvani, B. Mohammadi-Ivatloo, M. Nazari-Heris, and S. Rezaeian, "Optimal allocation of static synchronous series compensator (SSSC) in wind-integrated power system considering predictability," *Electric Power Systems Research*, vol. 191, p. 106871, 2021.
- [10] C. Maddela, and B. Subudhi, "Robust wide-area TCSC controller for damping enhancement of inter-area oscillations in an interconnected power system with actuator saturation," *International Journal of Electrical Power & Energy Systems*, vol. 105, pp. 478-487, 2019.
- [11] A. Movahedi, A. H. Niasar, and G. Gharehpetian, "Designing SSSC, TCSC, and STATCOM controllers using AVURPSO, GSA, and GA for transient stability improvement of a multi-machine power system with PV and wind farms," *International Journal of Electrical Power & Energy Systems*, vol. 106, pp. 455-466, 2019.
- [12] R. K. Singh, and N. K. Singh, "Power system transient stability improvement with FACTS controllers using SSSC-based controller," *Sustainable Energy Technologies and Assessments*, vol. 53, p. 102664, 2022.
- [13] J. Im, J. Ban, Y. Kim, and J. Zhao "PMU-based distributed state estimation to enhance the numerical stability using equality constraints," *IEEE Transactions on Power Systems*, vol. 39, no. 2, pp. 4409 - 4421, 2023.

- [14] Y. Yao, Y. Xu, M. Chow, "Distributed optimal dynamic communication paths planning for PMUs in the WAMS communication network," *IEEE Transactions on Industrial Informatics*, vol. 19, no. 9, pp. 9609-9618, 2023.
- [15] M. Bhadu, N. Senroy, I. N. Kar, and G. N. Sudha, "Robust linear quadratic Gaussian-based discrete mode wide area power system damping controller," *IET Generation, Transmission & Distribution*, vol. 10, no. 6, pp. 1470-1478, 2016.
- [16] H. Zhao, Z. Lin, Q. Wu, and S. Huang, "Model predictive control based coordinated control of multi-terminal HVDC for enhanced frequency oscillation damping," *International Journal of Electrical Power & Energy Systems*, vol. 123, p. 106328, 2020.
- [17] D. Roberson, J. F. O'Brien, "Multivariable loop-shaping control design for stability augmentation and oscillation rejection in wide-area damping using HVDC," *Electric Power Systems Research*, vol. 157, pp. 238-250, 2018.
- [18] M. Beiraghi, and A. M. Ranjbar, "Additive model decision tree-based adaptive wide-area damping controller design," *IEEE Systems Journal*, vol. 12, no. 1, pp. 328-339, 2016.
- [19] ME. Bento, "Fixed low-order wide-area damping controller considering time delays and power system operation uncertainties," *IEEE Transactions on Power Systems*, vol. 35, no. 5, pp. 3918-3926, 2020.
- [20] P. Gupta, A. Pal, and V. Vittal, "Coordinated wide-area damping control using deep neural networks and reinforcement learning," *IEEE Transactions on Power Systems*, vol. 37, no. 1, pp. 365-376, 2022.
- [21] M. R. Paternina et al., "Enhancing wide-area damping controllers via data-assisted power system linear models," *Electric Power Systems Research*, vol. 217, p. 109085, 2023.
- [22] C. O. Maddela, and B. Subudhi, "Delay-dependent supplementary damping controller of tscs for interconnected power system with time-delays and actuator saturation," *Electric Power Systems Research*, vol. 164, pp. 39-46, 2018.
- [23] A. Sengupta, and D. K. Das, "Mitigating inter-area oscillation of an interconnected power system considering time-varying delay and actuator saturation," *Sustainable Energy, Grids and Networks*, vol. 27, pp. 100484, 2021.
- [24] A. Paul, I. Kamwa, G. Joos, "Centralized dynamic state estimation using a federation of extended Kalman filters with intermittent PMU data from generator terminals," *IEEE Transactions on Power Systems*, vol. 33, no. 6, pp. 6109-6119, 2018.
- [25] A. Paul, I. Kamwa, G. Joos, "PMU signals responses-based RAS for instability mitigation through on-the fly identification and shedding of the run-away generators," *IEEE Transactions on Power Systems*, vol. 35, no. 3, pp. 1707-1717, 2019.
- [26] M. Bento, "A hybrid particle swarm optimization algorithm for the wide-area damping control design," *IEEE Transactions on Industrial Informatics*, vol. 18, no. 1, pp. 592-599, 2021.
- [27] S. Mukherjee, A. Chakraborty, H. Bai, A. Darvishi, and B. Fardanesh, "Scalable designs for reinforcement learning-based wide-area damping control," *IEEE Transactions on Smart Grid*, vol. 12, No. 3, pp. 2389-2401, 2021.
- [28] Y. J. Isbeih, S. Ghosh, M. S. Moursi, and E. F. El-Saadany, "Online DMDc based model identification approach for transient stability enhancement using wide area measurements," *IEEE Transactions on Power Systems*, vol. 36, no. 5, pp. 4884-4887, 2021.
- [29] W. Yao, et al, "Resilient wide-area damping control for inter-area oscillations to tolerate deception attacks," *IEEE Transactions on Smart Grid*, vol. 12, no. 5, pp. 4238-4249, 2021.
- [30] W. Wu, X. Wang, H. Rao, B. Zhou, "Delay-dependent wide-area damping controller synthesis approach using Jensen's inequality and evolution algorithm," *CSEE Journal of Power and Energy Systems*, vol. 9, no. 5, pp. 1774-1785, 2022.
- [31] F. Liu, R. Yokoyama, Y. Zhou, and M. Wu, "Free-weighting matrices-based robust wide-area FACTS control design with considering signal time delay for stability enhancement of power systems," *IEEE Transactions on Electrical and Electronic Engineering*, vol. 7, no. 1, pp. 31-39, 2012.
- [32] A. Prakash, K. Kumar, and S. Parida, "Energy capacitor system based wide-area damping controller for multiple inter-area modes," *IEEE Transactions on Industry Applications*, vol. 58, no. 2, pp. 1543-1553, 2022.
- [33] T. N. Pham, A. M. Oo, and H. Trinh, "Event-triggered mechanism for multiple frequency services of electric vehicles in smart grids," *IEEE Transactions on Power Systems*, vol. 37, no. 2, pp. 967-981, 2021.
- [34] C. W. Taylor, "BPA's wide-area stability and voltage control system (WACS) for blackout prevention," in *Proc. IEEE PES Power Systems Conference and Exposition*, vol. 3, p. 1610, 2004.
- [35] E. Fridman, U. Shaked, "Delay-dependent stability and H_∞ control: constant and time-varying delays," *International Journal of Control*, vol. 76, no. 1, pp. 48-60, 2010.
- [36] H. Gao, J. Lam, C. Wang, and Y. Wang, "Delay-dependent output-feedback stabilisation of discrete-time systems with time-varying state delay," *IEE Proceedings-Control Theory and Applications*, vol. 151, no. 6, pp. 691-698, 2004.
- [37] M. S. Sadabadi, and D. Peaucelle, "From static output feedback to structured robust static output feedback: A survey," *Annual Reviews in Control*, vol. 42, pp. 11-26, 2016.
- [38] H. Shayeghi, and A. Ghasemi, "A multi objective vector evaluated improved honey bee mating optimization for optimal and robust design of power system stabilizers," *International Journal of Electrical Power & Energy Systems*, vol. 62, pp. 630-645, 2014.

- [39] T. Surinkaew, and I. Ngamroo, "Adaptive signal selection of wide-area damping controllers under various operating conditions," *IEEE Transactions on Industrial Informatics*, vol. 14, no. 2, pp. 639-651, 2017.
- [40] M. Darabian, and A. Jalilvand, "Predictive control strategy to improve stability of DFIG-based wind generation connected to a large-scale power system," *International Transactions on Electrical Energy Systems*, vol. 27, no. 5, pp. 2300, 2017.
- [41] B. Lei, and S. Fei, "A brand new nonlinear robust control design of SSSC for transient stability and damping improvement of multi-machine power systems via pseudo-generalized Hamiltonian theory," *Control Engineering Practice*, vol. 29, pp. 147-157, 2014.
- [42] A. Samosir, and A. Yatim, "Implementation of dynamic evolution control of bidirectional DC–DC converter for interfacing ultracapacitor energy storage to fuel-cell system," *IEEE Transactions on Industrial Electronics*, vol. 57, no. 10, pp. 3468-3473, 2010.
- [43] V. Vittal, J. McCalley, P. Anderson, and A. Fouad, *Power system control and stability*. John Wiley & Sons, 2019.

Copyrights

© 2024 Licensee Shahid Chamran University of Ahvaz, Ahvaz, Iran. This article is an open-access article distributed under the terms and conditions of the Creative Commons Attribution –NonCommercial 4.0 International (CC BY-NC 4.0) License (<http://creativecommons.org/licenses/by-nc/4.0/>).





Review Article

Network Virtualization Utilizing Blockchain: A Review

Patikiri Arachchige Don Shehan Nilmantha Wijesekara *

Department of Electrical and Information Engineering, Faculty of Engineering, University of Ruhuna, Galle 80000, Sri Lanka

* Corresponding Author: nilmantha@eie.ruh.ac.lk

Abstract: Network Virtualization (NV) techniques enable high scalability and isolation by abstracting physical resources to provide a logical network representation that can coexist with a physical networking framework. Traditional NV is prone to security attacks and has lower privacy and trustfulness compared to blockchain-established NV. We diagnose the BC-established NV construct under 5 segments and closely appraise the literature in reference to NV technique, virtualization technology, BC-related properties, and network properties. We racked up a starting sample of 85 sources by filtering literary work for qualifying conditions searched from article retrieval platforms, engaging a rigorous and prolonged approach. Anchored from this research, in BC-established NV, we demonstrate that BC can act as a broker/manager for NV, act as a secure storage by preventing double-spending attacks, provide secure virtual network embedding with high fault tolerance, engage BC and smart contracts for resource trading in the process of NV, engage dedicated consensus approaches to reach agreement for NV among multiple parties for reducing security attacks, and establish BC-established access control for NV. Complete interpretation disseminates that from interpreted BC-established NV schemes, 45% engage BC and smart contracts for agreements and resource trading for NV, 95% engage regular BC architecture, Proof-of-Work (PoW) and Practical Byzantine Fault Tolerance (PBFT) being the most frequently used consensus, 80% engage the overlay network concept, and it has been engaged abundantly (27.5%) in 5G networks. Finally, we deliberate the possibilities and obstacles of the framework of blockchain-established NV and then provide suggestions to suppress them.

Keywords: Network virtualization, blockchain, slicing, entry coordination, cryptography, overlaying.

Article history

Received 14 February 2024; Revised 29 May 2024; Accepted 24 June 2024; Published online 30 October 2024.

© 2024 Published by Shahid Chamran University of Ahvaz & Iranian Association of Electrical and Electronics Engineers (IAEEE)

How to cite this article

P. A. D. S. N. Wijesekara, "Network virtualization utilizing blockchain: A review," *J. Appl. Res. Electr. Eng.*, vol. 3, no. 2, pp. 136-158, 2024. DOI: [10.22055/jaree.2024.46144.1110](https://doi.org/10.22055/jaree.2024.46144.1110)

1. INTRODUCTION

Network virtualization is a wide concept in networking that involves the abstraction of underlying physical resources to provide a logical network representation that can coexist with other virtual networks in the same physical network [1]. Due to network virtualization, many advantages can be realized, such as service provisioning flexibility, high manageability due to centralized management, high scalability, high isolation and fault tolerance, etc. [2]. These advantages in virtual network technologies such as virtual local area networks, virtual private networks, active and programmable networks, etc. can be evaluated by evaluating parameters, for instance, cost, revenue, throughput,

bandwidth, spectrum efficiency, energy efficiency, signalling latency, and so on [3]. In network virtualization, infrastructure providers offer network resources to service providers through virtual network providers and operators, where service providers utilize them to cater services to end users [4].

In the resource sharing concept of network virtualization, resources such as spectrum, infrastructure, etc. are shared across multiple virtual networks with the aid of concepts such as dynamic spectrum sharing [5]. In comparison to resource sharing, slicing is a core function in network virtualization that slices a given spectrum, infrastructure, network, or flow into multiple sub-sets and allocates each slice to different

network service providers, which promotes independent control and isolation among virtual networks [6]. Network virtualization also involves network function virtualization, where software instances of different network functions such as routing, load balancing, and intrusion detection are typically implemented in software-defined networking, which can function in the manner of a service chain of virtualized network functions [7].

A blockchain vitally comprises a sequence of blocks intertwined in a regular or irregular sequence, conforming to the framework of distributed ledger technology [8]. Distinctly, transactions/blocks are connected to each other by means of a designated block/transaction that stores the hash digest of several antecedent transactions/blocks, making them immutable [9]. Further, they enact a universal assent methodology, such as proof-established universal assent or vote-established universal assent, for validating the blocks among the peers before combining a transaction/block on the distributed ledger technology [10]. Precisely, they apply hashing methods to secure the integrity and computer-generated signatures for securing transaction non-repudiation [11]. Similarly, they can incorporate secure cryptographic practices such as zero knowledge proofs and quantum-safe cryptography for resisting quantum attacks [12], intensifying the component of privacy safeguarding in blockchain. Nevertheless, the original blockchain itself, which dodges cryptographic practices such as key-pair cryptography for securing privacy safeguarding, is not 100% privacy safeguarding as blockchain recordings/transactions are pseudo-anonymous, expressing that recordings/transactions are identified by a confidential pseudo-identifier instead of bona fide addresses of nodes [13]. Similarly, the level of privacy protection may be tailored by following the distributed ledger category: private, consortium, or public. The public blockchain is the common permissionless blockchain, whereas private and consortium blockchains carry a designated level of centralized authority, contributing more privacy and data rights administration than the public blockchain [14].

In light of this examination, we find that blockchain-established network virtualization can be five-fold in terms of the duty of blockchain in the process of network virtualization. First, blockchain has been engaged as a broker/manager/auditor/orchestrator for different slicing in network virtualization, such as network slicing to coordinate slices and security level agreements, etc. [15], infrastructure slicing to audit and orchestrate slices [16], and spectrum slicing for spectrum management [17]. Secondly, blockchains facilitate secure storage of data, securing privacy with additional cryptographic techniques for obstructing double-spending attacks when allocating the same physical infrastructure to multiple virtual networks [18], and providing better virtual network embedding with high fault tolerance [19]. Thirdly, in spectrum slicing frameworks such as Bloc6Tel [20] and spectrum sharing frameworks such as MOSS [21], Smart Contracts (SCs) on blockchain have been engaged for providing service-level agreements and auction algorithms for resource trading. Fourthly, blockchain consensus has been specifically engaged in network virtualization processes, such as proof-of-strategy to reduce administrative expenses [22], consensus having a dynamic tip selection strategy to improve universal utility pertaining to

the demand and supply of spectrum [23], Practical Byzantine Fault Tolerance (PBFT) to allocate more resources established on credibility values [24], etc. Finally, blockchain has been engaged to provide access control, making sure that only legitimate users are provided access to resources sliced or shared in network virtualization, such as devices belonging to different organizations that are provided access to a common VPN [25].

Currently, in this composition, to our present perception, no scholarly investigation has been conducted reviewing network virtualization in broad scope utilizing blockchain. Therefore, we are proud to be the primary appraisers to review in this field, which will provide a path for academicians to gain insight into current developments, discrepancies, obstacles, possibilities, and suggestions for network virtualization utilizing blockchain. However, there exist a survey that discusses the opportunities of network function virtualization in the blockchain domain [111]. In comparison to our work, the preceding work does not investigate blockchain applications in the broad scope of network virtualization.

Fig. 1 illustrates the subject catalogue of this interpretation of academic literature on network virtualization utilizing blockchain.

1.1. Contributions to Current Literature

- We classified and briefly presented a compendium of network virtualization (Section 3).
- The core concepts of network virtualization are briefly presented (Section 4).
- A compendium of blockchain technology is depicted (Section 5).
- Examine current blockchain-established network virtualization frameworks in telecommunication networks (Section 6).
- Interpret completely the examined blockchain-established network virtualization frameworks (Section 7).
- The possibilities and obstacles of blockchain-established network virtualization are deliberated (Section 8).
- Suggestions and prospective paths for engaging blockchain-established network virtualization are depicted (Section 9).

2. METHODOLOGY

This research examines the current original work on network virtualization utilizing blockchain available in print during the past years, engaging a rigorous and prolonged approach [26]. Further to that, it studies a wide spectrum of angles in network virtualization and blockchain systems. Henceforth, all unique scientific research reports and internet sites available in print on network virtualization, blockchain-established network virtualization, and blockchain inhabit the overall collection of data in this investigation. However, the whole data collection's references are impervious to inspection in the present investigation. Henceforth, engaging suitable search words and qualifying conditions, we gathered 88 references from unique scientific research reports and internet sites.

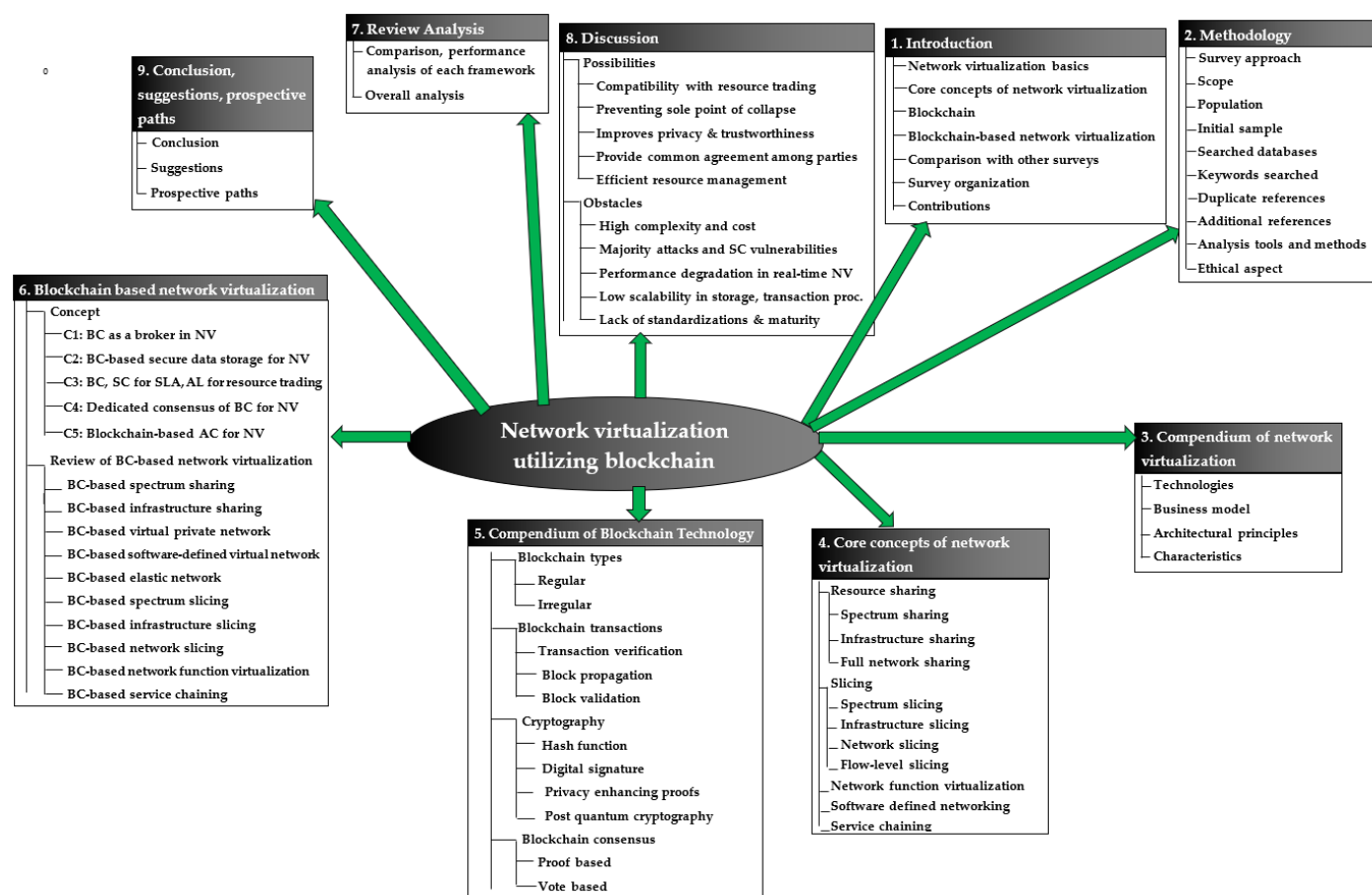


Fig. 1: Subject catalogue of this interpretation on network virtualization utilizing blockchain.

We searched IEEE Xplore technical database, Google Scholar educational content discovery platform, ACM electronic library, Wiley electronic library, ScienceDirect online scientific storage, and MDPI article retrieval platform. We commonly chose search words "Blockchain" OR "Network virtualization" OR "Blockchain-established network virtualization" OR "Blockchain-established spectrum sharing" OR "Blockchain-established infrastructure sharing" OR "Blockchain-established virtual private network" OR "Blockchain-established software-defined virtual networks" OR "blockchain-established elastic networks" OR "blockchain-established spectrum slicing" OR "Blockchain-established infrastructure slicing" OR "Blockchain-established network slicing" OR "Blockchain-established network function virtualization" OR "Blockchain-established service chaining".

A multitude of features for filtering the articles generated the qualifying conditions. The first qualifying condition dictates that the piece of writing imposes the use of English, and the second qualifying condition dictates a requirement of high pertinence to the search word. Thirdly, so as to augment the veracity of conducted research, journal articles were put in a position of prominence in contrast to meeting reports and preliminary publications. On the contrary, we didn't endorse research articles from a specific article producer in the qualifying conditions; in place of this, we treated all article producers equally. The last qualifying condition asserts that a specific piece of writing dictates public disclosure in the span of years since 1975.

The starting sample was minimized to 85 article sources; later, it was learned that 3 article sources were copies. Further to that, we adduced meanings and explanations pertaining to the heterogeneous topics presented in this research using 25 pieces of writing. To link this research with prior research, we reviewed multiple research articles; nevertheless, as only a single one examined related to blockchain-established network virtualization, we appended it to the assortment of electronic content, gaining the final summation of article sources to 111.

To evaluate the collected blockchain-established network virtualization by a multitude of features, such as blockchain characteristics, network virtualization characteristics, network factors, and effectiveness, we engaged the tabular dataset design for research qualitative assessment [27]. Further to that, we engineered visualizations engaging the Excel software to open-mindedly study research data linked with network virtualization-established and blockchain-established features.

Ethics do not apply, as this research pertains to telecommunication networks.

3. A COMPENDIUM OF NETWORK VIRTUALIZATION

3.1. Technologies

3.1.1. Virtual Local Area Network (VLAN)

A VLAN brings together network hosts within a singular broadcast domain logically, irrespective of physical-

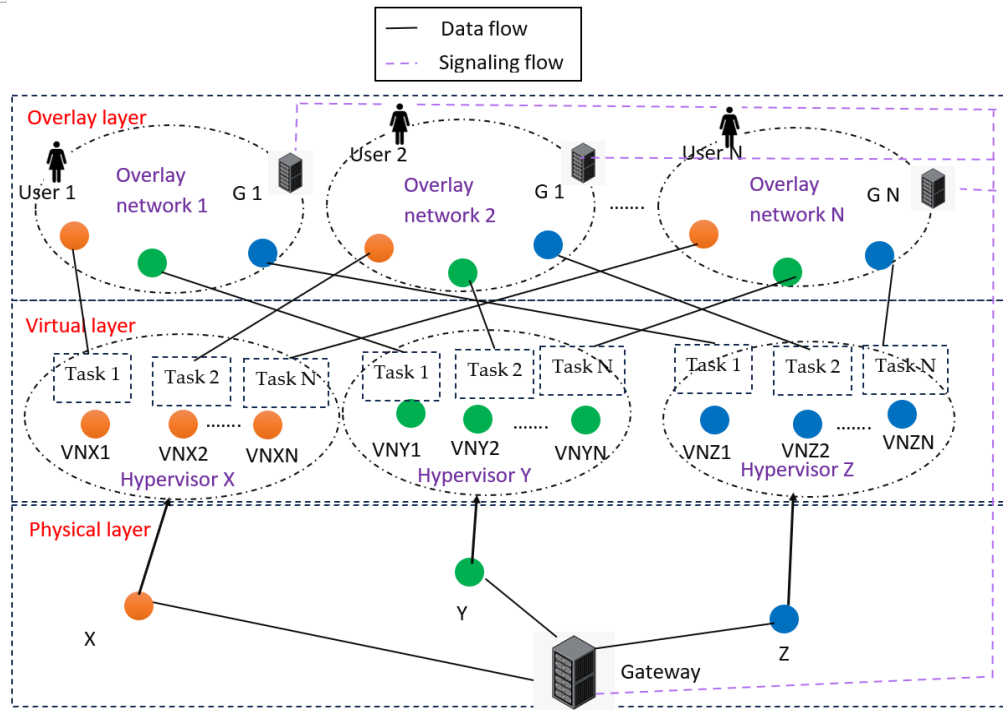


Fig. 2: Generic architecture of an Overlay network

-connectivity, where network administration and reconfiguration are simpler. These networks forward packets using the VLAN identifier and media access control address of the data link layer [28]. VLANs help in network segmentation, which allows network administrators to isolate devices in order to improve the security of the network by separating sensitive and critical resources from the rest of the network [29].

3.1.2. Virtual Private Network (VPN)

A VPN delivers secure and private encrypted tunnels for multiple sites over public communication networks that route users' traffic through a server belonging to the VPN provider, which is geographically distributed. In VPNs, customer-edge devices can be associated with provider-edge routers. They provide privacy and anonymity by hiding the real internet protocol address and are particularly useful when connecting public Wi-Fi networks to reduce potential hacking attacks [30].

VPNs can be categorized into tier 1, tier 2, and tier 3, established on the layer of the open-system interconnected model in which they operate. Tier 1 VPN is the physical layer VPN that is typically used in circuit switching networks and has the least level of application among VPN types. They use an asynchronous transfer mode for communication. Tier 2 VPN functions on the data link layer that extends the concept of VLAN over a large distance and uses multi-protocol label switching. On the other hand, tier 3 VPN operates in the network tier, which uses protocols such as internet protocol security, secure socket layer, etc. for establishing secure connections and is the most widely used VPN type [31].

3.1.3. Active and Programmable Network (APN)

An APN promotes programmability, where network administrators can program high-level network policies to be engaged in the network, and network isolation, allowing

multiple parties to implement conflicting codes on the same network equipment without any conflict. Network programmability promotes the logical separation of control functions from data-forwarding functions. There are two approaches for these networks: the active network approach and the open signalling approach. In the active networks approach, network services can be customized, involve implementing executable programmed code in network nodes, and are more flexible than the other approach [32]. In the open signalling approach, the exchange of control information among the network devices, known as signalling, is engaged to control the behavior of the network. NETKIT is a software-component established approach to structuring programmable networks that can accommodate multiple levels of networking systems in either of the approaches for active and programmable networks [33].

3.1.4. Overlay network

An overlay network, typically implemented at the application layer, is a logical network implemented over a physical network in which virtual links exist among the nodes [34]. Overlay networks have been engaged to realize numerous goals, such as reducing security attacks, improving the quality of service, enabling multicasting, etc. The architecture of a generic overlay network is illustrated in Fig. 2.

For instance, SIPTVMON is a SIP protocol and cryptography-established secure multicast overlay network that is capable of optimizing network latency and bandwidth utilization through load balancing [1]. These networks promote network virtualization by abstracting the complexities of the physical network and using tunnelling techniques to transmit data among the nodes. For instance, NoEncap is a software-established optimization scheme to reduce the overhead of packets in overlay-established virtual networks [35].

3.1.5. Elastic network

An elastic network is a conceptual network where the infrastructure can dynamically adapt the allocation of network resources to changing demands of the network, such as traffic patterns, congestion, events, etc. [36]. In these networks, physical resources are virtualized, and they can be scaled up or down established on network demands and typically provide elastic services using optimization techniques. The virtual network embedding (mapping virtual network resources into physical network resources) in elastic networks is typically solved using optimization techniques. For instance, in [37], virtual network embedding for an elastic optical network is realized by optimizing to select light paths from a set of light paths having diverse modulation schemes, forward error correction rates, baud rates, etc.

3.2. Business Model

Network virtualization involves multiple parties during its process, as in Infrastructure Providers (InPs), Service Providers (SPs), Mobile Virtual Network Providers (MVNPs), Mobile Virtual Network Operators (MVNOs), and end users.

3.2.1. Infrastructure provider

Infrastructure providers offer the network resources (such as servers, routers, and switches) owned by them to other parties using programmable interfaces. They are responsible for managing the underlying physical assets of the virtual network. Multiple infrastructure providers can allocate resources to single MVNP and also multiple MVNPs can lease resources from a single InP in network virtualization [4].

3.2.2. Mobile virtual network provider

MVNP is an organization that leases network infrastructure from InPs and creates virtual resources to be used by MVNO in the wireless mobile virtual network [38].

3.2.3. Mobile virtual network operator

The MVNO utilizes the virtual resources provided by the MVNPs and assigns them to service providers. MVNOs have more control than MVNPs over the services they provide. MVNOs can sometimes act as MVNPs and lease infrastructure from InPs as well. In such cases, matching theory and auction approaches have been utilized to allocate resources (slices) from multiple InPs to MVNOs to maximize their revenue [39].

3.2.4. Service provider

Service providers involve using virtual network resources provided by MVNOs and using them to provide services like data services, voice communication, etc. to end users in order to create virtual networks. SPs can program allocated virtual network resources to offer services. It can partition the virtual network services, creating multiple child virtual networks. Since there is competition among service providers, the expenditure of leased assets in SPs and client latency can be minimized while meeting client service level agreements under server bandwidth constraints [40].

3.2.5. End user

End users are the customers or subscribers that utilize the services bestowed by service providers. Note that in the network virtualization model, a given end user has the capability to connect to multiple virtual networks provided by multiple service providers. In network virtualization, multi-layer games have been suggested as an approach for allocating services and resources among multiple parties, such as InPs, MVNOs, end users, etc., where there exists a balancing act among the quality of service of EUs and the compensation of MVNOs and InPs, where end users attempt to find an optimal policy to obtain services from the service providers [41].

3.3. Architectural Principles

3.3.1. Abstraction

In network virtualization, underlying physical resources are abstracted and encapsulated to provide a more simplified logical network representation. This promotes simplified and easier network management, as it can be achieved without having to know about the details of complex network infrastructure. For instance, in [42], diverse types of information sources in vehicular networks are abstracted as broadcasting nodes and agents, and the controller is abstracted as a sink and a global solution optimizer for simplified data collection. Moreover, in [43], an enhanced logical view for network virtualization in distributed overlay virtual networks by achieving an advanced network abstraction in order to provide tenant contracts and provide application layer network services has been suggested.

3.3.2. Coexistence

Coexistence states the characteristic that multiple virtual networks provided by multiple service providers can exist together in the same physical network (partially or fully sharing the physical infrastructure) without having interference with each other. In the interest of achieving coexistence, there should be efficient isolation and resource allocation techniques such that one virtual network does not negatively contribute towards the performance of another virtual network. For instance, Ipv4-only networks can be virtualized over Ipv6 networks to facilitate communication among Ipv4 virtual network segments through an Ipv4-Ipv6 tunnel, allowing the coexistence of both types of networks [44].

3.3.3. Recursion/Nesting

Virtual networks can appear as a hierarchy of virtual networks where one virtual network is nested within another, in which multiple child virtual networks can be spawned from a parent virtual network. This hierarchical existence is known as recursion, and it allows scalability, as each virtual network in the hierarchy can have its own set of policies and configurations. BrFusion and Hostlo have been presented as frameworks to address the issues of network virtualization duplication and pod engagements bounded by virtual machines in nested network virtualization by shortening the packet lengths and reducing resource fragmentation [45].

3.3.4. Inheritance

In hierarchical virtual networks, inheritance refers to the property that a child virtual network automatically inherits

rules, configurations, policies, etc. from its parent virtual network. This simplifies the management of virtual networks, as network administrators need not be involved in redefining policies and configurations for virtual networks at the lower level of the hierarchy, as most of them are inherited from upper-layer virtual networks. In service-oriented hierarchical network virtualization, there exist different layers of services bestowed by different players that can be dynamically uncovered, where the lower layers inherit from the upper layers [46].

3.3.5. Revisitation

Revisitation refers to the ability of virtual networks to be revisited and to be dynamically reconfigured and modified during their lifecycle. They can be either automatically reconfigured, established on dynamic network conditions or manually reconfigured by network administrators with updated policies, rules, etc. Moreover, for one physical node, multiple virtual nodes of the matching virtual network can be configured and updated dynamically by revisiting to rearrange the virtual network structure. Thus, the virtual network embedding in virtual networks can be dynamically configured. In [47], virtual network embedding is dynamically configured by modelling as an integer linear programming problem considering resource fragmentation cost along with a virtual network embedding algorithm to consider resource fragmentation degree relying on the present network status and virtual network requests.

3.4. Characteristics

Virtual networks are characterized by several features that distinctly identify them, which are discussed in brief in the following subsections.

3.4.1. Flexibility

Flexibility refers to the freedom that exists within the service providers to adjust network topology, forwarding policies, security policies, etc. without being influenced by the underlying physical infrastructure or other virtual networks. For instance, sensors can be virtualized to provide data fusion tasks by selecting an appropriate technique to create flexible and virtual sensors in a sensor network without needing to know sensor-related details [48]. It allows customization of network environments to match applications. In [2], flexibility of a virtual network is defined as the ability to cater to new requests, such as requirement changes, and provide quantitative measures to measure the degree of flexibility in softwarized networks, such as virtual networks, while proving that these networks have a high degree of flexibility.

3.4.2. Manageability

Virtualized networks allow central management capabilities, allowing network administrators to manage the network centrally without having to configure hardware manually. Service providers are given full control permission for the virtual network. HYVI is a hybrid virtualization system that combines the benefits of software and hardware virtualization to seek a balance between the performance and manageability of virtualization [49]. Moreover, as InPs are separated from SPs, manageability is easier since SPs deal with virtual resources and not with physical infrastructure.

3.4.3. Scalability

Network virtualization allows the creation of new virtual networks or the expansion of existing ones when network demand increases without significant changes to the physical infrastructure. However, in cases where physical resources are inadequate to meet the increasing demand, InPs should provide more resources to be converted into virtual resources by MVNPs. For instance, SVLAN is a scalable VLAN that can scale to a high number of distributed systems and can provide network isolation at different granularities [50].

3.4.4. Isolation

When numerous virtual networks survive in a physical network, there should be isolation among them to improve fault tolerance and security in simultaneous operation. This isolation allows faults or security attacks in one virtual network to not affect other core virtual networks. For instance, FlowVisor provided network virtualization in the data plane, where the same hardware forwarding resources can be shared between numerous logical networks having distinct forwarding policies, providing isolation among the virtualized networks [51].

3.4.5. Programmability

Programmability refers to the ability of the virtual networks to be programmed such that service providers can engage customized protocols using application programming interfaces that allow a high degree of automation for network management. Programmability allows conveying application policies to the underlying network infrastructure. VNode has been suggested as a virtual infrastructure that can achieve high performance and programmability so that network developers can implement high level policies in network virtualization [52].

3.4.6. Heterogeneity

Virtual networks can be engaged on top of a combination of heterogeneous networks such as optical, cellular, vehicular, Wi-Fi, wired, etc., and each of the multiple virtual networks within the given physical infrastructures can also be heterogeneous with respect to each other. Specifically, virtualization can be realized in vehicular networks with the aid of network function virtualization, SDN, and network slicing to improve the functionality of traditional locally trained and machine learning-driven autonomous driving [53]. As network virtualization can abstract diverse network functions, virtual networks tend to have a high degree of heterogeneity. Network virtualization enables heterogeneous network platforms from different vendors having diverse programming environments, protocols, etc. to be interoperable [3].

3.4.7. Multi-tenancy

Virtual networks support multi-tenancy by allowing multiple users or groups to have their own secluded virtual networks; however, they share the corresponding (same) physical infrastructure. This allows logical separation of user functions, despite the fact that they use the same physical resources. Typically, software-defined networking and network function virtualization can be engaged to allow multi-tenancy by slicing the network [54].

Table 1: A compendium of current literature on diverse aspects of network virtualization.

| Virtualization aspect | Sub-aspect | Stratagem | Performance |
|--------------------------|------------------------------|--|---|
| Technologies | Virtual local area network | Topology discovery using VLAN ID, MAC addresses [28] | Function in heterogeneous networks |
| | | Network segmentation for sensitive and critical resources [29] | Simplify network management and provide improved security |
| | Virtual private network | Associating customer edge devices with provider routers [30] | Provide privacy and anonymity |
| | | Layer 2 and Layer 3 VPN implementation [31] | No performance evaluation presented |
| | Active & program. network | Customized services, executable programmed code [32] | In capsule processing, Java network I/O is a bottleneck |
| | | Accommodate multiple levels of networking system [33] | Able to incorporate all programmable networking levels |
| Business model | Overlay network | SIP, cryptography established secure multicast overlaying [1] | Optimized network latency and bandwidth utilization |
| | | Software-established optimization scheme [35] | Eliminate encapsulation overheads |
| | Elastic network | Optimization to select light paths for VNE [37] | Save 60% spectrum resources, faster solution |
| | | Resource allocation with multiple InPs [4] | Low processing time, successful embedding, high acceptance |
| | Infrastructure provider MVNP | 3-sided matching using size and cyclic preference [38] | Enhance user throughput, less running time |
| | | MVNO | Allocate resources using matching theory, auctioning [39] |
| Architectural principles | Service provider | Leased resource cost minimization by server selection [40] | Maximize social welfare, stable matching |
| | | End user | Low response time, link utilization, and jitter |
| | Abstraction | Multi-layer game to allocate resources [41] | Maximize payoffs of InPs, MVNOs, offer spectrum to users |
| | | Advanced network abstraction using overlay network [43] | Provide tenant contracts and network services |
| | Coexistence | Virtualizing IPv4 over Ipv6 networks using tunnelling [44] | No performance evaluation |
| | | Recursion | Avoid NV duplication-short packets, resource fragmenting [45] |
| Characteristics | Inheritance | Layered services with inheritance [46] | 40% reduction in cloud utilization cost |
| | | Revisitation | Services can be dynamically discovered |
| | Flexibility | ILP to dynamically configure VNE [47] | Reduce fragmented resources |
| | | Quantitative measures flexibility in softwarized networks [2] | Provide a trade-off between cost and flexibility |
| | Manageability | Hybrid software and hardware virtualization [49] | Strike a balance in performance and manageability |
| | | Scalability | A VLAN scaling to a high number of distributed systems [50] |
| | Isolation | FlowVisor to share hardware resources with isolation [51] | Offer communication isolation with different granularities |
| | | Programmability | Does not require programmable hardware |
| | Heterogeneity | VNode to implement high-level network policies [52] | Coexistence performance and programmability |
| | | Heterogeneous network platforms using virtualization [3] | High interoperability and scalability |
| | Multi-tenancy | Using SDN and NFV [54] | Flexible and efficient resource allocation for multiple tenants |
| | | | |

Table 1 illustrates a compendium of current literature on diverse aspects of network virtualization.

4. CORE CONCEPTS OF NETWORK VIRTUALIZATION

4.1. Resource Sharing

4.1.1. Spectrum sharing

Spectrum sharing essentially means that multiple MVNOs can share the same spectrum established by agreements among the operators. This considers the wireless spectrum resource as a whole and shares it among virtual networks [55]. Dynamic Spectrum Sharing (DSS) is the most widely used spectrum sharing technique that allocates spectrum dynamically, considering real-time demands, and is used in intelligent networks. In [56], a spectrum sharing framework supporting any number of radio networks engages machine learning for forecasting and clustering in order to allocate spectrum for 5G virtualized networks.

4.1.2. Infrastructure sharing

Infrastructure sharing refers to network operators sharing infrastructure resources such as passive buildings and sites, power and energy infrastructure, radio frequency antennas

and eNodeBs, backhaul and backbone networks, routers, switches, etc., not being limited to network infrastructure. This reduces the cost per mobile network operator, and it can be achieved by varying technical and economic parameters, for instance, achievable throughput and pricing strategies in different infrastructure sharing strategies [5].

4.1.3. Full Network Sharing (FNS)

FNS is the combination of spectrum and infrastructure sharing, where both spectrum and infrastructure can be shared between numerous MVNOs using agreements. Full network sharing is supported in multi-operator core networks and gateway core network configurations. Virtualization is more efficient and flexible for full network sharing. In the 3GPP standard for full network sharing, multi-operator and gateway core networks coexist [57].

4.2. Slicing

4.2.1. Spectrum slicing

Spectrum slicing involves slicing (dividing) a given spectrum into multiple non-overlapping slices in a specific domain, such as time, frequency, or space, where multiple service providers can be allocated to different slices of the

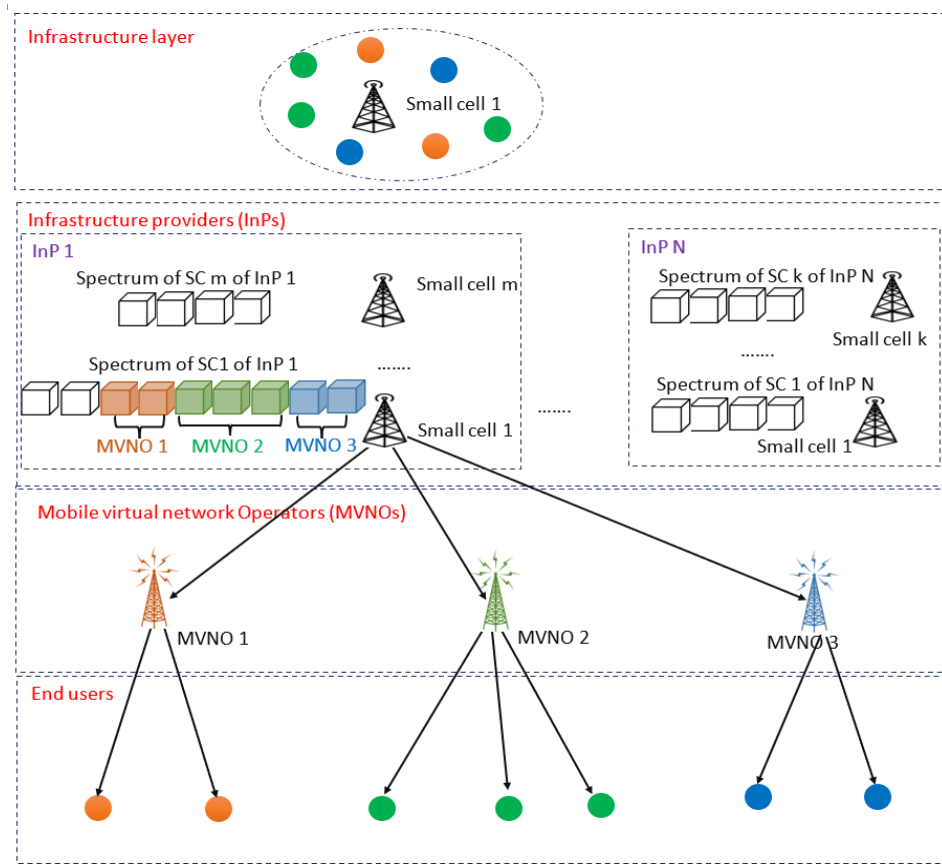


Fig. 3: Generic spectrum slicing concept within a small cell.

sliced spectrum. This allows multiple users/services to transmit simultaneously without causing interference to each other. In [6], the spectrum is sliced by minimizing the bandwidth blocking rate and the total number of slicers using mixed integer linear programming in an elastic optical network.

The generic spectrum slicing concept within a small cell in a mobile network is illustrated in Fig. 3.

4.2.2. Infrastructure slicing

Infrastructure slicing involves slicing the physical resources (creating multiple virtual instances of the same physical infrastructure) such as base stations, antennas, and other hardware resources such as computing, storage, etc. by MVNPs into virtual slices and allocating each infrastructure slice to different virtual networks (MVNOs) [58]. For instance, when a MVNO needs to lease spectrum from an InP, the MVNP has to slice and virtualize the infrastructure and allocate it to the corresponding MVNO. In [59], OpenFlow has been engaged to provide cross-layer infrastructure virtualization, allowing multiple virtual infrastructures to share a given physical infrastructure.

4.2.3. Network slicing

Network slicing involves creating logically isolated virtual networks that are implemented on a shared physical infrastructure. This can be achieved using infrastructure slicing and other concepts such as spectrum slicing and network sharing. Per each virtual network slice, different parameters, for instance, quality of service, bandwidth, latency, etc., can be defined as required, allowing the coexistence of multiple isolated virtual networks providing

different services [60]. The generic network slicing concept in a mobile communication network is illustrated in Fig. 4.

For instance, a dynamic network slicing scheme for 5G networks implements a virtual network embedding task by using an algorithm to predict traffic demands and a tactic to uncover the number of virtual network functions and resources needed for each network slice [61].

4.2.4. Flow-level slicing

Flow-level slicing occurs within a network slice. For a given network slice (virtual network), slicing will occur established on the characteristics of different flows. It allows fine-grained control in a network slice. For instance, high-priority flows can allocate more resources even under high-resource usage instances, and vice versa. For instance, in a software-defined wireless virtual network, multi-flow transmissions are realized by virtual resource allocation considering quality of service requirements by modelling it as a social assistance maximization task having distance as the transaction expense along with a shadow pricing scheme [62].

4.3. Network Function Virtualization (NFV)

NFV is the process of creating virtual network functions just like routers, load balancers, intrusion detectors, etc. instead of dedicated hardware resources for achieving them. NFV uses virtual machines or containers to implement software instances of network functions, and it promotes resource sharing and efficiency as multiple network functions can be virtually implemented on the same physical device. In [63], for forward graph embedding of network function virtualization of an elastic optical network, computational

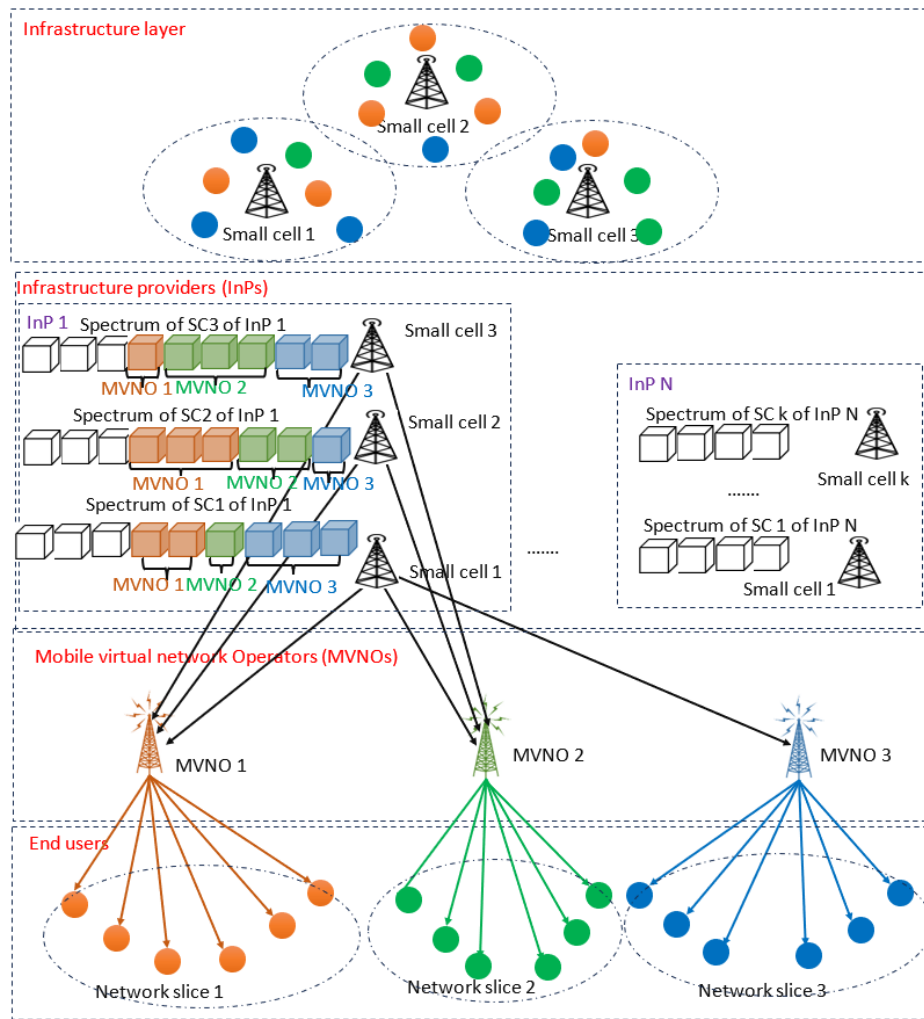


Fig. 4: Generic network slicing concept in a mobile network.

resources and optical bandwidth are allocated using an integer linear programming model for smooth operation of virtual network functions having interconnections among them.

4.4. Software-Defined Networking (SDN)

SDN embarks on logical decoupling of the control layer from the data layer, allowing centralized network control and management using a software-established controller [64]. SDN and NFV are often engaged in combination, where the SDN engages multiple instances of NFV in its network. Deep Reinforcement Learning (DRL) has been engaged to manage virtual network data flows in a programmable software-defined IoT edge network implementing NFV [65].

4.5. Service Chaining

Service chaining involves creating a chain of virtualized network services through which network traffic should pass in sequence. It is a customizable service path that can be dynamically updated if required without requiring dedicated hardware. Service chaining is often engaged in combination with NFV and SDN. For instance, LASH-5G implements virtualized functions in edge clouds to provide adaptive and latency-aware service chaining of network function virtualization-established virtual functions across network domains interconnected using software-defined networking [66].

Table 2 illustrates a compendium of current literature on network virtualization concepts.

5. A COMPENDIUM OF BLOCKCHAIN TECHNOLOGY

A sequence of intertwined blocks or recordings/transactions comprises the distributed ledger called the blockchain.

5.1. Arrangements

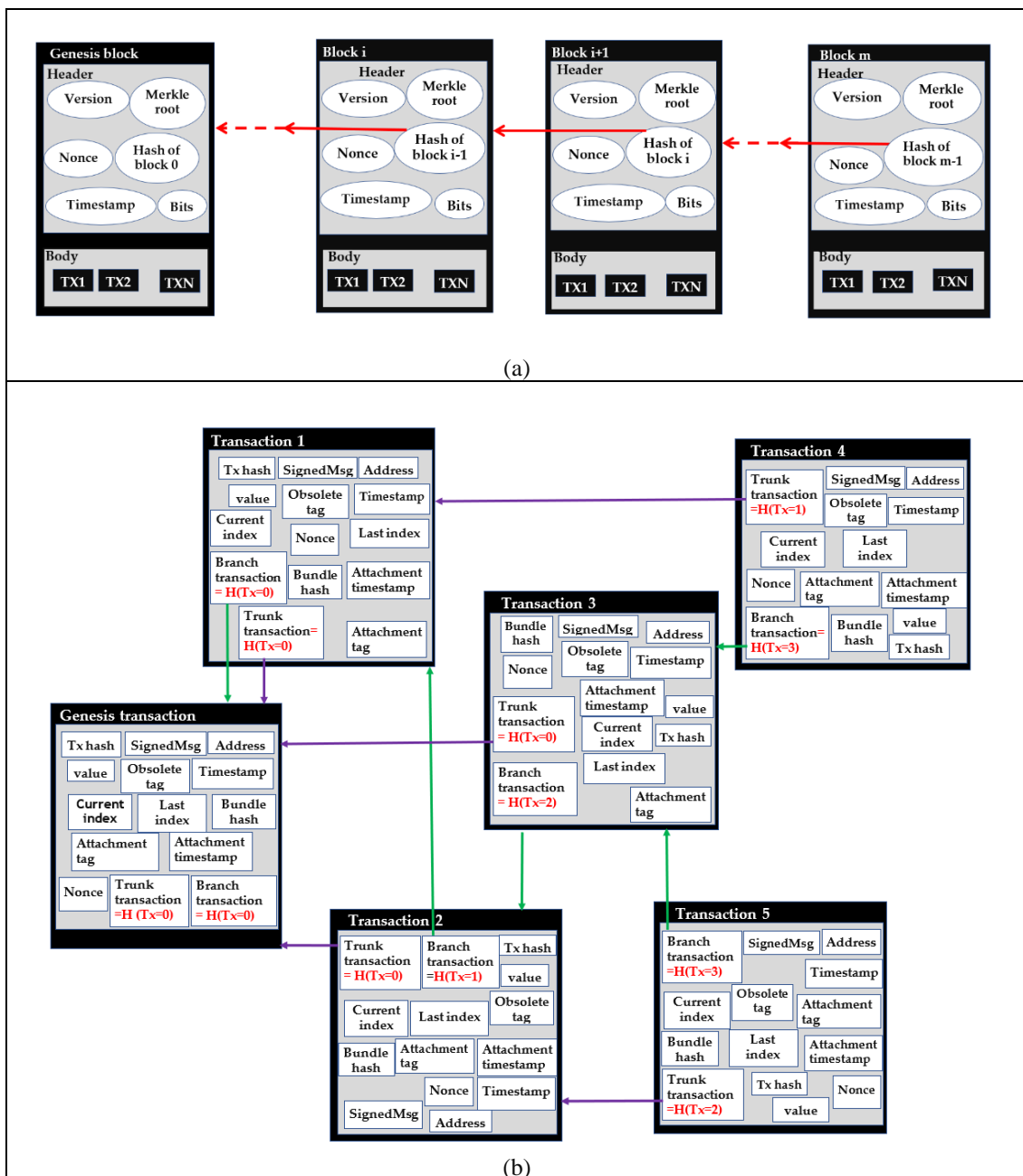
Every block within the regular blockchain, which comprises a header section and record section, is related to its precursive block (excluding the origin block), putting to use the precursive block's hash digest, and the recordings/transactions within the record section are structured as a Merkle tree structure [9].

Irregular blockchain comprises an assortment of intertwined recordings/transactions where one recording/transaction might validate various other recordings/transactions that originated prior to it. These recordings/transactions are deficient in header sections and record sections; due to this, Merkle trees are absent [8].

Fig. 5 illustrates the architecture of regular and irregular blockchains.

Table 2: A compendium of current literature on network virtualization concepts.

| Virtualization concept | Specific concept | Stratagem | Performance |
|---------------------------------|---------------------------|--|--|
| Resource sharing | Spectrum sharing | Machine learning for forecasting and clustering [56] | Allow arbitrary network slices to share resources |
| | Infrastructure sharing | IS by varying technical and economic parameters [5] | Sharing configurations affected by number of paying users |
| | Spectrum sharing | Coexistence of multi-operator and gateway core networks [57] | No performance evaluation |
| Slicing | Spectrum slicing | Integer linear programming-Min. BW blocking rate [6] | 68% increment in bandwidth blocking rate |
| | Infrastructure slicing | OpenFlow for cross-layer infrastructure virtualization [59] | Capability of manipulating virtualization behavior independently |
| | Network slicing | Strategy to find VNF, resources for slicing [61] | No performance evaluation |
| | Flow-level slicing | Social welfare maximization problem [62] | Energy efficient slicing |
| Network function virtualization | Forward graph embedding | Allocate resources using integer linear programming [63] | Feasible VNF despite its complexity |
| Software defined networking | Network function virtual. | Deep RL to manage virtual network data flows [65] | Goal is met on average in 183 episodes |
| Service chaining | Network function virtual. | Virtual functions across network domains using SDN [66] | Low latency and self-adaptive |

**Fig. 5:** Blockchain architectures: (a) Regular, (b) Irregular (IOTA).

5.2. Transactions

A given peer node can commence a blockchain transaction/recording, which is subsequently sent to all network peers and secured by putting to use the sender's secret key. A consensus strategy will commence once each peer puts to use the non-secret key to validate the transaction/recording. Block generators should embroil in consensus/assent by combining the transaction/recording within a block, which is subsequently sent to the distributed ledger network and pitched in by each peer node in the distributed ledger network posterior to block validation [67].

5.3. Blockchain cryptography

To secure the integrity of recordings/transactions in the blockchain, a hashing method is put into use to dispense constant-size hash digests with lesser collisions [11].

Putting into use a computer-generated signature, key pair cryptography incorporating an asymmetric cryptographic key duet is put into use to validate recordings/transactions. For the purpose of intensifying the isolation of data, it's equally feasible to put it into use to encode blockchain recordings/transactions [10].

In the interest of validating recordings/transactions' accuracy, zero-knowledge proofs are put into use, concealing the identity-related data of recordings/transactions, intensifying isolation, and hindering the sending of confidential data [68].

Quantum-safe cryptography puts into use competent cryptographic techniques that are buffered from attacks from quantum machines, such as SIKE, Kyber, and so on [12].

5.4. Consensus/Universal Assent

Blockchain consensus puts widespread universal assent into use to generate and validate fresh blocks, securing the integrity of the distributed ledger.

In vote-established universal assent, data is sent out and brought in within the network peers as they collaborate closely to validate blocks. The beloved choice vote-established universal assent technique put into use, PBFT, in the course of which a chief combines recordings/transactions within a block, sends it, and peer nodes resend it to validate the block brought in through the agency of the parent, is the same [13]. If every given peer got the same reproduction of a fresh block through the agency of going past the two-thirds majority of the network's peers, the block would become combined with the distributed ledger.

Proof-established universal assent requires peers to dispense compelling support because they are vitally compensated for combining a fresh block into the distributed ledger. The most widespread proof-established universal assent technique is named proof-of-work, which demands a peer execute tasks by tackling a complex problem for the purpose of securing its faithfulness [69]. However, this approach is more energy-consuming.

6. BLOCKCHAIN-ESTABLISHED NETWORK VIRTUALIZATION

6.1. Construct

Grounded in this documentary analysis, the blockchain-established network virtualization construct can be segmented into the succeeding 5 segments.

- C1 -- Act as a broker/manager for slicing, NFV, etc. Ex: Blockchain and SCs can act as auditors or orchestrators in network/infrastructure/spectrum slicing, NFV, etc.
- C2 -- Secure storage of data, preserving privacy by engaging cryptographic techniques, and improving loyalty by preventing security attacks such as double spending attacks, etc. Ex: Virtual network embedding, allocating resources established on high credibility, etc.
- C3 -- Providing service level agreements, auction algorithms for resource trading, mechanisms to deal with own transactions, etc., engaging blockchain and SCs.
- C4 -- Dedicated distributed consensus to reach agreement for network virtualization among multiple parties, reducing security attacks. Ex: proof-of-strategy reducing administrative expenses, consensus with dynamic tip selection, learning algorithms for resource sharing, etc.
- C5 -- Blockchain-established access control for network virtualization.

Fig. 6 illustrates the construct of network virtualization utilizing blockchain.

6.2. Review on Existing Frameworks for Network Virtualization Utilizing Blockchain

6.2.1. Blockchain established spectrum sharing

An incentive-provider, privacy-preserving blockchain has been engaged for efficient spectrum sharing in 5G mobile networks, which has two stages: in the first stage, human-to-human users enter into a contract in conjunction with the base station to receive payments considering the contribution, and in the second stage, spectrum is allocated to machine-to-machine users [70]. Preventing the spectrum allocation process from singular vulnerability, work in [22] proposes a distributed citizens broadband radio service for 6G mobile networks established on blockchain, engaging a ring signature technique for privacy protection and a new proof-of-strategy consensus that is able to allocate spectrum, reducing administrative expenses. In cognitive radio-established internet of battlefield things networks, ProBLESS is a blockchain-established framework for secure sharing of spectrum sensing information amidst secondary user equipment in order to make collaborative spectrum sharing judgments. It engages a protocol known as proactive blockchain-established spectrum sharing (ProBLESS) in order to engage blockchain to counter-attack SSDF attacks using a novel consensus algorithm and SCs to validate

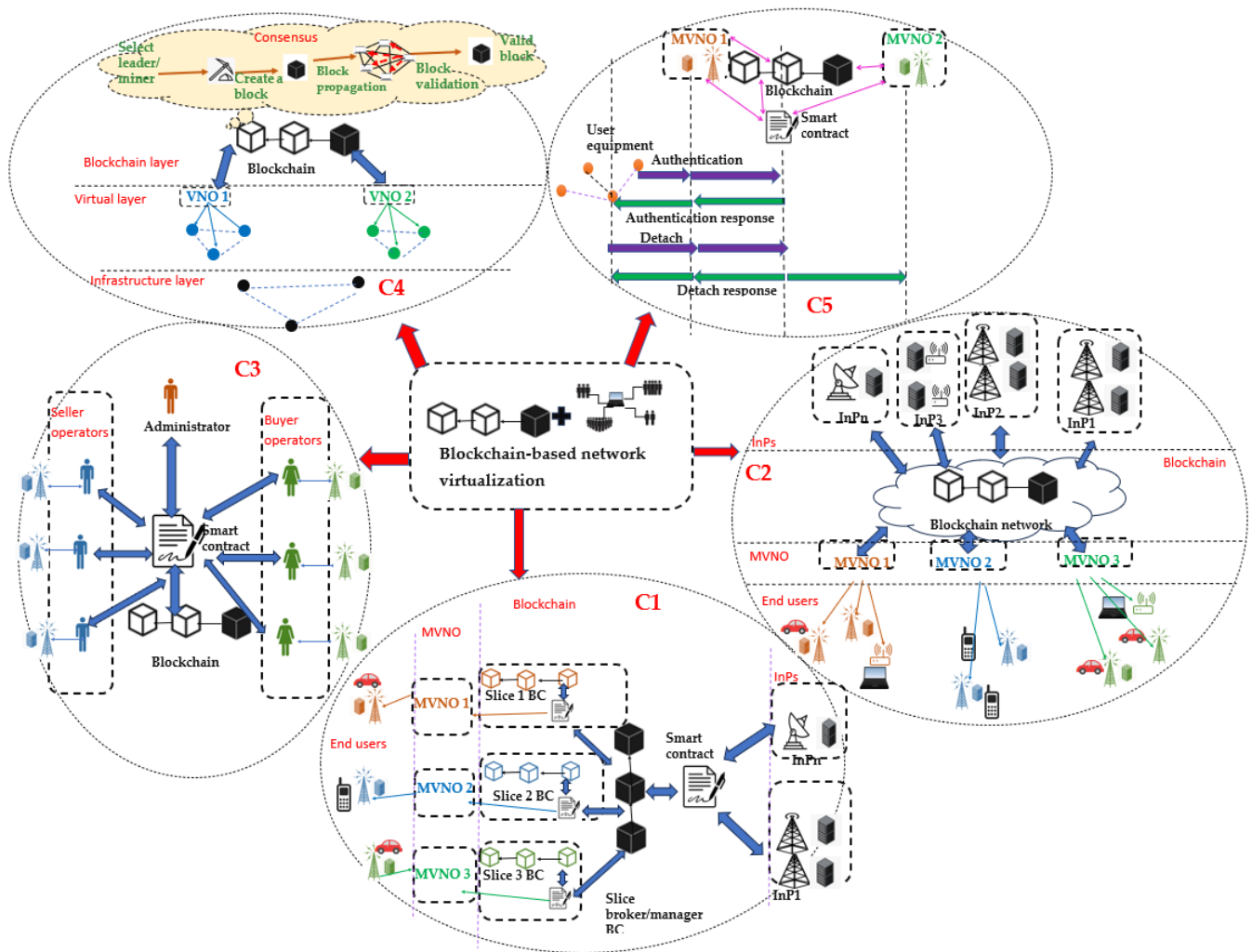


Fig. 6: Construct of network virtualization utilizing blockchain.

spectrum data [71]. In large-scale 6G-enabled IoT networks, a directed acyclic graph blockchain has been engaged for user autonomy spectrum sharing, providing a scalable solution where the swarm intelligence of users achieves convergence in blockchain consensus and a dynamic tip selection strategy to improve universal utility pertaining to the demand and supply of spectrum where the ring signature is integrated to improve the privacy of the spectrum sharing process [23]. In a blockchain-established spectrum sharing system engaged in a 5G-enabled IoT dense network where users can efficiently share spectrum using SCs, a game theoretic approach along with a tit-for-tat technique has been engaged to obtain corporation from non-cooperating users [72]. Alternatively, a blockchain-established dynamic spectrum sharing scheme for IoT considers privacy and transaction dynamical behavior by using a SC-implemented double auction technique considering differential privacy to remunerate spectrum sharing and considering time-varying valuations where a DRL technique is engaged to determine the winner of the auction game [73]. In a multiple mobile network operator wireless communication environment, Hyperledger fabric blockchain is utilized for recording spectrum allocation using SCs, where a multi-chief multi-disciple Stackelberg game is engaged to solve optimal spectrum pricing and buying strategies for spectrum sharing [74]. Similarly, MOSS is another multi-operator spectrum sharing platform that uses

SCs engaged on permissioned blockchain to implement spectrum trading among multiple operators, enabling trustful spectrum sharing with a punishment technique for malicious operators [21].

6.2.2. Blockchain established infrastructure sharing

A blockchain network is engaged in 5G small cell networks where blockchain provides a distributed home subscriber server in which core networks of different operators can utilize HSS in a secure approach and SCs are engaged to provide self-organizing network features in order to cope with own-transactions among mobile operators as a tribute for sharing small cell infrastructure [75]. BEAT is a permissioned blockchain-established trustworthy and honest infrastructure sharing framework for 6G and surpassing 6G mobile networks, providing accountability and transparency parameters where infrastructure is shared among providers having device-level accountability and SCs initializing service-level agreements [76].

6.2.3. Blockchain established virtual private network

In a blockchain-established framework for access control in large-scale inter-organizational IoT networks, IoT devices attached to various organizations but corporate with each other are included in the same VPN for optimizing time and

resources for access control using the blockchain in a per-VPN approach [25].

6.2.4. Blockchain established software-defined virtual networks

Virtual Network Embedding (VNE): efficient allocation and implementation of virtual network requests using a blockchain-established VNE algorithm has shown high fault tolerance performance in software-defined virtual networks [19]. A three-layered consortium blockchain with a joint proof-of-stake and a modified version of PBFT consensus along with a vehicle trust value prediction approach is engaged to allocate more resources to high-credibility vehicles of a software-defined virtual network, where the multipath mapping task of the virtual network is converted to a flow problem involving multiple commodities in order to improve resource allocation efficiency [24]. A framework integrating SDN, edge computing, and blockchain technology for achieving efficient and secure wireless network virtualization where SDN enables network programming, edge computing enables user signal processing at base stations with low delay, and blockchain allows to halt the double-spending attack of reserving the same physical wireless resource to multiple virtual networks [18]. Software-defined IoT management virtual resources that support multi-tenancy can be hosted on edge devices where permissioned blockchain is engaged to securely distribute code and act as storage, which has resulted in low delay performance [77].

6.2.5. Blockchain established elastic network

Blockchain has been engaged to receive and process device-to-device vehicular transactions, where a categorized and chiefless consensus approach is engaged to decrease communication burden and improve scalability, and Lyapunov optimization is engaged for elastic resource allocation of the vehicular network in order to achieve high throughput [78].

6.2.6. Blockchain established spectrum slicing

In cyber-physical social systems engaging wireless communication, SCs on blockchain have been used for spectrum management, where the spectrum of a local cell is sliced into multiple channels and each channel is allocated a blockchain, and then using a KM protocol for transaction processing, where users mine or lease to access spectrum [17]. Bloc6Tel is a blockchain-integrated, secure, and trusted 6G spectrum allocation framework among telecom providers, where a blockchain-established auction algorithm engaged using SCs allocates the sliced spectrums, while telecom providers act as bidders and government authorities as auctioneers [20]. STBC is a spectrum trading platform for trading multiple sliced spectra among virtual networks in an efficient and secure manner using blockchain, which has a consensus mechanism to tolerate up to 33% of malicious nodes and sharding to improve the blockchain efficiency, which can prevent DDoS attacks using anonymous transactions [79]. Similarly, another blockchain-supported spectrum trading platform for elastic virtual optical networks, which trades different sliced spectrums established on the capacity requirements of virtual networks, where a virtual network with unutilized spectra can trade away the unused spectra and be rewarded with credits, while blockchain ensures the trustworthiness of the trading records, has been

studied in [80]. For a wireless network operated by multiple virtual network operators, a decentralized blockchain-enabled spectrum acquisition system to dynamically acquire the downlink spectrum by minimizing the total transmit power while fulfilling the average transmission rate thresholds has been effective by automatically achieving spectrum acquisition, charging, and authorization with the aid of SCs [81].

6.2.7. Blockchain established infrastructure slicing

An infrastructure slicing framework for providing virtual network functions by creating network slices and engaging blockchain to provide auditability and orchestration operations of sliced infrastructure while guaranteeing privacy and isolation of slices has been suggested in [16]. In [82], SCs on consortium blockchain are engaged for safe resource slicing and trading amidst mobile virtual network operators in a 5G radio access network, where the incentive mechanism is formulated as a two-stage Stackelberg game and its equilibrium is achieved through a duelling deep Q network.

6.2.8. Blockchain established network slicing

DBNS is a scheme that enables distributed network slicing, which provides the opportunity for service and resource suppliers to lease resources dynamically to provide good performance for the services. It has a global service positioning component to provide admission control and dynamic resource assignment using a bidding system founded on blockchain [83]. In [15], blockchain is engaged as a secure network slice broker to provide a factory as a service that allows coordination of slice and security service level agreement managers to provide distributed network services for allocating resources using a federated slice selection algorithm with a Stackelberg game approach, where optimal prices are computed using DRL. Similarly, NSBchain is another blockchain-established network slicing brokerage framework that addresses new business models' requirements by defining an intermediate broker, allowing infrastructure suppliers to assign network assets to intermediate brokers with the aid of SCs and intermediate brokers to assign and distribute resources between tenants [84]. A hierarchical framework engages a consortium blockchain for spectrum trading amidst infrastructure suppliers acting as providers and mobile virtual network operators acting as buyers to create network slices and subsequent slice adjustment by considering underloaded and overloaded mobile virtual network operators, where incentive maximization by demand and pricing prediction is achieved using a 3-stage Stackelberg game whose equilibrium is realized using DRL [85]. BENS is a network slicing scheme using blockchain consensus that implements a leaning established algorithm that deals with the allocation of spectrum with proper primary user and secondary user interactions, minimizing 5G service provider costs, and providing the opportunity for resource providers to contract resources dynamically [86]. For service guarantee in inter-domain network slicing, SCs on blockchain are engaged to manage the lifecycle of service level agreements from service negotiation to decommissioning, using an artificial intelligence-driven closed loop to monitor exchanged services and predict service level agreement violations to activate mitigation actions [87]. A latency aware and user equipment state-established network slice allocation is realized in a transparent and secure manner for 5G mobile

Table 3: Interpretation of Blockchain-established network virtualization frameworks.

| Virtualization technique | Stratagem | BC construct | Blockchain arrangement | Blockchain consensus | Blockchain division | Virtual technology | Network division | Performance |
|--|-----------------|--------------|------------------------|------------------------|---------------------|-----------------------|-------------------|--|
| Spectrum sharing | B-ESSS [70] | C2 | Regular | PoW | Consortium | Overlay | 5G | Secure, efficient spectrum sharing, high throughput |
| | BEDSS [22] | C4 | Regular | PoStrategy | Generic | Overlay | 6G | Prevent SPoF, good system utility |
| | ProBLESS [71] | C3, C4 | Regular | PCA | Generic | Overlay | IoBT | Reduced CU-2.74%, Increased BR:8.3%, SD:5.5% |
| | DAG-EUA [23] | C4 | Irregular | DTS | Generic | Overlay | 6G-IoT | 10% enhancement in global utility |
| | GTAB-BSS [72] | C3 | Regular | Generic | Generic | Overlay | 5G-IoT | Improve spectrum sharing by 55.1% |
| | WDP-DRL [73] | C3 | Regular | PoW | Consortium | Overlay | IoT | Satisfy differential privacy, rationality, truthfulness |
| | MODSS [74] | C3 | Regular | PBFT, RAFT, Kafka | Consortium | Overlay | Wireless | Average latency increases with participants |
| | MOSS [21] | C3 | Regular | PBFT | Permissioned | Overlay | Wireless | High privacy, openness, and fairness |
| Infrastructure sharing | B-IS [75] | C5 | Regular | dBFT | Consortium | Overlay | 5G-SC | No performance evaluation |
| | BEAT [76] | C3 | Regular | PoAuthority | Permissioned | Overlay | 6G | Low overhead processing time |
| Virtual private network Software-defined networking | VPNB-DAC [25] | C5 | Regular | Generic | Generic | VPN | IoT | Secure, decentralized, scalable access control |
| | B-BVNE [19] | C2 | Regular | Generic | Generic | APN, overlay, elastic | SDVN | High fault-tolerant performance |
| | CB-BSSDN [24] | C4 | Regular | PoS + PBFT | Consortium | APN, overlay, elastic | SDVN | Better safety, LB, low consensus time |
| | SDN-EC-BC [18] | C2 | Regular | Generic | Generic | APN, overlay, elastic | Wireless | Increased trust, throughput, transparency |
| | V-IoT-EH [77] | C2 | Regular | PBFT | Permissioned | APN, overlay, elastic | SD-IoT | Permissioned BC can store virtual resource state data |
| Elastic network Spectrum slicing | ERA-D2D [78] | C2 | Regular | Grouped and leaderless | Generic | Elastic | Vehicular | Low communication overhead |
| | BBDSA-CPSS [17] | C3 | Regular | PoS + PoW | Private | Elastic | Cyber-physical | High security, prevent SPF |
| | Bloc6Tel [20] | C3 | Regular | Generic | Generic | Elastic | 6G | Better resource utilization, request overhead, fairness |
| | STBC [79] | C4 | Regular | Custom | Generic | Elastic | 5G-IoT | Prevent double spending, DDoS, 30% better spectrum utilization |
| | B-AST [80] | C4 | Regular | PoContribution | Generic | Elastic | Optical | Improves network capacity utilization, QoS |
| | DB-BDSA [81] | C3 | Regular | PBFT, Raft | Permissioned | Elastic | Wireless | Similar minimum sum power for spectrum allocation |
| Infrastructure slicing | ISIVF-B [16] | C1 | Regular | BFT | Consortium | Overlay | Generic | Secure, but consensus is challenging |
| | B-RTDRL [82] | C3 | Regular | PBFT | Consortium | Overlay | 5G | Reduce double spending attack by 12% |
| Network slicing | DBNS [83] | C3 | Regular | Generic | Private | Overlay | 5G | Improved throughput, acceptable average delay |
| | SNSB [15] | C1 | Regular | PBFT | Public/consortium | Overlay | 5G | High success rate, low mean federated slice cost |
| | NSBchain [84] | C1 | Regular | Kafka/Raft | Consortium | Overlay | 5G | Good throughput, SR collision increases with variance |
| | CB-STNS [85] | C3 | Regular | Generic | Consortium | Overlay | 5G | Utility is maximized, fair, secure |
| | BENS [86] | C4 | Regular | Custom | Private | Overlay | 5G | High energy efficiency, overall system throughput |
| | B-ZTSA [87] | C1 | Regular | Default Corda | Permissioned | Overlay | 5G | Predict dynamics in service demand accurately |
| | NS-5G [88] | C3 | Regular | PoAuthority | Generic | Overlay | 5G | Improved transparency and efficiency of resource handling |
| | B-SLAAS [89] | C3 | Regular | PoW | Public | Overlay | 5G | Low encryption time, gas consumption |
| | SliceBlock [90] | C2 | Irregular | PoSpace | Generic | Overlay | 6G | Secure and scalable network slicing |
| | NFV-MANO [91] | C4 | Regular | Custom | Generic | Overlay | IoV | Lower loss and high reward |
| Network function virtualization | BE-SLA [92] | C3 | Regular | PoW | Private | Overlay | Edge | Less time required for SLA, validation time increases with transactions, nodes |
| | B-NFV-MEC [93] | C4 | Regular | Custom | Generic | Overlay | Mobile edge cloud | Low latency and operational cost in resource allocation |
| | B-NFV-ASC [94] | C3 | Regular | Generic | Public | Overlay | Cloud | Throughput up to 20% |

| | | | | | | | | |
|------------------|--------------|----|---------|---------|---------|-----------------------|---------|---|
| Service chaining | BRAIN [95] | C3 | Regular | PoW | Public | Overlay | Generic | Feasible, consume additional fees, time |
| | NFV-B5G [96] | C2 | Regular | Generic | Generic | Overlay | 5G | Latency increases with nodes, arrival rate |
| | CMM-NFV [97] | C1 | Regular | PBFT | Generic | Overlay | Generic | Total data, consensus time increase with BC modules |
| | SCS-B [98] | C3 | Regular | PoW | Private | Overlay, APN, elastic | SDN | 28.7% saving in retrieval time |

network slicing using blockchain in order to improve resource handling operation efficiency [88]. Blockchain is engaged to store service parameters securely using an encryption algorithm (trapdoor order-revealing) to preserve privacy, where SCs are engaged to audit the network slicing-service level agreements and activate punishments automatically when violating such agreements [89]. SliceBlock utilizes generative adversarial networks for network slicing, considering slice capacity, QoS demands, etc., where an irregular blockchain with proof-of-space consensus is engaged per slice in 6G network function virtualization environments for ensuring the security and privacy of transactions in each slice [90].

6.2.9. Blockchain established Network function virtualization

Blockchain has been engaged in reaching distributed consensus between various administration and orchestration systems for network function virtualization, in which mobile edge computing is engaged to handle blockchain computations where node, administration and orchestration system, and edge server selection are formulated as a problem and solved using DRL [91]. In edge-established network function virtualization, in order to provide trusted service level agreements among the infrastructure provider and edge device owner, SCs engaged on a private blockchain have been engaged, replacing trustless centralized authority [92]. Similarly, for the mobile edge cloud paradigm for distributed network function virtualization under multiple management and orchestration systems, blockchain has been engaged to reach consensus among such systems along with an optimization approach to resource allocation considering service latency and operational cost [93]. Alternatively, network function virtualization has been engaged to virtualize the work of the blockchain using the autonomous operation of SCs among virtual nodes established on cloud computing, where transactions among the virtual nodes occur smoothly through the blockchain [94]. BRAIN is a blockchain established reverse auction mechanism where infrastructure providers compete to supply network function virtualization considering the demands of specific end users, which enables the monetization of network function virtualization and reduces the costs associated with it [95]. Blockchain has been engaged to dynamically share spectrum resources among industry applications that use network function virtualization gadgets while reaching extremely reliable low-latency communication requirements in 5G and beyond mobile networks [96]. Blockchain has been effective in secure administration, setup, and migration of virtual network functions by providing a robust framework for storing configuration updates in an immutable manner and providing anonymity for virtual network functions and tenants [97].

6.2.10. Blockchain established service chaining

Blockchain has been engaged to ensure the reliability and traceability of service chaining data in software-defined networking, where bloom filters and SCs are engaged to improve the retrieval efficiency from blockchain [98].

7. REVIEW INTERPRETATION

7.1. Interpretation of Each System

Table 3 illustrates the complete interpretation of each blockchain-established network virtualization framework in relation to blockchain-related parameters, network virtualization parameters, techniques, network-related parameters, etc.

7.2. Overall Interpretation

Fig. 7 chart-wise illustrates the overall allocation of BC-established network virtualization frameworks deliberated within this work.

As illustrated in Fig. 7a, the most prevalent blockchain-established network virtualization concept is held by C3 (45%), followed by C4 (22.5%), C2 (17.5%), C1 (12.5%), and C5 (5%). Thus, operating blockchain and SCs for providing service level agreements, auction algorithms for resource trading, and similar items in network virtualization are most prominent in existing literature, while blockchain-established access control for network virtualization is scarce. Moreover, as illustrated in Fig. 7b, 95% of blockchain-established network virtualization frameworks engage regular blockchain architecture, while only 5% use irregular blockchain. As illustrated in Fig. 7c, 22.5% of BC-established network virtualization frameworks do not emphasize a definitive universal assent technique apart from the remaining frameworks, where PoW (15%) is the most prevalent universal assent approach, followed by PBFT (12.5%), customized universal assent, PoAuthority, PoSpace, and so on. Furthermore, as illustrated in Fig. 7d, overlay networks are the most prevalent network virtualization technology (80%) used in the blockchain-established network virtualization frameworks reviewed, followed by elastic networks (27.5%), APN (12.5%), and VPN (2.5%). Additionally, as illustrated in Fig. 7e, BC-established network virtualization has been applied mostly to 5G networks (27.5%), followed by generic wireless networks, 6G, generic networks, IoT, 5G-IoT, SDVN, and so on. Finally, by looking at Fig. 7f, it is evident that the BC-established network virtualization concept was kickstarted in 2016 and eventually reached the highest level of concept proposals in 2020, then gradually contracted in publication volume afterwards.

As per the review, advantages such as enhanced privacy [70], reduced administrative expenses [22], prevention of SSDF attacks [71], high openness and fairness [21], high fault

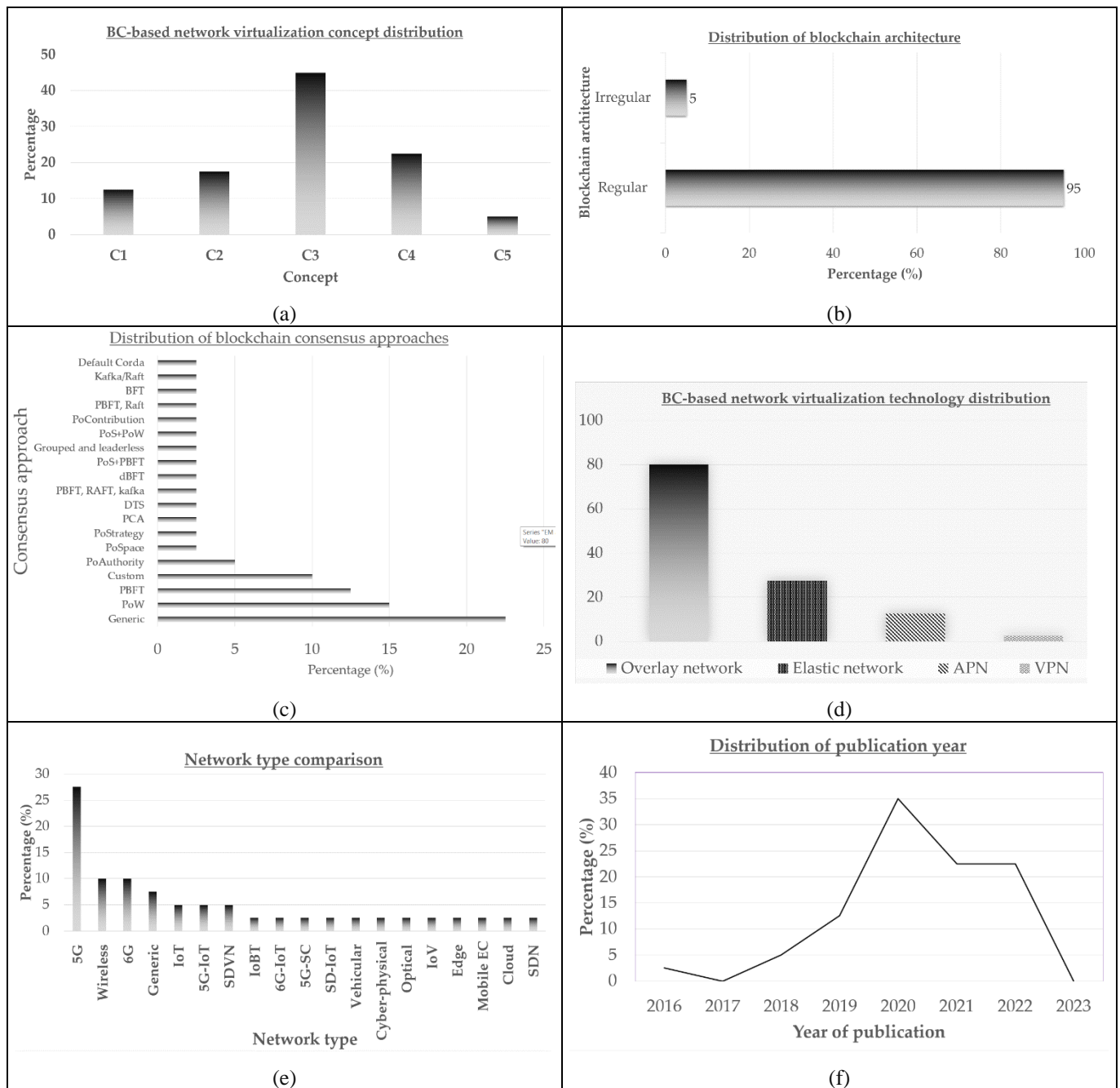


Fig. 7: Overall interpretation (a) BC-established virtualization construct, (b) BC form, (c) BC universal assent, (d) NV technology, (e) Network form, and (f) Instance of publication.

tolerance [19], prevention of SPF [17], better resource utilization [20], prevention of double spending and DDoS attacks [79], etc. exist in blockchain-established NV compared to traditional NV.

However, from the review, we can also highlight drawbacks like latency increment with participants [74], challenging consensus [16], consuming additional fees [95], latency increment with arrival rate [96], consensus time increment [97], etc. Some possibilities and obstacles are discussed in the following subsection.

As a summary, we can specify incentive-based spectrum sharing [70], ring signature technique and a new proof-of-strategy consensus [22], blockchain-established spectrum sharing (ProBLESS) protocol [71], dynamic tip selection

strategy [23], a game theoretic approach along with a tit-for-tat technique [72], DRL and double auction technique [73], Stackelberg game [74, 82, 15, 85], punishment technique [21], HSS [75], service level agreements [76, 87, 89, 92], access control [25], VNE [19], joint consensus and trust prediction [24], SDN and edge computing [18, 77], Lyapunov optimization [78], KM-protocol [17], auction algorithm [20], spectrum trading [79, 80], spectrum acquisition [81], BC-based infrastructure slicing [16], bidding system [83], slicing brokerage [84], slice allocation [88], leaning established algorithm [86], generative adversarial networks [90], DRL [15, 73, 85, 91], consensus and optimization [93], smart contracts [94], reverse auctioning [95], NFV [96, 97], and SDN and bloom filter [98], as algorithms, protocols, or technologies utilized for BC-established NV discussed in this interpretation.

8. DISCUSSION

8.1. Possibilities

8.1.1. Compatibility with resource trading platforms

Slicing and sharing operations in network virtualization can involve resources such as infrastructure and spectrum trading, where these resources are traded established on a pricing scheme. Blockchain is readily integrable with such platforms to trade resources among InPs and MVNOs as buyers, considering the load of the operators. In these systems, game theory is utilized for modelling interactions and deciding the optimum incentive scheme. Blockchains go hand in hand with resource trading frameworks, as blockchains support securely performing resource trading transactions automatically using SCs and consensus approaches with punishment techniques for malicious users using incentives decided using game theory for trading transactions.

8.1.2. Preventing central node of collapse

In a centralized architecture of networking, typically a centralized authority is responsible for making decisions related to network virtualization, such as spectrum allocation, such that these systems are vulnerable to the central node collapsing. However, in blockchain-integrated network virtualization, it is free from the central node of collapse, as the approach of blockchain is decentralized and collaborative network virtualization involving multiple parties, such as InPs and MVNOs, in decision-making. Thus, even if the activity of one party is broken due to failure, the network virtualization system can perform normally as it is not relying on a centralized authority. For instance, if blockchain is applied to traditionally centralized networks such as software-defined, NFV-driven underwater networks [99], it has the capability to reduce the drawbacks of central node collapse.

8.1.3. Improves the privacy and trustfulness

One of the main purposes of engaging blockchains for network virtualization is to improve the privacy and trustfulness of the process. In particular, blockchains use pseudonymous cryptographic addresses, making transactions partially private, whose privacy can be further improved by using cryptographic algorithms and privacy-aware SCs [100]. Moreover, blockchains provide a trustful environment for virtualizing the network due to the immutable nature of blockchain transactions, and untrusted devices can be identified using consensus approaches to remove them from network operation. For instance, in an NFV instance of data collection in SDN, blockchain can be effectively utilized to improve data collection security and privacy [101]. Furthermore, it can monitor the network devices to provide a trust value for each node to facilitate trust-value established resource allocation in network virtualization. Additionally, SCs can be engaged to provide trusted service level agreements among the infrastructure providers and device owners to implement a trust-established resource allocation scheme.

8.1.4. Provides opportunity for common agreement among multiple parties

Network virtualization involves network slicing and sharing operations with the involvement of multiple resource

providers and resource requestors [102]. In conventional network virtualization, it is challenging to come to a common agreement during network virtualization-related decisions. However, blockchain provides a handy framework to come to a common agreement thanks to its distributed consensus approach. These consensus approaches can additionally consider factors such as reducing administrative expenses, improving the global utility of demand and supply, reducing communication overhead, etc. while reaching agreement among multiple parties and being tolerated to a certain degree of malicious devices as decided by the consensus algorithm.

8.1.5. Efficient resource management

Blockchain-established network virtualization techniques bestow a platform for efficient resource allocation. For instance, in knowledge-defined networks, NFV can be utilized with the aid of machine learning techniques to manage network resources efficiently while achieving the desired network functions [103]. In these virtual networks, blockchains can improve the security of resource management. In these scenarios, efficiency is yielded as a result of sharing or slicing the same physical infrastructure among multiple virtual networks. The performance impact of engaging blockchain for security can be reduced by using energy-efficient blockchain implementations [104] such that the efficiency achieved for resource utilization by network virtualization is not degraded by blockchain. It includes using sharding techniques for blockchains [105], getting the support of edge computing to lower latency [106], etc. to improve the efficiency of blockchains.

8.2. Obstacles

8.2.1. High complexity and cost

When a new transaction is appended to the blockchain, it is only validated by the peers after several sessions of peer-to-peer broadcasts of the transaction and upon majority validation using a consensus approach [107]. Thus, when network virtualization is established on a blockchain network, the distributed approach for network virtualization transactions such as resource allocation data, virtual network embedding, etc., can cause additional complexity in the system compared to traditional network virtualization. Moreover, in order to engage blockchain, additional computation, memory, and communication resources will be required, which will elevate the total cost of the network virtualization process. Furthermore, as data analysis and decision-making are core processes in virtual networks, knowledge generation models like machine learning [108] can further make the system even more complex.

8.2.2. Majority attacks and SC vulnerabilities

Even though blockchain is secure under a smaller fraction of malicious devices, it can be vulnerable under a majority of malicious devices. This attack is known as the 51% vulnerability of the blockchain, where a majority of malicious devices can validate a malicious transaction in the blockchain [109]. In such a scenario, the security of the blockchain-established network virtualization process is compromised, and virtualization operations such as network slicing can be unfair and biased to the malicious users of the network. Moreover, SCs can be vulnerable if their code is not verified under all conditions. If SC code is not written without

errors, attackers may gain control over the blockchain upon execution of the SCs, putting the total process of network virtualization in danger.

8.2.3. *Performance degradation in real-time network virtualization*

Spectrum, infrastructure, and network slicing and sharing operations in network virtualization typically require making decisions in real-time relying on different types of data, such as spectrum allocation data, service provider availability and load, network latency, user equipment state, etc. [110]. However, blockchain networks may introduce an additional delay because of the distributed consensus process, and this delay will elevate with the rise in network extent. Therefore, the engagement of blockchain in securing the process of network virtualization will be challenging, as it may reduce the capability of making timely network virtualization decisions because of additional delays introduced in the blockchain network.

8.2.4. *Low scalability in storage and transaction processing*

When the network extent related to the network virtualization task is large, blockchains may struggle to perform efficiently, as in a low-size network, the storage requirements and transactions required to process them elevates rapidly with the network extent. So, the total throughput and efficiency of blockchain transactions will degrade with the rise of network extent, making it challenging to perform network virtualization operations such as slicing and resource allocation in real-time.

8.2.5. *Lack of standardizations and maturity*

Blockchain-established network virtualization is an emerging concept that has not yet been standardized to the best of our knowledge. This field is still evolving, so different researchers have recommended different realizations of blockchain-established solutions for achieving different network virtualization tasks. This lack of maturity can be stated as a challenge in the industrial implementation of blockchain-established network virtualization techniques, as it can be hard to find the best blockchain platform suitable for a given problem of network virtualization.

8.2.6 *Implementation difficulties*

As reviewed in this interpretation, blockchain-established NV has difficulties in scalability where there can be performance bottlenecks like latency being increased beyond an acceptable level when the number of nodes or blockchain modules increases [96, 97]. Moreover, as blockchain-established NV is still a less matured research domain, there exists a deficiency in industry standards to implement the system. Different networks may implement different blockchain systems from diverse vendors and diverse networking elements, which can act as a barrier for these systems to be compatible with each other and become interoperable. Moreover, as regulations for blockchains are still in the process of formulation, when practically implementing a blockchain-established NV instance, there can be regulatory challenges as well.

9. CONCLUSION, SUGGESTIONS, AND PROSPECTIVE PATHS

In this interpretation, we first denoted a compendium of network virtualization, denoting technologies, the business model, architectural principles, and characteristics. Next, the core concepts of network virtualization were briefly introduced. Following a concise prelude to the distributed ledger framework, we interpreted current frameworks of blockchain-established network virtualization under different virtualization techniques and concepts. Grounded in this documentary analysis, we identified 5 segments of the blockchain-established network virtualization construct: blockchain as a broker/manager for slicing, secure storage of data for network virtualization, SCs-established service level agreements, auction algorithms, etc., consensus approaches for network virtualization, and blockchain-established access control for network virtualization. Thereafter, we completely interpreted these frameworks in relation to network virtualization, blockchain features, and the blockchain-established network virtualization concept to examine directions and chasms. Finally, we deliberated the possibilities and obstacles of blockchain-established network virtualization.

This piece of work provides beneficial knowledge for current literature by providing state-of-the art blockchain-established frameworks for network virtualization along with a complete interpretation. Applying this examination, someone can instantly examine directions and chasms in blockchain-established network virtualization and also formulate anticipated time research, established on suggestions provided for the examined obstacles. Thus, forthcoming academicians can benefit from the complete interpretation and deliberation by getting insight into current works and examining where improvements are required.

Based on the detected obstacles, succeeding suggestions can be offered to mitigate them.

- Even though the infrastructure cost of transitioning from conventional network virtualization to blockchain-established virtualization is unavoidable, the operational cost and complexity can be reduced in several ways. First, SCs can be optimized for minimizing computations. In cases where blockchain-established authentication is engaged, lightweight authentication approaches using low computationally intensive cryptographic algorithms can be engaged for authentication during network virtualization. Moreover, administrative cost-reducing consensus approaches, for instance, proof-of-strategy, can be engaged.
- The 51% vulnerability of blockchain can be resisted by using a consensus approach such as delegated proof-of-stake instead of proof-of-work. Moreover, in the case of a 51% attack, an emergency response plan can help minimize the impact of such an attack. Before engaging SCs, they must be thoroughly verified formally to prove that they are mathematically and functionally correct. Moreover, regular auditing must be carried out to check whether the SCs perform in the manner specified once they are engaged in the blockchain.
- In the interest of satisfying the low latency and high throughput requirements of network slicing and sharing

operations, blockchains can engage several techniques. First, sharding can be engaged to partition the blockchain into a set of subsets, where each subset can execute transactions separately, enhancing the throughput. A major source of delay in blockchain networks is the consensus process; thus, a low-delay consensus approach such as proof-of-stake is more suitable for network virtualization than proof-of-work. Moreover, if possible, the resources of the communication network infrastructure can be upgraded, such as by increasing the bandwidth of the links to complete the consensus process in a short amount of time.

- In the interest of overcoming the issues with scalability for transaction processing, network managers can engage an irregular blockchain that has a higher scalability because of its parallel processing capacity. As a solution to the scalability issue of storage, off-chain storage can be supplemented with the blockchain, where less critical network virtualization data can be recorded off-chain. Alternatively, data can be recorded off-chain, which has the hash digest of the data recorded in blockchain to verify its validity, providing a scalable solution for secure data storage.
- In the interest of overcoming the lack of maturity for blockchain-established network virtualization, when selecting a blockchain framework for a given network virtualization task, one will have to refer to existing research work to select the type of blockchain, consensus approach, incentive mechanism, etc. because of the unavailability of industry standardizations. In the case that the existing literature does not provide satisfactory knowledge on the performance of combinations of the blockchain platform and network virtualization approach for a given network scenario, one can do a performance evaluation and select the best combination after inspecting the evaluation results.

Blockchains can be engaged to secure the integrity, privacy, authenticity, and trustfulness of different network virtualization processes, such as spectrum/infrastructure/network slicing/sharing. Forthcoming research amidst blockchain-established network virtualization may entangle developing standardizations for blockchain and network virtualization approach combinations. Furthermore, forthcoming work can probe the impact of quantum computing for authentication related to blockchain-established network virtualization.

CREDIT AUTHORSHIP CONTRIBUTION STATEMENT

Patikiri Arachchige Don Shehan Nilmantha Wijesekara: Conceptualization, Data curation, Formal analysis, Investigation, Methodology, Resources, Software, Validation, Visualization, Writing - original draft, Writing - review & editing.

DECLARATION OF COMPETING INTEREST

The author declares that he has no known competing financial interests or personal relationships that could have appeared to influence the work reported in this paper. The

ethical issues; including plagiarism, informed consent, misconduct, data fabrication and/or falsification, double publication and/or submission, redundancy has been completely observed by the author.

REFERENCES

- [1] C. H. Wang, Y. H. Chu, and T. T. Wei, "SIPTVMON: a secure multicast overlay network for load-balancing and stable IPTV service using SIP," in *2011 IEEE INFOCOM WKSHPs*, 2011, pp. 97-102.
- [2] W. Kellerer, A. Basta, P. Babarczy, A. Blenk, M. He, M. Klugel, and A.M. Alba, "How to measure network flexibility? A proposal for evaluating softwarized networks," *IEEE Communications Magazine*, vol. 56, no. 10, pp.186-192, 2018
- [3] H. B. Lim, M. Iqbal, and T. J. Ng, "A virtualization framework for heterogeneous sensor network platforms," in *7th ACM Conference on Embedded Networked Sensor Systems*, 2009, pp. 319-320.
- [4] M. M. Hasan, H. Amarasinghe, and A. Karmouch, "Network virtualization: Dealing with multiple infrastructure providers," in *2012 IEEE ICC*, 2012, pp. 5890-5895.
- [5] L. Cano, A. Capone, G. Carello, M. Cesana, and M. Passacantando, "On optimal infrastructure sharing strategies in mobile radio networks," *IEEE Transactions on Wireless Communications*, vol. 16, no. 5, pp.3003-3016, 2017
- [6] N. Kitsuwon, K. Akaki, P. Pavarangkoon, and A. Nag, "Spectrum allocation scheme considering spectrum slicing in elastic optical networks," *Journal of Optical Communications and Networking*, vol. 13, no. 7, pp.169-181, 2021
- [7] P. A. D. S. N. Wijesekara, and S. Gunawardena, "A machine learning-aided network contention-aware link lifetime- and delay-based hybrid routing framework for software-defined vehicular networks," *Telecom*, vol. 4, no. 3, pp. 393-458, 2023.
- [8] M. Bhandary, M. Parmar, and D. Ambawade, "A blockchain solution based on directed acyclic graph for IoT data security using IoTA tangle," in *2020 5th ICCES*, 2020, pp. 827-832.
- [9] P. A. D. S. N. Wijesekara, "A literature review on access control in networking employing blockchain," *Indonesian Journal of Computer Science*, vol. 13, no. 1, pp. 734-768, 2024.
- [10] Y. Li, Y. Yu, C. Lou, N. Guizani, and L. Wang, "Decentralized public key infrastructures atop blockchain," *IEEE Network*, vol. 34, no. 6, pp.133-139, 2020
- [11] M. Wang, M. Duan, and J. Zhu, "Research on the security criteria of hash functions in the blockchain," in *Proceedings of the 2nd ACM Workshop on Blockchains, Cryptocurrencies, and Contracts*, pp. 47-55, 2018.
- [12] P. A. D. S. N. Wijesekara, "A review of blockchain-rooted energy administration in networking," *Indonesian Journal of Computer Science*, vol. 13, no. 2, pp. 1607-1642, 2024.
- [13] Z. M. Khalid, and S. Askar, "Resistant blockchain cryptography to quantum computing attacks," *International Journal of Science and Business*, vol. 5, no. 3, pp.116-125, 2021.

- [14] P. A. D. S. N. Wijesekara, and S. Gunawardena, "A review of blockchain technology in knowledge-defined networking, its application, benefits, and challenges," *Network*, vol. 3, no. 3, pp. 343-421, 2023.
- [15] T. Hewa et al., "Blockchain-based network slice broker to facilitate factory-as-a-service," *IEEE Transactions on Industrial Informatics*, vol. 19, no. 1, pp.519-530, 2022
- [16] G. A. F. Rebello et al., "Providing a sliced, secure, and isolated software infrastructure of virtual functions through blockchain technology," in *2019 IEEE 20th International Conference on HPSR*, 2019, pp. 1-6.
- [17] X. Fan, and Y. Huo, "Blockchain based dynamic spectrum access of non-real-time data in cyber-physical-social systems," *IEEE Access*, vol. 8, pp.64486-64498, 2020.
- [18] D.B. Rawat, "Fusion of software defined networking, edge computing, and blockchain technology for wireless network virtualization," *IEEE Communications Magazine*, vol. 57, no. 10, pp.50-55, 2019.
- [19] H. Cao, Y. Hu, Q. Wang, S. Wu, and L. Yang, "A blockchain-based virtual network embedding algorithm for secure software defined networking," in *IEEE INFOCOM 2020*, 2020, pp.1057-1062.
- [20] F. Patel, P. Bhattacharya, S. Tanwar, R. Gupta, N. Kumar, and M. Guizani, "Block6Tel: Blockchain-based spectrum allocation scheme in 6G-envisioned communications," in *2021 IWCMC*, 2021, pp. 1823-1828.
- [21] S. Zheng, T. Han, Y. Jiang, and X. Ge, "Smart contract-based spectrum sharing transactions for multi-operators wireless communication networks," *IEEE Access*, vol. 8, pp.88547-88557, 2020.
- [22] H. Zhang, S. Leng, and H. Chai, "A blockchain enhanced dynamic spectrum sharing model based on proof-of-strategy," in *IEEE ICC 2020*, 2020, pp. 1-6.
- [23] H. Zhang, S. Leng, F. Wu, and H. Chai, "A DAG blockchain-enhanced user-autonomy spectrum sharing framework for 6G-enabled IoT," *IEEE Internet of Things Journal*, vol. 9, no. 11, pp.8012-8023, 2021.
- [24] N. Zhao, H. Wu, and X. Zhao, "Consortium blockchain-based secure software defined vehicular network," *Mobile Networks and Applications*, vol. 25, pp.314-327, 2020.
- [25] R. Trabelsi, G. Fersi, and M. Jmaiel, "Virtual private network blockchain-based dynamic access control solution for inter-organisational large scale IoT networks," in *International Conference on Risks and Security of Internet and Systems*, 2022, pp. 207-222.
- [26] P. A. D. S. N. Wijesekara, "A study in University of Ruhuna for investigating prevalence, risk factors and remedies for psychiatric illnesses among students," *Scientific Reports*, vol. 12, no. 1, pp. 12763, 2022.
- [27] P. A. D. S. N. Wijesekara, and Y.K. Wang, "A Mathematical Epidemiological Model (SEIQRDS) to Recommend Public Health Interventions Related to COVID-19 in Sri Lanka," *COVID*, vol. 2, no. 6, pp. 793-826, 2022.
- [28] L. Zichao, H. Ziwei, Z. Geng, and M. Yan, "Ethernet topology discovery for virtual local area networks with incomplete information," in *2014 4th IEEE International Conference on Network Infrastructure and Digital Content*, 2014, pp. 252-256.
- [29] A. Mehdizadeha, K. Suinggia, M. Mohammadpoorb, and H. Haruna, "Virtual Local Area Network (VLAN): segmentation and security," in *third ICCTIM2017*, 2017, vol. 78, p. 89.
- [30] E. Ramadhani, "Anonymity communication VPN and Tor: a comparative study," *Journal of Physics: Conference Series*, vol. 983, no. 1, p. 012060, 2018
- [31] P. Knight, and C. Lewis, "Layer 2 and 3 virtual private networks: taxonomy, technology, and standardization efforts," *IEEE Communications Magazine*, vol. 42, no. 6, pp.124-131, 2004.
- [32] T. Lavian, and P.Y. Wang, "Active networking on a programmable networking platform," in *2001 IEEE OPENARCH*, 2001, pp. 95-103.
- [33] G. Coulson et al., "NETKIT: a software component-based approach to programmable networking," *ACM SIGCOMM Computer Communication Review*, vol. 33, no. 5, pp.55-66, 2003.
- [34] M. Nkomo, G. P. Hancke, A. M. Abu-Mahfouz, S. Sinha, and A. J. Onumanyi, "Overlay virtualized wireless sensor networks for application in industrial internet of things: A review," *Sensors*, vol. 18, no. 10, p.3215, 2018.
- [35] S. Guenender, K. Barabash, Y. Ben-Itzhak, A. Levin, E. Raichstein, and L. Schour, "NoEncap: overlay network virtualization with no encapsulation overheads," in *1st ACM SIGCOMM Symposium on Software Defined Networking Research*, 2015, pp. 1-7.
- [36] M. Alaluna, N. Neves, and F. M. Ramos, "Elastic network virtualization," in *IEEE INFOCOM 2020-IEEE Conference on Computer Communications*, pp. 814-823, 2020.
- [37] N. Shahriar et al., "Achieving a fully-flexible virtual network embedding in elastic optical networks," in *IEEE INFOCOM 2019*, 2019, pp. 1756-1764.
- [38] N. Raveendran, Y. Gu, C. Jiang, N. H. Tran, M. Pan, L. Song, and Z. Han, "Cyclic three-sided matching game inspired wireless network virtualization," *IEEE Transactions on Mobile Computing*, vol. 20, no. 2, pp.416-428, 2019.
- [39] S. A. Kazmi, A. Ndikumana, A. Manzoor, W. Saad, and C. S. Hong, "Distributed radio slice allocation in wireless network virtualization: Matching theory meets auctions," *IEEE Access*, vol. 8, pp.73494-73507, 2020.
- [40] A. El Amri, and A. Meddeb, "Optimal server selection for competitive service providers in network virtualization context," *Telecommunication Systems*, vol. 77, pp. 451-467, 2021.
- [41] D. B. Rawat, A. Alshaikhi, A. Alshammari, C. Bajracharya, and M. Song, "Payoff optimization through wireless network virtualization for IoT applications: A three layer game approach," *IEEE Internet of Things Journal*, vol. 6, no. 2, pp.2797-2805, 2018.
- [42] P. A. D. S. N. Wijesekara, K. L. K. Sudheera, G. G. N. Sandamali, and P. H. J. Chong, "An optimization framework for data collection in software defined vehicular networks," *Sensors*, vol. 23, no. 3, pp. 1600, 2023.
- [43] L. Lewin-Eytan, K. Barabash, R. Cohen, V. Jain, and A. Levin, "Designing modular overlay solutions for network virtualization," IBM Technical Paper, IBM Research

Division, Haifa Research Laboratory, Mt. Carmel 31905, Haifa, Israel, 2012.

- [44] Y. Cui, P. Wu, M. Xu, J. Wu, Y. L. Lee, A. Durand, and C. Metz, "4over6: network layer virtualization for IPv4-IPv6 coexistence," *IEEE Network*, vol. 26, no. 5, pp.44-48, 2012.
- [45] M. Bacou, G. Todeschi, D. Hagimont, and A. Tchana, "Nested virtualization without the nest," in *48th International Conference on Parallel Processing*, 2019, pp. 1-10.
- [46] M. El Barachi, N. Kara, and R. Dssouli, "Towards a service-oriented network virtualization architecture," in *2010 ITU-T Kaleidoscope: Beyond the Internet?-Innovations for Future Networks and Services*, 2010, pp. 1-7.
- [47] H. Lu, and F. Zhang, "Resource fragmentation-aware embedding in dynamic network virtualization environments," *IEEE Transactions on Network and Service Management*, vol. 19, no. 2, pp.936-948, 2022.
- [48] C. Seneviratne, P. A. D. S. N. Wijesekara, and H. Leung, "Performance analysis of distributed estimation for data fusion using a statistical approach in smart grid noisy wireless sensor networks," *Sensors*, vol. 20, no. 2, pp. 567, 2020.
- [49] Y. Dong, X. Zhang, J. Dai, and H. Guan, "HYVI: a hybrid virtualization solution balancing performance and manageability," *IEEE Transactions on Parallel and Distributed Systems*, vol. 25, no. 9, pp.2332-2341, 2013.
- [50] J. Kwon, T. Lee, C. Hähni, and A. Perrig, "SVLAN: Secure & scalable network virtualization," in *NDSS 2020*, 2020, vol. 1, 2020, pp. 498-512.
- [51] R. Sherwood et al., "Flowvisor: A network virtualization layer," *OpenFlow Switch Consortium*, Tech. Rep, 1, p.132, 2009.
- [52] K. Yamada, Y. Kanada, K. Amemiya, A. Nakao, and Y. Saida, "VNode infrastructure enhancement—Deeply programmable network virtualization," in *2015 21st APCC*, 2015, pp. 244-249.
- [53] P. A. D. S. N. Wijesekara, "Deep 3D dynamic object detection towards successful and safe navigation for full autonomous driving," *Open Transportation Journal*, vol. 16, no. 1, pp. e187444782208191, 2022.
- [54] X. Li, R. Casellas et al., "5G-crosshaul network slicing: Enabling multi-tenancy in mobile transport networks," *IEEE Communications Magazine*, vol. 55, no. 8, pp.128-137, 2017.
- [55] H. Ahmadi, I. Macaluso, I. Gomez, L. DaSilva, and L. Doyle, "Virtualization of spatial streams for enhanced spectrum sharing," in *2016 IEEE Global Communications Conference (GLOBECOM)*, 2016, pp. 1-6.
- [56] A. J. Morgado, F. B. Saghezchi, S. Mumtaz, V. Frascolla, J. Rodriguez, and I. Otung, "A novel machine learning-based scheme for spectrum sharing in virtualized 5g networks," *IEEE Transactions on Intelligent Transportation Systems*, vol. 23, no. 10, pp.19691-19703, 2022.
- [57] C. Liang, and F. R. Yu, "Wireless virtualization for next generation mobile cellular networks," *IEEE Wireless Communications*, vol. 22, no. 1, pp.61-69, 2015.
- [58] A. Cárdenas, D. Fernández, C. M. Lentisco, R.F. Moyano, and L. Bellido, "Enhancing a 5G network slicing management model to improve the support of mobile virtual network operators," *IEEE Access*, vol. 9, pp.131382-131399, 2021.
- [59] R. Nejhati, S. Azodolmolky, and D. Simeonidou, "Role of network virtualization in future Internet innovation," in *2012 17th European Conference on Networks and Optical Communications*, 2012, pp. 1-4.
- [60] J. Navarro-Ortiz, O. Sallent, and J. Pérez-Romero, "Radio access network slicing strategies at spectrum planning level in 5G and beyond," *IEEE Access*, vol. 8, pp.79604-79618, 2020.
- [61] J.V. Ramrao, and A. Jain, "Dynamic 5G network slicing," *International Journal of Advanced Trends in Computer Science and Engineering*, vol. 10, no. 2, pp. 1006-1010, 2021.
- [62] D. Zhang, Z. Chang, T. Hämäläinen, and F.R. Yu, "Double auction based multi-flow transmission in software-defined and virtualized wireless networks," *IEEE Transactions on Wireless Communications*, vol. 16, no. 12, pp.8390-8404, 2017.
- [63] Y. Wang, L. Nguyen, and Q. Hu, "Network Function Virtualization in Elastic Optical Networks," *Journal of Lightwave Technology*, vol. 41, no. 16, pp.5183-5192, 2023.
- [64] P. A. D. S. N. Wijesekara, K. L. K. Sudheera, G. G. N. Sandamali, and P. H. J. Chong, "Machine learning based link stability prediction for routing in software defined vehicular networks," in *20th Academic Sessions*, p.60, 2023.
- [65] R. S. Alonso, I. Sittón-Candanedo, R. Casado-Vara, J. Prieto, and J. M. Corchado, "Deep reinforcement learning for the management of software-defined networks and network function virtualization in an edge-IoT architecture," *Sustainability*, vol. 12, no. 14, p.5706, 2020.
- [66] M. Gharbaoui et al., "An experimental study on latency-aware and self-adaptive service chaining orchestration in distributed NFV and SDN infrastructures," *Computer Networks*, vol. 208, p.108880, 2022.
- [67] P. A. D. S. N. Wijesekara, "A Review on deploying blockchain technology for network mobility management," *International Transactions on Electrical Engineering and Computer Science*, vol. 3, no. 1, pp. 1-33, 2024.
- [68] W. Li, H. Guo, M. Nejad, and C. C. Shen, "Privacy-preserving traffic management: A blockchain and zero-knowledge proof inspired approach," *IEEE Access*, vol. 8, pp.181733-181743, 2020.
- [69] P. A. D. S. N. Wijesekara, "Ethical knowledge sharing leveraging blockchain: An overview," *Science, Engineering, and Technology*, vol. 4, no. 1, pp.112-136, 2024.
- [70] Z. Zhou, X. Chen, Y. Zhang, and S. Mumtaz, "Blockchain-empowered secure spectrum sharing for 5G heterogeneous networks," *IEEE Network*, vol. 34, no. 1, pp.24-31, 2020.
- [71] M. Patnaik, G. Prabhu, C. Rebeiro, V. Matyas, and K. Veezhinathan, "ProBLESS: A proactive blockchain based spectrum sharing protocol against SSDF attacks in cognitive radio IoT networks," *IEEE Networking Letters*, vol. 2, no. 2, pp.67-70, 2020.
- [72] Y. Choi, and I.G. Lee, "Game theoretical approach of blockchain-based spectrum sharing for 5G-enabled IoTs in dense networks," in *2019 IEEE 90th VTC2019-Fall*, 2019, pp. 1-6.
- [73] K. Zhu, L. Huang, J. Nie, Y. Zhang, Z. Xiong, H.N. Dai, and J. Jin, "Privacy-aware double auction with time-

dependent valuation for blockchain-based dynamic spectrum sharing in IoT systems,” *IEEE Internet of Things Journal*, vol. 10, no. 8, pp. 6756-6768, 2022.

[74] Z. Li, W. Wang, Q. Wu, and X. Wang, “Multi-operator dynamic spectrum sharing for wireless communications: a consortium blockchain enabled framework,” *IEEE Transactions on Cognitive Communications and Networking*, vol. 9, no. 1, pp.3-15, 2022.

[75] B. Mafakheri, T. Subramanya, L. Goratti, and R. Riggio, “Blockchain-based infrastructure sharing in 5G small cell networks,” in *2018 14th International CNSM*, 2018, pp.313-317.

[76] T. Faisal, M. Dohler, S. Mangiante, and D. R. Lopez, “BEAT: Blockchain-enabled accountable and transparent infrastructure sharing in 6G and beyond,” *IEEE Access*, vol. 10, pp.48660-48672, 2022.

[77] M. Samaniego, and R. Deters, “Hosting virtual iot resources on edge-hosts with blockchain,” in *2016 IEEE International conference on CIT*, 2016, pp.116-119. IEEE.

[78] Y. Lin, J. Kang, D. Niyato, Z. Gao, and Q. Wang, “Efficient consensus and elastic resource allocation empowered blockchain for vehicular networks,” *IEEE Transactions on Vehicular Technology*, vol. 72, no. 4, pp.5513-5517, 2022.

[79] L. Xue, W. Yang, W. Chen, and L. Huang, “STBC: A novel blockchain-based spectrum trading solution,” *IEEE Transactions on Cognitive Communications and Networking*, vol. 8, no. 1, pp.13-30, 2021.

[80] S. Ding, G. Shen, K. X. Pan, S. K. Bose, Q. Zhang, and B. Mukherjee, “Blockchain-assisted spectrum trading between elastic virtual optical networks,” *IEEE Network*, vol. 34, no. 6, pp.205-211, 2020.

[81] M. Jiang, Y. Li, Q. Zhang, G. Zhang, and J. Qin, “Decentralized blockchain-based dynamic spectrum acquisition for wireless downlink communications,” *IEEE Transactions on Signal Processing*, vol. 69, pp.986-997, 2021.

[82] G. O. Boateng, D. Ayepah-Mensah, D. M. Doe, A. Mohammed, G. Sun, and G. Liu, “Blockchain-enabled resource trading and deep reinforcement learning-based autonomous RAN slicing in 5G,” *IEEE Transactions on Network and Service Management*, vol. 19, no. 1, pp.216-227, 2021.

[83] M. A. Togou et al., “DBNS: A distributed blockchain-enabled network slicing framework for 5G networks,” *IEEE Communications Magazine*, vol. 58, no. 11, pp.90-96, 2020.

[84] L. Zanzi, A. Albanese, V. Sciancalepore, and X. Costa-Pérez, “NSBchain: A secure blockchain framework for network slicing brokerage,” in *IEEE ICC 2020*, 2020, pp.1-7.

[85] G. O. Boateng, G. Sun, D.A. Mensah, D. M. Doe, R. Ou, and G. Liu, “Consortium blockchain-based spectrum trading for network slicing in 5G RAN: A multi-agent deep reinforcement learning approach,” *IEEE Transactions on Mobile Computing*, vol. 22, no. 10, pp.5801 – 5815, 2022.

[86] S. Singh, C.R. Babu, K. Ramana, I.H. Ra, and B. Yoon, “BENS- B5G: blockchain-enabled network slicing in 5G and beyond-5G (B5G) networks,” *Sensors*, vol. 22, no. 16, article 6068, 2022.

[87] V. Theodorou et al., “Blockchain-based zero touch service assurance in cross-domain network slicing,” in *2021 Joint EuCNC/6G Summit*, 2021, pp.395-400.

[88] P. Gorla, V. Chamola, V. Hassija, and D. Niyato, “Network slicing for 5G with UE state based allocation and blockchain approach,” *IEEE Network*, vol. 35, no. 3, pp.184-190, 2020.

[89] K. Xiao, Z. Geng, Y. He, G. Xu, C. Wang, and Y. Tian, “A blockchain-based privacy-preserving 5G network slicing service level agreement audit scheme,” *EURASIP Journal on Wireless Communications and Networking*, vol. 2021, no. 1, p.165, 2021.

[90] I. H. Abdulqadder, and S. Zhou, “SliceBlock: context-aware authentication handover and secure network slicing using DAG-blockchain in edge-assisted SDN/NFV-6G environment,” *IEEE Internet of Things Journal*, vol. 9, no. 18, pp.18079-18097, 2022.

[91] X. Fu, F. R. Yu, J. Wang, Q. Qi, and J. Liao, “Performance optimization for blockchain-enabled distributed network function virtualization management and orchestration,” *IEEE Transactions on Vehicular Technology*, vol. 69, no. 6, pp.6670-6679, 2020.

[92] M. S. Rahman, I. Khalil, and M. Atiquzzaman, “Blockchain-enabled SLA compliance for crowdsourced edge-based network function virtualization,” *IEEE Network*, vol. 35, no. 5, pp.58-65, 2021.

[93] X. Fu, F. R. Yu, J. Wang, Q. Qi, and J. Liao, “Resource allocation for blockchain-enabled distributed network function virtualization (NFV) with mobile edge cloud (MEC),” in *IEEE INFOCOM 2019*, 2019, pp. 1-6.

[94] H. A. Jawdhari, and A.A. Abdullah, “A novel blockchain architecture based on network functions virtualization (NFV) with auto smart contracts,” *Periodicals of Engineering and Natural Sciences*, vol. 9, no. 4, pp.834-844, 2021.

[95] M.F. Franco, E.J. Scheid, L.Z. Granville, and B. Stiller, “BRAIN: Blockchain-based reverse auction for infrastructure supply in virtual network functions-as-a-service,” in *2019 IFIP Networking Conference*, 2019, pp. 1-9.

[96] H. Huang, W. Miao, G. Min, J. Tian, and A. Alamri, “NFV and blockchain enabled 5G for ultra-reliable and low-latency communications in industry: Architecture and performance evaluation,” *IEEE Transactions on Industrial Informatics*, vol. 17, no. 8, pp.5595-5604, 2020.

[97] I. D. Alvarenga, G. A. Rebello, and O. C. M. Duarte, “Securing configuration management and migration of virtual network functions using blockchain,” in *NOMS 2018*, 2018, pp. 1-9.

[98] L. Sun, “Service chaining security based on blockchain,” in *Journal of Physics: Conference Series*, vol. 1634, no. 1, p. 012031, 2020.

[99] P. A. D. S. N. Wijesekara, W. M. A. K. Sangeeth, H. S. C. Perera, and N. D. Jayasundere, “Underwater acoustic digital communication channel for an UROV,” in *5th Annual Research Symposium (ARS2018)*, p. E17, 2018.

[100] M. U. Hassan, M. H. Rehmani, and J. Chen, “Privacy preservation in blockchain based IoT systems: Integration issues, prospects, challenges, and future research directions,” *Future Generation Computer Systems*, vol. 97, pp.512-529, 2019.

- [101] P. A. D. S. N. Wijesekara, K. L. K. Sudheera, G. G. N. Sandamali, and P. H. J. Chong, "Data gathering optimization in hybrid software defined vehicular networks," in *20th Academic Sessions*, p. 59, 2023.
- [102] I. Afolabi, M. Bagaa, T. Taleb, and H. Flinck, "End-to-end network slicing enabled through network function virtualization, in *2017 IEEE Conference on Standards for Communications and Networking (CSCN)*, pp. 30-35, 2017.
- [103] P. A. D. S. N. Wijesekara, and S. Gunawardena, "A comprehensive survey on knowledge-defined networking," *Telecom*, vol. 4, no. 3, pp. 477-596, 2023.
- [104] P. Chithaluru, F. Al-Turjman, T. Stephan, M. Kumar, and L. Mostarda, "Energy-efficient blockchain implementation for cognitive wireless communication networks (CWCNs)," *Energy Reports*, vol. 7, pp.8277-8286, 2021.
- [105] J. Xie, K. Zhang, Y. Lu, and Y. Zhang, "Resource-efficient DAG blockchain with sharding for 6G networks," *Ieee Network*, vol. 36, no. 1, pp.189-196, 2021.
- [106] H. Wu, K. Wolter, P. Jiao, Y. Deng, Y. Zhao, and M. Xu, "EEDTO: An energy-efficient dynamic task offloading algorithm for blockchain-enabled IoT-edge-cloud orchestrated computing," *IEEE Internet of Things Journal*, vol. 8, no. 4, pp.2163-2176, 2020.
- [107] S. De Angelis, L. Aniello, R. Baldoni, F. Lombardi, A. Margheri, and V. Sassone, "PBFT vs proof-of-authority: Applying the CAP theorem to permissioned blockchain," in *CEUR workshop proceedings*, vol. 2058, 2018.
- [108] H. M. D. P. M. Herath, W. A. S. A. Weraniyagoda, R. T. M. Rajapaksha, P. A. D. S. N. Wijesekara, K. L. K. Sudheera, and P. H. J. Chong, "Automatic assessment of aphasic speech sensed by audio sensors for classification into aphasia severity levels to recommend speech therapies," *Sensors*, vol. 22, no. 18, pp. 6966, 2022.
- [109] F. A. Aponte-Novoa, A. L. S. Orozco, R. Villanueva-Polanco, and P. Wightman, "The 51% attack on blockchains:

A mining behavior study," *IEEE Access*, vol. 9, pp.140549-140564, 2021.

[110] Y. Li, L.T.X. Phan, and B. T. Loo, "Network functions virtualization with soft real-time guarantees," in *IEEE INFOCOM 2016-The 35th Annual IEEE International Conference on Computer Communications*, pp. 1-9, 2016.

[111] H. A. Jawdhari, and A. A. Abdullah, "The application of network functions virtualization on different networks, and its new applications in blockchain: A survey," *Management*, vol. 18, pp. 1007-1044, 2021.

Biography



Patikiri Arachchige Don Shehan Nilmantha Wijesekara obtained his first-class honors B.Sc. Engineering degree specialized in Electrical and Information Engineering in 2017 from University of Ruhuna. He has received 6 academic awards for his bachelor's degree including 2 gold medals and 1 scholarship. He has published his research works in reputed journals and holds an H-index of 12. He is currently pursuing Ph.D. degree from the same university in computer networking. He has been recruited as a lecturer in university of Ruhuna since 2018. His research interests include networking, machine learning, and blockchain.

Copyrights

© 2024 Licensee Shahid Chamran University of Ahvaz, Ahvaz, Iran. This article is an open-access article distributed under the terms and conditions of the Creative Commons Attribution –NonCommercial 4.0 International (CC BY-NC 4.0) License (<http://creativecommons.org/licenses/by-nc/4.0/>).





Research Article

Voltage Regulation in Low Voltage Distribution Networks Using Reactive Power Capability of Photovoltaic Inverters and PID Consensus Algorithm

Iman Ali Hassanvand¹ , Javad Ebrahimi² , and Mahyar Abasi^{3,4} *

¹ Bakhtar Regional Company, Arak, Iran

² Department of Education and Training of Isfahan province, Management of District 4, Isfahan, 8145813331, Iran

³ Department of Electrical Engineering, Faculty of Engineering, Arak University, Arak 38156-8-8349, Iran

⁴ Research Institute of Renewable Energy, Arak University, Arak 38156-8-8349, Iran

* Corresponding Author: m-abasi@araku.ac.ir

Abstract: The dominant measures taken in distribution networks to solve the voltage instability problem include feeder reconfiguration techniques, allocation of capacitor banks, use of tap changers, etc. However, these traditional methods suffer from numerous issues. Many studies have been carried out to solve these problems in recent years. Compared with traditional methods, reactive power control (RPC) of photovoltaic (PV) inverters does not require additional investment, and given that PV inverters often function at a capacity below their rated value, the excess capacity can be utilized to assist in supplying reactive power to the grid. However, achieving voltage regulation in imbalanced distribution networks via RPC is a complex issue. Hence, the primary objective of this work is to utilize the reactive power capacity of photovoltaic inverters to achieve decentralized regulation of the effective voltage of the network using a consensus algorithm and a PID controller in two stages.

Keywords: Distributed generation sources, consensus algorithm, unbalanced four-wire distribution network, PID voltage control.

Article history

Received 27 November 2023; Revised 26 February 2024; Accepted 11 August 2024; Published online 30 October 2024.

© 2024 Published by Shahid Chamran University of Ahvaz & Iranian Association of Electrical and Electronics Engineers (IAEEE)

How to cite this article

I. A. Hassanvand, J. Ebrahimi, and M. Abasi, "Voltage regulation in low voltage distribution networks using reactive power capability of photovoltaic inverters and PID consensus algorithm," *J. Appl. Res. Electr. Eng.*, vol. 3, no. 2, pp. 159-167, 2024. DOI: [10.22055/jaree.2024.45398.1092](https://doi.org/10.22055/jaree.2024.45398.1092)



1. INTRODUCTION

1.1. Problem Statement and Motivation

In the field of electricity generation and reduction of air and environment pollution, the use of distributed generation sources (DGs) has been given much attention in recent years. In this regard, the restructuring of power systems and a competitive electricity market have been established. In fact, the connection of micro-resources with a capacity of several hundred kilowatts to low-voltage networks enhances the reliability of consumers and reduces the costs of investment and expansion of transmission networks [1]. With the ever-increasing expansion of power system in the 20th century, centers of generation and consumption of electrical energy have been connected in meshed configurations. In these

networks, the direction of power transfer was always from the generation centers to the consumer. The 21st century and the increasing need for energy resources at the global level provided the basis for the participation of consumers in the power system. This participation can be realized in three sectors: generation, storage, and management of electrical energy. The expansion of renewable energy sources, which both have a very low marginal cost and thus very high efficiency, leads to the reduction of air pollution. Also, the emergence of, which are mostly installed at the distribution level and on the consumer side, the discussion on stability and adaptability of the network has resulted in changes in the structure of power systems. The necessity of investment at the end of lifespan of the system and also investment to resolve the lines congestion by electricity market methods, along with

the progress made in the field of telecommunication systems that have significantly changed the speed of information transmission and significant progress in the field of information technology and the possibility of applying their economic utilization in power systems are among the factors that make it necessary to change the traditional integrated power system [1, 2].

1.2. Literature Review

A study conducted by the World Energy Council has forecasted that the proportion of worldwide electricity production derived from renewable energy sources will rise from 23% in 2010 to approximately 34% by 2030. In an ideal power system, the voltage and frequency at every supply point remain consistent and devoid of harmonics. The three-phase voltages and currents exhibit balance, with a power factor of unity. These qualities are unaffected by the size and characteristics of the loads. Regarding the voltage stability of distribution networks, many studies and methods have been proposed so far. For example, a distributed hierarchical control technique has been proposed to utilize the probable capacity of PV inverters in developing a distributed reactive power compensation plan for regulating voltage in balanced LV 3ph 4-wire distribution systems and deal with the problems of voltage fluctuations through the real-time adjustment of the reactive power injection or the consumption of fast-response PV inverters.

So far, many methods have been carried out for optimal operation of distributed generation resources and voltage control in the distribution system. In most of these studies, centralized control methods have been adopted to address the optimization problem. For instance, the authors in [1] used the method of real-time prediction of reactive power injection into the network. BESS is regarded as a fusion of storage units and voltage source converter (VSC) that enables autonomous regulation of active and reactive power injection into the grid. [2]. In [3], the issue was initially defined as a convex quadratic optimization problem with linear constraints. Subsequently, a distributed accelerated dual descent (DADD) algorithm was introduced to address the optimization problem by employing the anticipated dual decomposition and accelerated gradient methodologies.

In another study [4], the voltage regulation of distribution networks was considered by optimally regulating the reactive power of distributed energy sources (DER). The task is initially described as a convex quadratic optimization problem with linear constraints, using the linearized Dist. Flow model. Subsequently, a DADD algorithm was introduced to address the optimization problem by employing anticipated dual decomposition and accelerated gradient approaches. A method to control the voltage and ensure the security of reactive power reserve in steady-state mode was also proposed, especially since the static synchronous compensator (STATCOM) reference voltage is regulated to maintain the voltage in the sensitive buses according to the load variation. The proposed algorithm in this method includes two parts of the voltage control algorithm and the SVC reactive power reserve control algorithm. Once the reactive power reserve is terminated, the bus voltage deviation can be minimized by adjusting STATCOM reference voltage within the reactive power reserve range [4]. The proposed algorithm in [4] includes two parts: voltage

control algorithm and SVC reactive power reserve control algorithm. Reference [5] examined the most efficient method of compensating for active and reactive power in a power system under continuous loading conditions, utilizing a battery energy storage system (BESS). In order to achieve this objective, a voltage stability assessment model is utilized, which incorporates data regarding the flow of active and reactive power down the transmission line.

Conversely, a comprehensive technique for controlling reactive power in PV inverters was suggested [5]. This method is categorized into four control modes based on weather and load conditions: normal operation control mode, reverse power control mode, cloud control mode, and night control mode. The four control modes alternate based on particular switching rules to ensure the precise quantity of reactive power is injected or consumed by the PV inverter. The impacts of four control types were statistically significant in isolated operations. The integrated control method resulted in a reduction of approximately 2% in the PCC voltage deviation from its standard value. Hence, the suggested control technique holds significant practical significance in enhancing power quality and optimizing the utilization of PV inverters. The proposal in [6] suggests a coordinated optimization of both active and reactive power of BESS in order to minimize power losses and voltage variations in the active distribution network (AND). Next, a tailored solution for this optimal problem is introduced, utilizing the particle swarm algorithm. Reference [7] suggests implementing constant reactive power control (CRPC) as a means to mitigate the transient overvoltage of the AC system at the sending end. The proposed CRPC system can enhance the consumption of reactive power by the rectifier, diminish the interchange of reactive power between the AC and DC systems, and mitigate the occurrence of transient overvoltage.

However, in many studies conducted in the field of voltage regulation of unbalanced four-wire networks, a suitable and efficient method has not been proposed. For example, in [8, 9], only centralized methods are mentioned regarding voltage correction. Increasing the cross-section of the conductors and reducing their impedance is proposed in [10]. Ref. [11, 13, 14] focused on investigating the Volt-Var control method by adopting a smart PV inverter. On the other hand, the use of a powerful search algorithm in finding the optimal solution has not been considered. A majority of the research focus only on balanced networks.

1.3. Research Gaps

According to the conducted research, there are the following research gaps that need further investigation and research, these gaps are:

- The issue of unbalance and voltage regulation at the same time has not been considered in other sources.
- The use of particle consensus algorithm and PID controller to solve similar problems has not been considered
- Voltage angle adjustment has not been investigated in other articles.

1.4. Novelty and Contributions

Therefore, to overcome the shortcomings in the research on voltage correction of unbalanced distribution network using, this paper presents a new method of voltage profile correction in two stages by DGs. The proposed method provides a suitable solution for balancing the three-phase voltage in the first stage and correcting the voltage to the optimum level by means of the centralized consensus algorithm and the PID controller using the DGs. The evaluation and comparison of the proposed model is done by implementing it on the standard IEEE 14-bus network. The main contributions of this paper include:

- Utilization of the centralized consensus algorithm for precise correction of the network voltage
- Also, the work of this article has been done in two steps. In the first step, the unbalance is fixed, and in the second step, the voltage is adjusted optimally with the PID controller.
- Implementation of the proposed method on a standard IEEE network
- In most of the articles, voltage imbalance and voltage balancing have been discussed, while in the purpose of this article, in addition to voltage imbalance resolution, voltage regulation and its improvement have also been considered.

In the continuation of the paper, [Section 2](#) is dedicated to the formulation and outline of the problem. [Section 3](#) describes the solution method. The analysis of the results is presented in [Section 4](#) and finally [Section 5](#) provides the conclusion.

2. PROBLEM FORMULATION

This section presents a novel approach for regulating the reactive power of both single-phase and three-phase PV inverters, which can be linked to any combination of the three phases of a LVDN. The control algorithm enables PV inverters to transfer reactive power with LVDN in order to rectify voltage imbalance and enhance voltage profiles. Collaborative inverters can effectively achieve desired outcomes while relying solely on local measurements and restricted communication lines. The control strategy is comprised of two distinct parts. Voltage imbalance compensation is achieved in the initial stage by employing distributed single-phase compensators. During the second phase, the reactive power of the PV inverters is modified in order to enhance the voltage profile along the feeder. This adjustment is achieved by utilizing three-phase inverters.

2.1. Voltage Imbalance Compensation (Step 1)

The definition of voltage imbalance in international communities has different complexity and practical limitations. But the National Electric Manufacturers Association (NEMA) definition of line voltage unbalance rate (LVUR) is as (1) and (2).

$$LVUR\% = \frac{\max\{\Delta|V_i^{AB}|, \Delta|V_i^{BC}|, \Delta|V_i^{CA}|\}}{|V_i^{ave}|} \quad (1)$$

$$|V_i^{ave}| = \frac{|V_i^{AB}| + |V_i^{BC}| + |V_i^{CA}|}{3} \quad (2)$$

where $\Delta|V_i^{AB}|, \Delta|V_i^{BC}|, \Delta|V_i^{CA}|$ are the phase-to-phase voltage deviation from $|V_i^{ave}|$ (the average voltage of PP) at the i th bus. According to (2), the lower value of LVUR means that the network suffers from low imbalance. We have adopted the definition of the LVUR for the purpose of evaluation and compensation of voltage imbalance as it is effective and leads to straightforward computing. To make sure the electrical appliances work safely, the European EN50160 standard specifies allowable range for LVDNs as the rate of voltage unbalance of less than 2% for 10 minutes.

This approach relies solely on measuring the PP voltage, eliminating the need for intricate calculations. The suggested method employs a distributed delta compensator that delivers varying levels of reactive power in each phase. The primary objective is to minimize the voltage disparity between the PP points at the measurement location in order to enhance the voltage imbalance ratio as specified in (3).

$$UR_{PV,i}^{PP}(t) = \begin{cases} k_v^{ind/cap} (V_i^{PP}(t) - V_i^{ave}) + UR_{PV,i}^{PP}(t - \Delta t) & V_i^{PP}(t) \neq V_i^{ave} \\ 0 & V_i^{PP}(t) = V_i^{ave} \end{cases} \quad (3)$$

In general, $V_i^{PP}(t)$ is the voltage across the PP inverter, V_i^{ave} represents the average voltage across the PP compensator. k_v^{cap} and k_v^{ind} are two constant parameters for setting and regulating the speed and accuracy of the controller design, and Δt represents the sampling time. $UR_{PV,i}^{PP}(t)$ controls the active power exchanged by PP inverters by taking into account the voltage difference and $UR_{PV,i}^{PP}$ of the previous step. When the voltage across the PV inverter, i.e., $V_i^{PP}(t)$, is greater than average V_i^{ave} , then $UR_{PV,i}^{PP}(t)$ is positive. This means that the PV requires absorbing reactive (inductive) power to reduce the voltage of the connection point. Nonetheless, negative $UR_{PV,i}^{PP}$ enforces the PV inverter to feed reactive (capacitive) power to increase the voltage. Eventually, the reactive power exchange by PP inverters can be given as (4).

$$Q_{PV,i}^{ref,PP} = UR_{PV,i}^{PP}(t) \times Q_{PV,i}^{max} \quad (4)$$

$$Q_{PV,i}^{max} = \pm \sqrt{(S_{PV,i}^{max})^2 - (P_{PV,i})^2}$$

where $Q_{PV,i}^{ref,PP}$ is reactive power that should be exchanged by the inverter, and $Q_{PV,i}^{max}$ is the maximum reactive power of the PV inverter [22].

2.2. Distributed Consensus Algorithm and Local PID Controllers (Step2)

After implementing the suggested technique to balance the network, the voltage regulation algorithm can be applied separately to each phase of the LVDN to ensure that the bus voltages remain within the acceptable range. The approach suggested relies on distributed consensus control to coordinate PV inverters without requiring a central controller. Implementing RPC for PV inverters has the potential to enhance voltage profiles along the feeder. In this section, we design a consensus control mechanism and a PID controller to proportionally distribute the reactive power needed for

voltage regulation. The voltage limit should be equal to the value represented by (5).

$$V_{thr}^{cap} < V_i^{PN}(t) < V_{thr}^{ind} \quad (5)$$

The V_i^{PN} is the phase-to-ground voltage in bus i , V_{thr}^{cap} is the lower voltage boundary for voltage exchange and V_{thr}^{ind} is the upper power boundary for voltage exchange. Finally, the information is shared between the PID controllers of different inverters, then the local PIDs exchange reactive power with the network by using this information to regulate the voltage within the permissible limit. The PID controller is commonly employed in applications related to engineering because of its operational and architectural flexibility [22, 24]. The design of this controller does not necessitate advanced expertise. It decreases the steady state inaccuracy and enhances the transient and steady state responses [25]. The process of choosing PID controller parameters is crucial as the controller's effectiveness relies on the precise selection of these parameters. The Ziegler-Nichols method, Youla parametric method, Lambda tuning method, Cohen-Kuhn method, and Wang-Jung-Chan method are considered the most effective approaches for building PID controllers. These techniques enable the creation of PID controllers with increased flexibility and extra functionalities, while maintaining a straightforward layout complexity. Implementing advanced PID controller design techniques increase the level of intricacy and necessitates a deeper understanding of mathematics [21, 26].

The PID controller integrates the proportional, integral, and derivative structures into a unified package. The PID controller's basic transfer function can be expressed as (6):

$$C(s) = k_p + \frac{k_i}{s} + k_d s = \frac{k_d s^2 + k_p s + k_i}{s} \quad (6)$$

where, k_p , k_i , and k_d are proportional, integral, and derivative gains. The inclusion of the proportional term in the controller enhances the system's transient response. The integral term is the key component of the controller and is employed to minimize the steady-state error, while the derivative term is adopted for over-reduction of the system. The structure of a PID controller and problem flowchart are given in Fig. 1. Voltage control based on the distributed consensus algorithm and PI controller.

To set voltage on a desirable value in this study, which is 1 p.u., the following control dynamics is used as (7):

$$V_{ni} = (V_i^{mg} - V_i^{con})(P_i^T + \frac{P_i^I}{s}) \quad (7)$$

In general, V_{ni} is the control voltage, reference voltage of the desirable voltage, V_i^{con} denotes the output voltage of the consensus algorithm for each agent (bus), P_i^T is the proportional coefficient of the PI controller, and P_i^I is the integral coefficient of the controller [23].

2.3. Problem Constraints

There are constraints in the power output of DGs, which are of great importance and all of them must be observed to reach the correct solution. The constraints of the proposed optimization problem are described below:

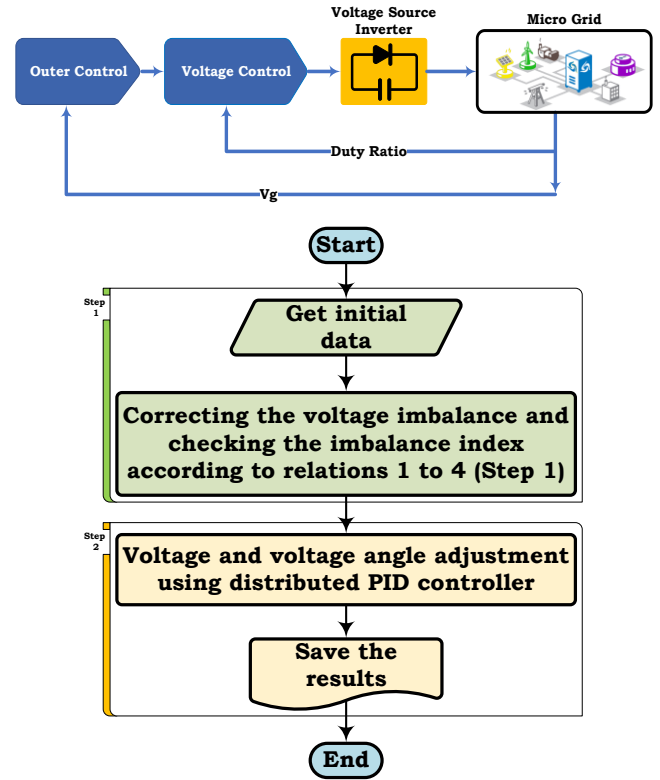


Fig. 1: Structure of a PID controller and process flowchart.

2.3.1. Power balance constraint

The presence of DG in the network should be such that all control variables and system variables satisfy the power flow equations of the network. In the following equations, active and reactive power is shown according to power flow equations.

$$\begin{aligned} P_{gi} - P_{di} - V_i \sum_{j=1}^N V_j Y_{ij} \cos(\delta_i - \delta_j - \theta_{ij}) &= 0 \\ Q_{gi} - Q_{di} - V_i \sum_{j=1}^N V_j Y_{ij} \sin(\delta_i - \delta_j - \theta_{ij}) &= 0 \end{aligned} \quad (8)$$

2.3.2. Voltage limits

The presence of DG in the network should not make bus voltages exceed the defined limits. So we have:

$$V_i^{min} < V_i < V_i^{max}, \quad i = 1 \dots, N_i \quad (9)$$

2.3.3. Line capacity limits

The limitation on the power flowing through the lines is given by:

$$|S_i| \leq |S_i^{max}| \quad i=1, \dots, N_b \quad (10)$$

2.3.4. Limits on generators power output

$$P_{gi}^{min} < P_{gi} < P_{gi}^{max} \quad (11)$$

3. SOLUTION METHOD

This section introduces a novel approach for regulating the reactive power of PV inverters that are linked in an arbitrary manner to the three phases of a power system. The control algorithm enables PV inverters to interchange

reactive power in order to rectify voltage disparities and enhance voltage profiles. Inverters can work together to achieve desired results only through local measurements and limited communication links. The control strategy is divided into two stages. In the first stage, voltage imbalance compensation is done using distributed single-phase compensators. The second stage takes the reactive power of the PV inverters to enhance the voltage profile on the feeder with the help of the existing PP inverters that are connected to the grid in three phases.

Compared with centralized and decentralized control strategies, distributed control systems offer superior control performance but require communication links as a trade-off. The benefits of this technique include the capacity to easily adjust the system's size, strength against failures, decreased computing demands, great adaptability, absence of a single point of weakness, and the distribution of tasks among local controllers [15-17].

3.1. Problem Solution Using the Consensus Algorithm

The communication network of a multi-agent cooperative system can be modeled with a directed graph (digraph). A digraph is usually a set $G_r = (V_G, E_G, A_G)$ with a non-empty finite set with N groups $V_G = \{v_1, v_2, \dots, v_N\}$ and a set of arcs $E_G \subset V_G \times V_G$ and an adjacency matrix $A_G = [a_{ij}] \in R^{N \times N}$. In a microgrid, DGs perform the role of communication digraph nodes. The arcs of the communication digraph network diagram represent the communication links. In the current study, the digraph is assumed time invariant, that is, A_G is constant, and an arc from node j to node i is specified by (v_j, v_i) , which means that node i receives information from node j . a_{ij} is the weight of the arc (v_j, v_i) , and $a_{ij} > 0$ if $(v_j, v_i) \in E_G$; otherwise, $a_{ij} = 0$. Node i is a neighbor of node j if $(v_j, v_i) \in E_G$. The set of neighbors for node j is denoted by $N_j = \{i \mid (v_j, v_i) \in E_G\}$. In a digraph, if i is a neighbor of j , then node j can receive information from node i , but the opposite is not necessarily true [18, 19]. In a microgrid, DGs are considered as communication digraph nodes. The arcs of the communication network diagram represent the communication links. Due to the fact that in this article, distributed solar generation sources are used for voltage balancing and regulation, therefore, ten selected points were selected by a simple genetic algorithm location with the aim of improving voltage stability and voltage division. The genetic algorithm with the initial population of 50 and the number of iterations of 600 has been implemented on a 14-base network. 10 candidate buses for DG installation are selected in such a way that the grid voltage stability is improved.

In this study, we have considered a graph with 10 nodes (agents) on buses 4, 5, 7, 8, 9, 10, 11, 12, 13, and 14 for the distributed consensus algorithm. To better understand, the communication graph between the agents on the buses is shown in Fig. 2.

Also, the Laplacian matrix and its eigenvalues are given as (12):

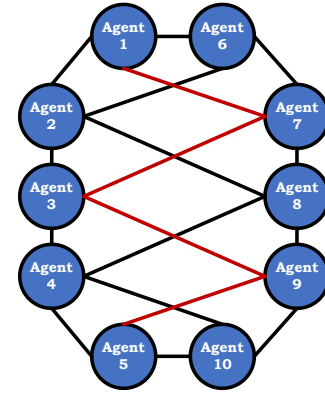


Fig. 2: A communication diagram for protocol of the average distributed consensus algorithm.

$$L = \begin{bmatrix} 3 & -1 & 0 & 0 & 0 & -1 & -1 & 0 & 0 & 0 \\ -1 & 4 & -1 & 0 & 0 & -1 & 0 & -1 & 0 & 0 \\ 0 & -1 & 4 & -1 & 0 & 0 & -1 & 0 & -1 & 0 \\ 0 & 0 & -1 & 4 & -1 & 0 & 0 & -1 & 0 & -1 \\ 0 & 0 & 0 & -1 & 3 & 0 & 0 & 0 & -1 & -1 \\ -1 & -1 & 0 & 0 & 0 & 3 & -1 & 0 & 0 & 0 \\ -1 & 0 & -1 & 0 & 0 & -1 & 4 & -1 & 0 & 0 \\ 0 & -1 & 0 & -1 & 0 & 0 & -1 & 4 & -1 & 0 \\ 0 & 0 & -1 & 0 & -1 & 0 & 0 & -1 & 4 & -1 \\ 0 & 0 & 0 & -1 & -1 & 0 & 0 & 0 & -1 & 3 \end{bmatrix} \quad (12)$$

with eigenvalues:

$$\lambda_{g1} = 0.7639, \lambda_{g2} = 2.7639, \lambda_{g3} = 0, \lambda_{g4} = 4, \lambda_{g5} = 4, \lambda_{g6} = 4, \lambda_{g7} = 4, \lambda_{g8} = 4, \lambda_{g9} = 5.2361, \lambda_{g10} = 7.2361 \quad (13)$$

After defining the communication graph of PV inverters, the distributed consensus algorithm receives the data shared for each PV with other PVs using the defined graph, and sends an estimated average of the PV values of the neighboring systems to each local controller based on the distributed consensus equations.

Here, according to the communication graph on the target buses which has the Laplacian matrix L , the output of the consensus algorithm, which is the estimated average of the voltage values of the neighboring PVs, is shown in Fig. 1. Distributed PV inverters are connected to each other through the network communication graph $\ell(v, \varepsilon)$, where $v = \{1, \dots, N\}$ is the points and ε shows the communication arcs between the points. Each point represents a PV inverter and each arc represents a communication link between them. If the points are connected, the data is shared through that. A set of points linked to point i is called the neighborhood of point i and is denoted by N_i . Node degree is equal to the number of neighbours' of that node, which is displayed as $d_i = |N_i|$.

Degree matrix D of a graph is defined by the d_i and also an adjacency matrix A , the elements of matrix A are $a_{ij} = 1$ if $(i, j) \in \varepsilon$; otherwise, $a_{ij} = 0$.

$L = D - A$ is the Laplacian matrix of the graph. In an undirected matrix, the Laplacian matrix has zero eigenvalues and the rest of values have an eigenvalue greater than zero. The i th PV controller receives the estimated mean state from its neighbors. The controller estimator then adopts the following average consensus protocol, as described in (14).

$$\tilde{x}_i(t) = x_i(t) + \int \sum_{j \in N_t} a_{ij}(\tilde{x}_j - \tilde{x}_i) \quad (14)$$

where x_i shows a local state variable, and \tilde{x}_i represents the estimated average of PV values of neighboring systems.

The vector form of a distributed average consensus protocol is given in (15).

$$\dot{\tilde{x}} = \tilde{x} - L\tilde{x} \quad (15)$$

where, $x = [x_1, x_2, \dots, x_N]$ and $\tilde{x} = [\tilde{x}_1, \tilde{x}_2, \dots, \tilde{x}_N]$. Using the Laplace transform from Eq. (21), the transfer matrix of the distributed consensus algorithm is as (16).

$$H^{avg} = \frac{\tilde{x}}{x} = s(sI_N + L)^{-1} \quad (16)$$

In this equation, X and \tilde{X} represents the Laplace transfer matrix of x and \tilde{x} , respectively [20].

4. SIMULATION RESULTS

4.1. Standard IEEE 14-bus System

The system used for simulations is the standard 14-bus network, whose data can be found in [12] and it's shown in Fig. 3.

4.2. Results of Applying the Control Strategy of Step 1 (Voltage Imbalance Compensation)

The proposed method for controlling Step 1 described in the previous sections is presented here. Its results were implemented on a standard IEEE 14-bus network and the following results were obtained. The voltage of different buses before applying the control method was as follows. As can be seen, the system is imbalanced in all buses, which is well shown in Table 1.

As shown in Table 1, before network control, the network is unbalanced, but after that the network is balanced. The amount of imbalance should be less than 2%. All the values in these buses are in p.u. form and the values in the table are reported as percentages. Fig. 4 shows the voltage of Bus 10 before balancing. Using (1), the voltage imbalance rate is equal to 5.6%. According to the standard, the imbalance rate should not exceed 2%, so the voltage of this bus needs balancing.

Fig. 5 shows the voltage of Bus 10 after applying the control method of Step 1. After it was found that there is more voltage drop in phase A compared to the other two phases, 0.01984 p.u reactive power is injected to this phase by using equation (1), resulting in an unbalance of 0.8%, which is less than 2%, so the voltage on this bus is balanced.

4.3. Results of Applying the Control Strategy of Step 2 (Voltage Amplitude and Degree Compensation)

In this research, as previously said, 10 PVs have been used to control Step 2. These 10 PVs are connected with their neighbors according to the communication graph that is defined for them. There is a PI controller in each PV that sends a control signal to the PI controller based on the voltage received from the consensus algorithm and comparing it with the desired voltage. Next, the PI controller sends the control information to the inverter power controller. The results for voltage control are in the following form for Bus 10 of the network.

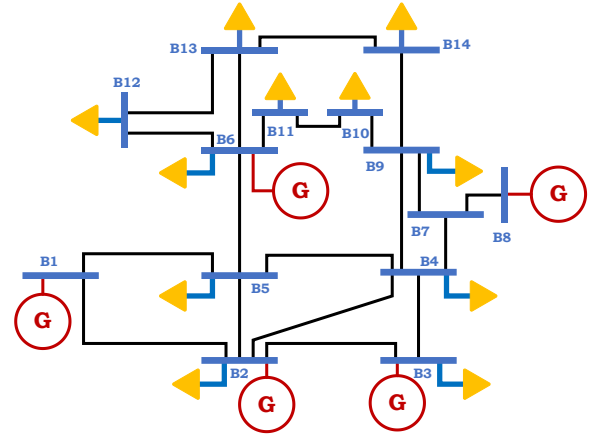


Fig. 3: IEEE 14-bus network.

Table 1: LVUR values before and after applying the control method of Step 1.

| Bus | Before control method | After control method |
|-----|-----------------------|----------------------|
| 1 | 2.6 | 0.1 |
| 2 | 3.3 | 0.5 |
| 3 | 3 | 0.3 |
| 4 | 3.8 | 0.4 |
| 5 | 3.8 | 0.3 |
| 6 | 7.3 | 0.3 |
| 7 | 3.6 | 0.2 |
| 8 | 2.6 | 1.1 |
| 9 | 4.3 | 0.8 |
| 10 | 5.6 | 0.8 |
| 11 | 8.3 | 1.1 |
| 12 | 7.7 | 1.2 |
| 13 | 8.5 | 1.4 |
| 14 | 7.8 | 1.3 |

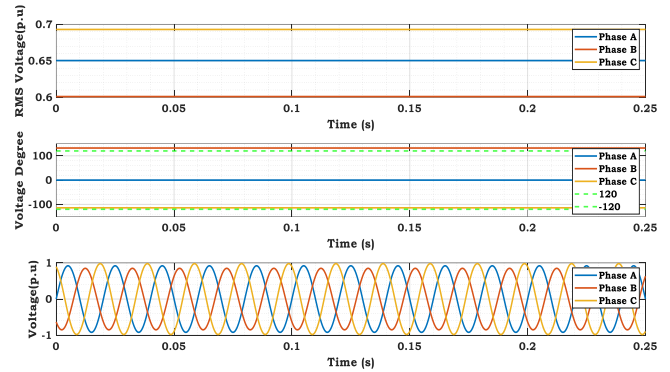


Fig. 4: Three-phase AC RMS voltage in Bus 10 before balancing the network.

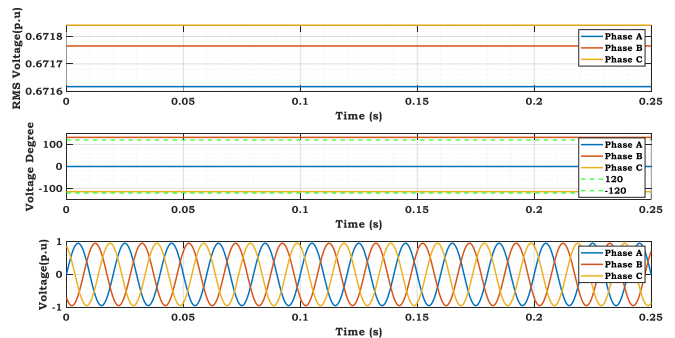


Fig. 5: Three-phase AC RMS voltage in Bus 10 after balancing the network in Step 1.

Fig. 6 depicts the rms instantaneous voltage of Bus 10 after applying the control method of Step 2. In this study, the voltage level of interest is 1 p.u. or 0.71 rms. The network error value is calculated using $e = \frac{v_{ref} - v_b}{v_{ref}} \times 100$, where v_{ref} is the reference voltage (1 p.u.) and v_b is instantaneous voltage of the considered bus. Before applying the control method, the value of this error in the bus is 5.7%, and after using the control method it becomes 1.2%.

4.4. Sensitivity Analysis of the Results of Changing the Number of Candidate Bases

In this article, in order to investigate the sensitivity of the voltage regulation error to the number of solar sources, it has been tried to investigate the error changes in three scenarios with the number of digraph points 10, 5 and 3.

Table 2 shows the error value of each bus before and after the application of the control strategy. As per Table 2, the control strategy was able to control the network voltage in all the network buses well and with high accuracy. In our proposed strategy, by using the consensus algorithm, we were able to increase the reliability of the network, eliminate the imbalance error, reduce the possibility of cyberattacks, and the decision for each bus is made according to the information of other neighboring buses, which is very effective in performance and improving the voltage profile. The results of Table 2 show that: by reducing the amount of candidate buses in the control network, the consensus of the particles in the network is reduced, and this raises in the voltage error and drops the voltage stability in the network.

Also, in order to compare the results and check their validity, it has been tried to compare them in terms of the percentage difference of reactive power passing through the lines in [1], the results of which are checked in Table 3. As it can be seen, the particle consensus algorithm used in this article has been able to qualitatively improve the imbalance of the reactive power passing through the lines better compared to [1]. This issue is one of the advantages of this article compared to its reference sample.

5. CONCLUSION

Various types of microgrid control strategies include centralized, decentralized, and distributed. In this study, considering the advantages of distributed control strategy compared to other control strategies, it is used. Autonomous agents in distributed control strategy utilize their individual local information and engage in communication with neighboring agents over a distributed communication graph network in order to accomplish shared objectives. The distributed control technique enhances system efficiency when compared to both centralized and decentralized control strategies. This technique has several benefits, including resilience, scalability, great adaptability, decreased computing complexity, absence of a single point of failure, and task distribution among local controllers in the microgrid. Hence, the use of a distributed control technique via a distributed communication graph network enhances the resilience of the microgrid.

Since there is an imbalance between the three-phase voltages in most power systems, it means that the voltage value of each phase may be different from the other phase,

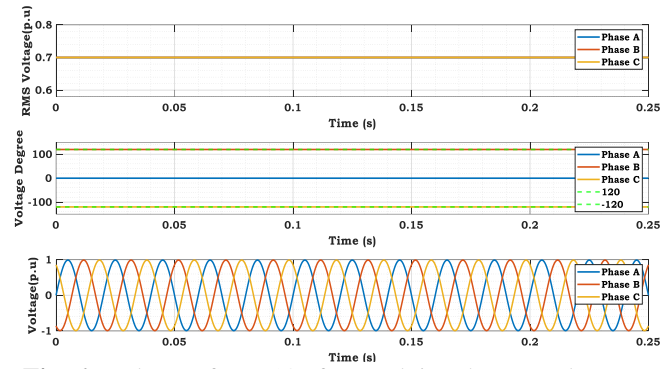


Fig. 6: Voltage of Bus 10 after applying the control strategy Step 2.

Table 2: Error values of each bus before and after applying the control strategy of Step 2.

| Bus | Before control method | After control method (10 bus) | After control method (5 bus) | After control method (3 bus) |
|-----|-----------------------|-------------------------------|------------------------------|------------------------------|
| 1 | 8% | 1.40% | 2.36% | 4.93% |
| 2 | 11% | 2.70% | 3.70% | 6.15% |
| 3 | 9% | 1.40% | 2.25% | 5.27% |
| 4 | 12% | 1.50% | 1.90% | 3.23% |
| 5 | 9.80% | 1.48% | 2.96% | 6.21% |
| 6 | 5.50% | 1.42% | 3.25% | 4.27% |
| 7 | 6.70% | 2.80% | 4.74% | 5.28% |
| 8 | 12% | 1.54% | 3.36% | 6.12% |
| 9 | 8.60% | 1.38% | 2.90% | 5.46% |
| 10 | 5.70% | 1.20% | 3.60% | 4.37% |
| 11 | 8.90% | 1.40% | 2.82% | 5.24% |
| 12 | 7.70% | 2.80% | 4.69% | 5.21% |
| 13 | 8.50% | 2.90% | 5.23% | 7.14% |
| 14 | 7.80% | 2% | 4.36% | 6.21% |

Table 3: Error values of reactive power in different cases.

| Cases | ΔQ_{AB} (%) | ΔQ_{AC} (%) | ΔQ_{BC} (%) |
|--------------|---------------------|---------------------|---------------------|
| [1] Case 2 | 38.9 | 58.12 | 31.41 |
| [1] Case 3 | 1.94 | 11.54 | 9.7 |
| This article | 1.23 | 3.24 | 4.69 |

which causes damage to consumers. According to the European standard EN50160, the acceptable range of the voltage imbalance rate is less than 2% for 10 minutes. According to Table 1, the network under study in this research has an imbalance rate higher than the standard limit under normal conditions before applying the control method, so with an absolute control method, the imbalance has been returned to the standard level, whose results are shown in Fig. 5 and Table 1. Then, the network voltage has reached the desirable value.

To regulate the voltage to the desired level, which is 1 p.u. in this study, the voltage of the neighbors is shared with a communication graph between the neighbors using a consensus algorithm, so that the entire network reaches a general consensus. After that, the output information of the consensus algorithm is sent to each local controller of each inverter so that these controllers can make decisions based on the local information and the information received from the

consensus algorithm for accurate voltage regulation. The results obtained are shown in Fig. 6 and Table 2. As is observed, the proposed method is very accurate. The important results of this article in summary are:

- Reducing line voltage unbalance and improving voltage regulation by particle consensus algorithm compared to similar works
- Improved network voltage regulation
- Balancing grid voltage angle adjustment
- Balancing the reactive power passing through the lines

5.1. Remaining Challenges and Future Works

In this article, it was tried to use the particle consensus algorithm to improve the voltage imbalance, voltage profile and voltage stability, but there are certainly still a number of issues in this field that can be addressed as a continuation of the work. Some of these are:

- Considering the uncertainty of solar sources and its effect on voltage stability
- Using sliding mode controller instead of PID for network control
- Considering other voltage unbalance standards and its effect on the results

CREDIT AUTHORSHIP CONTRIBUTION STATEMENT

Iman Ali Hassanvand: Conceptualization, Data curation, Formal analysis, Funding acquisition, Investigation, Project administration. **Javad Ebrahimi:** Methodology, Resources, Software, Supervision, Validation. **Mahyar Abasi:** Visualization, Writing - original draft, Writing - review & editing.

DECLARATION OF COMPETING INTEREST

The authors declare that they have no known competing financial interests or personal relationships that could have appeared to influence the work reported in this paper. The ethical issues; including plagiarism, informed consent, misconduct, data fabrication and/or falsification, double publication and/or submission, redundancy has been completely observed by the authors.

REFERENCES

- [1] M. Zeraati, M. E. Hamedani Golshan, and J. M. Guerrero, "Voltage quality improvement in low voltage distribution networks using reactive power capability of single-phase PV inverters," *IEEE Transactions on Smart Grid*, vol. 10, no. 5, pp. 5057-5065, 2018.
- [2] O. B. Adewuyi, R. Shigenobu, K. Ooya, T. Senjyu, and A. M. Howlader, "Static voltage stability improvement with battery energy storage considering optimal control of active and reactive power injection," *Electric Power Systems Research*, vol. 172, pp. 303-312, 2019.
- [3] F. J. Zimann, A. L. Batschauer, M. Mezaroba, and F. A. Neves, "Energy storage system control algorithm for voltage regulation with active and reactive power injection in low-voltage distribution network," *Electric Power Systems Research*, vol. 174, 105825, 2019.
- [4] J. H. Park, and Y. S. Baek, "Coordination control of voltage between STATCOM and reactive power compensation devices in steady-state," *Journal of Electrical Engineering and Technology*, vol. 7, no. 5, pp. 689-697, 2012.
- [5] H. Li, C. Wen, K. H. Chao, and L. L. Li, "Research on inverter integrated reactive power control strategy in the grid-connected PV systems," *Energies*, vol. 10, no. 7, 2017.
- [6] W. Wang, W. He, J. Cheng, X. Huang, and H. Liu, "Active and reactive power coordinated control strategy of battery energy storage system in active distribution network," in *32nd Youth Academic Annual Conf. of Chinese Association of Automation*, 2017, pp. 462-465.
- [7] C. Yin, and L. Fengting, "Reactive Power Control Strategy for Inhibiting Transient Overvoltage Caused by Commutation Failure," *IEEE Transactions on Power Systems*, vol. 36, no. 5, pp. 4764-4777, 2021.
- [8] H. Li, M. A. Azzouz, and A. A. Hamad, "Cooperative voltage control in MV distribution networks with electric vehicle charging stations and photovoltaic DGs," *IEEE Systems Journal*, vol. 15, no. 2, pp. 2989-3000, 2022.
- [9] Y. Liu, J. Bebic, B. Kroposki, J. De Bedout, and W. Ren, "Distribution system voltage performance analysis for high-penetration PV," in *Proc. IEEE Energy 2030 Conference*, IEEE; 2008, pp. 1-8.
- [10] R. Tonkoski, L. A. Lopes, T. H. El-Fouly, "Coordinated active power curtailment of grid connected PV inverters for overvoltage prevention," *IEEE Transactions on Sustainable Energy*, vol. 2, no. 2, pp. 139-147, 2010.
- [11] A. M. Howlader, S. Sadoyama, L.R. Roose, and S. Sepasi, "Distributed voltage control method using Volt-Var control curve of photovoltaic inverter for a smart power grid system," in *12th International Conf. Power Electronics and Drive Systems*, 2017, pp. 630-634.
- [12] M. Abasi, A. Torabi Farsani, A. Rohani, and M. Aghazadeh Shiran, "Improving differential relay performance during cross-country fault using a fuzzy logic-based control algorithm," in *5th Conf. Knowledge-Based Engineering and Innovation*, 2019, pp. 193-199.
- [13] M. Abasi, A. Rohani, F. Hatami, M. Joorabian, and G. B. Gharehpetian, "Fault location determination in three-terminal transmission lines connected to industrial microgrids without requiring fault classification data and independent of line parameters," *International Journal of Electrical Power & Energy Systems*, vol. 131, 107044, 2021.
- [14] A. Rohani, M. Abasi, A. Beigzadeh, M. Joorabian, and G. B. Gharehpetian, "Bi-level power management strategy in harmonic-polluted active distribution network including virtual power plants," *IET Renewable Power Generation*, vol. 15, no. 2, pp. 462-476, 2021.

- [15] M. Abasi, M. Joorabian, A. Saffarian, and S. G. Seifossadat, "A comprehensive review of various fault location methods for transmission lines compensated by FACTS devices and series capacitors," *Journal of Operation and Automation in Power Engineering*, vol. 9, no. 3, pp. 213-225, 2021.
- [16] J. Ebrahimi, and M. Abedini, "A two-stage framework for demand-side management and energy savings of various buildings in multi smart grid using robust optimization algorithms," *Journal of Building Engineering*, vol. 53, 104486, 2022.
- [17] M. Abasi, M. Joorabian, A. Saffarian, and S. G. Seifossadat, "An algorithm scheme for detecting single-circuit, inter-circuit, and grounded double-circuit cross-country faults in GUPFC-compensated double-circuit transmission lines," *Electrical Engineering*, vol. 104, pp. 2021–2044, 2022.
- [18] H. Makvandi, M. Abasi, S. Soltani, J. Ebrahimi, M. Joorabian, and J. Barati, "Design of an optimal STATCOM controller to enhance dynamic stability of the smart grid," *In 27th Int. Electrical Power Distribution Networks Conf. (EPDC)*, 2023, pp. 94-101.
- [19] M. Sadeghi, and M. Abasi, "Optimal placement and sizing of hybrid superconducting fault current limiter to protection coordination restoration of the distribution networks in the presence of simultaneous distributed generation," *Electric Power Systems Research*, vol. 201, 107541, 2021.
- [20] J. Ebrahimi, M. Abedini, M. M. Rezaei, and M. Nasri, "Optimum design of a multi-form energy in the presence of electric vehicle charging station and renewable resources considering uncertainty," *Sustainable Energy, Grids and Networks*, vol. 23, 100375, 2020.
- [21] M. Abasi, A. Torabi Farsani, A. Rohani, and A. Beigzadeh, "A new fuzzy theory-based differential protection scheme for transmission lines," *International Journal of Integrated Engineering*, vol. 12, no. 8, pp. 149-160. 2020.
- [22] H. Makvandi, M. Joorabian, and H. Barati, "A new optimal design of ACD-based UPFC supplementary controller for interconnected power systems," *Measurement* vol. 182, 109670, 2021.
- [23] B.N. Gohil, and D. R. Patel, "An improved Grey Wolf Optimizer (IGWO) for load balancing in cloud computing environment," *International Conference on Algorithms and Architectures for Parallel Processing*, 2018, pp. 3-9.
- [24] M. Abasi, H. Bahmani, M. Joorabian, J. Ebrahimi, and M. Razavi, "Designing an energy managing system for distributed dispersion in smart microgrids based on environmental constraints," *In 2022 12th Smart Grid Conference (SGC)*, 2022, pp. 1-6.
- [25] M. Basiri Abarghouei, and M. R. Saadat, "Full-Duplex device-to-device relays in a novel hybrid and adaptive joint relaying network: symbol error analysis and optimum power allocation," *Journal of Applied Research in Electrical Engineering*, vol. 2, no. 2, pp. 194-205, 2023.
- [26] A. Morsagh Dezfouli, M. Abasi, M. E. Hasanzadeh, and M. Joorabian, "Voltage and frequency control considering disturbance in input power of DG," *Journal of Applied Research in Electrical Engineering*, vol. 3, no. 1, pp. 9-18, 2024.

BIOGRAPHY



Iman Ali Hassanvand was born in Iran, in 1974. He received his M.Sc. degrees in Electrical Engineering (Power system) from Afarinesh Higher Education Institute of Borujerd, in 2021. He is currently working as electrical substations operation expert in Bakhtar Regional Company. His current research interest includes power quality, demand side management and microgrids.



Javad Ebrahimi was born in Iran, in 1988. He received his Ph.D. degrees in Electrical Engineering (Power system) from Khomeinishahr Branch, Islamic Azad University, Khomeinishahr/Isfahan, Iran, in 2020. He is currently working as a technical teacher in Technical and Vocational Academy of Isfahan province. Also, he taught for 10 years at Borujerd Islamic Azad University and Ayatollah Borujerd University. he has published 10 research paper, 8 conference paper and 1 industrial research project. His current research interest includes power quality, smart Grid, demand side management and microgrids.



Mahyar Abasi was born in 1989 in Iran. He graduated with a Ph.D. in Electrical Power Engineering from Shahid Chamran University of Ahvaz, Ahvaz, Iran in 2021. He has published more than 60 journal and conference papers, more than 10 authored books, 11 industrial research projects and a patent in the field of power systems. In 2021, he was introduced as the top researcher of Khuzestan province, Iran, and in the years 2021 to 2023, he was successful in receiving 4 titles from the membership schemes of the National Elite Foundation in Iran. He is currently an assistant professor in the Electrical Engineering department of Arak University, Arak, Iran. His specialized interests are fault protection, detection, classification and location in HVAC and HVDC transmission lines, control of reactive power and FACTS devices, evaluation and improvement of power quality and power system studies.

Copyrights

© 2024 Licensee Shahid Chamran University of Ahvaz, Ahvaz, Iran. This article is an open-access article distributed under the terms and conditions of the Creative Commons Attribution –NonCommercial 4.0 International (CC BY-NC 4.0) License (<http://creativecommons.org/licenses/by-nc/4.0/>).





Iranian Association of
Electrical and Electronics
Engineers

Journal of Applied Research in Electrical Engineering

E-ISSN: 2783-2864

P-ISSN: 2717-414X

Homepage: <https://jaree.scu.ac.ir/>



Research Article

Optimization of PSS and UPFC Controllers to Enhance Stability by Using a Combination of Fuzzy Algorithm and Shuffled Frog Leaping Algorithm

Mohammad Abedini¹ , and Mahyar Abasi^{2,3,*}

¹ Faculty of Engineering, Department of Electrical Engineering, Ayatollah Boroujerdi University, Boroujerd, Iran

² Department of Electrical Engineering, Faculty of Engineering, Arak University, Arak 38156-8-8349, Iran

³ Research Institute of Renewable Energy, Arak University, Arak 38156-8-8349, Iran

* Corresponding Author: m-abasi@araku.ac.ir

Abstract: Power system operation sometimes encounters low-frequency fluctuation. Power system stabilizer (PSS) and unified power flow controller (UPFC) are a solution to this problem. In this paper, to enhance the stability during various disturbances, power system stabilizers such as PSS and UPFC are used simultaneously. An optimized fuzzy control system is proposed to make PSS and UPFC more efficient so that the system damping is boosted. Angular speed changes and power angle changes are the inputs to the fuzzy controller. Moreover, to respond to changes applied to the system, an optimization algorithm called shuffled frog leaping algorithm is adopted to set the gains of fuzzy functions. To evaluate the performance of the controller, three loading levels are considered for the studied system and the simulations of each stage are presented separately. According to the results, the amount of overshoot is reduced and system damping is improved.

Keywords: Metaheuristic, optimization, stabilizer, damping.

Article history

Received 21 January 2024; Revised 15 April 2024; Accepted 12 August 2024; Published online 30 October 2024.

© 20xx Published by Shahid Chamran University of Ahvaz & Iranian Association of Electrical and Electronics Engineers (IAEEE)

How to cite this article

M. Abedini, and M. Abasi, "Optimization of PSS and UPFC controllers to enhance stability by using a combination of fuzzy algorithm and shuffled frog leaping algorithm," *J. Appl. Res. Electr. Eng.*, vol. 3, no. 2, pp. 168-176, 2024.

DOI: [10.22055/jaree.2024.45910.1104](https://doi.org/10.22055/jaree.2024.45910.1104)



1. INTRODUCTION

Nowadays, with the expansion of power systems and with the increase of power transmission, dynamic and transient stability are of special importance for safe operation [1]. To preserve the system's security, the power system is expected to have normal condition, during which the magnitude of voltage and range of frequency are maintained in the allowed range. Stability control of electrical power systems examines if the synchronism of generation units is established in the case a significant perturbation is added to the system. Power system stabilizers (PSS) have widespread applications, such as being adopted as complementary controllers to improve stability. In addition, flexible alternating current transmission systems (FACTS) are suitable options for transient stability improvement in almost a short time [2-4]. Among all FACTS devices, unified power flow controllers (UPFCs) are of special attention, which present maximum flexibility and can be used for voltage control, series compensations, and phase shift. UPFCs can quickly control active and reactive power flow on a line. Normally, a UPFC follows two control objectives, known as

primary and supplementary controls. The purpose of the former is to supervise and control active and reactive power flows independently so that bus voltages can be controlled during the power system operation. Among the most common control methods for UPFC is the one based on vector control. This design allows active and reactive power to be controlled separately, where the balanced three-phase system is converted to the synchronous rotating reference frame. Also, proportional-integral (PI), fuzzy, and neural controls have been introduced in this field [5-6]. On the other side, supplementary control is beneficial only in the case the system encounters major disturbances. This complementary control strategy concerns improving the transient stability on the line, which is traditionally expressed using the Lyapunov stability method based on an energy function [7]. Although developments in improving control methods have been presented, they need to provide complete power system models and dynamic models of the UPFC. In the following, the related literature is reviewed. In case a power oscillation damping (POD) controller is used in the control design, FACTS can improve stability by boosting the damping to the inter-area modes [8-10]. In 2010, literature [11] introduced a

design method based on the particle swarm optimization (PSO) algorithm, which aimed to coordinate thyristor-controlled series compensator (TCSC) and PSS in power systems that contain several generation units. In 2014, reference [12] adopted the genetic algorithm (GA) to determine the UPFC installation location along with adjusting the PSS parameters so that the system damping reaches the maximum possible value. In 2016, literature [13] presented a hybrid method for damping power fluctuations in the power system; the method consisted of offline and online stages that simultaneously adjusted the parameters of the UPFC and PSS controllers using the PSO. In 2018, reference [14] suggested adjusting controllers by adopting optimal control theory for different conditions and the studies were implemented using two-area symmetric system. PI controllers propose widespread applications in load frequency control, even though they suffer from many problems due to changes in the operating point of the system as well as network regulatory parameters [15-16]. Many articles have also discussed the design of the optimal performance of PSS in the power system, some of which use pole displacement techniques. Some other studies utilized artificial intelligence techniques [17-18]. Reference [19] used the fuzzy algorithm to adjust PSS parameters with the aim of boosting system stability. In reference [20], to coordinate between UPFC and PSS, the eigenvalue method was used to identify the largest real value of the system and minimize its value. The purpose was to reduce the fluctuations of the power system when applying a disturbance to the system. In [21], genetic algorithm was incorporated to coordinate PSS and UPFC to optimize electromechanical modes, thus improve system damping. In [22], a neural network with single-neuron layers was developed with a radial function to optimize the performance of the PSS and UPFC. Then the GA was used to optimize the network weights, and applied to a four-machine network. Methods based on robust control have also been proposed to overcome system uncertainty and increase damping with UPFC [23], [24].

By proposing a variable structure controller and deriving the appropriate control law in terms of fuzzy logic for UPFC and PSS, as well as using the shuffled frog leaping algorithm (SFLA) to adjust the proposed gain coefficients in the fuzzy controller in the single-machine power network, the present study attempts to reduce low frequency fluctuations in a faster time during a disturbance. Fig. 1 shows the structure of the developed control scheme. Accordingly, the output of the fuzzy system provides the required control signal for PSS and UPFC; in addition, the gains designed in the fuzzy controller for PSS and UPFC are optimized by the SFLA to enhance the system damping. The contributions of this study are described as follows:

- Designing fuzzy controllers for PSS and FACTS;
- Optimizing the parameters of the proposed fuzzy controller;
- Minimization of the objective function of speed changes to reduce fluctuations and improve system damping; and
- Comparing the proposed controller at three different levels of system loading with conventional controllers and showing the high capability of the proposed system.

2. CONTROL SYSTEM MODELING

Here, models of the PSS, UPFC, and dynamic modeling of a power system are introduced.

2.1. Power System Stabilizer

The PSS enhances the dynamic behavior of the system by introducing supplementary signals to the excitation system. The PSS typically receives data such as motor speed, frequency, and generator output power, and effectively improves the dynamic behavior by reducing its fluctuations [25]. PSS basically has three blocks: phase compensator block, signal effect removal block, and gain block. The phase compensator block gives the most suitable phase-lead characteristic for phase-lag compensation of the system between the excitation input and the electric torque of the generator. Fig. 2 demonstrates the PSS structure based on the phase lag-lead controller.

2.2. Modeling the UPFC

UPFC is a device placed between two buses known as sending and receiving ends of the UPFC. This device consists of two interconnected voltage source converters via a DC link (refer to Fig. 3). This damping controller produces electric torque and the speed derivative to compensate the damping torque. The control parameters of the UPFC are m_B , m_E , δ_B and δ_E that help to produce the damping torque. Parameters m and δ respectively indicate the amplitude modulation coefficient and the initial angle of the reference signal of individual converters. In this article, δ_E was adopted for generating the control signal. The structure of UPFC for damping controller is also similar to the phase lag-lead controller of the PSS.

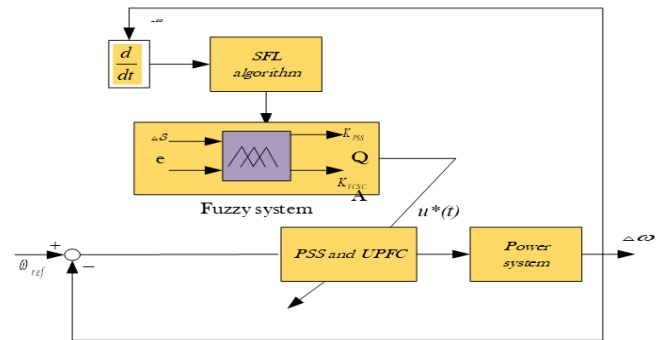


Fig. 1: Structure of the developed control design using a fuzzy controller.

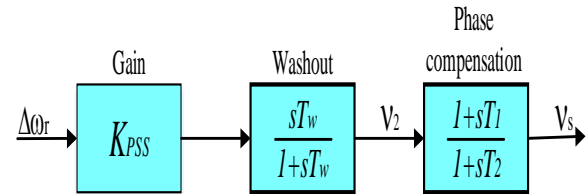


Fig. 2: Structure of the PSS.

2.3. Modeling the Power System

Equations (1)-(7) describe the dynamic behavior of the studied system with a UPFC (Fig. 3) in the state space form related to the single-machine system [26]:

3.2. Fuzzy Theory for Design of the UPFC Controller

A similar method to design of the PSS fuzzy controller has been used for UPFC. Angular velocity changes and power angular changes are considered as fuzzy input. The fuzzy system output is fed into the converter angle (δ_e^{UPFC}), according to Fig. 6.

According to Fig. 6, two constant parameters are used in the input and one constant parameter in the fuzzy system output, which will be optimized by the SFLA in Section 4.

3.3. Step 2: Fuzzification Rules

This part forms the foundation and main logic of the control action, where the whole data needed for the control operation is stored in the form of fuzzy rules. For example, if the output value is significantly dissimilar to the desired value, the fuzzy part applies more control value in a different direction. The fuzzy control rules that are necessary to generate the control signals of δ_e^{UPFC} and V_{PSS} are given in Tables 1 and 2, which will be applied to the studied system according to Fig. 4. It should be noted that the fuzzy functions used for ω and $\Delta\delta$ are triangular.

3.4. Step 3: Fuzzy Inference Method

Normally, Mamdani and Takagi Sugeno methods are mainly utilized in control applications. The former is used in this section, because it is a very powerful method at the same time. Using Mamdani method, equation (15) is written:

$$\mu_{Ri}(\omega, \Delta\delta) = \mu_{Ai}(\omega) \times \mu_{Bi}(\Delta\delta) \quad (15)$$

where ω and $\Delta\omega$ represent the speed and changes of the speed. Also, u is the output value. $\mu_{Ai}(\omega)$ and $\mu_{Bi}(\Delta\delta)$ are the fuzzified value of the speed and the rate of change of speed.

3.5. Step 4: Fuzzy to Crisp Transformation

The transformation of the fuzzy central average value to the crisp value is used here. In this way, the output value is given as (16):

$$\mu(\omega, \Delta\delta) = \frac{\sum_{i=1}^n u_i' \min(\mu_{Ai}(\omega), \mu_{Bi}(\Delta\delta))}{\sum_{i=1}^n \min(\mu_{Ai}(\omega), \mu_{Bi}(\Delta\delta))} \quad (16)$$

where u_i' indicates the central value of the fuzzy output. The fuzzy logic output is used for the excitation system signal in PSS and also for the converter angle in UPFC. The signals are changed instantaneously using fuzzy logic according to (17) and (18):

$$V_{PSS} = V_{PSS0} + \Delta U_{PSS} \quad (17)$$

$$\delta_e^{UPFC} = \delta_e^{UPFC0} + \Delta U_{UPFC} \quad (18)$$

V_{PSS0} and δ_e^{UPFC0} are the initial values related to the PSS and UPFC signals. ΔU_{PSS} and ΔU_{UPFC} are the output of the fuzzy section.

4. SFLA

The SFLA can be categorized as a metaheuristic optimization method, which mimics the mimetic evolution of a group of frogs as they search for a location with the maximum food. In metaheuristic algorithms, the objective function has a conscious process and the decision space is intelligently discovered [28].

4.1. Structure of the SFLA

SFLA has both certainty and random strategy elements in finding the optimal solution. The certainty strategy allows the algorithm to effectively use the shallow information of the solution to guide a heuristic search such as the PSO algorithm. Random elements guarantee the flexibility and strength of the search pattern in the proposed method. The steps of the SFLA are given below.

Step 1: an initial population containing N solutions to the problem $P = \{X_1, X_2, \dots, X_n\}$ is generated. A solution to the problem for primary gains in the controller of Figs. 5 and 6 is considered as follows.

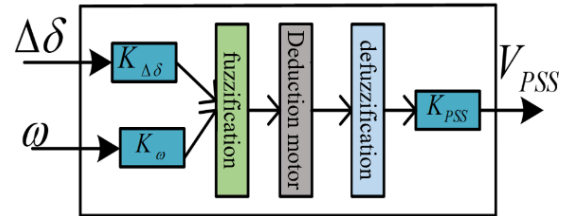


Fig. 5: Block diagram of the fuzzy controller for the PSS.

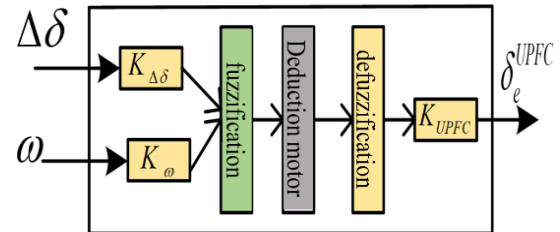


Fig. 6: Block diagram of the UPFC's fuzzy controller.

Table 1: Fuzzy rules needed in the UPFC controller.

| ω | $\Delta\delta$ | | | | | | |
|----------|----------------|----|----|----|----|----|----|
| | NB | NM | NS | Z | PS | PM | PB |
| NB | NH | NH | NH | NS | PM | PS | Z |
| NM | NB | NB | NM | NM | NS | Z | PS |
| NS | NB | NM | NM | NS | Z | PS | PM |
| Z | NM | NM | NS | Z | PS | PM | PM |
| PS | NM | NS | Z | PS | PM | PM | PB |
| PM | NS | Z | PS | PM | PM | PB | PB |
| PB | Z | PS | PM | PM | PB | PB | PB |

Table 2: Fuzzy rules needed in the PSS controller.

| ω | $\Delta\delta$ | | | | | | |
|----------|----------------|----|----|----|----|----|----|
| | NB | NM | NS | Z | PS | PM | PB |
| NB | NH | NH | NH | NB | NM | NS | Z |
| NM | NB | NB | NM | NM | NS | Z | PS |
| NS | NB | NM | NS | NS | Z | PS | PM |
| Z | NM | NM | NS | Z | PS | PM | PM |
| PS | NM | NS | Z | PS | PM | PM | PB |
| PM | NS | Z | PS | PM | PM | PB | PB |
| PB | Z | PS | PM | PB | PB | PB | PB |

$$X_i = [K_{\Delta\delta}^{PSS}, K_{\omega}^{PSS}, K_{PSS}, K_{\Delta\delta}^{UPFC}, K_{\omega}^{UPFC}, K_{UPFC}]^T$$

Step 2: using the fitness function defined in (19), each of the solutions to the problem is evaluated and the solutions are sorted in descending order as per their fitness values.

$$J = \int_0^T t |\Delta\omega| dt \quad (19)$$

The objective function is introduced to improve the system damping.

Step 3: the whole population is divided into m equal parts, and each of these sub-parts is called Memeplex. In each memeplex, n solutions of the problem are placed ($n = \frac{N}{m}$); the solution with the highest fitness value is placed in the first memeplex, the second solution is placed in the second memeplex, the m^{th} solution is placed in the m^{th} memeplex, and the $(m+1)^{th}$ solution is placed again in the first memeplex. This process continues until all the solutions are distributed.

Step 4: Since the frogs' preference is centered around a specific frog that may be the local optimum, it is not always desirable to use the best frog; therefore, a subset of memeplexes called sub-memeplexes is considered. In each of the memeplexes, the solutions with the worst and the best degree of fitness are specified and denoted by X_w and X_b , respectively. Also, the solution with the best amount of fitness among the entire population is also defined by X_g . During the evolution process of memeplexes, the worst solution moves towards the best solution. Fig. 7 shows the evolution of memeplexes.

Step 5: the new position of the worse solution is calculated using the leaping law of frogs in the SFLA, as (20)-(21):

$$D = rc(x_b - x_w) + w \quad (20)$$

$$x_w^{new} = \begin{cases} x_w + D & \|D\| \leq D_{max} \\ x_w + \frac{D}{\sqrt{D^T D}} D_{max} & \|D\| > D_{max} \end{cases} \quad (21)$$

where r is a random number between 0 and 1, C is a fixed number between 1 and 2, r is a random number between -1 and 1, D show the maximum allowed leap distance, and w represents the maximum allowed movement and penetration. **Step 6:** update the worst solution using (22):

$$if: f(x_w^{new}) < f(x_w) \quad then \quad x_w = x_w^{new} \quad (22)$$

Otherwise, X_b is replaced by X_g , and x_w^{new} is recalculated from (21). If there is still no improvement in the solution, X_w is deleted and a new solution is randomly replaced.

Step 7: This stage is called the combination process, where the population of memeplexes are combined with each other. Then, return to Step 2.

Step 8: As soon as the specified number of iterations is met, the optimization process is completed.

5. SIMULATION

Simulations of all samples were performed on a single-machine IEEE standard system (Fig. 3). Table 3 lists the information of the standard single-machine network under study along with the UPFC. Also, the number of memeplexes is 7 and the population of each memeplex is 15. The number of iterations is 50. To evaluate the efficacy of the controller designed in this study, its response was assessed using PSS and UPFC damping controllers independently and at different load percentages. Table 4 summarizes the results in the presence of a three-phase fault occurring at $t = 0.5$ s with different network loading conditions. In addition to the objective function of (19), the index given in (23) was also used when comparing different controllers:

$$F = (100 \times OS)^2 + (500 \times US)^2 + TS^2 \quad (23)$$

where OS is the overshoot of the system, US is the undershoot, and TS is the settling time of the machine speed deviation.

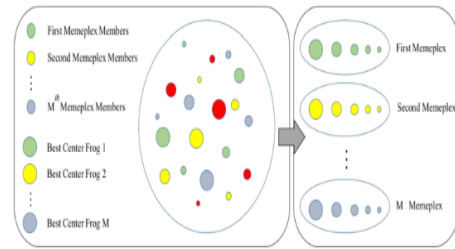


Fig. 7: Leaping process in the SFLA [28].

Table 3: Standard single-machine network information.

| | |
|-----------------------|--|
| Generator | M = 8, D = 0, T _{do} = 5.044, X _q = 0.6, X _d = 1, X' _d = 0.3 |
| Excitation | K _A = 10, T _A = 0.05 |
| Transmission line | X _{TE} = 0.1, X _{BV} = 0.5 |
| Operating condition | P _e = 0.8, V _i = 1, V _b = 1 |
| UPFC Transformers | X _E = 0.1, X _B = 0.1 |
| Parameters of DC link | V _{DC} = 2, CDC = 1 |

Table 4: A comparison between the performance of different controllers in network load conditions.

| Controller | 80% | | 100% | | 110% | |
|--------------|--------|-------|--------|-------|--------|--------|
| | F | J | F | J | F | J |
| PSS | 0.0126 | 14.02 | 0.0159 | 15.17 | 0.0170 | 16.76 |
| UPFC | 0.0143 | 14.25 | 0.0167 | 15.26 | 0.0184 | 16.89 |
| Proposed | 0.0126 | 6.05 | 0.0146 | 8.43 | 0.0158 | 10.61 |
| PSS&UPFC-PID | 0.0159 | 14.85 | 0.0172 | 16.37 | 0.0193 | 17.055 |

Table 3 shows that the optimized fuzzy controller based on the SFLA performs better in comparison with the traditional PID controller, and this demonstrates the capability of the proposed method. In addition, in Table 4, a comparison between the proposed method based on the optimized fuzzy with conventional methods such as PID and reference [29] has been made in terms of the generator angle performance, which shows that the proposed controller has a lower generator angle during the loading conditions of the studied system. Table 5 shows the performance of the suggested controller when only the fuzzy combination of PSS and UPFC is used, which shows that it will not perform well without optimization. It can be seen from tables 4 and 5 that the use of UPFC alone can even have a negative effect on the generator oscillation, which is due to the UPFC's attempt to keep the line power constant after a fault occurs in the

network. Fig. 7 shows the convergence of the optimization problem using the SFLA method. As is observed in the figure, the objective function converged after 50 iterations, which shows the optimal performance of the SFLA in finding the fuzzy controller coefficients.

The response of different controllers considering different load levels of 80%, 100%, and 110% are shown in Figs. 8 to 13. Fig. 8 compares the speed response of four controllers, including the proposed method in which the parameters of the fuzzy controller are optimized with the SFLA; the fuzzy controller; the conventional control including only PID; and finally, when no controller is applied to the single-machine system. After disturbing the input mechanical power of the generator, the generator speed fluctuates and these fluctuations are comparable for these four controllers in Fig. 8 for the capacity equivalent to 80% of the nominal load, which show that the optimized fuzzy controller gives the best response with suitable settling time and damping.

Fig. 9 shows the changes in the system voltage for 80% of the rated load, where the proposed fuzzy optimized controller (PSS and UPFC) with overshoot of less than 0.5% and without undershoot was able to reach a stable state. On the other hand, the graph has higher overshoot and undershoot for the fuzzy controller. The conventional PID controller has also reached the steady state after several overshoots and undershoots.

In Figs. 10 and 11, the diagram of speed deviation and voltage changes of the studied system at rated load is displayed. At rated load, the suggested controller has a faster damping response and a shorter settling time. In Fig. 10, the system lacks any controller and the excitation system lacks PSS.

Table 5: A comparison between the performance of different controllers in terms of network loading according to the generator angle (δ°).

| Controller | 80% | 100% | 110% |
|-------------------------|-------|-------|-------|
| PSS | ----- | 55.01 | 69.83 |
| UPFC | 42.79 | 58.74 | 70.65 |
| PSS&UPFC-PID | 40.52 | 53.91 | 67.52 |
| PSS&UPFC-Fuzzy | 42.86 | 54.19 | 68.42 |
| Ref. [29] | 39.72 | 52.45 | 66.61 |
| The proposed controller | 38.16 | 51.39 | 64.17 |

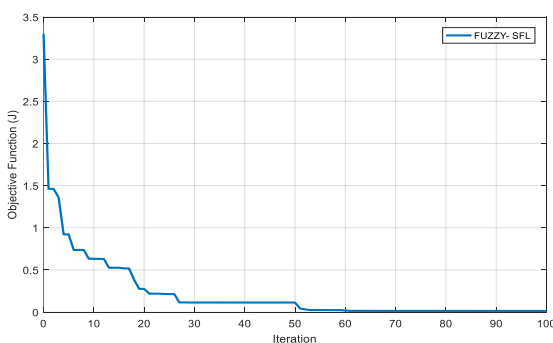


Fig. 7: Convergence curve of the SFLA for minimization of the proposed objective function.

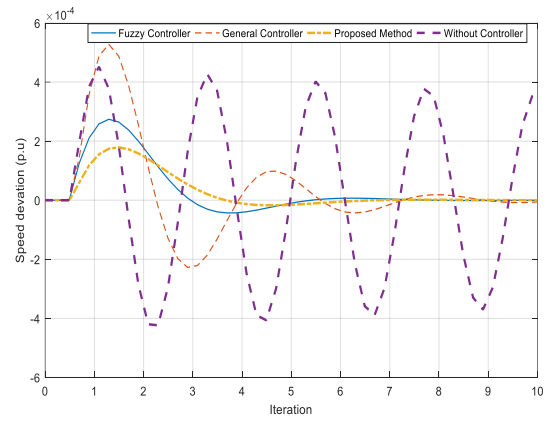


Fig. 8: Comparison of response of speed changes of three controllers for UPFC and PSS in 80% of the rated load.

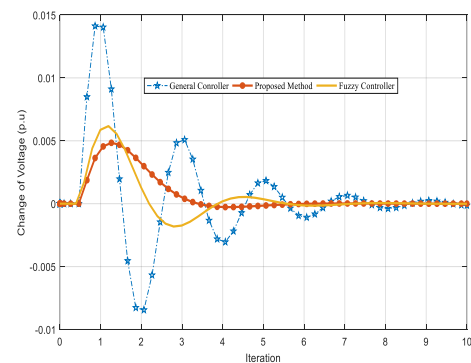


Fig. 9: Generator voltage deviation to show performance of three controllers at 80% of the rated load.

By sorting the linearized state equations of the system that were extracted in Section 2, they were implemented in the MATLAB software under normal load conditions and the outputs were displayed. After disturbing the mechanical power input of the generator, the generator speed fluctuates and the fluctuations are not dampened. Even though the PID controller has been able to reduce the magnitude of oscillations, the number of overshoots and undershoots is high. However, the fuzzy controller has reached the damping state after almost two oscillations, and finally the optimized fuzzy control has been able to show a fast-damping response.

In Figs. 12 and 13, for a 10% increase in rated load, the time response of generator speed changes along with voltage changes for the three state controllers are shown. It can be seen from Fig. 12 that the optimized fuzzy controller responded well to the changes and was able to dampen the response, while the other two controllers reached the damping mode after several oscillations. If the PSS and UPFC controls are not used, the system remains unstable. Fig. 13 shows that the voltage deviation is fixed after approximately three seconds.

The simplest method among the three used controllers is the PID controller, which is designed by the phase compensation method considering the state of the system poles. By installing these controllers, it is possible to obtain feedback from the speed changes and damp the system by applying changes to the PSS and UPFC inputs. Nonetheless,

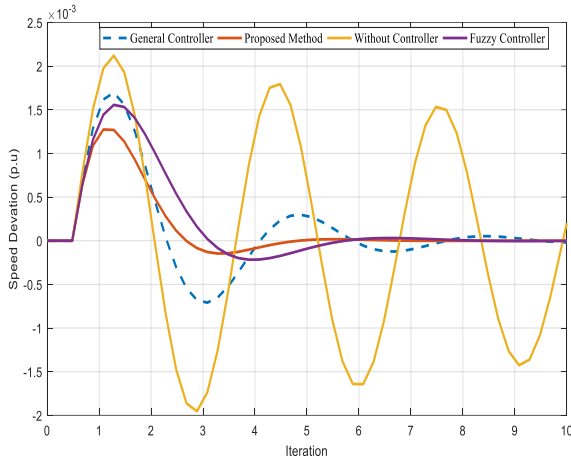


Fig. 10: Comparison of the response of speed changes of three controllers for UPFC and PSS in the rated load mode.

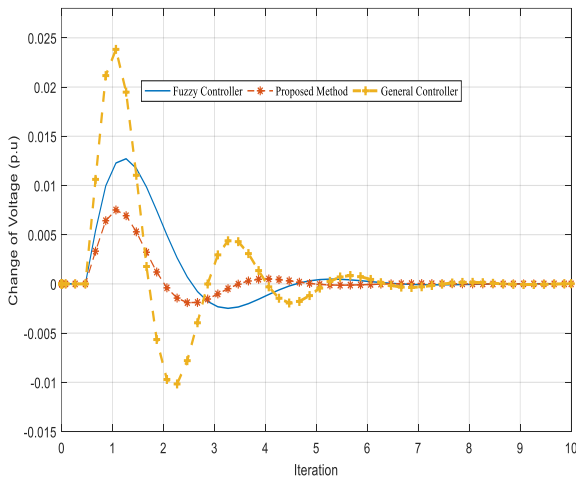


Fig. 11: Generator voltage deviation to show the performance of three controllers at the rated load.

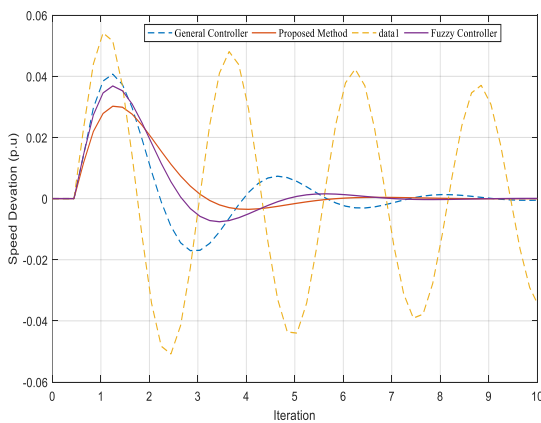


Fig. 12: Comparison of the speed changes response of three controllers for UPFC and PSS at 110% of the nominal load.

the results showed that the settling time of the system as well as the overshoot in this method is more compared to the fuzzy and optimized fuzzy methods. The comparison between these two methods in the design of the controller also shows that using the optimized gains in the fuzzy method, the damping

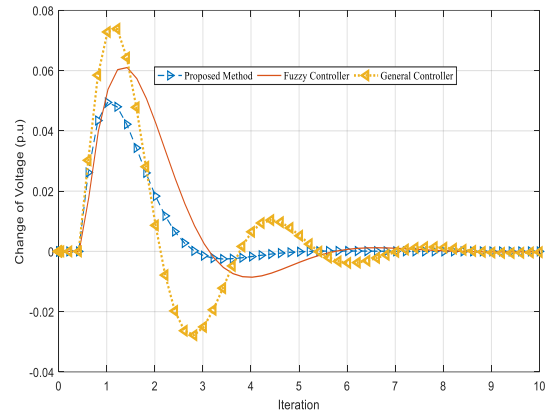


Fig. 13: Generator voltage deviation to show performance of three controllers at 110% of the rated load

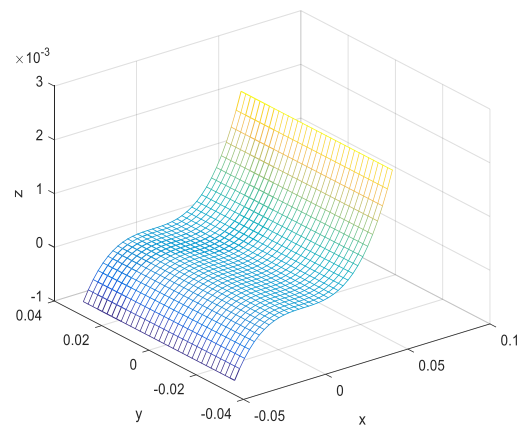


Fig. 14: Optimized fuzzy controller output for input δ_e^{UPFC}

speed of the system and the magnitude of oscillations have decreased. It should be noted that the simultaneous use of both PSS and UPFC controllers will have a significant impact on the system performance after a disturbance appears in the system, while the absence of these controllers, as shown in Figs. 8, 10, and 12, causes system instability. Fig. 14 depicts the output of the fuzzy signals based on the inputs used for the UPFC controller.

6. CONCLUSION

The paper presented a new control strategy that coordinated PSS and UPFC controllers by applying fuzzy rules. Moreover, SFLA was utilized to adjust parameters of fuzzy functions to deal with sub synchronous oscillation. An outstanding benefit of the proposed technique, in contrast to conventional controllers, is its ability to deliver a time-varying control signal continuously. This ensures that the system consistently adheres to the correct trajectory, and it can be implemented for non-linear systems without the need for mathematical modeling of the system. The simulation results including the optimized fuzzy controller showed its proper performance under different loading conditions of the system during a disturbance in the system. By introducing a combined index of the amounts of overshoot, undershoot, and settling time for the suggested fuzzy controller, this index showed up to 100% improvement compared to that obtained

by conventional PID controllers. In addition, the first angle of the generator in different loading condition was lower compared to other methods. For future works, other methods can be incorporated in optimizing the gains of the fuzzy controller, or the effect of adding the UPFC in a suitable place to boost the system damping can be investigated.

CREDIT AUTHORSHIP CONTRIBUTION STATEMENT

Mohammad Abedini: Conceptualization, Data curation, Formal analysis, Methodology, Project administration, Software, Roles/Writing - original draft. **Mahyar Abasi:** Conceptualization, Supervision, Validation, Roles/Writing - original draft.

DECLARATION OF COMPETING INTEREST

The authors declare that they have no known competing financial interests or personal relationships that could have appeared to influence the work reported in this paper. The ethical issues; including plagiarism, informed consent, misconduct, data fabrication and/or falsification, double publication and/or submission, redundancy has been completely observed by the authors.

REFERENCES

- [1] J. Ruan, Z. Shi, M. Yu, and S. Wang, "Simplified damping analysis and suppression method for low-frequency oscillation introduced by virtual synchronous generator", *Journal of Power Electronics*, vol. 21, no. 10, pp. 1600–1610, Oct. 2021.
- [2] P. Dey, S. Anulekha, M. Sourav, D. Bishwajit, B. Aniruddha, and M. Boonruang. "Improvement of small-signal stability with the incorporation of FACTS and PSS." In *2021 Control Applications in Modern Power System: Select Proceedings of EPREC 2020*, 2021, pp. 335-344.
- [3] S. Kumar, A. Kumar, and G. Shankar, "Crow search algorithm based optimal dynamic performance control of SVC assisted SMIB system," *2018 20th National Power Systems Conference (NPSC)*, 2018, pp. 1-6.
- [4] N. Sahu, M. Singh, and S. Ralhan, "Performance analysis of hybrid controller in SMIB system using metaheuristic optimization techniques under different design criteria," *Journal on Future Engineering & Technology*, vol. 16, no. 1, 2020.
- [5] E. Afzalan, and M. Joorabian, "Analysis of the simultaneous coordinated design of STATCOM-based damping stabilizers and PSS in a multimachine power system using the seeker optimization algorithm", *International Journal of Electrical Power & Energy Systems*, vol. 53, pp. 1003–1017.
- [6] L. -J. Cai, and I. Erlich, "Simultaneous coordinated tuning of PSS and FACTS damping controllers in large power systems," in *IEEE Transactions on Power Systems*, vol. 20, no. 1, pp. 294-300, Feb. 2005.
- [7] M. Chandhari, G. Andersson and I. A. Hiskens, "Control Lyapunov functions for controllable series devices," *2002 IEEE Power Engineering Society Winter Meeting. Conference Proceedings*, 2002, pp. 753.
- [8] L. F. B. Martins, P. B. de Araujo, E. de Vargas Fortes, and L. H. Macedo, "Design of the PI-UPFC-POD and PSS damping controllers using an artificial bee colony algorithm", *Journal of Control, Automation and Electrical Systems*, vol. 28, no. 6, pp. 762–773, 2017.
- [9] E. d. V. Fortes, L. H. Macedo, P. B. d. Araujo, and R. Romero, "A VNS algorithm for the design of supplementary damping controllers for small-signal stability analysis", *International Journal of Electrical Power & Energy Systems*, vol. 94, pp. 41–56, 2018.
- [10] E. de Vargas Fortes, P. B. de Araujo, and L. H. Macedo, "Coordinated tuning of the parameters of PI, PSS and POD controllers using a specialized Chu-Beasley's genetic algorithm", *Electric Power Systems Research*, vol. 140, pp. 708–721, 2016.
- [11] H. Shayeghi, A. Safari, and H. A. Shayanfar, "PSS and TCSC damping controller coordinated design using PSO in multimachine power system", *Energy Conversion and Management*, vol. 51, no. 12, pp. 2930–2937, 2010.
- [12] L. H. Hassan, M. Moghavvemi, H. A. F. Almurib, and K. M. Muttaqi, "A coordinated design of PSSs and UPFCbased stabilizer using genetic algorithm", *IEEE Transactions on Industry Applications*, vol. 50, no. 5, pp. 2957– 2966, 2014.
- [13] M. Khaksar, A. Rezvani, and M. H. Moradi, "Simulation of novel hybrid method to improve dynamic responses with PSS and UPFC by fuzzy logic controller", *Neural Computing & Applications*, vol. 29, no. 3, pp. 837–853, 2016.
- [14] B. Mohandes, Y. L. Abdelmagid, and I. Boiko, "Development of PSS tuning rules using multi-objective optimization", *International Journal of Electrical Power & Energy Systems*, vol. 100, pp. 449–462, 2018.
- [15] M. Saini, M. R. Djalal and A. M. S. Yunus, "Optimal coordination PID-PSS control based on craziness particle swarm optimization in sulselrabar system", *2022 5th International Seminar on Research of Information Technology and Intelligent Systems (ISRITI)*, 2022, pp. 695-699.
- [16] M. R. Djalal, M. Saini and A. S. Yunus, "Optimization power system stabilizer and energy storage using ant colony optimization" in *2021 International Seminar on Machine Learning Optimization and Data Science (ISMODE)*, 2022, pp. 120-124.
- [17] D. K. Sambariya, and R. Prasad, "Design of PSS for SMIB system using robust fast output sampling feedback technique," in *2013 7th International Conference on Intelligent Systems and Control (ISCO)*, 2013, pp. 166-171.
- [18] M. Rais, M. R. Djalal, V. A. Tandirerung, R. Aminuddin, I. Syarif, and Rosmiati, "Coordination PID-PSS control based on ant colony optimization in Sulselrabar system",

- in 2022 2nd International Seminar on Machine Learning, Optimization, and Data Science (ISMOL), Jakarta, Indonesia, pp. 254-258, 2022.
- [19] Tang K. S. Kim Fung Man, Guanrong Chen, and Sam Kwong, "an optimal fuzzy pid controller", *IEEE Transactions on Industrial Electronics*, Vol. 48, No. 4, August 2001.
- [20] G. Shahgholian, H. Karimi, H. Mahmoodian, "Design a power system stabilizer based on fuzzy sliding mode control theory", *International Review on Modelling and Simulations*, vol. 5, no. 5, pp. 2191-2196, Oct. 2010.
- [21] W. Fang, H.W. Ngan, "Enhancing small signal power system stability by coordinating unified power flow controller with power system stabilizer", *Electric Power Systems Research*, Vol. 65, No. 2, pp.91-99, May 2003.
- [22] S. Mishra, "Neural-network-based adaptive UPFC for improving transient stability performance of power system", *IEEE Trans. Neural Networks*, vol. 17, pp. 461-470, 2006.
- [23] B.C. Pal, "Robust damping of interarea oscillations with unified power flow controller", *IEE Proceedings-Generation, Transmission and Distribution*, vol. no. 6, pp. 733-8. 2022.
- [24] H. Wang, "A unified model for the analysis of FACTS devices in damping power system oscillations. III. Unified power flow controller," in *IEEE Transactions on Power Delivery*, vol. 15, no. 3, pp. 978-983, July 2000.
- [25] M. Jokarzadeh, M. Abedini, and A. Seifi, "Improving power system damping using a combination of optimal control theory and differential evolution algorithm", *ISA transactions*, vol. 90, pp. 169-77, July 2019.
- [26] Y. Zhang, S. Guan, and Y. Zhang, "Single-Stage AC-AC converter with controllable phase and amplitude", *IEEE Transactions on Power Electronics*, vol. 34, no. 7, pp. 6991-7000, 2019.
- [27] J. C. Bezdec, *Pattern Recognition with Fuzzy Objective Function Algorithms*, Plenum Press, 1981.
- [28] H. Moayedi, D. T. Bui, P. T. Thi Ngo, "Shuffled frog leaping algorithm and wind-driven optimization technique modified with multilayer perceptron", *Applied Sciences*, vol. 10, no. 2, pp. 689, 2020.
- [29] T. K. Mok, H. Liu, Y. Ni, F. F. Wu, and R. Hui, "Tuning the fuzzy damping controller for UPFC through genetic algorithm with comparison to the gradient descent training", *International Journal of Electrical Power & Energy Systems*, vol. 27, no. 4, 2005.

BIOGRAPHY



Mohammad Abedini was born in Boroujerd, Iran, in 1986. He received his B.Sc degree in electrical engineering from the Islamic Azad university of Boroujerd, Boroujerd, Iran in 2006. M.Sc. and Ph.D degrees in electrical engineering from Bu-Ali Sina University in 2008 and 2010, respectively. He is currently an associate professor at ayatollah Boroujerdi university. His current research interest includes microgrids and distribution systems.



Mahyar Abasi was born in 1989 in Iran. He graduated with a Ph.D. in Electrical Power Engineering from Shahid Chamran University of Ahvaz, Ahvaz, Iran in 2021. He has published more than 60 journal and conference papers, more than 10 authored books, 11 industrial research projects and a patent in the field of power systems. In 2021, he was introduced as the top researcher of Khuzestan province, Iran, and in the years 2021 to 2023, he was successful in receiving 4 titles from the membership schemes of the National Elite Foundation in Iran. He is currently an assistant professor in the Electrical Engineering department of Arak University, Arak, Iran. His specialized interests are fault protection, detection, classification and location in HVAC and HVDC transmission lines, control of reactive power and FACTS devices, evaluation and improvement of power quality and power system studies.

Copyrights

© 2024 Licensee Shahid Chamran University of Ahvaz, Ahvaz, Iran. This article is an open-access article distributed under the terms and conditions of the Creative Commons Attribution –NonCommercial 4.0 International (CC BY-NC 4.0) License (<http://creativecommons.org/licenses/by-nc/4.0/>).





Research Article

Economic Analysis of Photovoltaic Systems During Peak Load of the Electric Power Distribution System in the Presence of Electric Vehicles

Musa Khosravi¹ , Saeed Hasanvand^{1,*} , Mahyar Abasi^{2,3} , Mohammad Esmaeil Hassanzadeh¹

¹Department of Electrical Engineering, Firouzabad Higher Education Center, Shiraz University of Technology, Shiraz, Iran

²Department of Electrical Engineering, Faculty of Engineering, Arak University, Arak 38156-8-8349, Iran

³Research Institute of Renewable Energy, Arak University, Arak 38156-8-8349, Iran

* Corresponding Author: s.hasanvand@sutech.ac.ir

Abstract: Considering the challenges of using fossil fuels, including price, pollution, and the increasing development of electric vehicles, the energy supply from other sources should be considered. One of the main challenges of electric vehicles is their impact on the distribution network, especially the time of charging and its coincidence with the peak load of the network, which causes an increase in power consumption, double pressure on the network, and more and faster depreciation of distribution network equipment. Also, producing more energy during peak times leads to increased costs and air pollution. In this paper, the use of renewable energy to charge electric vehicles is investigated in such a way that the consumers of electric vehicles use solar panels and batteries to store solar energy so that it can be used for charging during peak times. The costs of installing solar panels, the consumption of electric vehicles, the amount of energy generation, as well as the emission of fossil fuel pollutants that fossil power plants produce at peak times have been investigated. Furthermore, a comparison has been made between the use of renewable and non-renewable energy. Consequently, the proposed method is about 112494 dollars more economical than the system without renewable energy. It is also suggested to consider incentives from the government for the consumer to reduce the capital and operating cost of the photovoltaic system to diminish the investment return time.

Keywords: Electric vehicle, peak load, solar energy, economic analysis.

Article history

Received 02 December 2023; Revised 02 March 2024; Accepted 13 August 2024; Published online 30 October 2024.

© 2024 Published by Shahid Chamran University of Ahvaz & Iranian Association of Electrical and Electronics Engineers (IAEEE)

How to cite this article

M. Khosravi, S. Hasanvand, M. Abasi, and M. E. Hassanzadeh, "Economic analysis of photovoltaic systems during peak load of the electric power distribution system in the presence of electric vehicles," *J. Appl. Res. Electr. Eng.*, vol. 3, no. 2, pp. 177-184, 2024. DOI: 10.22055/jaree.2024.45461.1093



1. INTRODUCTION

The increase in fuel prices and environmental concerns cause changes in the structure of power systems and energy management [1] becomes more crucial than before. One of these changes is the increasing use of renewable energies and electric vehicles which advents microgrids [2]. With the significant increase in the number of electric vehicles that can solve the challenge of environmental pollution, it has created new challenges such as creating overload on the network and simultaneity of charging this type of vehicle with peak load for the power system. By developing the utilization of renewable energy, electric vehicles can be

adopted optimally and cleanly at a low cost, which improves energy efficiency. The research concerning this field is on the problem of electric vehicle charging timing and the use and optimization of the vehicle battery to reduce peak load and the use of algorithms for vehicle charging and discharging time, which will be investigated in the following. Concerning the connection of the electric vehicle to the grid, the opportunities, challenges, and executive structure, reference [3] after introducing electric vehicles as the future of the transportation industry, describes their challenges for the electricity industry and the vehicle to grid (V2G) connection and explains their requirements. In [4], the presence of electric vehicles with V2G system and

different charging strategies in the distribution network has been considered and it has been shown that the use of electric vehicles without planning and control can cause tension and overload. Ref. [5] addresses the generation, distribution, and transmission costs of a unit of electrical energy imposed on the electricity industry of a country and compares it with the income of that industry, which can play an effective role in the macro-planning and development of the electricity industry excluding government subsidies which can be a respectable criterion for power system with renewable energies. A two-stage charging strategy for solving electric vehicle charging control problems based on fuzzy control is proposed in [6], in which the optimal charging of each vehicle is calculated in the first stage, and in the second stage, the accumulated power of the first stage is distributed between vehicles using fuzzy control. The probabilistic planning of the power system in the presence of an electric vehicle, considering the uncertainty of renewable sources, has been investigated in [7] which using a mixed-integer linear model. In [8], the power quality problems of the distribution system caused by the charging of electric vehicles are first mentioned, and then solutions to solve these problems are presented. In [9], with the aim of energy management and minimizing the negative effects of the electric vehicle load pattern, a new method for installing solar parking lot for electric vehicles in a network with uncontrollable distributed resources is presented. Modelling and optimization of energy consumption in a smart home with the presence of an electric vehicle, energy storage, solar cell, and load response has been investigated in [10]. In this study, according to the importance of the energy management process, the performance of a smart home in the presence of an electric vehicle capable of bidirectional exchange of power with the power grid, energy storage system and solar panels has been modelled and evaluated in the framework of a linear programming. In [11], the economic evaluation and feasibility of using a photovoltaic system to supply the electrical load required for household use has been investigated using statistics and real information. The results show that the use of this photovoltaic system is justified. In [12] the optimal placement of electric vehicle charging stations in a distribution network considering rooftop photovoltaic systems has been discussed, but the cost issues related to this consideration have not been conducted. The authors in [13] present the photovoltaic rooftop and electric vehicle parking lot models to provide the benefit in peak load as well as the spinning and regulation reserves. Power distribution impacts considering photovoltaic and electric vehicles have been assessed in [14, 15]. These two studies show that the load supplying, and the voltage profile are improved, which can serve more the EV charging demand. In [16] a bi-directional charger for electric vehicles is considered which causes operational profit for distribution power system integrated with photovoltaic and electric vehicles. In previous studies, the economic evaluation and the costs of using the photovoltaic system in the presence of the electric vehicle have not been addressed, and the effect of renewable energy and the electric vehicle on the actual reduction of the cost of electric energy supply has not been investigated. The present paper addresses this gap by adopting real data.

In this paper, with the aim of supplying the required energy for charging the electric vehicle, the solutions to reduce the costs considering the importance of environmental pollution have been investigated. These costs include the cost of electricity for charging and household consumption, fuel cost, emission cost, and maintenance cost. Furthermore, economic issues have been investigated in two cases of using and not using renewable solar energy to supply electric vehicle. Also, when renewable energy is used, it will be seen that by using a home solar power plant, the pollution and fuel cost for energy production can be reduced compared to the production of electricity by traditional power plants, and the challenges of charging an electric vehicle at peak times can be resolved.

The rest of the paper is organized as follows. In the next section, the description of the problem and the modelling of different parts are mentioned. The costs include consumer cost, power system cost and solar panel energy production, power plant fuel cost, pollution cost, and transformer cost, and the results are interpreted in the next section, and the conclusion is presented at the end.

2. PROBLEM DESCRIPTION

In this study, the challenge of simultaneity of electric vehicle charging with the peak time of electricity consumption and the use of renewable energy in homes and the costs of consumers and the electricity distribution network in terms of emissions, fuel costs, and transformer depreciation costs have been modeled and investigated. The understudy system is a power distribution system and consists of 1000 EVs and household solar systems with 25 kilowatts output.

2.1. Photovoltaic System

In this section, the costs related to the production of solar energy in a small domestic power plant and the power generation relationships of this power plant have been examined. The construction of a solar power plant has different costs according to the type of equipment and installation conditions. Usually, for the construction of a solar power plant, two types of general costs can be imagined, which are mentioned below. These expenses are related to January 2022.

1. Cost of solar power plant equipment: Table 1 details the cost of each of the different parts of a small-scale solar power plant.
2. Ancillary costs: This type of cost includes the variable costs of panel washing and maintenance during operation.

One of the important parameters in photovoltaic power plant design calculations is the output power of the solar system, which is obtained from (1).

$$P_{PV} = E_{PV} E_{in} A_{PV} G \quad (1)$$

where P_{pv} is the output power of the solar system, E_{pv} is the efficiency of the panel, E_{in} is the efficiency of the electric power converter, A_{pv} is the area of the panel (m^2), and G is the irradiance (W/m^2) on the panel surface [17].

Table 1: The costs of a 5-kW solar power plant at home.

| | Type of panel | No. | Price (\$) |
|---|--|-----|-----------------|
| 1 | 290 W crystalline solar panel | 17 | 166.6 |
| 2 | 5200 W, 48 V tp-series inverter | 1 | 572.6 |
| 3 | Steel structure | 3 | 89 |
| 4 | Electrical panel and the related equipment | 1 | 166.6 |
| 5 | Installation cost | | 10% of the cost |
| 6 | Controller charger | 1 | 463 |
| 7 | 100 Ah, 48 V battery | 1 | 187 |
| 8 | Total cost | | 3666-4266 \$ |

According to the relationship between the output power of the panel, the output power depends on the parameters of the panel's efficiency in the ambient temperature and the inverter's efficiency, as well as the area of the panel and the intensity of sunlight [18]. There are 17 units of 290 W mono crystal type panels, considering 78% efficiency fore the whole solar system, and peak sun hour (PHS) equal to 6.5 for Shiraz, it is possible to produce 25kWh ($17 \times 290 \times 0.78 \times 6.5$) of energy for each day. If 5 kW of this power are used for electric vehicle charging, 20 kW can be injected into the main grid, which according to the tariff rate for purchasing electricity by the grid from domestic producers of electricity, below 20 kW was 0.073\$/kW in the year 2022 which earns monthly income of about 53\$ [17].

2.2. Electric vehicles

The electrical energy required by electric vehicles is different from the gasoline fuel consumption of internal combustion cars. The fuel consumption of internal combustion vehicles with the consumption of each liter of fuel per 100 km is analyzed, but electric vehicles are measured in terms of electricity consumption per kWh, which some examples are presented below.

1. Nissan Leaf consumes 10 kWh per 100 km with a battery capacity of 40-62 kWh.

2. Jaguar E-Pace consumes 19 kW of energy per 100 km with a 90-kW battery.

3. Carmania EK1 with a 44.5-kW battery and a distance of 3054 km with each charge, i.e., 4.5 kW for every 100 km.

4. Renault Zoe model 2020 with a 52-kW battery and a distance of 245 miles with each charge, i.e., 13.19 kW for every 100 kilometers

5- Kia e-niro 2019 electric vehicle with a 64-kW battery and a distance of 480 km with each charge, i.e., 13.3 kW for every 100 km.

In this paper, on average, for every 100 kilometers of distance, about 14 kW consumption is considered, which considering a 60-kW battery and considering that the minimum and maximum charge is 5 and 85%, the vehicle with each charge can travel 342 km.

Each type of battery has limitations based on its physical structure and manufacturing technology, one of which is the charge and discharge limit per hour, which is in the form of (2):

$$p_{batt}^{min} \leq p_{batt} \leq p_{batt}^{max} \quad (2)$$

And another variable of the battery is the state of charge, which is 1 in the fully charged state, and 0 in the fully discharged state, which is according to Eq. (3).

$$soc_h = soc_{h-1} - \left(\frac{p_{batt}}{E_{batt}} \right) \quad h=1,2,3,\dots,24 \quad (3)$$

where soc_h is the state of charge of the battery at hour h , E_{batt} is the rated power of the battery.

Since p_{batt} is for 24 hours, we have

$$\sum_{j=1}^j p_{batt} \leq (soc_0 - (1 - d)) * E_{batt} \quad j=1,2,3,\dots,24 \quad (4)$$

D represents the maximum discharge deep of the battery. For instance, if $D = 0.8$, the battery charging should not be below 20% [19].

2.3. Distribution Transformer

Power transformers are one of the most important and expensive equipment of the power system, which can be used for more than 40 years if properly operated [20]. The way of loading is the most determining factor in the lifetime of the transformer and the aging of its insulation, so that by increasing the temperature of the hot spot of the winding by 6 points compared to its nominal value, the insulation life of the transformer is reduced by half. In addition, loading more than the nominal value of the transformer, especially in power transformers, can cause many risks, such as increasing the amount of moisture and gas production in the paper and oil insulation, increasing the leakage flux density outside the core and increasing the stress on the bushings, tap changer, end turns, and current transformers [21]. According to the standard IEEE Std.C57.91, the insulation life of the transformer is considered to be 180000 hours, the increase in the temperature of the transformer causes a certain amount of the life of the transformer to decrease. Equations (4)-(6) express the modeling of the decrease in life due to the increase in the temperature of the transformer for the reference temperature of 110°C [22-23].

$$FAA = e^{\left[\frac{15000}{\theta_h - 273} - \frac{15000}{383} \right]} \quad (5)$$

FAA is the life reduction factor and θ_h is the temperature of the coils in K.

In order to calculate the amount of reduction in the life of the transformer, it is possible to obtain the value of the temperature changes of the windings due to the variations in the transformer loading by using the relation of power losses in the resistance [24]. In this paper, taking into account solar generation and electric vehicle charging, less power is absorbed from the network and the load of the 2 MVA transformer is reduced to about 12%. According to Fig. 1, a 10% decrease in loading reduces the temperature by 20%. Assuming the normal working temperature of the transformer, which is 110°C, the new temperature of the transformer is reduced and reaches 88°C. On average, reducing the temperature to 88°C, according to the diagram in Fig. 2, increases the life of the transformer by 0.1 per year, which adds 2 years to the total life of the transformer for a transformer with a life of 180,000 hours or 20 years.

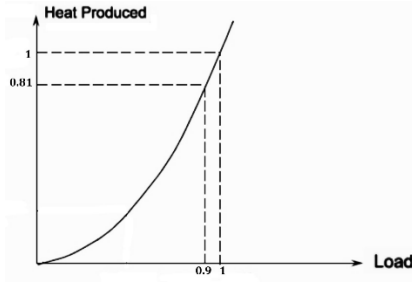


Fig. 1: The relation between loading in p.u. and temperature of transformer in p.u.

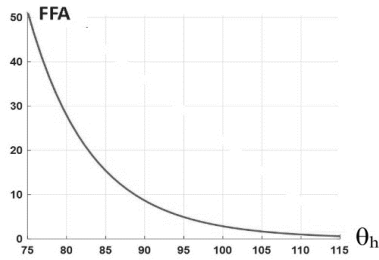


Fig. 2: The relation between temperature in °C and lifespan of transformer in p.u.

3. Costs

3.1. Consumer's Costs

Consumer costs include the fixed cost, which is the cost of construction of a solar power plant, and the variable costs include the maintenance of the solar power plant, as well as the costs of purchasing electricity from the grid for home consumption. The amount of electricity obtained from solar panels is deducted from the total cost and the excess energy obtained is sold. The cost relationship is in the form of (6):

$$\begin{aligned} C_{L_{Total}} &= C_{Load} + C_{Ch} - C_{PV} \\ C_{PV} &= C_A + C_B \end{aligned} \quad (6)$$

In the mentioned equation, $C_{L_{TOTAL}}$ is the total cost of the consumer, C_{LOAD} is the cost of buying electricity for household consumption, C_{Ch} is the cost of charging an electric vehicle, and C_{PV} is the cost of producing electricity by solar panels.

3.2. Power system's Cost

The costs are related to the production of electric energy and delivering it to the consumer, which include the cost of fuel, pollution, and distribution transformers.

$$C_{Total} = C_{Tr} + C_P + C_F \quad (7)$$

where C_{Tr} is the cost of transformer, C_P is the cost of pollution, and C_F is the cost of fuel. The cost related to the transformer is checked in terms of the transformer's lifespan according to the amount of peak loads that are applied to it. To elucidate, the increase in loading causes a decrease in lifespan and, as a result, its replacement cost, which was explained in the previous section. On average, the amount of electricity consumed by each household is 186 kWh/hour, which is equivalent to 6.5 kWh/day. According to the tariff announced in January 2021, it was on average 0.0003\$ to 0.002 \$ for consumption of higher than 100 to 300 kWh, and this cost is for households without electric vehicles.

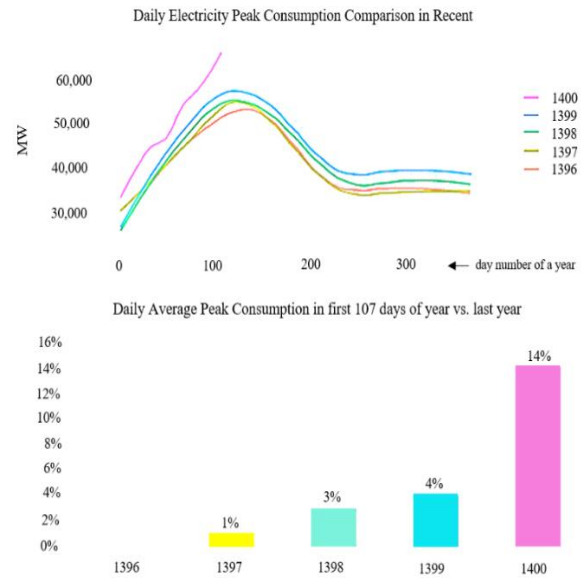


Fig. 3: Electricity consumption peaks within the last five years.

For an electric vehicle, taking into account 14 kW to travel every 100 km with a 60-kWh battery and traveling a distance of 342 km with each charge, and taking into account the fact that the charging of the electric vehicle is according to the domestic tariff, an electric vehicle requires 1800 kWh/day for charging if it is charged every day. According to the tariff of 150 Tomans, the vehicle requires an average of 10\$/month for charging above 30 kWh. Fig. 3 shows the consumption of electricity in the last five years. According to the graph, electricity consumption is at its highest in the hot three months of the year, which was about 58,000 MW. But, in the year 2021, the peak of electricity consumption reached 62,000 MW [25]. In this paper, an average peak consumption of 52,000 MW is considered.

3.3. Power Plant's Fuel Cost

The electricity produced in winter in the country is significantly more polluted than the electricity produced in the first nine months of the year, which is due to the multiple growth of liquid fuels with higher polluting capability and reduced gas consumption. When gas is used for heating homes, power plants have a shortage of gas, so they have to use liquid fuel. Table 2 lists the consumption of different types of fuel to produce one kWh of electricity in the average form of their consumption in the first nine months of the year and three months of winter, the information obtained for the year 2018 per kWh of electricity production [26]. For a 12 MW power plant, it is as shown in Table 3.

Table 2: Amount of fuel consumption in the power plant for 1 kW of energy.

| First nine months | | | Winter | | |
|-----------------------|-----------|--------------|-----------------------|-----------|--------------|
| Gas (m ³) | Mazut (L) | Gasoline (L) | Gas (m ³) | Mazut (L) | Gasoline (L) |
| 0.252 | 0.009 | 0.01 | 0.153 | 0.030 | 0.071 |

Table 3: Fuel consumption for 12 MW power plant.

| First nine months | | | Winter | | |
|-----------------------|-----------|--------------|-----------------------|-----------|--------------|
| Gas (m ³) | Mazut (L) | Gasoline (L) | Gas (m ³) | Mazut (L) | Gasoline (L) |
| 3024 | 108 | 120 | 1836 | 360 | 852 |

Table 4: Cost of fuel consumption for one kW.

| Fuel cost in the first nine months | | |
|--|------------------------------|---------------------------------|
| Gas (10 ³ m ³) | Mazut (10 ³ L) | Gasoline (10 ³ L) |
| 75 | 42 | 681 |
| Fuel cost in winter | | |
| Gas (10 ³ m ³) | Mazut (10 ³ L) | Gasoline (10 ³ L) |
| 213 | 90 | 459 |
| Fuel cost of 12 MW for 12 months | | |
| Gas (10 ³ m ³) | Mazut (10 ³ L) | Gasoline (10 ³ L) |
| 30 | 27 | 756 |

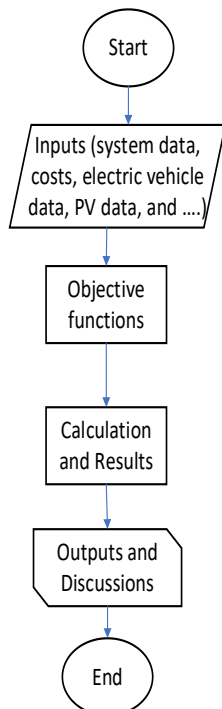
3.4. Pollution Cost

Power plants need fossil fuel for power generation, leading to the emission of pollution. The pollutants produced are impose external costs to the power plant, which cannot be examined directly. So, the costs including the treatment of diseases and the costs caused by pollutants by destroying the environment should be investigated. Table 5 shows the cost of pollutants in general, which includes the external costs of polluting gases based on studies by the World Bank and Environmental Protection Organization in 2013 based on \$/kWh [27].

SO₂, NO_x, and CO₂ are the most important air pollutants that every year, especially in winter, cause air pollution and the occurrence of various diseases. Table 6 provides the amount of pollution each of the pollutants cause by burning fossil fuel for electricity generation per unit of fuel consumed [27]. The flowchart of proposed model is shown in Fig.4.

4. RESULTS AND ANALYSIS

At first, the costs related to the combined cycle power plant, the household solar power plant, and the consumer's cost are discussed. Therefore, in the first stage, charging of electric vehicles without solar panels is considered.

**Fig. 4:** Illustrative process flowchart.

As mentioned in the electric vehicle section, to charge an electric vehicle on average if it covers a distance of 20,000 km per year, about 2800 kW of electric energy is needed. Considering that the vehicle is charged at home from 6 pm to 6 am, which coincides with the peak hours, the challenges of the network increase during peak hours. Thus, according to the graph below, the peak load reached more than 65,000 MW in 2021, and its minimum value is 40,000 MW. Now, the electricity used to charge the electric vehicle should be added to it, and it should be emphasized that this amount is for one car, and if the result is checked for 1000 vehicle, it is expressed in the form of Table 7. (The amount of peak consumption is considered to be 52500 MW per year on average.)

As it is clear from Table 7, with the presence of 1000 electric vehicles, gas fuel consumption increased by 635,600 m³, and fuel consumption increased by 39,200 liters and diesel by 70,000 liters, and the pollutants are also according to Table 8.

Now, considering the solar system for charging the vehicle in such a way that the battery is used to store energy for charging the vehicle, and even if more energy can be used for the peak hour of consumption with more batteries, solar power plant supplies about 7.3 MW to the power system on average. And, if it is considered for 1000 houses, it will be about 7300 MW. The description of costs is according to Table 9. The cost of pollutants with the presence of solar cells is shown in Table 10.

Generally, the total cost of fuel and emissions without using the solar power plant system and with the presence of an electric vehicle is \$212,737.72 per year, and when a 5-kW home power plant is used, the costs reach \$102,381.55 per year, which saves 110,356.17 \$ for the network. By reducing the load on the transformer by about 12%, the temperature of the transformer winding decreases by about 20%, after which 0.1% is added to the insulation life of the transformer. In other words, the insulation life of the transformer is added 2 years on top of its lifespan of 20 years. According to the price of 2000 KVA transformer which is 21387 \$ in 2023, with the increase of 2 years insulation lifespan of the transformer, 2138.7 \$ will be saved economically for each stage of transformer replacement. The power system owner can support domestic electricity producers by using incentive schemes such as loans with low interest, support schemes, buying electricity with a more expensive tariff, can make it attractive more for small scale producers to solve the overload challenge created by electric vehicles.

Table 5: The cost of pollutants based on \$/kWh.

| | NO _x | SO ₂ | CO ₂ |
|----------------------------|-----------------|-----------------|-----------------|
| Combined cycle power plant | 0.0004 | 0.00045 | 0.0011 |

Table 6: Emissions production rate for each type of fuel and for each unit of fuel.

| | NO _x (g per unit of fuel) | SO ₂ (g per unit of fuel) | CO ₂ (g per unit of fuel) |
|-------------|--|--|--|
| Gasoline | 19 | 8.7 | 2900 |
| Natural gas | 7 | 0 | 210 |
| Mazut | 9 | 5.4 | 3900 |

Table 7: The amount of fuel consumption in peak load with and without an electric vehicle.

| | Fuel consumption during peak load and charging of 1000 vehicles | | | Fuel consumption during peak load | | |
|------------|---|-------|----------|-----------------------------------|-------|----------|
| | Gas | Mazut | Gasoline | Gas | Mazut | Gasoline |
| 1000 Liter | 11917.5 | 735 | 1313.5 | 12553.1 | 7742 | 1382.5 |
| \$ | 11.47 | 0.51 | 0.89 | 8.57 | 0.51 | 0.94 |

Table 8: Pollutants for charging the vehicles.

| Pollution produced in the presence of 1000 electric vehicles | | | |
|--|-----------------|-----------------|-----------------|
| | NO _x | CO ₂ | SO ₂ |
| Gas | 83422500 | 2507675000 | 0 |
| Mazut | 107257500 | 46478250000 | 64354500 |
| Gasoline | 226432500 | 34560750000 | 103683250 |
| Cost (\$) | 21000 | 57750 | 23625 |

Table 9: Costs considering household solar power plant.

| | Gas | Mazut | Gasoline |
|----------------------|----------|--------|----------|
| Fuel consumption (L) | 10260400 | 632800 | 1120000 |
| Cost (\$) | 701.12 | 432.4 | 765.3 |

Table 10: The cost of pollution with the presence of a solar power plant.

| Amount of pollution produced in the presence of the solar cell | | | |
|--|-----------------|-----------------|-----------------|
| | NO _x | CO ₂ | SO ₂ |
| Gas | 71822800 | 2154684000 | 0 |
| Mazut | 5695300 | 2467920000 | 3417120 |
| Gasoline | 21280000 | 3248000000 | 9764000 |
| Cost (\$) | 18080 | 49720 | 30340 |

5. CONCLUSION

In this paper, economic studies related to the use of household power plants and its effect overall network costs with the presence of electric vehicles were investigated. As the results show, when the solar power plant is used, not only the cost of fuel, pollution and maintenance of the power plant is reduced, but also two years are added to the lifespan of the transformer compared to the state without the solar system. On the other hand, consumer expenses are also reduced and can have income. Finally, as it can be seen in the results, from the economic point of view, the use of household solar power plant is appropriate choice, and it is about 112,494.87 dollars more economical than the system without solar system.

CREDIT AUTHORSHIP CONTRIBUTION STATEMENT

Musa Khosravi: Data curation, Formal analysis, Investigation, Resources, Software, Visualization, Writing - original draft. **Saeed Hasanvand:** Conceptualization, Formal analysis, Methodology, Project administration. **Mahyar Abasi:** Supervision, Validation, Writing - original draft, Writing - review & editing. **Mohammad Esmail Hassanzadeh:** Project administration, Writing - review & editing.

DECLARATION OF COMPETING INTEREST

The authors declare that they have no known competing financial interests or personal relationships that could have appeared to influence the work reported in this

paper. The ethical issues; including plagiarism, informed consent, misconduct, data fabrication and/or falsification, double publication and/or submission, redundancy has been completely observed by the authors.

REFERENCES

- [1] M. Mohseni, M. Joorabian, and A. Lashkarara, "Energy management in distribution systems considering consumer behavior and internet of things" *J. Appl. Res. Electr. Eng.*, vol. 1, no. 2, pp. 186-196, 2022.
- [2] M. Tofghi-Milani, S. Fattaheian-Dehkordi, and M. Fotuhi-Firuzabad, "A new peer-to-peer energy trading model in an isolated multi-agent microgrid," *J. Appl. Res. Electr. Eng.*, vol. 1, no. 1, pp. 33-41, 2022.
- [3] C. Gschwendtner, S. R. Sinsel and A. Stephan, "Vehicle-to-X (V2X) implementation: An overview of predominate trial configurations and technical social and regulatory challenges", *Renewable and Sustainable Energy Reviews*, vol. 145, pp. 110977, 2021.
- [4] S. Rezaee, E. Farjah and B. Khorramdel, "Probabilistic Analysis of Plug-In Electric Vehicles Impact on Electrical Grid Through Homes and Parking Lots," *IEEE Transactions on Sustainable Energy*, vol. 4, no. 4, pp. 1024-1033, Oct. 2013.
- [5] H. Mohaghegh, and Sh. Yousefi "Calculating the cost of production, transmission and distribution of each unit of electric energy without taking into account the government subsidy" in *Proc. 31st international power system conference (PSC)*, 2016.
- [6] M. F. Bandpey, and K. G. Firouzjah, "Two-stage charging strategy of plug-in electric vehicles based on fuzzy control", *Computers & Operations Research*, vol. 96, pp. 236-243, Aug. 2018.
- [7] I. Gohbi Sarood, and M. J. Shahriari, "probabilistic planning of the power system in the presence of an electric vehicle considering the uncertainty of renewable resources", *Computational Intelligence in Electrical Engineering*, vol. 1, no. 1, pp. 111-130, Spring 2019.
- [8] A. Srivastava, M. Manas, and R. K. Dubey, "Electric vehicle integration's impacts on power quality in distribution network and associated mitigation measures: A review", *Journal of Engineering and Applied Science*, vol. 70, no. 1, pp. 1-12, Dec. 2023.
- [9] M. Farrokhi Far, and S. Jabedar, "Management and improvement of technical parameters using electric vehicle in the network with uncontrollable scattered resources", in *31st International Electricity Conference*, 2015.
- [10] M. Alizadeh, M. Jafari, and Y. Soltani, "Modeling and optimization of energy consumption in a smart home with the presence of an electric vehicle, energy storage, solar cell and load response", *Journal of Modeling in Engineering*, vol. 17, no. 57, pp. 215-226, 2018.

- [11] M. H. Mahdavi Adeli, M. Salimifar, and A. Ghazelpash, "Economic evaluation of the use of solar electricity and fossil electricity in household use", *Scientific Research Journal of Economic Policy*, vol. 6, no. 11, pp. 123-147, 2014.
- [12] W. S. Tounsi Fokui, M. J. Saulo and L. Ngoo, "Optimal placement of electric vehicle charging stations in a distribution network with randomly distributed rooftop photovoltaic systems" *IEEE Access*, Vol: 9, pp. 397-411, 2021.
- [13] U. C. Chukwu, and S. M. Mahajan, "V2G parking lot with PV rooftop for capacity enhancement of a distribution system," *IEEE Transactions on Sustainable Energy*, vol. 5, pp. 119-127, 2013.
- [14] J. Van Roy, N. Leemput, F. Geth, R. Salenbien, J. Büscher, and J. Driesen, "Apartment building electricity system impact of operational electric vehicle charging strategies," *IEEE Transactions on Sustainable Energy*, vol. 5, pp. 264-272, 2013.
- [15] S. Faddel and O. A. Mohammed, "Automated distributed electric vehicle controller for residential demand side management," *IEEE Transactions on Industry Applications*, vol. 55, pp. 16-25, 2018.
- [16] R. Luthander, M. Shepero, J. Munkhammar, and J. Widén, "Photovoltaics and opportunistic electric vehicle charging in the power system—a case study on a Swedish distribution grid," *IET Renewable Power Generation*, vol. 13, pp. 710-716, 2019.
- [17] M. R. Abutalebi and S. Yaqoubi, "Designing a 100 kW Photovoltaic Power Plant in Isfahan - Economic and Environmental Review", *Journal of Novel Research in Electrical power*, vol. 11, no. 1, Spring 2022.
- [18] M. Sadeghi and M. Abasi, "Optimal placement and sizing of hybrid superconducting fault current limiter to protection coordination restoration of the distribution networks in the presence of simultaneous distributed generation", *Electric Power Systems Research*, vol. 201, pp. 107541, 2021.
- [19] R. Marvi Khayabani, and M. Qaini, "Energy supply management in electric vehicle fast charging station with photovoltaic system and battery bank", *Asr-E-Barq Quarterly*, vol. 1, no. 6, pp. 53-57, Spring 2016.
- [20] M. Abasi, A. T. Farsani, A. Rohani, and M. A. Shiran, "Improving differential relay performance during cross-country fault using a fuzzy logic-based control algorithm," in *2019 5th Conference on Knowledge Based Engineering and Innovation (KBEI)*, Tehran, Iran, 2019, pp. 193-199.
- [21] A. Aghaei Far, and H. Azizi, "Calculation of thermal jumps and lost life of brush transformer for line-on load monitoring", in *19th International Electricity Conference*, 2004.
- [22] V. M. Montsinger, "Loading transformers by temperature", *AIEE Transactions*, vol. 49, pp. 776-792, 1930.
- [23] M. K. Pradhan and T. S. Ramu, "Prediction of Hottest Spot Temperature (HST) in power and station transformers", *IEEE Transactions Power Delivery*, vol. 18, pp. 1275-1283, 2003.
- [24] M. Abasi, M. Joorabian, A. Saffarian, and S. Seifossadat, "A comprehensive review of various fault location methods for transmission lines compensated by FACTS devices and series capacitors", *J. Oper. Autom. Power Eng.*, vol. 9, no. 3, pp. 213-225, 2021.
- [25] B. Ajdari, and A. Kadivar. (September 2021). *Electricity consumption growth puzzle in Iran* (in Persian) [Online]. Available: <https://d-mag.ir/p4197/>
- [26] M. E. Raeisi. (2019). *You use more polluted electricity in winter* (in Persian) [Online]. Available: <https://zistonline.com/vdcgtn97.ak9wu4prra.html>
- [27] M. Abbaspour, S. A. Haji, S. M. Hosseini, and T. Taheri, "Technical, economic and environmental evaluation of solar power plant using RETScreen software according to the law of targeting subsidies", *Man and Environment*, vol. 9, no. 3, pp. 9-16, 2011.

BIOGRAPHY



automation.

Musa Khosravi : received his BSc. degree in electrical engineering from Firouzabad Higher Education Center. He currently works in the field of industrial automation at Faraz Machine Company. His research interests include renewable energies, electric vehicles, fault detection in transmission lines and industrial



Saeed Hasanvand: received his BSc. degree in electrical engineering from Shahid Chamran University of Ahvaz, Iran, in 2009, the MSc. degree from University of Isfahan, Iran, in 2012, and the PhD. From Shiraz University of Technology, Iran, in 2017. He is currently an assistant professor in electrical engineering at Firouzabad Higher Education Center, Shiraz university of technology. His research interests include power system stability and optimization, micro-grids, renewable energies, FACTS devices, and power system reliability.



Mahyar Abasi: was born in 1989 in Iran. He graduated with a Ph.D. in Electrical Power Engineering from Shahid Chamran University of Ahvaz, Ahvaz, Iran in 2021. He has published more than 60 journal and conference papers, more than 10 authored books, 11 industrial research projects and a patent in the field of power systems. In 2021, he was introduced as the top researcher

of Khuzestan province, Iran, and in the years 2021 to 2023, he was successful in receiving 4 titles from the membership schemes of the National Elite Foundation in Iran. He is currently an assistant professor in the Electrical Engineering department of Arak University, Arak, Iran. His specialized interests are fault protection, detection, classification and

location in HVAC and HVDC transmission lines, control of reactive power and FACTS devices, evaluation and improvement of power quality and power system studies.



Mohammad Esmaeil Hassanzadeh: received his MSc. and Ph.D. degrees from Shiraz University of Technology, Iran, in 2015 and 2022 respectively. He is currently an assistant professor in electrical engineering at Firouzabad Higher Education Center, Shiraz University of Technology. His research interests include power system stability and optimization, micro-grids, renewable energies, FACTS devices, and power electronics.

Copyrights

© 2024 Licensee Shahid Chamran University of Ahvaz, Ahvaz, Iran. This article is an open-access article distributed under the terms and conditions of the Creative Commons Attribution –NonCommercial 4.0 International (CC BY-NC 4.0) License (<http://creativecommons.org/licenses/by-nc/4.0/>).





Research Article

Improving Power Quality Using a Fuzzy Inference System-Based Variable Forgetting Factor Recursive Least Error Square Control Scheme of DSTATCOM

Arash Rohani^{1,*} , Javad Ebrahimi¹ , and Shirin Besati²

¹ Power Systems Engineer at APD Engineering, Perth WA 6000, Australia

² Department of Electrical and Computer Engineering, University of North Carolina at Charlotte, USA

* Corresponding Author: arash.rohani@apdeng.com.au

Abstract: A two-layer combined control method is developed for a four-leg Distribution Static Synchronous Compensator (DSTATCOM). The method aims at harmonics reduction, demand-generation equilibrium, power factor modification, voltage adjustment, and neutral current modification in a 3ph 4-wire distribution system. In the first layer, a recursive Least Error Square algorithm (RLES) based on a new fuzzy logic-based variable forgetting factor is used for Real-time estimation of voltage and current signals and their constituting components. The second layer's duty is to extract the reference currents using the outputs of the first layer. Besides the high accuracy and convergence speed, the suggested algorithm is independent of coordinate transformations and complex computation when attempting to derive the reference currents of DSTATCOM. To enhance the dynamic performance of DSTATCOM, an adaptive hysteresis band current controller was utilized to generate switching signals. The effectiveness of the presented control strategy was verified via simulation studies implemented in MATLAB/Simulink environment.

Keywords: DSTATCOM, power quality, recursive least error square, fuzzy logic variable forgetting factor, adaptive hysteresis band current control.

Article history

Received 14 January 2024; Revised 24 July 2024; Accepted 19 August 2024; Published online 30 October 2024.

© 2024 Published by Shahid Chamran University of Ahvaz & Iranian Association of Electrical and Electronics Engineers (IAEEE)

How to cite this article

A. Rohani, J. Ebrahimi, and S. Besati, "improving power quality using a fuzzy inference system-based variable forgetting factor recursive least error square control scheme of DSTATCOM," *J. Appl. Res. Electr. Eng.*, vol. 3, no. 2, pp. 185-199, 2024. DOI: [10.22055/jaree.2024.45680.1097](https://doi.org/10.22055/jaree.2024.45680.1097)



1. INTRODUCTION

Exponentially-increasing deployment of nonlinear loads has led to an elevation in the level of harmonic pollutions in the power grid, which creates many problems for performance, protection and control of electrical facilities. Nonlinear loads contain harmonic contents and draw reactive power from AC mains, causing power quality issues, especially voltage harmonics at the Point of Common Coupling (PCC), and thus, disrupting the load joined to the PCC [1, 2]. Harmonic estimation is one of the major aims of control systems. However, harmonic measurement is difficult because a majority of harmonic causes are inherently dynamic and contain voltage/current signals that vary over time. Thus, harmonic components should be estimated fast and accurately. This justifies the use of estimation algorithms

which have less complexity for the real-time implementation [3].

Phase Lock Loops (PLL)-based control algorithms [4-6] are conventional methods for estimating harmonic components of disturbed power signals. However, under unbalanced or disturbed voltage conditions, PLL shows a phase delay, which leads to a slow response and equipment failure in the power system. Many researchers have investigated different solutions for PLL tracking capability and performance improvement, such as Delay-Based PLLs [7] and Frequency Fixed Second-Order Generalized Integrator-based PLL (FFSOGI-PLL) [8]. In general, a trade-off between fast tracking and proper filtering is applied in the PLL optimization methods. Most of these methods are very sensitive to harmonic distortions. Subsequently, achieving fast tracking and strong robustness against dynamic changes of harmonics, simultaneously, seems to be very challenging.

In general, advanced signal processing methods are presented either in time or frequency domain strategies for the appropriate operation of a DSTATCOM control system. Frequency-domain strategies, such as Discrete Fourier Transform (DFT) [9] and Kalman Filter (KF) [10] generally show a slow time response and cannot track harmonic variations suitably. However, time-domain strategies, like Instantaneous Reactive Power Theory (IRPT) [11] and synchronous reference frame theory (SRFT) [12] show a better dynamic response and have effective compensation performance during different operation cases. Traditionally, Phase Lock Loops (PLL) are used to detect harmonic elements in disrupted power signals. When the voltage is unbalanced or disturbed, PLL can experience delays in phase, leading to slow reactions and potential system failures. Typically, PLL optimization involves balancing quick detection and effective filtration, which is tricky since these methods often struggle with harmonic distortions. Therefore, finding a solution that quickly tracks changes while also being resilient to harmonics is quite a challenge [13, 14].

Most of the advanced filtering control methods of DSTATCOM, such as the Least-Mean-Square algorithm (LMS) [15] and the Adaptive Notch Filter (ANF) [16] are accurate and represent appropriate dynamic responses, but introduce slow convergence speed. The authors in [17] propose the Amplitude Adaptive Notch Filter (AANF) strategy as a control system for DSTATCOM to address deficiencies in the ANF control method. This method focuses on extracting reference signals in unbalanced and distorted networks. While successful in generating reference currents, it falls short in providing a rapid and precise response to the system's dynamics. Least Error Square (LES) method is another advanced control algorithm which is identified as an effective control technique for extracting reference sinusoidal components from distorted input signals [18-21]. A fast control scheme relying on the LES filter with a fixed window length was proposed for a Dynamic Voltage Restorer (DVR) control system in [18]. The control strategy estimates the load and source voltages. A novel Software Phase-Locked Loop (SPLL) control algorithm of DVR was proposed [19] based on non-recursive LES filters and realized in the 'abc' reference frame and entails a high computational burden. Recursive Least Error Square (RLES) algorithm has been introduced in [22, 23] as a useful fast and robust algorithm because it shows acceptable convergence speed and the harmonic estimated values are updated recursively as soon as signal samples are acquired. RLES can be used in a power system with time-varying loads because these changes create different types of nonlinearity and harmonics with varying amplitudes and phase angles, and harmonic estimated values need to be updated according to the recent signal samples [24]. The accuracy and convergence speed of RLES algorithm are in proportion to the value of forgetting factor. RLES with a fixed forgetting factor fails to properly track time-varying parameters that have large oscillations. So, an adaptive approach should be incorporated in the estimation process to obtain a Variable Forgetting Factor (VFF) [25-27]. The following presents some of the recent papers that have adopted VFF in various applications of electrical engineering. Reference [28] suggests a VFF Recursive Least Squares (RLS) parameter identification approach to precisely determine the parameters used in modelling the lithium

battery in real-time. The method utilizes the terminal voltage of the system identification parameter and the measurement terminal voltage to create a window for error calculation. It then dynamically adjusts the forgetting factor based on the error, thereby enhancing the accuracy of system parameter identification through the least square method. The researchers adopted a VFF-RLS method to identify parameters and employed a mixture of covariance square root and noise statistics estimation methods so that the state of charge of batteries are obtained. This approach addressed the issue of dispersion in the unscented Kalman filter and the problem of the error covariance increasing indefinitely during iterative calculations, thereby ensuring accurate estimation of the state of charge [29]. The VFF-RLS method, as proposed in reference [30], incorporates a least square approach with forgetting factors to estimate the electrical parameters of a basic electrical model. A variable-rate forgetting factor was devised for the purpose of parameter identification in time-varying systems using recursive least squares. This factor employs the F-test to make a comparison between the variance of one-step prediction errors in the short and long terms for RLS [31]. Reference [32] proposed a methodology for parameter identification in the variable forgetting factors recursive least squares algorithm using global mean particle swarm optimization. Next, it suggested a global particle swarm optimization search mechanism that focuses on variable time double extended Kalman filtering. The contribution of this paper includes real-time realization of a developed two-layer method relying on the combination of VFF-RLES algorithm as the first layer and an algorithm for reference current extraction for the DSTATCOM control system as the second layer. In the first layer, the weights are updated using a new robust Fuzzy Inference System (FIS)-VFF-RLES algorithm. Therefore, amplitude and phase angle of the fundamental and selected harmonic terms of three-phase voltages and currents are estimated separately from the updated weights without a significant delay. In the second layer, the calculated amplitudes and phase angles help extract the current reference for DSTATCOM controller. Moreover, an Adaptive Hysteresis Band Current (AHBC) controller has been employed to produce switch signals and thus boost the dynamic performance of the DSTATCOM. The proposed control scheme allows DSTATCOM to detect and compensate harmonics with a high accuracy and appropriate convergence speed without losing the robustness against harmonics under linear and nonlinear loads. In the remaining of the paper, Section 2 introduces the DSTATCOM configuration in a three-phase four-wire distribution system. In Section 3, the suggested RLES control scheme and its formulations along with the AHBC controller are described to achieve the appropriate switching signals. In Section 4, the control system is tested to investigate the performance of the control strategy. The control design employed for DSTATCOM under different load conditions in MATLAB software is evaluated in Section 5. Finally, a conclusion is presented in the last section.

2. SYSTEM CONFIGURATION

Fig. 1 shows the layout of a 3ph 4-wire DSTATCOM with a four-leg Voltage Source Converter (VSC). As is observed, eight IGBT-based switches are turned on/off based on the control strategy of DSTATCOM. The system includes

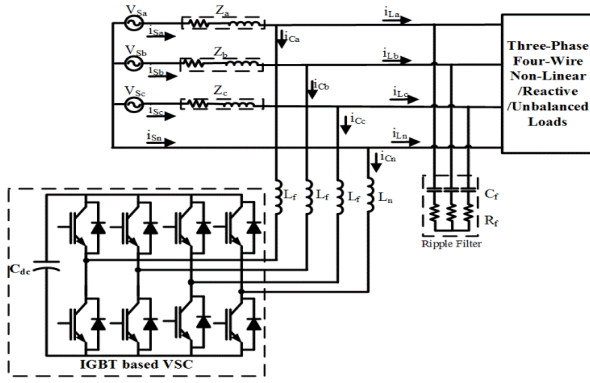


Fig. 1: Connection of a 4-wire DSTATCOM to the distribution network.

a three-phase voltage source with a source resistance (R_s) and a source inductance (L_s). A four-leg VSC with a DC-link capacitor is connected using interfacing inductors (L_f, L_n) so that high-frequency ripples are cancel out from the source currents. Three legs of the VSC are in connection with the PCC and the remaining leg is in connection with the neutral terminal of the load and source to compensate neutral current. An appropriately fixed capacitor (C_{dc}) is in joined to the DC link of the VSC to damp the transients. An RC filter (R_f, C_f) linked to PCC filters high-frequency ripples from the terminal voltage [33-35]. Various topologies exist for three-phase four-wire DSTATCOM, including the four-leg voltage source converter (VSC), capacitor midpoint VSC, and H Bridge VSC configurations. Among these, the four-leg VSC topology is selected for DSTATCOM applications due to its advantages in simplicity and reliability of control, reduced

requirement for solid-state devices, and effective neutral wire current compensation [36].

3. PROPOSED CONTROL SCHEME

3.1. Recursive Least Error Square Algorithm

For power quality purposes, an advanced amplitude, phase and frequency detecting algorithm is required to derive active and reactive components of the input signals. In general, the input signal of control system of DSTATCOM is defined as:

$$y_\alpha(t) = \sum_{i=1}^n A_{i\alpha} \sin(i\omega_0 t + \varphi_{i\alpha}) + A_{dc\alpha} e^{-\frac{t}{\tau}}; \alpha = a, b, c \quad (1)$$

where i represents the order of harmonic components, $A_{i\alpha}$ is the corresponding amplitude of each phase component, $\varphi_{i\alpha}$ is the initial angle, $e^{-\frac{t}{\tau}}$ is the dc offset term, and ω_0 is the fundamental angular frequency. The main aim of the RLES algorithm here is the estimation of the unknown parameters ($A_{i\alpha}, \varphi_{i\alpha}, A_{dc\alpha}$). The estimation must be exact and not sensitive to harmonics, inter-harmonics, and noise. In addition, the proposed RLES algorithm is able to operate under small frequency deviations on the supply side because the frequency deviation in the power system is less than 0.2 Hz, whereas the sampling frequency can be about 10 kHz. This makes the algorithm fast and reliable in the case of small frequency deviations.

Considering $y_a(t)$ as the input signal which is sampled at a preselected rate (Δt), then M samples are obtained as (2). The, (2) is written in matrix form as (3).

$$\left\{ \begin{aligned} y_a(t) &= A_{1a} \cos \varphi_{1a} \sin(\omega_0 t) + A_{1a} \sin \varphi_{1a} \cos(\omega_0 t) + \sum_{i=2}^n A_{ia} \cos \varphi_{ia} \sin(i\omega_0 t) + \sum_{i=2}^n A_{ia} \sin \varphi_{ia} \cos(i\omega_0 t) + A_{dc} - \frac{A_{dc}}{\tau} t \\ y_a(t - \Delta t) &= A_{1a} \cos \varphi_{1a} \sin \omega_0(t - \Delta t) + A_{1a} \sin \varphi_{1a} \cos \omega_0(t - \Delta t) + \sum_{i=2}^n A_{ia} \cos \varphi_{ia} \sin i\omega_0(t - \Delta t) \\ &+ \sum_{i=2}^n A_{ia} \sin \varphi_{ia} \cos i\omega_0(t - \Delta t) + A_{dc} - \frac{A_{dc}}{\tau}(t - \Delta t) \\ &\vdots \\ y_a[t - (M-1)\Delta t] &= A_{1a} \cos \varphi_{1a} \sin \omega_0[t - (M-1)\Delta t] + A_{1a} \sin \varphi_{1a} \cos \omega_0[t - (M-1)\Delta t] \\ &+ \sum_{i=2}^n A_{ia} \cos \varphi_{ia} \sin i\omega_0[t - (M-1)\Delta t] + \sum_{i=2}^n A_{ia} \sin \varphi_{ia} \cos i\omega_0(t - \Delta t) \\ &+ A_{dc} - \frac{A_{dc}}{\tau}[t - (M-1)\Delta t] \end{aligned} \right. \quad (2)$$

$$[Y_a]_{M \times 1} = [A_a]_{M \times 2n+2} \times [X_a]_{2n+2 \times 1}$$

$$[X_a] = \begin{bmatrix} A_{1a} \cos \varphi_{1a} & A_{1a} \sin \varphi_{1a} & \dots & A_{na} \cos \varphi_{na} & A_{na} \sin \varphi_{na} & A_{dc} & \frac{A_{dc}}{\tau} \end{bmatrix}$$

$$[Y_a] = [y_a(t) \quad y_a(t - \Delta t) \quad \dots \quad y_a[t - (M-1)\Delta t]]^T$$

$$[A_a] = \begin{bmatrix} \sin(\omega_0 t) & \cos(\omega_0 t) & \dots & \sin n(\omega_0 t) & \cos n(\omega_0 t) & 1 & t \\ \sin \omega_0(t - \Delta t) & \cos \omega_0(t - \Delta t) & \dots & \sin n \omega_0(t - \Delta t) & \cos n \omega_0(t - \Delta t) & 1 & t - \Delta t \\ \vdots & \vdots & \ddots & \vdots & \vdots & \vdots & \vdots \\ \sin \omega_0[t - (M-1)\Delta t] & \cos \omega_0[t - (M-1)\Delta t] & \dots & \sin n \omega_0[t - (M-1)\Delta t] & \cos n \omega_0[t - (M-1)\Delta t] & 1 & t - (M-1)\Delta t \end{bmatrix} \quad (3)$$

The solution of (3), based on the least error square method, is calculated by:

$$[X_a] = [[A_a]^T \times [A_a]]^{-1} \times [A_a]^T \times [Y_a] \quad (4)$$

To implement (4) in a recursive mode and to estimate the desired parameter by RLES algorithm, the following error function should be minimized in each iteration:

$$E(n) = \sum_{i=1}^n \{\lambda^{n-i} e^2(i)\} \quad (5)$$

where $\lambda \in (0,1]$ is the forgetting factor which adapts the parameters according to the input signal variations.

According to (5), the updated parameter vector can be found as follows:

$$\hat{A}(k) = \hat{A}(k-1) + \mu(k)e(k) \quad (6)$$

where the error is

$$e(k) = y(k) - \hat{A}^T(k-1)X(k) \quad (7)$$

The gain $\mu(k)$ is the covariance of parameter vector as:

$$\mu(k) = R(k-1)X(k)[\lambda + X^T(k)R(k-1)X(k)]^{-1} \quad (8)$$

$$R(k) = \frac{1}{\lambda} [R(k-1) - \mu(k)X^T(k)R(k-1)] \quad (9)$$

Equations (6)-(9) are estimated by the following initial values:

$\hat{X}(-1) = 0$, $R = \pi_0 I$, where R is the initial covariance matrix, π_0 is a large number, and I is a square identity matrix [22].

Note that π_0 influences the convergence gain; faster convergence can be achieved by choosing a larger π_0 . The convergence speed and tracking capability of RLES algorithm are directly related to the initial values and the forgetting factor (λ). Forgetting factor highly impacts the estimation speed of RLES algorithm and the proper value is chosen considering the convergence speed and tracking capability [25]. A smaller value of λ leads to a faster estimation speed, however, inappropriate tracking capability. On the other hand, a larger value of λ (close to 1) represents an appropriate tracking capability with the reduced convergence speed. Consequently, this problem can be addressed by a time-varying adaptive control method for the selection of forgetting factor during both steady-state and dynamic situations where the system parameters are changed abruptly. Since FIS theory does not rely on the mathematical formulation of the object to be controlled, and is robust than the traditional control methods, a FIS-based VFF (λ) is developed in this paper and an appropriate forgetting factor is chosen by a FIS so that higher convergence rate and lower steady-state oscillation are achieved.

Here, the squared error $e^2(k)$ and its variation $\Delta e^2(k) = |e^2(k) - e^2(k-1)|$ are considered as input variables of the fuzzy logic control system at the k th iteration and $\lambda = FIS[e^2(k), \Delta e^2(k)]$ is considered as the

output. Four triangle Membership Functions (MFs), Very Large (VL), Large (L), Medium (M), and Small (S), are selected as the input and output variables (Fig. 2). A set of fuzzy IF-THEN rules are established in Table 1 which come from a combination of a small value of λ during transient conditions (for the improvement of the RLES estimation speed) and a fixed (near to 1) in steady state conditions.

The MFs of the input and output variables are chosen in a way that they are not influenced by the noise of the input signal. In general, MFs of the proposed FIS-VFF is tuned based on the fast transient performance, steady state response, and noise rejection capability. The suggested method allows for the efficient and accurate estimation of frequency components in the observed signal, adapting to changes in frequency both during steady-state and transient circumstances.

Having updated unknown parameter vectors using the proposed algorithm, the amplitude and phase angle of each harmonic component is evaluated as follows:

$$\begin{cases} A_i = \sqrt{(A_i \cos \varphi_i)^2 + (A_i \sin \varphi_i)^2} \\ \varphi = \arctan(A_i \sin \varphi_i, A_i \cos \varphi_i) \end{cases} \quad (10)$$

The main term of the input signal can be represented as

$$y_1 = A_1 \sin \varphi_1 \quad (11)$$

For simplification of the proposed algorithm, only fundamental, fifth, and seventh harmonic terms are considered in the calculations.

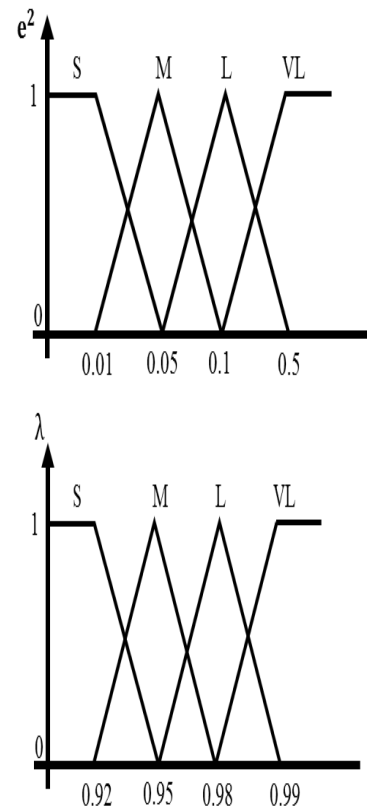


Fig. 2: The MFs of inputs and output.

TABLE 1: Fuzzy decision table.

| Δe^2 | S | M | L | VL | |
|--------------|----|----|----|----|---|
| e^2 | S | VL | VL | VL | L |
| | M | L | L | M | M |
| | L | M | M | S | S |
| | VL | S | S | S | S |

Subsequent harmonic elimination/extraction and subsequent harmonic analysis are both possible with the assistance of this algorithm, which ensures the rapid and accurate extraction of individual harmonics. Furthermore, this structure is insensitive to different load and grid conditions, and does not require any synchronizing tools such as PLL.

3.2. Proposed Compensation Strategy

The inputs to this section are the calculated amplitude and phase angle of the fundamental components of the measured voltage and current which are calculated by the VFF-RLES in Section 3.1.

The fundamental component of line current, $i_b(t)$, is divided into active current, $i_{ba}(t)$ and the reactive current, $i_{br}(t)$:

$$i_b(t) = i_{ba}(t) + i_{br}(t) \quad (12)$$

Equation (13) expresses the active and reactive currents of (12):

$$\begin{cases} i_{ba}(t) = I_m \cos(\varphi_i - \varphi_v) \cdot \sin(\varphi_v) \\ i_{br}(t) = I_m \sin(\varphi_i - \varphi_v) \cdot \cos(\varphi_v) \end{cases} \quad (13)$$

where I_m is the amplitude of $i_b(t)$, φ_i is the total phase angle of $i_b(t)$, and φ_v represents the total phase angle of the fundamental component of relative phase-to-ground voltage. By re-arranging (13) for three phases:

$$\begin{cases} i_{aa}(t) = [I_{ma} \cos(\varphi_{ia}) \cdot \cos(\varphi_{va}) + I_{ma} \sin(\varphi_{ia}) \cdot \sin(\varphi_{va})] \cdot \sin(\varphi_{va}) \\ i_{ab}(t) = [I_{mb} \cos(\varphi_{ib}) \cdot \cos(\varphi_{vb}) + I_{mb} \sin(\varphi_{ib}) \cdot \sin(\varphi_{vb})] \cdot \sin(\varphi_{vb}) \\ i_{ac}(t) = [I_{mc} \cos(\varphi_{ic}) \cdot \cos(\varphi_{vc}) + I_{mc} \sin(\varphi_{ic}) \cdot \sin(\varphi_{vc})] \cdot \sin(\varphi_{vc}) \end{cases} \quad (14)$$

and:

$$\begin{cases} i_{ra}(t) = [I_{ma} \sin(\varphi_{ia}) \cdot \cos(\varphi_{va}) - I_{ma} \cos(\varphi_{ia}) \cdot \sin(\varphi_{va})] \cdot \cos(\varphi_{va}) \\ i_{rb}(t) = [I_{mb} \sin(\varphi_{ib}) \cdot \cos(\varphi_{vb}) - I_{mb} \cos(\varphi_{ib}) \cdot \sin(\varphi_{vb})] \cdot \cos(\varphi_{vb}) \\ i_{rc}(t) = [I_{mc} \sin(\varphi_{ic}) \cdot \cos(\varphi_{vc}) - I_{mc} \cos(\varphi_{ic}) \cdot \sin(\varphi_{vc})] \cdot \cos(\varphi_{vc}) \end{cases} \quad (15)$$

In addition, the amplitude of phase voltage (V_i), in-phase unit templates (u_{ap}, u_{bp}, u_{cp}), and quadrature unit templates (u_{aq}, u_{bq}, u_{cq}) are evaluated by the fundamental component of PCC voltage driven by the RLES algorithm [37, 38]. According to reference [39], the angle φ itself is a function of t , but in the article, to avoid lengthening the equations, we only mention it with the symbol (φ).

The proposed RLES algorithm can be incorporated in many operation states of the DSTATCOM, like power factor modification, zero-voltage adjustment, load equilibrium, and current harmonic removal.

3.3. Power Factor Correction (PFC) operation of DSTATCOM

The compensatory method for the PFC operation involves injecting the average active term of the load current, besides the active power term, so that the magnitude of the DC bus voltage is adjusted to the desired magnitude.

The active power term of the load current should have an identical amplitude across all phases. This can be determined using (14) to ensure imbalances are cancelled out from the reference source currents. The mean magnitude of the active term of load currents will be calculated as:

$$I_{ad}(t) = (i_{aa}(t) + i_{ab}(t) + i_{ac}(t))/3 \quad (16)$$

A self-supporting DC bus capacitor is in connection with the DC side of the VSC and its voltage controlled by a PI controller to compensate for active power losses in the DSTATCOM. The output of PI (proportional– integral) controller of the dc bus voltage of the DSTATCOM is taken as the loss term of the current (I_{loss}).

The magnitude of the reference source active current is determined via summing the fundamental active power term of the load currents with the current's loss term:

$$I_{as}(t) = I_{ad}(t) + I_{loss} \quad (17)$$

The magnitude of reference source currents is multiplied by in-phase unit templates to produce the instantaneous reference source currents:

$$i_{sap}^* = I_{as} * u_{ap}, i_{sbp}^* = I_{bs} * u_{bp}, i_{scp}^* = I_{cs} * u_{cp} \quad (18)$$

These generated reference active source current components are in-phase with the phase voltages for power factor correction operation. Thereby, the reactive power demand of the load is fully fed via the DSTATCOM.

3.4. Zero Voltage Regulation (ZVR) operation of DSTATCOM

The compensatory approach for the ZVR operation assumes that the source provides equivalent active current components in addition to the total of reactive current components, which is evaluated by (15), and the component found from a PI controller (I_{vt}) utilized for adjusting the voltage at PCC. The magnitude of AC terminal voltage (V_t) at the PCC's voltage is regulated to the reference voltage (V_t^*) by the PI controller.

The average amplitude of the reactive power term of the load currents will be obtained as:

$$I_{rq}(t) = (i_{ra}(t) + i_{rb}(t) + i_{rc}(t))/3 \quad (19)$$

In addition, the output of the PI controller of the PCC voltage is the reactive power term used for regulating the PCC voltage at the load terminals.

The calculation for determining the total reactive current term of the reference source currents involves deducting the average fundamental reactive current term from the reactive power component:

$$I_{rs}(t) = -I_{rq}(t) + I_{vt}(t) \quad (20)$$

The reference reactive source current components which are in quadrature with the three phase voltages are estimated as:

$$i_{saq}^* = I_{rs} * u_{aq}, i_{sbq}^* = I_{rs} * u_{bq}, i_{scq}^* = I_{rs} * u_{cq} \quad (21)$$

Finally, the reference source currents are expressed by summing the active and reactive reference terms of the source currents for each of the three phases:

$$\begin{aligned} i_{sa}^* &= i_{sap}^* + i_{saq}^*, i_{sb}^* = i_{sbp}^* + i_{sbq}^*, i_{sc}^* \\ &= i_{scp}^* + i_{scq}^* \end{aligned} \quad (22)$$

The reference current for the source neutral current is assumed zero:

$$i_{sn}^* = 0 \quad (23)$$

A comparison is made between the derived reference source currents ($i_{sa}^*, i_{sb}^*, i_{sc}^*$) and the corresponding measured source currents (i_{sa}, i_{sb}, i_{sc}), where the error is applied to the current controller to produce the gate signals for the DSTATCOM switches.

Fig. 3 shows the compensation strategy.

3.5. Switching Algorithm

Fig. 2 compares the measured source currents (i_{sa}, i_{sb}, i_{sc}) and the estimated reference source currents ($i_{sa}^*, i_{sb}^*, i_{sc}^*$), where the error signals are applied to the adaptive hysteresis band current controller to produce the gating signals for insulated gate bipolar transistor (IGBT) switches of the VSC-based DSTATCOM.

The hysteresis band current control technology has been extensively adopted for active power filters. The hysteresis band current control exhibits inherent stability,

rapid response, and high precision. However, the standard hysteresis technique also has various drawbacks, including an asymmetrical switching frequency that results in acoustic noise and additional switching losses. Narrow bandwidth results in a fast and fairly tracking of currents, while significantly raising the switching frequency. A wide bandwidth also does not offer an accurate tracking and may cause instability. To avoid these drawbacks, a system is equipped with an adjustable hysteresis band. This enables the hysteresis band to be adjusted based on the system characteristics so that a nearly constant switching frequency is preserved.

For almost constant switching frequency, the hysteresis band will be:

$$HB = \frac{V_{dc}}{8 \cdot f_c \cdot L_f} \left[1 - \frac{4L^2}{V_{dc}^2} \left(\frac{V_s(t)}{L_f} + m \right)^2 \right] \quad (24)$$

where f_c is the modulation frequency and $m = \frac{di_{sa}^*}{dt}$ shows the slope of command current wave. Adaptive hysteresis band changes the hysteresis bandwidth (HB) based on the modulation frequency, supply voltage, dc capacitor voltage, and slope of the source reference current. Moreover, modulation can be applied to it to manage the switching scheme of the inverter [40, 41].

Power circuit parameters including DC bus voltage, AC inductors, and the VSC in three-phase four-leg DSTATCOM are given in Appendix and selected based on [41-44] with respect to the system configuration.

4. PERFORMANCE EVALUATION

By means of computer simulations carried out inside the MATLAB/Simulink environment, this part evaluates the

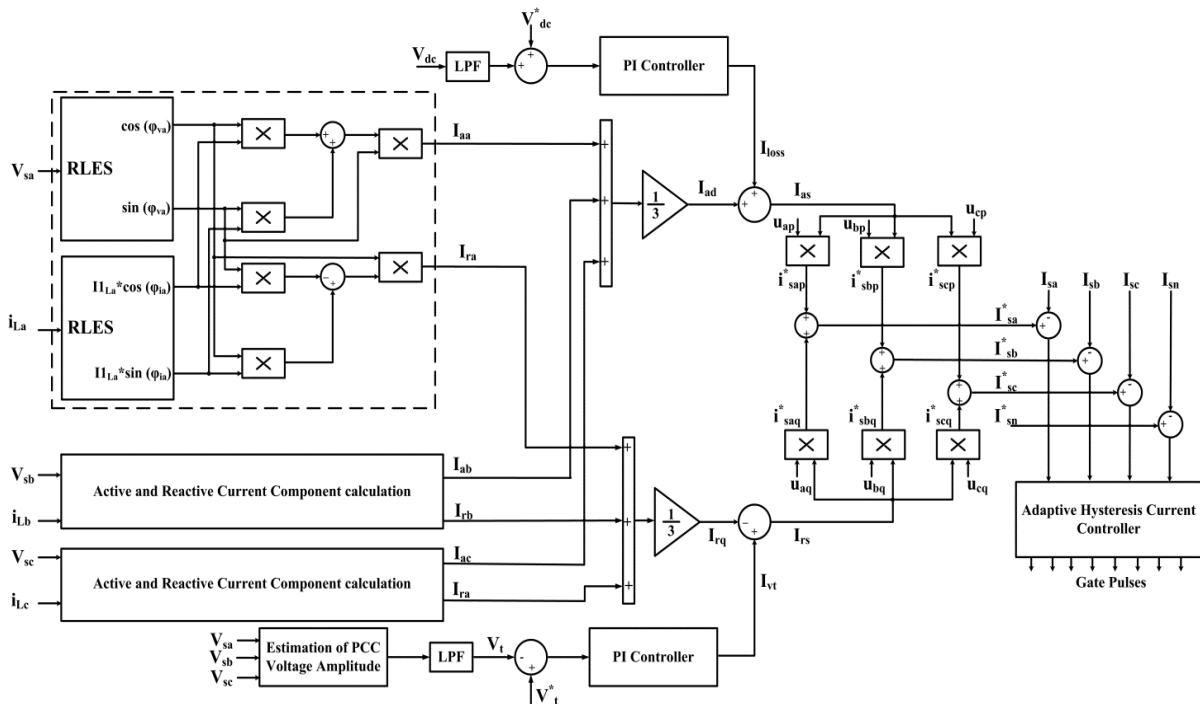


Fig. 3: Schematic diagram of the compensation strategy.

efficacy of the control method suggested for DSTATCOM. In this section, the tracking capability and harmonic removal potential of the suggested RLES are examined. Additionally, the performance of the entire system with regard to load equilibrium, harmonic removal, neutral current compensation, and power factor modification are discussed in Section 5.

4.1. Initial Performance

The input signal of the RLES is assumed as (25):

$$y(t) = \sin(\omega_0 t + \varphi_1) + 0.2 \sin(5\omega_0 t + \varphi_5) + 0.3 \sin(7\omega_0 t + \varphi_7) + 0.3 \sin(30\omega_0 t + \varphi_{30}) \quad (25)$$

where $\omega_0 = 100\pi$ rad/s and the initial phase angles φ_i 's are chosen in a random process in the range of 0 and 2π rad. The system's response to the input signal of (25), i.e., four extracted signals including the fundamental, the fifth, and the seventh harmonic terms, are shown in Fig. 4.

4.2. Harmonic Detection Capability

In this section, the proposed structure is used to track and extract harmonic components of an input signal as follows:

$$y(t) = \sin(\omega_0 t + \varphi_1) + 0.3 \sin(5\omega_0 t + \varphi_5) + 0.2 \sin(7\omega_0 t + \varphi_7) \quad (26)$$

A step change of (-0.2 pu) in the amplitude of the fundamental and the 5th harmonic component, and (+ 0.2 pu) in the amplitude of the 7th harmonic at $t = 0.2$ s with comparison between fixed forgetting factor RLES and the proposed RLES algorithms are considered. As it is shown in Figs. 5 and 6, both schemes track the step changes of the fundamental, the 5th and the 7th components amplitudes and phase angles, and compared to the fixed forgetting factor RLES scheme, proposed RLES performs satisfactorily with regard to tracking the changes of amplitude of the fundamental component of the input signal during transient condition.

5. ANALYTICAL STUDIES AND DISCUSSION

To modify power factor correction, regulate voltage, remove harmonic terms, balance the load, and compensate neutral current, the performance of the three-phase four-leg DSTATCOM is demonstrated by utilizing the proposed RLES-based control design. In this study, the model is examined in four distinct scenarios, each of which involves linear and non-linear load circumstances. Four different worst possible conditions are discussed in this section. Voltage source is unbalanced and distorted and unbalanced linear and non-linear loads are presented to survey the performance DSTATCOM with RLES-based control algorithm.

5.1. PFC Operation of DSTATCOM During Linear Lagging Power Factor Load (Case A)

The power factor correction and load balancing operation of the suggested RLES-based control algorithm

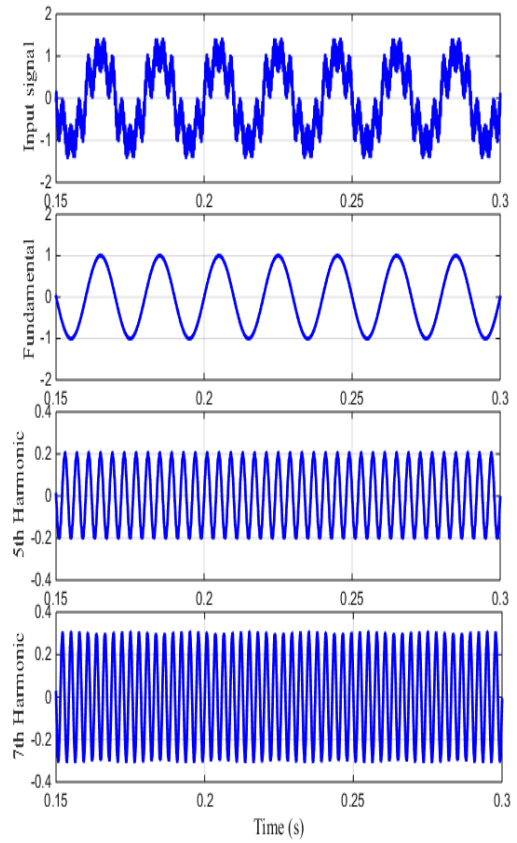


Fig. 4: The input signal and its fundamental, 5th and 7th harmonic components of the input signal using proposed RLES

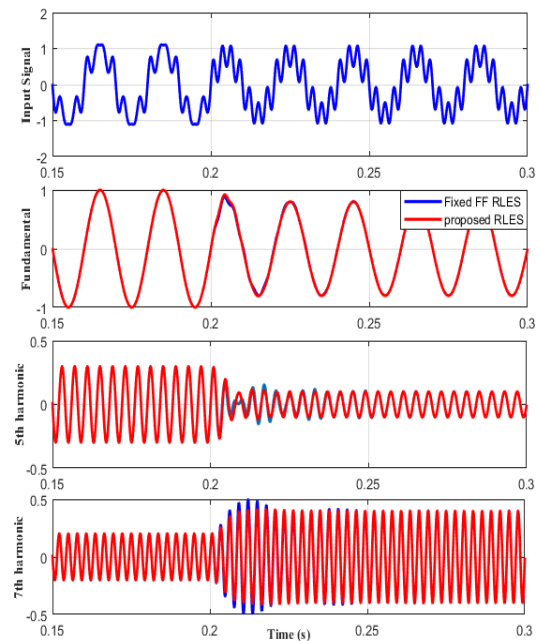


Fig. 5: Amplitude tracking changes of the fundamental, 5th and 7th harmonic components.

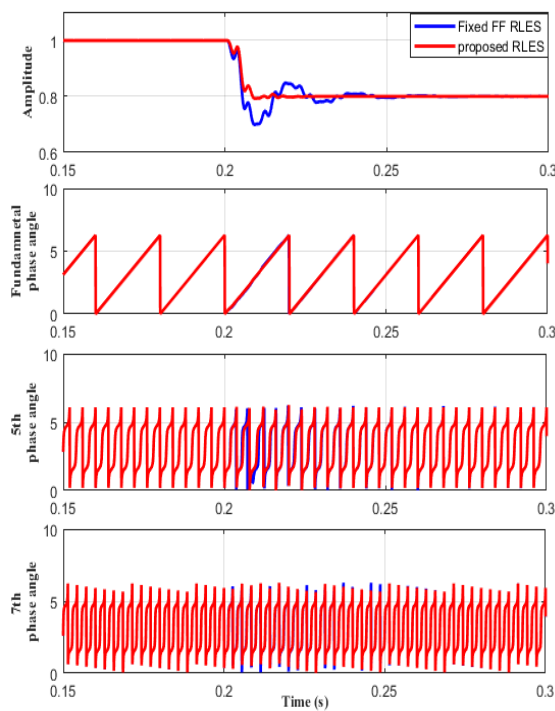


Fig. 6: Amplitude and phase tracking changes of fundamnetal, fifth and seventh harmonic terms.

of the four-leg DSTATCOM are described in this subsection. At $t = 0.4$ and $t = 0.5$ s, phases 'A' and 'B' are disconnected, respectively, and at $t = 0.7$ s and $t = 0.8$ s, phases 'A' and 'B' are reconnected. Fig. 7 displays the three-phase source voltage (v_{source}), load currents (i_{load}), compensating currents ($i_{DSTATCOM}$), source currents (i_{source}), and DC bus voltage (V_{dc}). It is observed that after $t = 0.4$ s, DSTATCOM injects currents in order to maintain three phase source currents balanced in spite of unbalancing in the load currents. As a result, three phase source currents appear balanced and DC bus voltage is fixed at almost its reference value even in unbalanced conditions. It shows the function of DSTATCOM for load balancing and also observed the fast action of RLES during sudden load injection. Fast action of RLES algorithm can be seen at a time of load injection in the estimation of reference supply current with other signals. Just at the time of load injection, nature of DSTATCOM current is changed quickly which validates the fast action of this proposed control method. These results show satisfactory performance of the proposed control algorithm used in DSTATCOM for reactive power compensation and harmonics suppression under linear and nonlinear loads respectively.

Figs. 8 and 9 show reactive power compensation performance and the neutral current elimination of the proposed control method, respectively. Simultaneously, DSTATCOM compensates for the reactive current of the load, modifies power factor, and removes zero-sequence current terms. It is observed that although the power factor of the load is about 0.8, the source side power factor is maintained equal to unit and the supply voltages and currents are in-phase. DSTATCOM also injects compensation currents so that the source-side neutral current is maintained near zero.

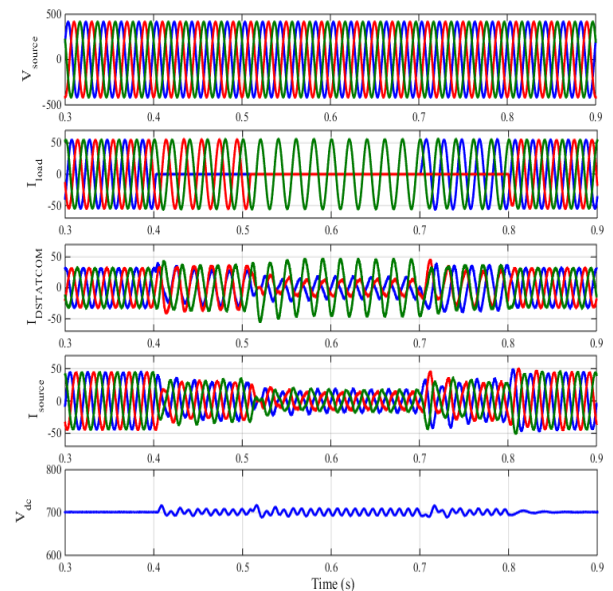


Fig. 7: DSTATCOM performance for load current balancing in Case A.

5.2. ZVR Operation of DSTATCOM During Linear Lagging Power Factor Load (Case B)

Fig. 10 shows the ZVR performance of DSTATCOM for linear unbalanced load operation. In this mode, the magnitude of load terminal voltage is adjusted to the desired value. The performance indices are as load currents (i_{load}), compensator currents ($i_{DSTATCOM}$), source currents (i_{source}), magnitude of voltages at the PCC (V_{PCC}), and DC-link voltage (V_{dc}) when time-varying linear loads are present. This figure shows the balanced source currents at PCC and its smooth change over when load currents are not balanced. It means that during load dynamics, the reference source currents generated through control algorithm are exactly follow the sensed source currents. It shows almost balanced supply currents when load currents are unbalanced. These results show satisfactory performance of the RLES used in DSTATCOM for load balancing under non-linear loads in voltage regulation mode. The source current is made balanced and the PCC voltage range and the DC-bus voltage remain almost close to the reference values. The power factor on supply side is leading as the terminal voltage is regulated by the DSTATCOM. It is observed that PCC voltage is regulated near to rated value. In this mode, supply currents are slightly leading with respective voltages because extra leading reactive power is required to regulate PCC voltages. These results demonstrate satisfactory performance of the control algorithm used for PCC voltage regulation with harmonics elimination in DSTATCOM under nonlinear load.

5.3. PFC Operation of DSTATCOM During Nonlinear Load (Case C)

Fig. 11 illustrates the dynamic operation of the suggested control algorithm for DSTATCOM in the PFC operation during non-linear load condition. The load unbalancing situation is realized by disconnecting phases 'A' (during $t = 0.4$ s to 0.7 s) and 'B' loads (during $t = 0.5$ s to

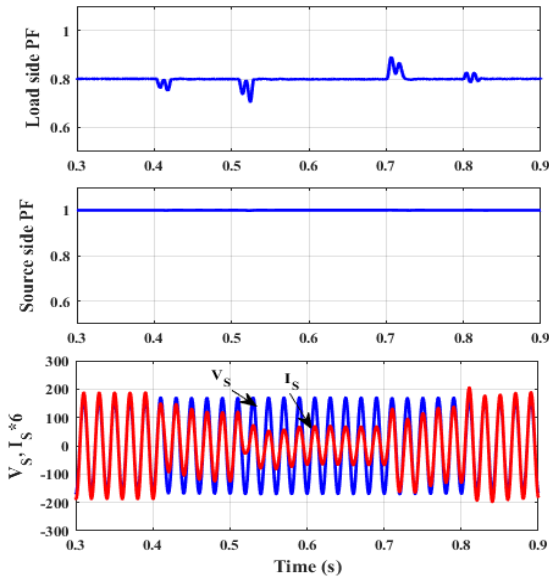


Fig. 8: DSTATCOM performance for power factor correction in Case A.

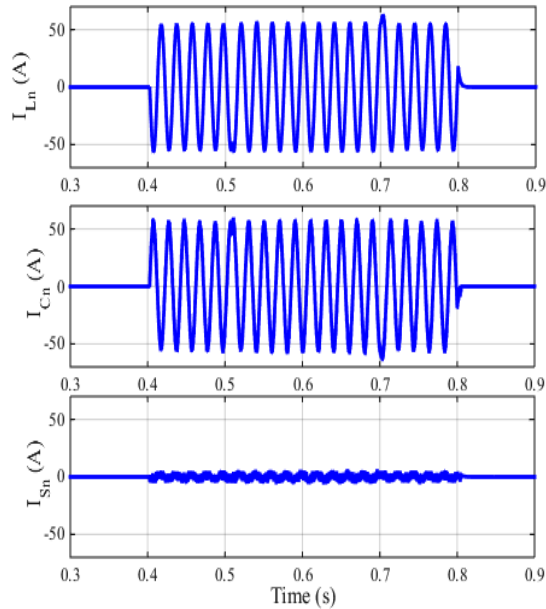


Fig. 9: DSTATCOM performance for neutral current compensation in Case A.

0.8s). DSTATCOM injects compensating currents such that the three-phase source currents are balanced and without harmonics. It demonstrates sinusoidal balanced source currents, despite load currents being unbalanced and distorted. Also, it demonstrates the fast characteristics of the suggested control design in the case the two phases of the load are disconnected. These simulation findings confirm the functionalities of DSTATCOM for power factor modification and load balancing, as well as harmonic correction under varied non-linear loads. They also demonstrate that the control algorithm is capable of performing its tasks effectively. The operation indicators for this case are three phase load currents (i_{load}), compensating currents ($i_{DSTATCOM}$), balanced sinusoidal

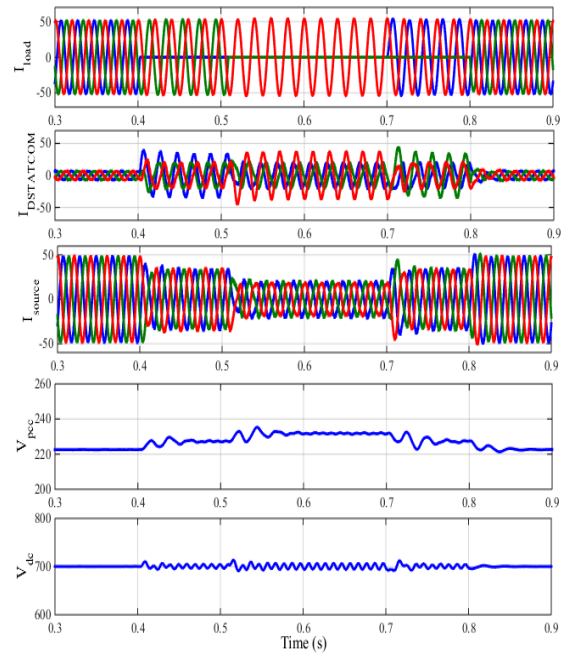


Fig. 10: DSTATCOM performance for load equilibrium and zero-voltage adjustment in Case B.

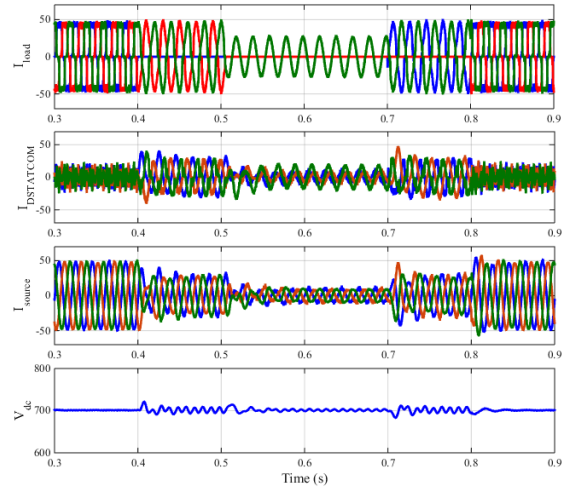


Fig. 11: DSTATCOM performance for load current balancing and harmonic compensation in Case C.

source currents (i_{source}), and DC link voltage (V_{dc}). It is shown that the dc bus voltage (V_{dc}) is maintained to the reference dc bus voltage of 700 V. For a better observation of the DSTATCOM performance of harmonic compensation in case C, the THD% of the load current, and the source current in phase 'A' for the PFC operation of DSTATCOM can be observed in Figs. 12 and 13, respectively. The source current THD is 3.27% while the THD% of phase 'A' load current is 24.27%. Furthermore, by checking phase 'A' PCC voltage (V_{sa}) and the corresponding source current (i_{sa}) in Fig. 14, one can see that both are in-phase and the source power factor is fixed to 1, thus proving the suitable PFC operation mode of DSTATCOM under load dynamics.

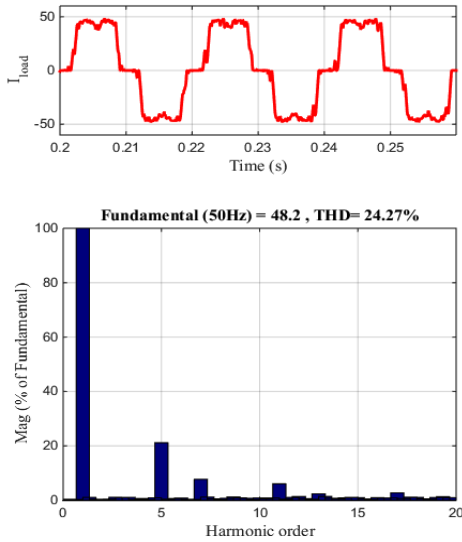


Fig. 12: THD% of load current in Case C.

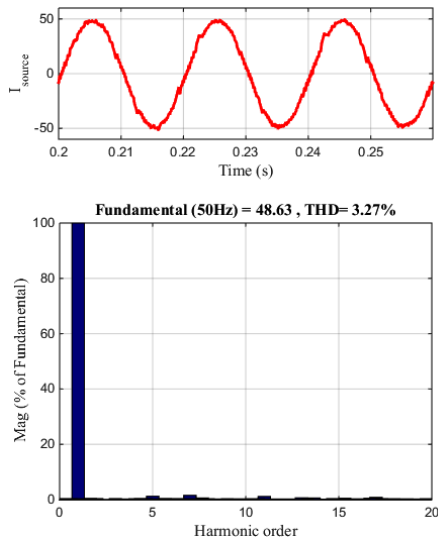


Fig. 13: THD% of source current in Case C.

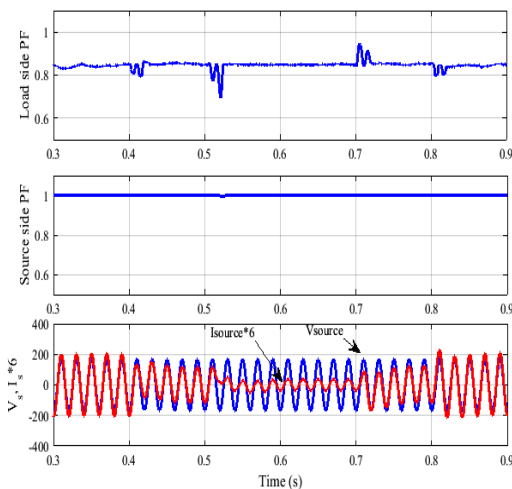


Fig. 14: DSTATCOM performance for power factor correction in Case C.

5.4. ZVR Operation of DSTATCOM for Nonlinear Loads (Case D)

Fig. 15 illustrates the dynamic behaviour of the proposed control theory for four-leg VSC based DSTATCOM employed for load balancing, harmonics current elimination, voltage regulation, and neutral current compensation under non-linear load condition. In the ZVR mode, the operation indicators for dynamic performance are load currents (i_{load}), compensator currents ($i_{DSTATCOM}$), source currents (i_{source}), magnitude of PCC voltage (V_{PCC}), and DC-link voltage (V_{dc}). In this case, source currents become balanced and perfectly sinusoidal. It also shows the appropriate performance of DSTATCOM in neutral current compensation. Furthermore, the magnitude of PCC voltage (V_{PCC}) is adjusted to the reference value by supplying reactive power. These results show satisfactory performance of the proposed control algorithm in four-leg DSTATCOM for its multi-functions such as reactive power compensation, harmonics suppression and neutral current compensation under non-linear loads, respectively.

In this paper, one of the powerful and famous optimization algorithms (e.g. Genetic Algorithm) is applied for precise calculation of optimized coefficients (PI gains) and accurate comparison between PI and Fuzzy controllers. In the first step individuals with random chromosomes are generated that set up the initial population. In this step, initial population of 20, 50 100 are used and compared which the solutions are similar. Furthermore, integral time absolute error (ITAE) criterion is employed to find the optimum PI controller gains. The new PI coefficients, calculated in these ways, are implemented in controller to demonstrate the improvement of convergence speed, reduction of error, the overshoot in capacitor voltage and other circuit parameters.

Fig. 16 depicts the DSTATCOM operation for neutral current compensation in ZVR operation. Load neutral current (i_{Ln}), injected DSTATCOM neutral current (i_{Cn}), and source neutral current (i_{Sn}) are depicted in this figure, which shows the appropriate operation of DSTATCOM in neutral current compensation.

Fig. 17 demonstrates the harmonics spectra and waveforms of phase 'A' source current. THDs % of phase 'A' at source current is equal to 1.98%.

The waveforms demonstrate that even following the compensation, the mains currents remain sinusoidal. The results demonstrate the effective performance of the suggested algorithm as a control method for load balancing, reactive power compensation, and harmonic removal of both linear and nonlinear loads.

A comparison in terms of THD% between RLES and LES algorithm is done in for case D. It can be seen from Table 2 that RLES algorithm perform more successful than LES algorithm during transients.

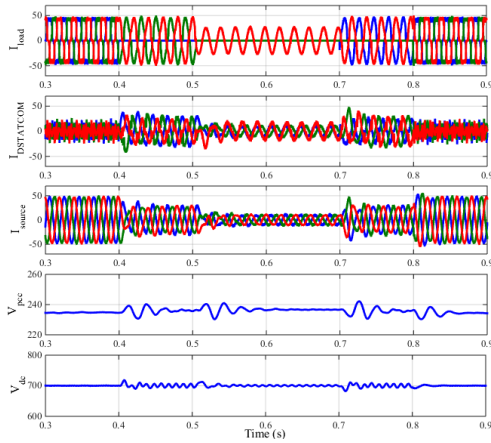


Fig. 15: DSTATCOM performance for load balancing, harmonic compensation and zero voltage regulation in Case D.

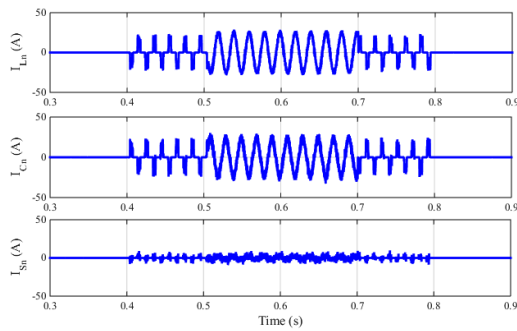


Fig. 16: DSTATCOM performance for neutral current compensation in Case D.

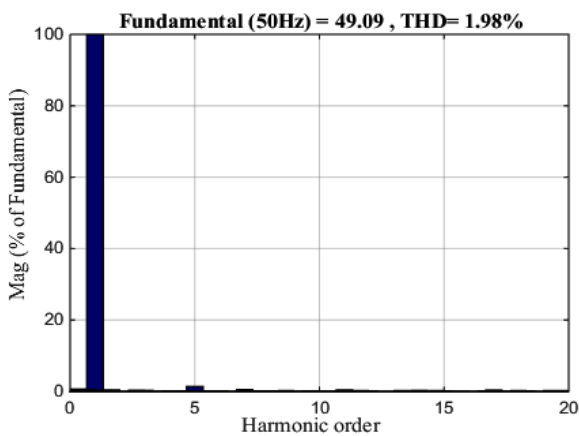
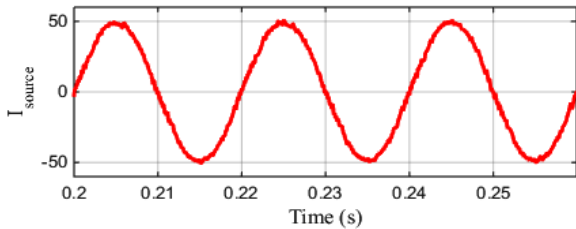


Fig. 17: THD% of source current in Case D.

Table 2: Comparison of RLES and LES algorithms in terms of THD%.

| Three phases | THD% of source currents ($0.4 < t < 0.5$) | |
|--------------|---|---------------|
| | RLES algorithm | LES algorithm |
| Phase A | 4.21% | 4.72% |
| Phase B | 3.4% | 4.43% |
| Phase C | 3.48% | 4.15% |

To survey the load and source currents and comparison of using different controllers in terms of harmonic components and THD% value, harmonic measurements are performed based on the IEEE Std. 519-2014 [45] by measuring harmonics in a considerably short period. The assessment of very short time harmonics is performed during a 3-second period by aggregating 15 successive 10-cycle windows for power systems operating at a frequency of 50 Hz. The aggregation of individual frequency components is performed by applying *rms* calculation, as depicted in Equation (27). In this equation, F represents the rms value of voltage or current, n indicates the harmonic order, and i shows a basic counter. The subscript "vs" is utilized to indicate "very short" [43]. Table 3 shows the results for harmonic orders up to 50. The THD percentage values are found based on these harmonic orders.

$$F_{n,vs} = \sqrt{\frac{1}{15} \sum_{i=1}^{15} F_{n,i}^2} \quad (27)$$

Table 3 illustrates the three-phase load currents and source currents with a comparison of the conventional hysteresis current controller, adaptive hysteresis band current controller, fixed forgetting factor RLES control strategy and the suggested RLES control strategy. According to the findings, the DSTATCOM with the presented RLES control strategy along with an adaptive hysteresis band current controller outperforms their counterparts when THD% values are considered.

6. CONCLUSION

The research presented a novel control scheme for DSTATCOM integration, focusing on a two-layer approach for enhanced power system performance. The first layer introduced a Recursive Least Error Square (RLES) algorithm, refined by a newly designed Fuzzy Inference System-Variable Forgetting Factor (FIS-VFF). This layer efficiently estimated fundamental and select harmonic components of three-phase voltages and currents. The second layer utilized these estimations to derive reference source currents for a three-phase four-wire DSTATCOM system. The contributions are significant for several reasons. The proposed scheme exhibited exceptional speed and accuracy in response to dynamic changes in power systems, confirming its suitability for real-world applications. Through simulation, the THD% in supply current was significantly reduced, aligning with IEEE-519

Table 3: The harmonic measurements result for load a source current.

| harmonics measurement in a very short period based on the IEEE Std 519-2014 | | | | | | | | | | | | | | | |
|---|--------------|---------|---------|--|---------|---------|--------------------------------|---------|---------|------------------------------------|---------|---------|--------------------------------|---------|---------|
| Harmonic order | Load current | | | Source current | | | | | | | | | | | |
| | | | | The proposed variable forgetting factor RLES | | | | | | Fixed forgetting factor RLES | | | | | |
| | | | | Conventional Hysteresis controller | | | Adaptive Hysteresis controller | | | Conventional Hysteresis controller | | | Adaptive Hysteresis controller | | |
| | Phase A | Phase B | Phase C | Phase A | Phase B | Phase C | Phase A | Phase B | Phase C | Phase A | Phase B | Phase C | Phase A | Phase B | Phase C |
| 1 | 100.00 | 100.00 | 100.00 | 100.00 | 100.00 | 100.00 | 100.00 | 100.00 | 100.00 | 100.00 | 100.00 | 100.00 | 100.00 | 100.00 | 100.00 |
| 2 | 0.11 | 0.12 | 0.16 | 0.09 | 0.06 | 0.04 | 0.62 | 0.50 | 0.39 | 0.08 | 0.10 | 0.09 | 0.55 | 0.50 | 0.80 |
| 3 | 0.16 | 0.06 | 0.15 | 0.02 | 0.07 | 0.03 | 0.02 | 0.03 | 0.08 | 0.16 | 0.02 | 0.08 | 0.04 | 0.06 | 0.02 |
| 4 | 0.12 | 0.14 | 0.23 | 0.03 | 0.06 | 0.07 | 0.14 | 0.12 | 0.20 | 0.05 | 0.06 | 0.14 | 0.26 | 0.16 | 0.16 |
| 5 | 20.75 | 20.72 | 20.61 | 1.19 | 1.22 | 1.16 | 0.68 | 0.72 | 0.69 | 1.21 | 1.22 | 1.25 | 0.63 | 0.68 | 0.78 |
| 6 | 0.17 | 0.23 | 0.21 | 0.04 | 0.04 | 0.11 | 0.03 | 0.07 | 0.02 | 0.03 | 0.06 | 0.03 | 0.06 | 0.05 | 0.05 |
| 7 | 8.65 | 8.53 | 8.69 | 0.56 | 0.59 | 0.63 | 0.36 | 0.38 | 0.38 | 0.60 | 0.63 | 0.60 | 0.34 | 0.60 | 0.39 |
| 8 | 0.08 | 0.14 | 0.14 | 0.07 | 0.13 | 0.13 | 0.21 | 0.20 | 0.14 | 0.02 | 0.07 | 0.08 | 0.13 | 0.22 | 0.19 |
| 9 | 0.23 | 0.06 | 0.20 | 0.06 | 0.03 | 0.05 | 0.04 | 0.05 | 0.02 | 0.11 | 0.05 | 0.08 | 0.03 | 0.03 | 0.04 |
| 10 | 0.21 | 0.19 | 0.28 | 0.06 | 0.04 | 0.07 | 0.12 | 0.17 | 0.22 | 0.02 | 0.09 | 0.03 | 0.25 | 0.15 | 0.18 |
| 11 | 6.11 | 6.19 | 6.00 | 0.63 | 0.57 | 0.55 | 0.65 | 0.64 | 0.70 | 0.63 | 0.63 | 0.65 | 0.74 | 0.77 | 0.61 |
| 12 | 0.18 | 0.21 | 0.25 | 0.05 | 0.03 | 0.12 | 0.01 | 0.08 | 0.09 | 0.05 | 0.07 | 0.03 | 0.09 | 0.04 | 0.04 |
| 13 | 3.40 | 3.21 | 3.42 | 0.11 | 0.15 | 0.09 | 0.07 | 0.07 | 0.15 | 0.10 | 0.13 | 0.17 | 0.11 | 0.20 | 0.09 |
| 14 | 0.23 | 0.17 | 0.06 | 0.05 | 0.03 | 0.05 | 0.12 | 0.13 | 0.05 | 0.04 | 0.09 | 0.02 | 0.06 | 0.08 | 0.14 |
| 15 | 0.12 | 0.14 | 0.16 | 0.04 | 0.09 | 0.03 | 0.04 | 0.03 | 0.08 | 0.07 | 0.02 | 0.08 | 0.04 | 0.05 | 0.05 |
| 16 | 0.25 | 0.16 | 0.26 | 0.06 | 0.15 | 0.04 | 0.05 | 0.07 | 0.09 | 0.06 | 0.07 | 0.12 | 0.12 | 0.03 | 0.09 |
| 17 | 2.88 | 3.00 | 2.80 | 0.48 | 0.48 | 0.44 | 0.49 | 0.49 | 0.53 | 0.55 | 0.54 | 0.52 | 0.56 | 0.52 | 0.49 |
| 18 | 0.13 | 0.13 | 0.26 | 0.06 | 0.04 | 0.06 | 0.08 | 0.09 | 0.09 | 0.04 | 0.03 | 0.07 | 0.07 | 0.07 | 0.05 |
| 19 | 1.58 | 1.49 | 1.54 | 0.14 | 0.14 | 0.12 | 0.13 | 0.07 | 0.05 | 0.11 | 0.13 | 0.14 | 0.12 | 0.11 | 0.08 |
| 20 | 0.24 | 0.09 | 0.18 | 0.05 | 0.02 | 0.06 | 0.18 | 0.17 | 0.08 | 0.04 | 0.03 | 0.04 | 0.09 | 0.11 | 0.11 |
| 21 | 0.16 | 0.11 | 0.08 | 0.05 | 0.13 | 0.03 | 0.05 | 0.04 | 0.03 | 0.05 | 0.07 | 0.07 | 0.03 | 0.01 | 0.08 |
| 22 | 0.23 | 0.07 | 0.18 | 0.06 | 0.07 | 0.05 | 0.11 | 0.07 | 0.14 | 0.10 | 0.03 | 0.05 | 0.18 | 0.12 | 0.13 |
| 23 | 1.63 | 1.56 | 1.45 | 0.51 | 0.46 | 0.48 | 0.39 | 0.36 | 0.48 | 0.47 | 0.49 | 0.55 | 0.40 | 0.43 | 0.36 |
| 24 | 0.06 | 0.20 | 0.18 | 0.04 | 0.03 | 0.04 | 0.06 | 0.02 | 0.10 | 0.07 | 0.07 | 0.12 | 0.08 | 0.07 | 0.03 |
| 25 | 1.11 | 1.22 | 1.13 | 0.22 | 0.23 | 0.26 | 0.23 | 0.19 | 0.21 | 0.24 | 0.26 | 0.27 | 0.34 | 0.21 | 0.26 |
| 26 | 0.08 | 0.16 | 0.13 | 0.04 | 0.01 | 0.02 | 0.16 | 0.09 | 0.03 | 0.04 | 0.05 | 0.03 | 0.15 | 0.21 | 0.13 |
| 27 | 0.23 | 0.10 | 0.14 | 0.10 | 0.12 | 0.09 | 0.05 | 0.02 | 0.08 | 0.17 | 0.04 | 0.04 | 0.09 | 0.12 | 0.05 |
| 28 | 0.13 | 0.13 | 0.11 | 0.03 | 0.03 | 0.07 | 0.14 | 0.07 | 0.16 | 0.04 | 0.08 | 0.06 | 0.19 | 0.13 | 0.17 |
| 29 | 1.05 | 0.80 | 0.70 | 0.28 | 0.30 | 0.29 | 0.26 | 0.35 | 0.24 | 0.26 | 0.22 | 0.30 | 0.20 | 0.31 | 0.24 |
| 30 | 0.07 | 0.09 | 0.05 | 0.06 | 0.03 | 0.04 | 0.02 | 0.01 | 0.09 | 0.02 | 0.05 | 0.03 | 0.06 | 0.12 | 0.02 |
| 31 | 0.36 | 0.45 | 0.44 | 0.20 | 0.21 | 0.26 | 0.08 | 0.09 | 0.17 | 0.23 | 0.22 | 0.17 | 0.24 | 0.11 | 0.07 |
| 32 | 0.11 | 0.13 | 0.08 | 0.05 | 0.06 | 0.06 | 0.06 | 0.06 | 0.05 | 0.03 | 0.05 | 0.06 | 0.05 | 0.03 | 0.10 |
| 33 | 0.30 | 0.09 | 0.24 | 0.10 | 0.07 | 0.08 | 0.06 | 0.06 | 0.05 | 0.04 | 0.04 | 0.09 | 0.05 | 0.03 | 0.03 |
| 34 | 0.12 | 0.14 | 0.08 | 0.06 | 0.07 | 0.04 | 0.12 | 0.09 | 0.04 | 0.03 | 0.07 | 0.02 | 0.12 | 0.08 | 0.17 |
| 35 | 0.32 | 0.15 | 0.34 | 0.17 | 0.11 | 0.13 | 0.20 | 0.21 | 0.18 | 0.11 | 0.18 | 0.18 | 0.14 | 0.15 | 0.17 |
| 36 | 0.07 | 0.06 | 0.11 | 0.03 | 0.09 | 0.03 | 0.09 | 0.08 | 0.10 | 0.03 | 0.03 | 0.09 | 0.07 | 0.08 | 0.06 |
| 37 | 0.64 | 0.63 | 0.70 | 0.22 | 0.16 | 0.19 | 0.13 | 0.16 | 0.18 | 0.17 | 0.17 | 0.16 | 0.17 | 0.07 | 0.16 |
| 38 | 0.05 | 0.06 | 0.07 | 0.02 | 0.03 | 0.06 | 0.04 | 0.03 | 0.09 | 0.02 | 0.06 | 0.02 | 0.07 | 0.03 | 0.02 |
| 39 | 0.14 | 0.03 | 0.15 | 0.04 | 0.06 | 0.05 | 0.05 | 0.05 | 0.07 | 0.12 | 0.04 | 0.06 | 0.04 | 0.09 | 0.08 |
| 40 | 0.04 | 0.07 | 0.08 | 0.03 | 0.08 | 0.07 | 0.04 | 0.04 | 0.08 | 0.05 | 0.05 | 0.04 | 0.06 | 0.03 | 0.07 |
| 41 | 0.30 | 0.24 | 0.30 | 0.15 | 0.13 | 0.14 | 0.10 | 0.16 | 0.10 | 0.13 | 0.09 | 0.10 | 0.07 | 0.12 | 0.14 |
| 42 | 0.05 | 0.06 | 0.04 | 0.03 | 0.04 | 0.01 | 0.03 | 0.12 | 0.09 | 0.04 | 0.03 | 0.01 | 0.10 | 0.04 | 0.09 |
| 43 | 0.36 | 0.28 | 0.34 | 0.08 | 0.12 | 0.02 | 0.14 | 0.16 | 0.13 | 0.12 | 0.07 | 0.06 | 0.07 | 0.05 | 0.09 |
| 44 | 0.06 | 0.05 | 0.10 | 0.02 | 0.05 | 0.06 | 0.12 | 0.13 | 0.09 | 0.01 | 0.06 | 0.05 | 0.05 | 0.05 | 0.04 |
| 45 | 0.03 | 0.05 | 0.05 | 0.02 | 0.04 | 0.04 | 0.04 | 0.08 | 0.09 | 0.06 | 0.02 | 0.04 | 0.06 | 0.06 | 0.05 |
| 46 | 0.04 | 0.17 | 0.18 | 0.03 | 0.02 | 0.08 | 0.08 | 0.05 | 0.10 | 0.06 | 0.10 | 0.04 | 0.08 | 0.04 | 0.12 |
| 47 | 0.09 | 0.18 | 0.22 | 0.07 | 0.11 | 0.07 | 0.15 | 0.11 | 0.19 | 0.11 | 0.11 | 0.14 | 0.13 | 0.10 | 0.07 |
| 48 | 0.08 | 0.04 | 0.04 | 0.06 | 0.04 | 0.02 | 0.05 | 0.06 | 0.11 | 0.05 | 0.06 | 0.03 | 0.02 | 0.08 | 0.06 |
| 49 | 0.09 | 0.13 | 0.16 | 0.04 | 0.11 | 0.06 | 0.10 | 0.11 | 0.15 | 0.05 | 0.05 | 0.05 | 0.17 | 0.04 | 0.11 |
| 50 | 0.07 | 0.06 | 0.05 | 0.03 | 0.05 | 0.02 | 0.12 | 0.04 | 0.09 | 0.06 | 0.04 | 0.06 | 0.03 | 0.08 | 0.09 |
| THD% | 23.91 | 23.83 | 23.75 | 1.73 | 1.75 | 1.70 | 1.53 | 1.50 | 1.55 | 1.79 | 1.79 | 1.84 | 1.60 | 1.63 | 1.64 |

standards, thereby showcasing the system's efficacy in improving power quality. The control strategy demonstrated robust performance, effectively handling various types of power system pollution. This attribute is critical for ensuring system stability and reliability under fluctuating conditions. Incorporation of an adaptive hysteresis band current controller for generating VSC switch gate signals significantly improved the DSTATCOM's dynamic response. This aspect of the design was pivotal in achieving optimal power factor compensation, harmonic balance, and neutral current management. In scenarios involving linear and non-linear loads, the DSTATCOM, governed by the proposed control

scheme, adeptly compensated for reactive power and balanced loads, illustrating the system's versatility. The novel FIS-VFF RLES algorithm outperformed conventional methods in accurately tracking and compensating for harmonics, underscoring the advanced capability of the proposed solution. In conclusion, this research successfully demonstrates a comprehensive and innovative approach to DSTATCOM control, offering significant improvements in power quality management. The findings underscore the potential of the proposed scheme to serve as a robust solution for contemporary and future power system challenges.

APPENDIX

System Parameters:

Source Voltage: 415 V
 Frequency: 50 Hz
 Source resistance: 0.01 Ω
 Source Inductance: 2 mH
 Linear Load: 20 KVA, PF= 0.8 lag
 Non-linear Load: A three single-phase bridge rectifier with an R-L Load $R = 9 \Omega$, $L = 1 \text{ mH}$
 Ripple filter: $R_f = 5 \Omega$, $C_f = 5.25 \mu\text{F}$
 Interfacing inductor: $L_f = 3.5 \text{ mH}$ $L_n = 3.5 \text{ mH}$
 DC bus capacitance of DSTATCOM: 2000 μF
 DC bus voltage of DSTATCOM: 700 V
 DC voltage PI controller: $K_{pd} = 1.65$, $K_{id} = 0.22$
 PCC voltage PI controller: $K_{pq} = 2$, $K_{iq} = 0.2$

CREDIT AUTHORSHIP CONTRIBUTION STATEMENT

Arash Rohani: Conceptualization, Data curation, Formal analysis, Funding acquisition, Investigation, Methodology, Resources, Software, Validation, Writing - original draft, Writing - review & editing. **Javad Ebrahimi:** Conceptualization, Formal analysis, Methodology, Validation, Writing - original draft. **Shirin Besati:** Conceptualization, Investigation, Methodology, Resources, Writing - original draft, Writing - review & editing.

DECLARATION OF COMPETING INTEREST

The authors declare that they have no known competing financial interests or personal relationships that could have appeared to influence the work reported in this paper. The ethical issues; including plagiarism, informed consent, misconduct, data fabrication and/or falsification, double publication and/or submission, redundancy has been completely observed by the authors.

REFERENCES

- [1] E. L. L. Fabricio, S. C. S. Júnior, C. B. Jacobina, and M. B. de Rossiter Corrêa, "Analysis of main topologies of shunt active power filters applied to four-wire systems," *IEEE Transactions on Power Electronics*, vol. 33, no. 3, pp. 2100-2112, March 2018.
- [2] S. Aminzadeh, M. T. Hagh, and H. Seyedi, "Reactive power coordination between solid oxide fuel cell and battery for microgrid frequency control," *J. Appl. Res. Electr. Eng.*, vol. 1, no. 2, pp. 121-130, 2022.
- [3] D. Yazdani, M. Mojiri, A. Bakhshai, and G. Joós, "A fast and accurate synchronization technique for extraction of symmetrical components," *IEEE Transactions on Power Electronics*, vol. 24, no. 3, pp. 674-684, March 2009.
- [4] M. Benchouia, I. Ghabbane, A. Golea, K. Srairi, and M. E. H. Benbouzid, "Implementation of adaptive fuzzy logic and PI controllers to regulate the dc bus voltage of shunt active power filter," *Appl. Soft Comput.*, vol. 28, pp. 125-131, 2015.
- [5] B. Liu, F. Zhuo, Y. Zhu, H. Yi, and F. Wang, "A three-phase pll algorithm based on signal reforming under distorted grid conditions," *IEEE Transactions on Power Electronics*, vol. 30, no. 9, pp. 5272-5283, Sept. 2015.
- [6] S. Golestan, J. M. Guerrero, and J. C. Vasquez, "Three-phase PLLs: A review of recent advances," *IEEE Transactions on Power Electronics*, vol. 32, no. 3, pp. 1894-1907, March 2017.
- [7] S. Golestan, J. M. Guerrero, A. Vidal, A. G. Yepes, J. Doval-Gandoy and F. D. Freijedo, "Small-Signal modeling, stability analysis and design optimization of single-phase delay-based PLLs," *IEEE Transactions on Power Electronics*, vol. 31, no. 5, pp. 3517-3527, May 2016.
- [8] F. Xiao, L. Dong, L. Li and X. Liao, "A frequency-fixed sogi-based PLL for single-phase grid-connected converters," *IEEE Transactions on Power Electronics*, vol. 32, no. 3, pp. 1713-1719, March 2017.
- [9] S. Mishra, D. Das, R. Kumar, and P. Sumathi, "A power-line interference canceler based on sliding DFT phase locking scheme for ECG signals," *IEEE Transactions on Instrumentation and Measurement*, vol. 64, no. 1, pp. 132-142, Jan. 2015.
- [10] R. Panigrahi, and B. Subudhi, "Performance enhancement of shunt active power filter using a kalman filter-based H_∞ control strategy," *IEEE Transactions on Power Electronics*, vol. 32, no. 4, pp. 2622-2630, April 2017.
- [11] A. Boussaid, A. L. Nemmour, and A. Khezzar, "A novel strategy for shunt active filter control," *Electric Power Systems Research*, vol. 123, pp. 154-163, Jun. 2015.
- [12] S. D. Swain, and P. K. Ray, "Harmonic current and voltage compensation using HSAPF based on hybrid control approach for synchronous reference frame method," *International Journal of Electrical Power & Energy Systems*, vol. 75, pp. 83-90, 2016.
- [13] S. Golestan, J. M. Guerrero, A. Vidal, A. G. Yepes, J. D. Gandoy, and F. D. Freijedo, "Small-Signal modeling, stability analysis and design optimization of single-phase delay-based PLLs," *IEEE Trans. Power Electron.*, vol. 31, no. 5, pp. 3517-3527, 2016.
- [14] F. Xiao, L. Dong, L. Li, X. Liao, "A Frequency-Fixed sogi-based PLL for single-phase grid-connected converters," *IEEE Trans. Power Electron.*, vol. 32, no. 3, pp. 1713-1719, 2017.
- [15] B. Singh, S. K. Dube and S. R. Arya, "Hyperbolic tangent function-based least mean-square control algorithm for distribution static compensator," *IET Generation, Transmission & Distribution*, vol. 8, no. 12, pp. 2102-2113, Dec. 2014.
- [16] R. Niwas, B. Singh, S. Goel and C. Jain, "Unity power factor operation and neutral current compensation of diesel generator set feeding three-phase four-wire loads," *IET Generation, Transmission & Distribution*, vol. 9, no. 13, pp. 1738-1746, 2015.
- [17] Rohani, M. Joorabian, M. Abasi, M. Zand, "Three-phase amplitude adaptive notch filter control design of

- DSTATCOM under unbalanced/distorted utility voltage conditions", *Journal of Intelligent & Fuzzy Systems*, vol.37, no. 1, pp. 847-865, 2019.
- [18] F. B. Ajaei, S. Afsharnia, A. Kahrobaei and S. Farhangi, "A fast and effective control scheme for the dynamic voltage restorer," *IEEE Transactions on Power Delivery*, vol. 26, no. 4, pp. 2398-2406, Oct. 2011.
- [19] G. Chen, L. Zhang, R. Wang, L. Zhang and X. Cai, "A novel SPLL and voltage sag detection based on LES filters and improved instantaneous symmetrical components method," *IEEE Transactions on Power Electronics*, vol. 30, no. 3, pp. 1177-1188, March 2015.
- [20] M. Bettayeb and U. Qidwai, "Recursive estimation of power system harmonics", *Electric Power Systems Research*, vol. 47, pp. 143-152, Oct. 1998.
- [21] M. Joorabian, S. S. Mortazavi, and A. A. Khayyami, "Harmonics estimation in a power system using a novel-hybrid least square-ADALINE algorithm", *Electric Power Systems Research*, vol. 79, no. 1, pp. 107-116, Jan. 2009.
- [22] P. Garanayak, G. Panda, and P. K. Ray, "Harmonic estimation using RLS algorithm and elimination with improved current control technique based SAPF in a distribution network", *International Journal of Electrical Power & Energy Systems*, vol. 73, pp. 209-217, 2015.
- [23] R. V. Rocha, D. V. Coury, and R. M. Monaro, "Recursive and nonrecursive algorithms for power system real time phasor estimations", *Electric Power Systems Research*, vol. 143, pp. 802-812, 2017.
- [24] M. M. H. Alhaj, N. M. Nor, V. S. Asirvadam, and M. F. Abdullah, "Comparison of power system harmonics prediction", *Procedia Technology*, vol. 11, pp. 628-634, Jan. 2013.
- [25] M. Beza, and M. Bongiorno, "Application of recursive least squares algorithm with variable forgetting factor for frequency component estimation in a generic input signal," *IEEE Transactions on Industry Applications*, vol. 50, no. 2, pp. 1168-1176, March-April 2014.
- [26] C. Paleologu, J. Benesty and S. Ciochina, "A robust variable forgetting factor recursive least-squares algorithm for system identification," *IEEE Signal Processing Letters*, vol. 15, pp. 597-600, 2008.
- [27] A. Domahidi, B. Chaudhuri, P. Korba, R. Majumder, and T. C. Green, "Self-tuning flexible ac transmission system controllers for power oscillation damping: A case study in real time", *IET generation, transmission & distribution*, vol. 3, no. 12, pp. 1079-1089, Dec. 2009.
- [28] C. Yu, R. Huang, and Y. Zhang, "Online identification of lithium battery equivalent circuit model parameters based on a variable forgetting factor recursive least square method", in *Proc. 16th Annual Conference of China Electrotechnical Society: Volume III*, 2022, pp. 1286-1296.
- [29] M. Zhang, S. Wang, X. Yang, W. Xu, X. Yang, and C. Fernandez, "A novel square root adaptive unscented Kalman filter combined with variable forgetting factor recursive least square method for accurate state-of-charge estimation of lithium-ion batteries", *International Journal of Electrochemical Science*, vol. 17, no. 9, pp. 220915, September 2022.
- [30] Y. Mao, J. Bao, Y. Zhang and Y. Yang, "An ultrafast variable forgetting factor recursive least square method for determining the state-of-health of Li-Ion batteries," *IEEE Access*, vol. 11, pp. 141152-141161, 2023.
- [31] N. Mohseni, and D. S. Bernstein, "Recursive least squares with variable-rate forgetting based on the F-Test," in *2022 American Control Conference (ACC)*, Atlanta, GA, USA, 2022, pp. 3937-3942.
- [32] T. Long et al., "An improved variable forgetting factor recursive least square-double extend Kalman filtering based on global mean particle swarm optimization algorithm for collaborative state of energy and state of health estimation of lithium-ion batteries", *Electrochimica Acta*, vol. 450, pp. 142270, 2023.
- [33] S. Biricik, and H. Komurcugil, "Three-level hysteresis current control strategy for three-phase four-switch shunt active filters", *IET Power Electron.*, vol. 9, no. 8, pp. 1732-1740, Jun. 2016.
- [34] M. Mohammadi, M. Abasi, and A. M. Rozbahani, "Fuzzy-GA based algorithm for optimal placement and sizing of distribution static compensator (DSTATCOM) for loss reduction of distribution network considering reconfiguration", *J. Central South Univ.*, vol. 24, no. 2, pp. 245-258, Feb. 2017.
- [35] B. Singh, A. Chandra, and K. Al-Haddad, *Power Quality: Problems and Mitigation Techniques*, Hoboken, NJ, USA: Wiley, 2014.
- [36] D. Sreenivasarao, P. Agarwal, B. Das, "Neutral Current compensation in three-phase, four-wire systems: A review," *Electric Power Systems Research*, vol. 86, pp. 170-180, 2012.
- [37] B. Singh, S. R. Arya, C. Jain, and S. Goel, "Implementation of four-leg distribution static compensator", *IET Generation, Transmission & Distribution*, vol. 8, no. 6, pp. 1127-1139, Jun. 2014.
- [38] S. Shivam, I. Hussain and B. Singh, "Real-time implementation of SPV system with DSTATCOM capabilities in three-phase fourwire distribution system", *IET Generation Transmission and Distribution*, vol. 11, no. 2, pp. 495-503, Jan. 2017.
- [39] A. K. Panda, and R. Patel, "Adaptive hysteresis and fuzzy controlled based shunt active power filter resistant to shoot-through phenomenon", *IET Power Electron*, vol. 8, no. 10, pp. 1963-1977, April 2015.
- [40] M. Karimi-Ghartemani, H. Mokhtari, M.R. Iravani, & M. Sedighy, "A signal processing system for extraction of harmonics and reactive current of single-phase systems", *IEEE Transactions on Power Delivery*, vol. 19, no. 3, pp. 979-986, 2004.

- [41] A. Rohani, and M. Joorabian, "Modeling and control of DSTATCOM using adaptive hysteresis band current controller in three-phase four-wire distribution systems," in *5th Annual International Power Electronics, Drive Systems and Technologies Conference (PEDSTC 2014)*, 2014, pp. 291-297.
- [42] M. Tofighi-Milani, S. Fattaheian-Dehkordi, and M. Fotuhi-Firuzabad, "A new peer-to-peer energy trading model in an isolated multi-agent microgrid", *J. Appl. Res. Electr. Eng.*, vol. 1, no. 1, pp. 33-41, 2022.
- [43] M. Abasi, M. F. Nezhadnaeini, M. Karimi, and N. Yousefi, "A novel metaheuristic approach to solve unit commitment problem in the presence of wind farms", *Rev. Roum. Sci. Techn.–Électrotechn. Et Énerg*, vol. 60, no. 3, pp. 253-262, 2015.
- [44] M. Abasi, A.T. Farsani, A. Rohani, and M.A. Shiran, "Improving differential relay performance during cross-country fault using a fuzzy logic-based control algorithm", in *2019 5th Conference on Knowledge Based Engineering and Innovation (KBEI)*, 2019 (pp. 193-199).
- [45] M. Abedini, R. Eskandari, J. Ebrahimi, M.H. Zeinali, and A. Alahyari, "Optimal placement of power switches on malayer practical feeder to improve system reliability using hybrid particle swarm optimization with sinusoidal and cosine acceleration coefficients", *Computational Intelligence in Electrical Engineering*, vol. 11, no.2, pp. 73-86, 2020.
- [46] IEEE Std 519-2014, *IEEE recommended practices and requirements for harmonic control in electrical power systems*, 2015.

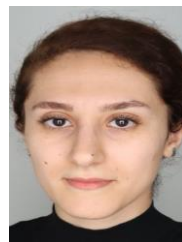
BIOGRAPHY



Arash Rohani received his B.Sc. and M.Sc. degrees in electrical engineering from Shahid Chamran University of Ahvaz, Iran, in 2009 and 2013, respectively. With 8 years of experience at the Khuzestan Regional Electric Company, he currently contributes his expertise at APD Engineering in Australia. Arash's research interests encompass power quality, protection, power system operation, and energy management.



Javad Ebrahimi was born in Iran, in 1988. He received his Ph.D. degrees in Electrical Engineering (Power system) from Khomeinishahr Branch, Islamic Azad University, Khomeinishahr/Isfahan, Iran, in 2020. He is currently working as a technical teacher in Technical and Vocational Academy of Isfahan province. Also, he taught for 10 years at Borujerd Islamic Azad University and Ayatollah Borujerd University. he has published 10 research paper, 8 conference paper and 1 industrial research project. His current research interest includes power quality, smart Grid, demand side management and microgrids.



Shirin Besati was born in Iran in 1994. She obtained her B.Sc. degree in Electrical Engineering from Shahid Chamran University of Ahvaz, Ahvaz, Iran, and her M.Sc. degree in Electrical Power Engineering from Shahid Beheshti University, Tehran, Iran in 2018, and 2021, respectively. Currently, she is a Ph.D. student in Power Electronics at the University of North Carolina at Charlotte. Her research interests include control of utility applications, microgrids, power electronic converters, and FACTS devices.

Copyrights

© 2024 Licensee Shahid Chamran University of Ahvaz, Ahvaz, Iran. This article is an open-access article distributed under the terms and conditions of the Creative Commons Attribution –NonCommercial 4.0 International (CC BY-NC 4.0) License (<http://creativecommons.org/licenses/by-nc/4.0/>).





Research Article

Comparative Analysis of Lithium-ion Battery for Long and Short Pulse Discharge Experiments in State-of-Charge Estimation with Extended Kalman Filter

Behnam Ersi Alambaz¹ , Mohsen Ghalehnoie^{1,*} , and Hamid Reza Moazami²

¹ Faculty of Electrical Engineering, Shahrood University of Technology, Shahrood, Iran

² Nuclear Fuel Cycle Research School, Nuclear Science and Technology Research Institute (NSTRI), Tehran, Iran

* Corresponding Author: ghalehnoie@shahroodut.ac.ir

Abstract: This paper explores the impact of two types of experiments, known as "long pulse" and "short pulse" experiments, on identifying models for Lithium-ion batteries. The focus is on improving the estimation of the state of charge (SoC) using an extended Kalman filter. The results consistently demonstrate that applying the extended Kalman filter to models identified through long pulse experiments outperforms those identified through short pulse experiments in estimating battery SoC and terminal voltage. The article delves into the reasons for this improvement from both circuit and electrochemical perspectives, providing insights into the obtained results. Thus, the study advocates for the preference of long pulse strategies to enhance the performance of Lithium-ion batteries, offering insights that contribute to the development of innovative and sustainable energy storage solutions.

Keywords: Lithium-ion batteries, long-pulse, short-pulse, state of charge.

Article history

Received 24 April 2024; Revised 26 August 2024; Accepted 5 September 2024; Published online 30 October 2024.

© 2024 Published by Shahid Chamran University of Ahvaz & Iranian Association of Electrical and Electronics Engineers (IAEEE)

How to cite this article

B. Ersi Alambaz, M. Ghalehnoie, and H. R. Moazami, "Comparative analysis of lithium-ion battery for long and short pulse discharge experiments in state-of-charge estimation with extended kalman filter," *J. Appl. Res. Electr. Eng.*, vol. 3, no. 2, pp. 200-206, 2024. DOI: 10.22055/jaree.2024.46715.1117



1. INTRODUCTION

Lithium-ion batteries (LIBs) have become indispensable components not only in portable electronics and electric vehicles but also in advanced energy systems like microgrids, where they contribute to frequency control and energy management through fast-response capabilities [1]. The integration of LIBs in such systems underscores their versatility and critical role in ensuring stability and efficiency, especially in scenarios where precise energy balance is paramount. The precise estimation of the state of charge (SoC) in LIBs plays a pivotal role in battery management systems, directly influencing their overall performance and lifespan. As Lithium-ion batteries find extensive applications in electric vehicles and portable electronics, ensuring reliable and accurate SoC estimation becomes imperative for optimizing their usage and achieving efficient energy management. A plethora of techniques have been devised to tackle the SoC estimation challenge, encompassing methods such as coulomb counting [2], neural networks [3], and model-based observers [4]. Notably, among

the model-based observers, the extended Kalman filter (EKF) has gained substantial attention from researchers due to its adeptness in assimilating system dynamics and uncertainties. However, the performance of traditional EKF-based approaches can degrade under dynamic operating conditions, leading to the development of more robust methods, such as the modified adaptive extended Kalman filter (MAEKF), which incorporates adaptive mechanisms to address transient disturbances and bias issues [5]. This adaptability empowers the EKF to deliver more precise and robust SoC predictions.

Model-based observers demand a dynamic model that aptly represents the intricate behavior of the battery. This dynamic model can take various forms, such as an electrochemical model [6], a neural network model [7], or an equivalent circuit model [8]. Electrochemical models, renowned for their detailed representation of battery physics, often require substantial computational resources, limiting their real-time applicability. Neural network models, while exhibiting promise in certain applications, face challenges in providing transparent insights into the underlying battery behavior. The "black-box" nature of neural networks makes

it challenging to interpret the model's decisions, hindering their utility in safety-critical applications where understanding the reasoning behind predictions is paramount. Moreover, neural networks may struggle with generalization across a wide range of operating conditions, limiting their effectiveness in dynamic and diverse battery environments.

In contrast, equivalent circuit models [9] have gained widespread acceptance due to their ability to strike a harmonious balance between accuracy and computational efficiency. Their simplified yet effective representation of electrochemical processes makes them suitable for real-time applications, providing precise SoC estimates without compromising speed. This popularity underscores the pragmatic advantages of equivalent circuit models in delivering reliable and efficient solutions for Lithium-ion battery management systems.

Despite these advantages, one potential drawback of equivalent circuit models is their reliance on accurate parameter identification, which can be sensitive to variations in operating conditions. Additionally, while integer-order models are simpler and computationally efficient, they may lack the flexibility to capture more complex battery dynamics, which could be addressed in future work by exploring fractional-order models or incorporating advanced machine learning techniques.

Equivalent circuit models play a pivotal role in estimating SoC in LIBs, offering flexibility to represent various configurations, from single-cell [10] to multi-cell [11] setups. The selection of model complexity, whether single-cell or multi-cell, involves a trade-off between computational efficiency and accuracy. Single-cell models, while computationally efficient, may oversimplify the intricate behavior of LIBs, leading to inaccuracies in predicting responses during dynamic conditions. The simplicity of these models comes at the cost of potentially overlooking crucial nuances in the battery's behavior. On the other hand, multi-cell models capture system-level dynamics but encounter challenges when applied to individual cells, especially in the presence of pulse-related phenomena. The complexities introduced by inter-cell interactions and the difficulty in accurately extrapolating system-level behaviors to individual cells can compromise the accuracy of predictions. To address these challenges, advanced techniques such as the three-time-scale dual extended Kalman filtering method have been developed, which enables more accurate parameter and state estimation by adjusting the sampling time based on the impact of each parameter on terminal voltage [12]. This method enhances the model's ability to accurately represent the dynamic behavior of LIBs, particularly under varying operational conditions.

However, the dynamics of these equivalent circuit models can be expressed in terms of integer-order or fractional-order derivatives. While fractional-order models offer increased complexity, their adoption faces challenges in parameter identification and computational efficiency. The fractionalization introduces intricacies, making the identification of model parameters more complex. In light of these considerations, the prevailing preference leans towards integer-order dual-cell models. These models involve parameters that require identification based on battery voltage and current under various experimental conditions. Common

methods for parameter identification include short pulse and long pulse experiments, each offering insights into the dual-cell model's behavior under specific dynamic conditions.

This research aims to refine the state of charge (SoC) estimation in Lithium-ion batteries by employing an integer-order dynamic model. By conducting separate pulse experiments—long pulses and short pulses—we identify parameters for the dynamic model. This approach yields two distinct models, one from each experiment, offering flexibility in Kalman filter application for SoC estimation. The results reveal that models derived from long pulse experiments generally exhibit higher accuracy, providing crucial guidance for model selection under various battery operating conditions. This nuanced approach enhances the precision of SoC estimation, contributing valuable insights to Lithium-ion battery management systems.

The paper unfolds in a structured manner, commencing with the extraction of an integer-order dynamic model for a dual-cell equivalent circuit in Section 2. Section 3 delves into the intricacies of parameter identification, encompassing the identification of open-circuit voltage, internal resistance, and other battery parameters. Following this, the results obtained from data acquired in both long pulse and short pulse experiments for parameter estimation are presented. The estimation outcomes, achieved by deploying an extended Kalman filter on each model, are thoroughly compared. The concluding section encapsulates the key findings and insights derived from the study.

2. DYNAMIC MODELING OF LITHIUM-ION BATTERIES

We highlighted the significance of equivalent electrical circuit models for lithium-ion batteries and addressed the limitations of both single-cell and multi-cell models. Recognizing these challenges, the focus shifted towards a prevalent solution—the dual-cell electrical equivalent circuit, renowned for its effectiveness in capturing the battery's dynamic behavior (refer to Fig. 1). This model incorporates crucial elements, such as internal resistance (R_0), polarization resistances due to electrochemical polarization (R_1 and R_2), and polarization capacitances (C_1 and C_2).

The dual-cell model is expressed through a set of dynamic equations that govern the system's continuous-time behavior. Let's consider the following components and variables:

- i_1, i_2 : Currents through R_1 and R_2 , respectively.
- SOC : State of charge, the battery's charge level.
- V_t : Terminal voltage.
- I_t : Terminal current.
- V_{OC} : Open-circuit voltage, depends on the SOC .

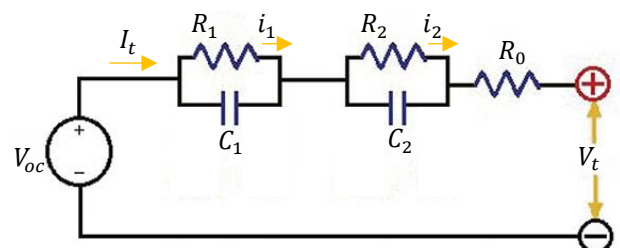


Fig. 1: Two-cell equivalent circuit model for LIBs.

$$SOC(t) = SOC(0) - \frac{1}{C_n} \int_0^t I_t(t) dt, \quad (1)$$

where C_n is the nominal capacity of battery. Using Kirchhoff's laws, Ohm's law, and the definition of state of charge (1), the continuous-time dynamic equations for the dual-cell model are given by:

$$\frac{di_1}{dt} = -\frac{1}{R_1 C_1} i_1 + \frac{1}{R_1 C_1} I_t, \quad (2)$$

$$\frac{di_2}{dt} = -\frac{1}{R_2 C_2} i_2 + \frac{1}{R_2 C_2} I_t, \quad (3)$$

$$\frac{dSOC}{dt} = -\frac{I_t(t)}{C_n}, \quad (4)$$

and the output equation is,

$$V_t(t) = -R_1 i_1 - R_2 i_2 - R_0 I_t + V_{OC}(SOC) \quad (5)$$

The dynamic equations (2)-(4) governing the derivatives of the state variables in the battery system are linear. However, the output equation becomes non-linear due to the dependence of the open-circuit voltage (V_{OC}) on the state of charge (SOC), and as a result, the entire battery system can be considered non-linear when viewed from the input current (I_t) to the output voltage (V_t). Consequently, in the subsequent sections, an extended Kalman filter technique is employed to estimate the state of charge. To facilitate the application of the extended Kalman filter, these continuous-time equations (2)-(5) are discretized using the Euler method with a sampling rate Δt , resulting in the following discrete-time system equations:

$$\begin{bmatrix} i_1(k+1) \\ i_2(k+1) \\ SOC(k+1) \end{bmatrix} = A \begin{bmatrix} i_1(k) \\ i_2(k) \\ SOC(k) \end{bmatrix} + \begin{bmatrix} 1 - \exp\left(\frac{-\Delta t}{R_1 C_1}\right) \\ 1 - \exp\left(\frac{-\Delta t}{R_2 C_2}\right) \\ \frac{-\Delta t}{C_n} \end{bmatrix} I_t(k), \quad (6)$$

$$V_t(k+1) = C \begin{bmatrix} i_1(k) \\ i_2(k) \\ SOC(k) \end{bmatrix} - R_0 I_t(k) + V_{OC}(SOC(k)), \quad (7)$$

where,

$$A = \begin{bmatrix} \exp\left(\frac{-\Delta t}{R_1 C_1}\right) & 0 & 0 \\ 0 & \exp\left(\frac{-\Delta t}{R_2 C_2}\right) & 0 \\ 0 & 0 & 1 \end{bmatrix}, \quad (8)$$

$$C = [-R_1 \quad -R_2 \quad 0] \quad (9)$$

3. PARAMETER ESTIMATION

In the previous section, we developed the dynamic equations of a lithium-ion battery based on a dual-cell equivalent circuit model, which includes parameters that require identification for accurate representation. Two methods, the long pulse and short pulse experiments, are employed for parameter identification. Here, we provide further insights into these experiments and present the terminal current and voltage profiles for both scenarios in Fig. 2 and Fig. 3 (both refer to short and long terminal current,

respectively), although Fig. 4 and Fig. 5 (both refer to long and short terminal voltage, respectively), for a commercially available Maxell ER3 14250 lithium-ion battery (Japan) with a nominal capacity of 500mAh and nominal voltage of 3.7 volts. The battery under examination has a maximum voltage of 4.2 volts and a cut-off voltage of 3 volts. The testing procedure involve cycling the battery at a temperature of 25°C.

Utilizing these precise current measurements, the state of charge (SOC) at each time step, especially at the end of the resting period, is determined using (1).

For instance, considering the magnitude of the current drawn from the battery and its duration in the long pulse

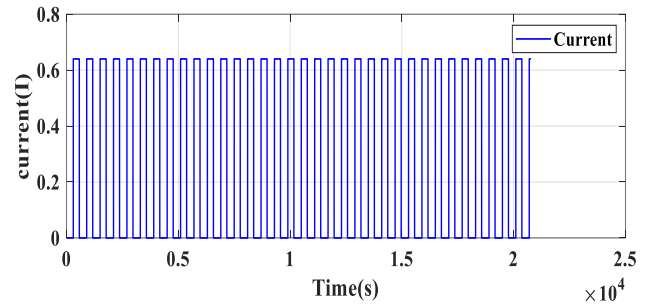


Fig. 2: Terminal current during short pulse experiments.

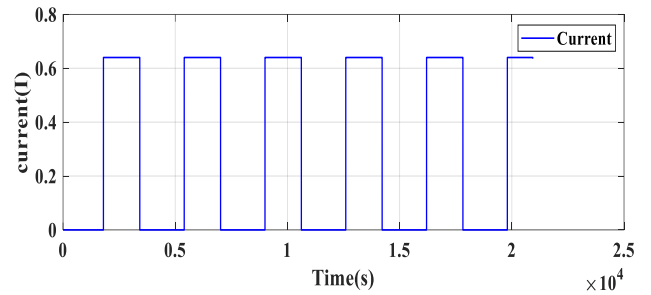


Fig. 3: Terminal current during long pulse experiments.

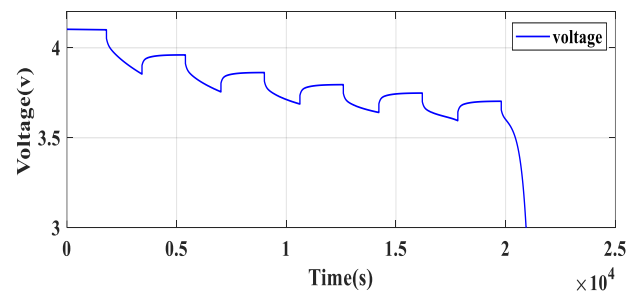


Fig. 4: Terminal voltage during long pulse experiments.

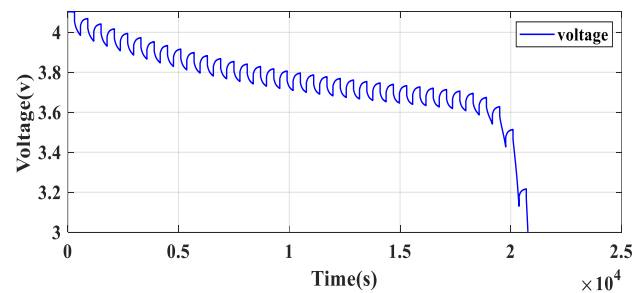


Fig. 5: Terminal voltage during short pulse experiments.

experiment, it can be observed that during each discharge and rest cycle, 10% of the battery charge is depleted.

Consequently, since the battery starts with a full charge, the battery charge level decreases to 0.9 at the end of the rest cycle after the first discharge and continues to decrease to 0.8 at the end of the subsequent cycle, and so forth. So, considering that no current flows during resting intervals, and the battery is in a quiescent state, according to applying the voltage Kirchhoff's law, it is expected that the voltages across the RC branches become zero, resulting in the terminal voltage being equal to the open-circuit voltage (V_{OC}).

When V_{OC} as a function of SOC identified, the next step is to estimate the internal resistance (R_0) (according to the figure 6) using the following method during discharge-rest intervals [13]:

$$R_0 = \frac{(V_A - V_B) + (V_D - V_C)}{2I_t} \quad (10)$$

in which V_A , V_B , V_C , and V_D represent the battery voltages during each time interval corresponding to discharge and rest, as illustrated in Fig. 6. For further details, refer to [14]. In this way, the identified value for R_0 in this study are 0.0749 ohms and 0.0748 ohms for long pulse and short pulse experiments, respectively. This indicates that the type of experiment does not have a significant impact on estimating the internal resistance of the battery.

Now, armed with V_{OC} and R_0 , the relationship between the terminal currents and the output voltage (y , voltage of the total cells) for the dual-cell model can be established. By leveraging the ARX [15] or ARMAX [16] techniques, the transfer function from the output y to the input I_t is obtained.

$$\frac{Y}{I_t} = \frac{b_1 q^{-1} + b_2 q^{-2}}{1 + a_1 q^{-1} + a_2 q^{-2}} \quad (11)$$

Comparing this identified system with the ARX model, considering the system's governing equations akin to Equations (2)-(5), and considering the output as the voltage across the cell terminals (y):

$$y = [-R_1 \quad -R_2 \quad 0] \begin{bmatrix} i_{1,k} \\ i_{2,k} \\ SOC_k \end{bmatrix} + (-R_0)I_k, \quad (12)$$

the parameterized system transfer function becomes:

$$\frac{Y}{I_t} = \frac{A(q^{-1})}{B(q^{-1})}, \quad (13)$$

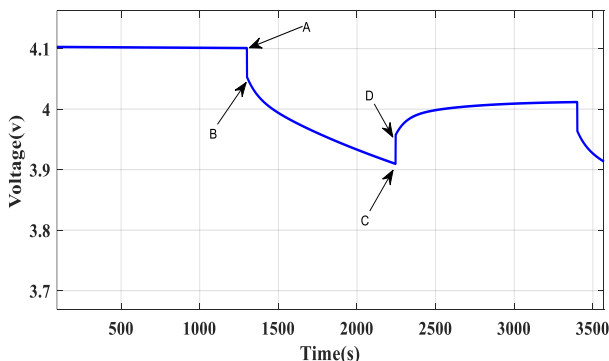


Fig. 6: Voltage profile during a discharge-rest cycle in both long and short pulse experiments.

$$A(q^{-1}) = (R_1 + R_2 - R_1\sigma_2 - R_2\sigma_1) q^{-2} + (R_1\sigma_2\sigma_1 - R_1\sigma_1 - R_2\sigma_2 + R_2\sigma_2\sigma_1) q^{-1} \quad (14)$$

$$B(q^{-1}) = q^{-2} + (-\sigma_2 - \sigma_1) q^{-1} + \sigma_2\sigma_1 \quad (15)$$

$$\sigma_1 = \exp\left(\frac{-\Delta t}{R_1 C_1}\right) \quad (16)$$

$$\sigma_2 = \exp\left(\frac{-\Delta t}{R_2 C_2}\right) \quad (17)$$

Comparison between the identified system and the ARX system yields,

$$R_1 = -\frac{2}{a_1 + \sqrt{a_1^2 - 4}} \quad (18)$$

$$R_2 = \frac{a_1 + \sqrt{a_1^2 - 4}}{-2} \quad (19)$$

$$\sigma_1 = \frac{1}{e^{C_2 R_2}} \quad (20)$$

$$\sigma_2 = \frac{1}{e^{C_1 R_1}} \quad (21)$$

$$C_1 = \frac{1}{\sigma_1 \cdot R_1} \quad (22)$$

$$C_2 = \frac{1}{\sigma_2 \cdot R_2} \quad (23)$$

This comprehensive approach ensures the accurate identification of key parameters and validates the dual-cell model's efficacy. The obtained parameters based on this method are summarized in Table 1.

4. STATE OF CHARGE ESTIMATION

The extended Kalman filter (EKF) [17], [18] is known as a widely used technique to estimate the state of charge (SoC) and state of health (SoH) in Li-ion battery systems. EKF, which acts as a recursive algorithm, uses a mathematical model to predict battery behavior and compares it with measured data, facilitating the estimation of internal parameters in the battery model. As an extension of the Kalman filter, the EKF is a special value system with nonlinear dynamics. The EKF algorithm consists of two main steps: the prediction step and the update step. During the prediction phase, the battery model predicts the behavior of the system in a short period based on the current state of the battery, with known inputs such as current and voltage as outputs for this estimation phase. This output includes the battery status and its covariance. Afterwards, in the update step, the measured data from the battery system is used to adjust the predicted state estimate. The Kalman gain, which acts as a weighting factor, determines the influence of the accuracy. Figs. 7-12 provide a quantitative representation of predicted state estimate and the measured data in determining the updated state estimate.

Table 1: Summary of identified battery parameters using different experimental methods.

| Experiment | Long Pulse | Short Pulse |
|---------------|--------------------|--------------------|
| R_1 (ohm) | 0.0496 | 0.0455 |
| R_2 (ohm) | 0.0473 | 0.0509 |
| C_1 (Farad) | 664.64 | 707.73 |
| C_2 (Farad) | 4.83×10^3 | 4.30×10^3 |

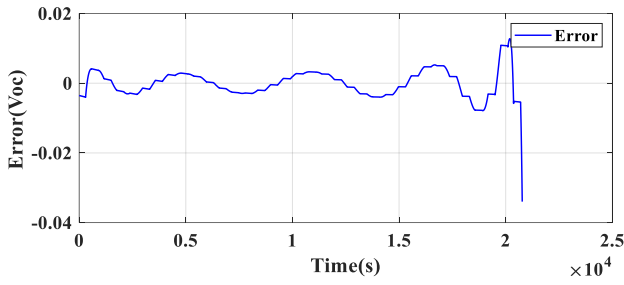


Fig. 7: Open circuit voltage error in short pulse mode.

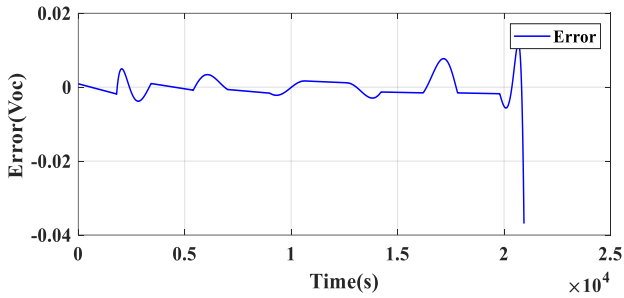


Fig. 8: Open circuit voltage error in long pulse mode.

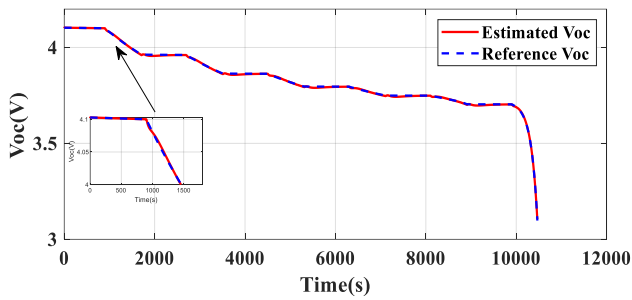


Fig. 9: Actual (solid line) and estimated (dashed line) values of open circuit voltage in long pulse mode.

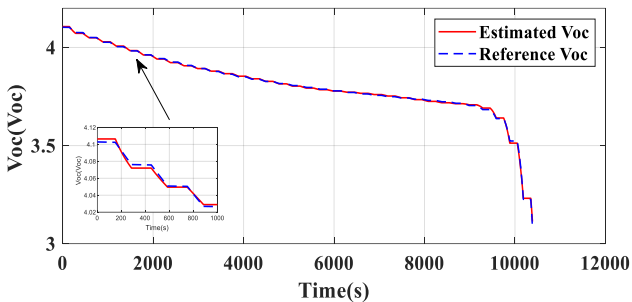


Fig. 10: Actual (solid line) and estimated (dashed line) values of open circuit voltage in short pulse mode.

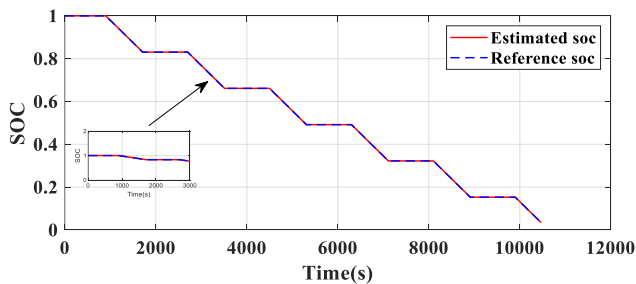


Fig. 11: Actual (solid line) and estimated (dashed line) values of SOC in long pulse mode.

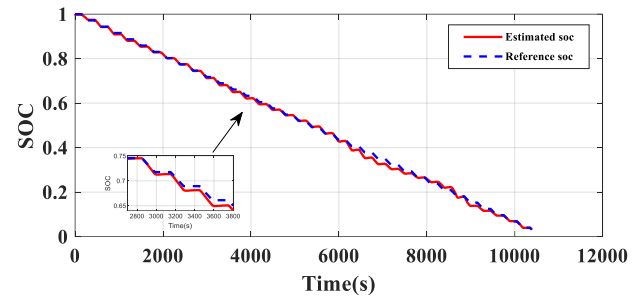


Fig. 12: Actual (solid line) and estimated (dashed line) values of SOC in short pulse mode.

This updated state estimate then serves as the initial state for the next prediction step. EKF has proven to be useful in estimating SoC and SoH [19] in Li-ion battery systems, primarily due to its ability to accommodate nonlinearities in the battery model. This includes factors such as changes in battery capacity as a function of temperature [20] and state of charge. The choice of the battery model, which can be physics-based or empirical, depends on the desired level of the EKF program under different pulsing conditions and optimization. It helps with battery performance and battery life. The robustness of EKF makes it a potential tool for real-time battery management applications in electric vehicles and renewable energy systems.

As seen in Fig. 7 and Fig. 8, the open circuit voltage error is evident in both short pulse and long pulse conditions. At the beginning of the current cycle, the extracted error value is lower in the short pulse condition. It can be concluded that the stability of the Li-ion battery is compromised by short cycles, starting at 100% charge, but as the current cycle continues and the central core of the Li-ion battery heats up, as shown in Fig. 10 and Fig. 12, the modeling errors appear during the short pulse cycle of the open circuit voltage and state of charge of the Li-ion battery.

Conversely, long pulses exhibit stable performance within the performance range of Li-ion batteries due to their longer rest intervals that allow the core to cool down in each current cycle and prepare the battery memory for the next cycle. This range extends from 70% to 30% under voltage 3.8 to 3.3, as clearly seen in Fig. 9 and Fig. 11. The observer estimated battery performance much more accurately in open circuit voltage and battery state of charge compared to short pulse conditions.

5. CONCLUSION

In conclusion, the exploration of open-circuit voltage errors under short and long-pulse conditions, as detailed in this conference paper, reveals a captivating narrative. Initially, there is an observation of lower error magnitudes in short-pulse scenarios. However, a nuanced trend emerges, highlighting that the system's accuracy diminishes with an increasing number of current flow and discharge cycles, especially in short-pulse conditions. Introducing the consideration of the charging state adds complexity to the analysis. In long-pulse scenarios, due to the longer rest time, there is a nearly 5RC duration where a higher confidence in the equality of terminal voltage and open-circuit voltage is observed at the end of each rest cycle. Despite these

advancements, one limitation of the current study is the potential for parameter drift over extended operation cycles, which could impact the long-term accuracy of the SoC estimation. Future work should explore adaptive estimation techniques or machine learning approaches that can dynamically adjust model parameters to account for such variations. Furthermore, the discussion extends to the topic of open-circuit voltage errors and the level of precision in estimating the state of charge in both short-pulse and long-pulse scenarios. It is noteworthy that in short-pulse conditions, the next significant aspect to be addressed is the accuracy of voltage circuit errors and the precision of the estimator in assessing the battery's charge state. These detailed insights contribute to a more comprehensive understanding of system dynamics, offering valuable considerations for the optimization of open circuit voltage configurations and charging state estimation in battery systems. As we advance, this research sets the stage for further studies and advancements in the field, enriching the knowledge base for future developments.

CREDIT AUTHORSHIP CONTRIBUTION STATEMENT

Behnam Ersi Alambaz: Conceptualization, Formal analysis, Methodology, Software, Writing - original draft, Writing - review & editing. **Mohsen Ghalehnoie:** Conceptualization, , Formal analysis, Methodology , Supervision, Validation, Writing - original draft, Writing - review & editing. **Hamid Reza Moazami:** Formal analysis, Methodology, Supervision, Validation, Writing - review & editing.

DECLARATION OF COMPETING INTEREST

The authors declare that they have no known competing financial interests or personal relationships that could have appeared to influence the work reported in this paper. The ethical issues; including plagiarism, informed consent, misconduct, data fabrication and/or falsification, double publication and/or submission, redundancy has been completely observed by the authors.

REFERENCES

- [1] S. Aminzadeh, M. T. Hagh, and H. Seyedi, "Reactive power coordination between solid oxide fuel cell and battery for microgrid frequency control," *Journal of Applied Research in Electrical Engineering*, vol. 1, no. 2, pp. 121–130, 2022.
- [2] K. Propp, D. J. Auger, A. Fotouhi, S. Longo, and V. Knap, "Kalman-variant estimators for state of charge in lithium-sulfur batteries," *J. Power Sources*, vol. 343, pp. 254–267, 2017.
- [3] M. Jiao, D. Wang, and J. Qiu, "A GRU-RNN based momentum optimized algorithm for SOC estimation," *J. Power Sources*, vol. 459, 2020.
- [4] D. Nissing and H. S. Birnale, "Core temperature observer design and model parameter uncertainty analysis for a lithium battery," *IFAC-PapersOnLine*, vol. 53, no. 2, pp. 12505–12510, 2020.
- [5] S. Rout, and S. Das, "A robust modified adaptive extended Kalman filter for state- of-charge estimation of rechargeable battery under dynamic operating condition," *Electr. Eng.*, 2024.
- [6] K. S. R. Mawonou, A. Eddahech, D. Dumur, D. Beauvois, and E. Godoy, "Improved state of charge estimation for Li-ion batteries using fractional order extended Kalman filter," *J. Power Sources*, vol. 435, no. March, p. 226710, 2019.
- [7] A. Pooladvand, and D. A. Abolmasoumi, "Dynamic State Estimation of Micro-grids by Using Accelerated Particle Filters," p. 99, 2020.
- [8] Z. Ren, and C. Du, "State of charge estimation for lithium-ion batteries using extreme learning machine and extended kalman filter," *IFAC-PapersOnLine*, vol. 55, no. 24, pp. 197–202, 2022.
- [9] X. Jiang, B. Zhang, Y. Wang, Y. Xiang, and W. Li, "Modeling and state of charge estimation of Lithium-ion Battery using the autoregressive exogenous model," *2020 IEEE 1st China Int. Youth Conf. Electr. Eng. CIYCEE 2020*, pp. 1–7, 2020.
- [10] X. Li, and S. Y. Choe, "State-of-charge (SOC) estimation based on a reduced order electrochemical thermal model and extended Kalman filter," *Proc. Am. Control Conf.*, pp. 1100–1105, 2013.
- [11] X. Hu, S. Li, and H. Peng, "A comparative study of equivalent circuit models for Li-ion batteries," *J. Power Sources*, vol. 198, pp. 359–367, 2012.
- [12] M. Zhu, K. Qian, and X. Liu, "A three-time-scale dual extended Kalman filtering for parameter and state estimation of Li-ion battery," in *Proc. Inst. Mech. Eng. Part D J. Automob. Eng.*, vol. 238, no. 6, pp. 1352–1367, 2024.
- [13] J. Lv, B. Jiang, X. Wang, Y. Liu, and Y. Fu, "Estimation of the state of charge of lithium batteries based on adaptive unscented Kalman filter algorithm," *Electron.*, vol. 9, no. 9, pp. 1–22, 2020.
- [14] L. Rozaqi, and E. Rijanto, "SOC estimation for Li-ion battery using optimum RLS method based on genetic algorithm," *Proc. 2016 8th Int. Conf. Inf. Technol. Electr. Eng. Empower. Technol. Better Futur. ICITEE 2016*, 2017.
- [15] X. K. Chen, and D. Sun, "Modeling and state of charge estimation of lithium-ion battery," *Adv. Manuf.*, vol. 3, no. 3, pp. 202–211, 2015.
- [16] A. Kaleli, and H. İ. Akolaş, "Recursive ARMAX-Based global battery SOC estimation model design using kalman filter with optimized parameters by radial movement optimization method," *Electr. Power Components Syst.*, vol. 51, no. 11, pp. 1027–1039, Jul. 2023.
- [17] W. Bai, X. Zhang, Z. Gao, S. Xie, K. Peng, and Y. Chen, "Sensorless coestimation of temperature and state-of-charge for lithium-ion batteries based on a coupled electrothermal model," *Int. J. Energy Res.*, vol. 2023, pp. 1–18, 2023.
- [18] T. Sun, R. Wu, Y. Cui, and Y. Zheng, "Sequent extended Kalman filter capacity estimation method for lithium-ion batteries based on discrete battery aging

model and support vector machine,” *J. Energy Storage*, vol. 39, no. May, p. 102594, 2021.

- [19] X. Wei, M. Yimin, and Z. Feng, “Identification of parameters in Li-Ion battery model by least squares method with variable forgetting factor,” *Int. J. Comput. Methods*, vol. 17, no. 7, pp. 1–20, 2020.
- [20] J. Sun *et al.*, “Online internal temperature estimation for lithium-ion batteries based on Kalman filter,” *Energies*, vol. 8, no. 5, pp. 4400–4415, 2015.

BIOGRAPHY



Behnam Ersi Alambaz was born in Mazandaran, Iran in 1994. He finished his M.Sc. in electrical control engineering at Shahrood University of Technology, Shahrood, Iran. His research interested are control and system identification.



Mohsen Ghalehnoie was born in Shahrood, Iran, in 1982, and holds Bachelor's, Master's, and Doctoral degrees in control engineering. He earned his B.Sc. and M.Sc. degrees from Iran University of Science and the University of Tehran in 2005 and 2008,

respectively. Additionally, he received his Ph.D. from Ferdowsi University of Mashhad in 2018. Currently, he serves as an assistant professor of control engineering at Shahrood University of Technology, Shahrood, Iran. His work focuses on control systems theory, optimization, fuzzy control, data fusion, and expert systems, especially for hybrid switched systems and industrial processes.



Hamid Reza Moazami received his bachelor's degree in Applied Chemistry from Isfahan University of Technology in 2002, and his master's degree in Analytical Chemistry from Tehran University in 2005. He received his PhD in Analytical Chemistry from the Shahid University in 2015. He is currently an assistant Professor at Nuclear Science and Technology Research Institute. His research focuses on the development of novel electrochemical systems for energy and environmental applications.

Copyrights

© 2024 Licensee Shahid Chamran University of Ahvaz, Ahvaz, Iran. This article is an open-access article distributed under the terms and conditions of the Creative Commons Attribution –NonCommercial 4.0 International (CC BY-NC 4.0) License (<http://creativecommons.org/licenses/by-nc/4.0/>).





Research Article

Investigating the Flashover Probability of Transmission Network Insulators During Dust Storms

Yasaman Abbasi Chahardah Cheriki^{1,2}, Hossein Farzin^{1,*} , and Elaheh Mashhour¹

¹ Faculty of Engineering, Shahid Chamran University of Ahvaz, Ahvaz, Iran

² Network Studies Expert, Ahvaz Electrical Power Distribution Company, Ahvaz, Iran

* Corresponding Author: Farzin@scu.ac.ir

Abstract: In recent decades, the probability of natural disasters has increased due to climate change. As a result, the discussion of resilience in the power system literature was raised. One consequence of these events is the unwanted operation of some power system equipment, which causes unexpected blackouts and increases the value of energy not supplied (ENS) in the system. Insulators are important components of the power system that have a great impact on the continuity of supply. Electrical flashover in insulators causes a decrease in their insulation strength and might lead to short-circuit faults in the power system. In this paper, the effect of dust storms and humidity on the probability of transmission network insulators flashover is investigated. The studied insulator is simulated in Electrical AutoCAD software, and after applying pollution and moisture in COMSOL-Multiphysics software, the distribution of potential and electric field on the studied insulator is obtained using the finite element method (FEM). In order to determine the probability of insulation flashover, the candidate points for arc occurrence are selected using the roulette wheel method in MATLAB software, and the insulation flashover probability curve is determined in different amounts of dust pollution and three humidity levels of 65%, 80%, and 95%. The effects of increasing the creepage distance and using silicone rubber materials that have hydrophobic properties are investigated, and various sensitivity analyses are conducted. The results indicate that both solutions can significantly reduce the flashover probability of transmission insulators.

Keywords: Humidity, dust storm, transmission network, insulator, fragility curve.

Article history

Received 26 October 2024; Revised 17 December 2024; Accepted 16 January 2025; Published online 11 March 2025.

© 2025 Published by Shahid Chamran University of Ahvaz & Iranian Association of Electrical and Electronics Engineers (IAEEE)

How to cite this article

Y. Abbasi Chahardah Cheriki, H. Farzin, and E. Mashhour, "Investigating the flashover probability of transmission network insulators during dust storms," *J. Appl. Res. Electr. Eng.*, vol. 3, no. 2, pp. 207-221, 2024.

DOI: 10.22055/jaree.2025.48231.1143



| NOMENCLATURE | |
|--------------|---|
| Symbol | Description |
| C | capacitance of each insulator |
| C_E | capacitance of the insulator relative to the ground |
| C_L | capacitance of the insulator relative to the line |
| H | the length of the insulator |
| x | the distance from the ground electrode |
| S_a | the hardness of the solution in g/cm ³ |

| | |
|---------------|--|
| σ_{20} | the electrical conductivity of the solution in $\mu\text{S}/\text{cm}$ at 20°C |
| V | the volume of the pollution solution in cm^3 |
| A | the surface area of the insulator in cm^2 |
| d | the distance between the two nodes of interest |
| Δv | the voltage difference between the given nodes |
| E_c | the electric strength of the air gap (3 kV/mm) |

| | |
|--------------------|----------------------------------|
| N | the number of iterations |
| $N_{No-Flashover}$ | the counter of no arc conditions |
| $N_{Flashover}$ | the flashover counter |
| $P_{Flashover}$ | the flashover probability |

1. INTRODUCTION

1.1. The Effect of Dust Storm on The Resilience of Power System

The main purpose of operating the power system is to provide stable electricity [1]. The stability of power systems is a critical requirement for modern societies. Natural events such as storms, floods and earthquakes, as well as cyber-attacks that are man-made, have destructive effects on the operation and control of the power system. Accurate modelling of these events is very difficult due to their random nature. Each of these events affects a part of the power system. In most researches, forecasts and historical data available in meteorological organizations have been used for modelling purpose [2]. Power system blackout is one of the challenges of the electricity industry and consumers. The loss of electrical power can be linked to three sources: power outages caused by natural disasters, technical problems, and human-made power outages. According to the reports provided by the US Department of Energy, among these blackout sources, the role of natural disasters is more severe. Due to climate change in recent decades, the number and severity of climate change related incidents have increased worldwide. It can be concluded that most outages originate from low-probability events that have a large impact on power systems and are known as high-impact, low-probability (HILP) events [3].

Dust storm is defined as solid particles resulting from surface soils that are suspended in the air and remain in the air for a long time due to their small dimensions and are easily moved by air flow [4]. The phenomenon of dust storm is one of the most important challenges in North Africa and the Middle East. According to the environmental standards, the permissible concentration of dust storm in the air is $150 \mu\text{gr}/\text{cm}^3$ during 24 hours. The diameter of dust storm with different origins is between 10 and 50 microns. If their diameter is less than 10 microns, they are harmful to human and animal health. Dust storm particles with a diameter of less than 2.5 microns have an unnatural origin and are usually caused by human factors [5].

1.2. Literature Review

In [6], the phenomenon of dust storm is investigated. Spatial analysis of this phenomenon shows that the main areas of dust activities are deserts, including sand dunes that have been destroyed by humans. Geographical location and climatic conditions are also other factors affecting the possibility of this phenomenon. In reference [7], the author investigated the effects caused by the phenomenon of dust storm on the insulation surfaces of the equipment and artificial contamination on the insulation surface was simulated using the IEC60507 standard. By applying low voltage to the insulator and measuring the amount of leakage current, the conductivity coefficient is calculated and the amount of pollution is determined from it. Reference [8] argues that the increase in pollution affects the performance

of insulators, and therefore, it is necessary for network operators to continuously wash insulators. The results showed that the leakage current does not increase significantly with the increase of pollution at noon. In [9], the test of uniform and non-uniform pollution in new and old polymer insulators have been evaluated. The results show that polymer insulators have higher endurance in uniform pollution than in non-uniform pollution. Moreover, aging in polymer insulators has reduced the arc voltage in them. In reference [10], the technical and economic issues related to washing insulators and applying RTV coating to combat dust were evaluated. It is shown that the number of washing cycles, the washing method, the level of contamination and the type of contamination in the area affect the cost of washing insulators. Moreover, it is argued that factors such as the quality of the selected coating, the volume of materials required and the quality of the applied coating affect the cost of using RTV coating. In paper [11], an analysis was conducted on the contaminating microparticles. The presence of moisture creates an electric current path on the insulator surface. The presence of contamination on the insulator is necessary to form a conductive path, but it is not sufficient. In other words, contamination and moisture alone cannot cause the insulator to fail. The results show that as the leakage current increases, the temperature of the insulator surface increases as a result of the passage of this current. In article [12], it was stated that the presence of sufficient moisture on the contaminated insulator creates a conductive layer on the insulator surface by converting dry salt into electrolyte, and causes leakage current which is one of the factors of insulator failure. Using nanoparticles to create a coating on glass and ceramic insulators can prevent dirt and pollution from adhering, prevent deep absorption of contaminants on the surface, make insulators easy to clean and resistant to acid rain, increase resistance to surface scratches, improve insulating properties and help insulators remain clean for a long time. In paper [13], electric arc voltage tests conducted on 20 kV polymer insulators under uniform and non-uniform contamination, and different humidity levels were examined. The results showed that in presence of non-uniform contamination along with humidity, the insulators break down occurs earlier than in the case of uniform contamination. Moreover, increasing the degree of non-uniformity of contamination causes an increase in the surface conductivity in the insulators and as a result, the occurrence of a complete arc is accelerated. In article [14], it was stated that the contamination layer will not have much effect on the insulation resistance of the insulation as long as it is dry, and if it gets wet, it causes the dissolution of particles, and the formation of a conductive layer on the surface of the insulator. The results show that by having an insulator leakage current monitoring system, it is possible to compare the performance of high-voltage insulators with different profiles and materials in real environmental conditions, and with timely notification, washing and repair and maintenance operations will be carried out in a timely manner. In [15], a reduced experimental model is used to simulate a practical insulator washing equipment. The leakage current is measured using a current transformer. The results show that the leakage current increases first and then decrease during the washing process. In reference [16], the porcelain (PI) and silicone rubber insulators (SRI) used in the distribution network are modelled using COMSOL-Multiphysics software. The results indicate

that at a certain level of humidity, for the same level of pollution on the insulators, the intensity of electrical flashover on silicon rubber insulators is lower than porcelain insulators. The influence of climatic and environmental conditions on high voltage insulators have been discussed in [17]. The results show that even by observing the appropriate creepage distance in these environmental conditions, the insulation strength against power frequency voltages is compromised, and electrical flashover has occurred in the insulators. In [18], the behavior of aging and electrical failure of silicone rubber insulators under pollution and dry tape conditions are investigated, and the breakdown voltage and electric field distribution at different levels of pollution intensity have been measured. The practical results and simulation show that with the reduction of the intensity of pollution, the strength of failure and the probability of electrical failure decreases. In [19], the fragility curve of transmission line conductors against storms has been estimated. Uncertainties related to the behavior of transmission line conductors due to the conductor capacity and the random nature of wind fluctuations are considered. In reference [20], the authors state that the majority of distribution network failures during storms are related to tree branches hitting network conductors, trees falling on distribution network feeders, bird bodies hitting distribution feeders, and breaking bridges due to strong winds. In order to estimate the probability of equipment failure, the concept of fragility curve is used. In [21, 22], the importance of hardening distribution feeder lines and installing distributed generations (DGs) has been discussed. Hardening of the distribution network is one of the most effective methods to improve the resilience of distribution networks against natural events [22]. The use of DGs has increased due to their effect in improving the voltage profile, reducing power losses, reducing greenhouse gas emissions, increasing power quality, and increasing the reliability and resilience of the distribution system [21, 22]. By comparing the results, it is possible to show the effect of increasing the resilience of the distribution system and reducing the risk of the system by hardening the line conductors and optimal installation of distributed generation resources [22]. Paper [23] proposes a resilience assessment framework focused on planning to increase the level of resilience of the transmission system. The probabilistic model of the storm is presented with respect to the wind field and using the uncertainty in the intensity and track of the storm by the probability distribution. In Ref [24], the importance of evaluating system components to improve resilience in strengthening the network structure and designing a recovery strategy is discussed. Firstly, the component failure rate model under wind storm conditions is presented. Based on this model, the state of the system in the conditions of wind storms is sampled using the non-sequential Monte Carlo (MC) simulation method. After sufficient sampling of the system state, the repair time of the components is obtained. Copeland's ranking method is used to rank the importance of the components. In article [25] the necessity of using energy storage systems with the aim of increasing the reliability of the network and its use during off-peak as well as on-peak times is stated. In this model, the failure of components such as generators, pumps, turbines, control and protection systems is considered. The results show that the use of energy storage systems increases the reliability of the power system. In paper [26], the importance of using clean energy has been emphasized due to its

advantages such as low cost and ease of installation. Moreover, the problem of Generation Expansion Planning (GEP) in presence of demand response has been examined. Using the Weibull distribution function, the uncertainty of wind power plants and rewards and penalties have been modeled. Using the genetic algorithm in the proposed model, the optimal number of turbines has been determined and the results show that the expected unsupplied energy index has decreased. The paper [27] proposes a quantitative resilience assessment framework for power transmission systems operating under typhoon conditions that considers both the spatial and temporal impacts of the typhoon. Finite element component modelling is developed to model component failure probability. The simulation results have highlighted the capability of the proposed method in assessing and quantifying the resilience of power transmission systems against hurricanes.

1.3. Methodology and Contributions

Since most of the power system customers are fed from the distribution network, it is essential to have a high level of reliability and resilience at the distribution network level. Considering that the transmission network is located upstream of the distribution network and the transmission of energy from power plants to consumers is the responsibility of the transmission network, the need to have an acceptable level of stability and resilience is crucial to meet the needs of customers on the distribution network side. Therefore, it is necessary to evaluate the reliability and resilience of transmission network against various types of unforeseen natural events to help system operators determine preventive and corrective measures. Review of the above-mentioned researches reveals that the importance and impact of the dust storms, especially in the transmission network, have been rarely discussed. Meanwhile, a number of Middle Eastern countries such as Iran, Iraq, Saudi Arabia, etc. are currently dealing with this phenomenon. Moreover, the historical investigation of the occurrence of dust storm in Khuzestan province in Iran in 2017 shows that the impact of this phenomenon on the distribution and transmission network was high and it resulted in a lot of damages, blackouts and ENS [7]. In most of the studies conducted, the impact of wind storm was examined, while due to the climatic conditions of the Middle East, the occurrence of dust storms has increased significantly in recent years. According to the explanations given, the main problems in previous articles are:

- Less attention is paid to modeling the impact of dust storm phenomenon on power system.
- Failure probability of transmission system equipment during dust storm is not evaluated.

Therefore, in this paper we will evaluate the probability of transmission network insulators failure during dust storms and in various levels of humidity. In Table 1, the features of the reviewed articles are discussed and the features of the presented model are also shown.

On this basis, the main goal of this paper is to find the flashover probability of transmission network insulators in different levels of humidity and fine dust pollution. It is necessary to firstly examine the equations and relationships between the electric field and the electric potential distribution on the surfaces of the insulators.

Table 1: Comparison between the reviewed articles and the proposed model.

| Feature | Network | | Resilience | | | | Reliability |
|----------------|---------|---|------------|----|-----|----|-------------|
| | T | D | I | II | III | IV | |
| [8] | ✓ | x | x | x | x | x | ✓ |
| [15] | ✓ | x | x | x | x | x | x |
| [16] | x | ✓ | x | x | x | ✓ | x |
| [19] | ✓ | x | x | ✓ | x | x | x |
| [20] | x | ✓ | x | ✓ | x | x | x |
| [21] | x | ✓ | x | ✓ | ✓ | x | x |
| [22] | x | ✓ | x | ✓ | x | x | x |
| [23] | ✓ | x | x | ✓ | x | x | x |
| [25] | ✓ | x | ✓ | x | x | x | x |
| [27] | ✓ | x | ✓ | x | x | x | x |
| Proposed Model | ✓ | x | x | x | x | ✓ | x |

T: Transmission Network, D: Distribution Network, I: Wind, II: Storm, III: Flood, IV: Dust storm & Humidity.

On this basis, the main goal of this paper is to find the flashover probability of transmission network insulators in different levels of humidity and fine dust pollution. It is necessary to firstly examine the equations and relationships between the electric field and the electric potential distribution on the surfaces of the insulators. Then, a sample transmission insulator is created in simulation software, and by applying different amounts of moisture and fine dust on its surface, the possibility of electrical breakdown is examined. Finally, the effect of different levels of fine dust and humidity on transmission insulators is investigated.

Based on this, the contributions of this paper can be listed as follows:

- Simulating a sample 230 kV insulator in AutoCAD software, and applying moisture and fine dust to the designed insulator in COMSOL software.
- Investigating the flashover probability of the studied insulator in MATLAB software.
- Investigating the effects of fine dust and humidity on the flashover probability of different models of transmission network insulators.

The remainder of this paper is organized as follows: In [Section 2](#), the role of the insulator in power system and its types, as well as how the electric field and potential are distributed on its surface are discussed. In [Section 3](#), the process of calculating the probability of electrical failure in the modelled insulator is examined. Numerical results are provided in [Section 4](#) and conclusions are presented in [Section 5](#).

2. INSULATOR MODELLING

2.1. Insulator Types

An insulator is a device that has a high electrical strength and is installed between the live conductor and supporting structures such as transmission towers and distribution poles. In addition to insulating the conductor from the pole, insulators also form a mechanical connection between the conductor and the supporting structure [28]. The main functions of insulators include:

- Insulators must isolate the conductor from the pole while being able to withstand the highest voltage under

normal conditions without any leakage current. They should also have the necessary electrical strength when overvoltage occurs.

- The insulator must have the ability to withstand the mechanical forces caused by the weight of the conductor and the applied force caused by wind and ice on the conductor, without reducing the permissible distance of the conductor from the body and the base arm.

- The insulator must be resistant to severe weather changes and temperature changes and not lose its electrical and mechanical properties over time [28].

Classification of types of insulators is done based on the type of insulating material used in them and they are classified into three main categories of ceramic, glass and polymer insulators [28]. In the following, we briefly review the characteristics of different insulators.

2.1.1. Ceramic insulator

These types of insulators have high electrical strength against discharge caused by electric arc and corona phenomena, because the ceramic used in them has a high melting temperature of about 1500°C. Due to being brittle, special care should be paid when carrying these types of insulators. A special type of ceramic insulators is used in areas with high pollution, where a type of semiconductive glaze is used instead of the usual insulating glaze [7, 28]

2.1.2. Glass insulators

Raw materials such as silica, feldspar, dolomite, etc. are used to make this type of insulator. These materials are melted, homogenized and moulded in special furnaces. Then they are cooled by air jets for hardening. The mechanical endurance of this type of insulator is 1.5 times that of porcelain insulators. Moreover, the electrical strength of this type of insulator is higher than that of porcelain insulators. Moisture is easily distilled from the surface of these types of insulators; But these insulators attract more dust. The most widely used types of glass and ceramic insulators in the world are cap and pin insulators [7, 28].

2.1.3. Polymer insulators

The body of this class of insulators is made of organic materials and hydrocarbons. These types of insulators have weaker electrostatic strength than ceramic and glass insulators. Over time, they lose their electrical and mechanical properties and become worn-out. Since organic materials have low energy, they are not easily wetted by water and have high hydrophobic properties. Compared to ceramic and glass insulators, it is lighter and less brittle [7, 28].

2.2. Potential Distribution on the Insulator Surface

The potential distribution on the surface of the insulator is non-uniform due to the presence of metal parts. [Fig. 1](#) shows the capacitance model of the insulator chain, where C is the capacitance of each insulator, C_E is the capacitance of the insulator relative to the ground, and C_L is the capacitance of the insulator relative to the line. H is the length of the insulator, and x is the distance from the ground electrode.

We assume that the capacities C , C_E and C_L are constant, and their relationship with the length of the insulator is shown

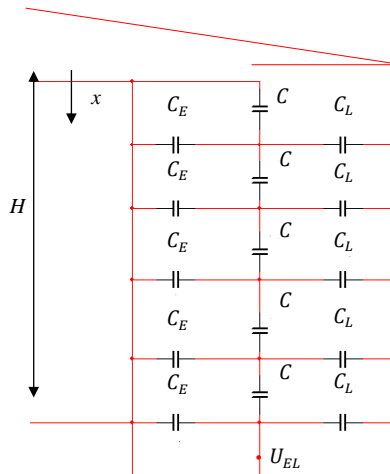


Fig. 1: Insulator capacitance model [29].

as (1) to (3) [30]:

$$C' = C \times H \quad (1)$$

$$C'_L = \frac{C_L}{H} \quad (2)$$

$$C'_E = \frac{C_E}{H} \quad (3)$$

The voltage and current equations will be in the form of (4) and (5) [30]:

$$\frac{dU_x}{dX} = \frac{1}{j\omega C'} \quad (4)$$

$$\frac{dI}{dX} = U_x j\omega C' + (U_x - U_{EL}) j\omega C' \quad (5)$$

2.3. Electric Field

In the design of high voltage equipment, it is very important to know the electric field distribution, because the field intensity must be tolerable for electrical insulation at all points. The critical value of electric field intensity (E_c) refers to the maximum electric field intensity that can be tolerated without causing electrical failure in insulating materials. This value depends on the physical and chemical characteristics of the insulators, including their composition and structure. Humidity is one of the important factors that can affect the critical value of electric field intensity. In conditions where the humidity in the environment increases, water can act as a poor conductor and thus reduce the insulation resistance. Studies show that the critical value of electric field intensity in the air should not exceed 3 (kV/mm) [31]. Some electric fields, such as homogeneous fields, can be obtained analytically, but if the geometrical shape of insulators and electrodes is complicated, it will be difficult to perform calculations analytically, and as a result, it is done using numerical methods and iterative calculations. The intensity of the electric field is considered as the gradient of the electric potential, and we will have [32]:

$$E = -\text{grad } V = -\nabla V \quad (6)$$

Since the field is created by the presence of electric charges, the divergence of the electric flux density will be equal to the volume density of the electric charge [32]:

$$\text{div } \bar{D} = \rho \quad (7)$$

If there is no charge in the space under study, the relationship between E and D is obtained from (8) [32]:

$$D = \epsilon E \quad (8)$$

$$\text{div } \bar{E} = \frac{\rho}{\epsilon} \quad (9)$$

Using (6) and (8), we will have [32]:

$$\text{div } \nabla V = -\frac{\rho}{\epsilon} \quad (10)$$

Moreover, the divergence of the gradient is equal to the Laplacian [32]:

$$\nabla^2 V = -\frac{\rho}{\epsilon} \quad (11)$$

Using Poisson's equation, equation (11) in Cartesian coordinate axes will be as follows [32]:

$$\nabla^2 V = \frac{\partial^2 V}{\partial x^2} + \frac{\partial^2 V}{\partial y^2} + \frac{\partial^2 V}{\partial z^2} = -\frac{\rho}{\epsilon} \quad (12)$$

It is very difficult to solve voltage equations in non-homogeneous field distribution, and for this purpose, an iterative numerical method is used. Among the numerical methods, we can mention finite difference method, finite element method, charge simulation method and boundary element method [32].

2.3.1. Finite Difference Method

The finite difference method (FDM) is one of the numerical techniques used to solve partial differential equations (PDEs). To use this method, the desired domain is divided into a discrete network and the coordinates of each point in the network are determined as (i,j). Then the spatial derivatives in the equations are approximated using finite differences. By replacing the approximated derivatives in the original equations, a set of linear equations is obtained which can be represented as a matrix, and can be solved by different numerical methods such as Gauss-Seidel. Finally, the results should be analysed and checked to confirm their accuracy [32].

2.3.2. Finite Element Method

The main idea of the finite element method is to divide the object or area under analysis into a large number of finite elements. These elements may be one, two or three-dimensional. The classic and popular type of element for the two-dimensional case is the triangular element. The nodes of this type of element are conveniently located at the vertices of the triangle. In the two-dimensional case, rectangular elements can also be used, but triangular elements are more suitable for meshing complex shapes. After discretization, it is time to obtain the stiffness matrix for each element. In this method, a digital computer is required due to the high computational burden. Solving problems with this method is done using commercial finite element software such as COMSOL, ANSYS, Abaqus, CATIA, etc [32].

2.3.3. Charge Simulation Method

Charge simulation method is one of the simple and effective techniques in the analysis of electric fields. This method is based on the principle of superposition, which

states that the electric field caused by several point charges is equal to the sum of the electric fields caused by each charge. In this context, the charges in the system are identified and their positions are determined, and then the associated electric fields are calculated and aggregated to yield the total field [32].

2.3.4. Boundary Element Method

The boundary element method (BEM) is based on the principle of superposition and the theory of potentials. In this method, physical fields are expressed as integral equations on the boundary of the domain. Firstly, the boundary conditions and the field type are determined. Then the governing equations of the field are written in integral form. Then, using the boundary conditions and basic functions, the integral equations are established, and solved using numerical techniques to obtain the field values at the boundary points. In this method, due to the fact that only the boundaries are analysed, the number of variables required to solve the problem is reduced. In many problems, BEM can provide higher accuracy than other methods [32].

Table 2 shows the advantages and disadvantages of each of the presented methods. Due to the complex and different geometric shapes in the structure of the insulator cap and pin, and since we use COMSOL software, which is one of the most powerful engineering software in analysis, and considering the other advantages of the finite element method over other methods stated in Table 2, FEM has been chosen to conduct electrostatic field studies.

2.4. Insulator Modelling

2.4.1. Introduction of the studied insulator

The modelled insulator is shown in Fig.2, which is a porcelain type with a rated voltage of 230 kV from the catalogue of 120 kilonewton insulators of POWER TRIGOLD. Using the insulator catalogue in Table 3, its exact dimensions are extracted. This insulator is called type 1 insulator in this paper.

2.4.2. Calculation of Electrostatic Fields

According to the review of the literature, the presence of dust alone does not cause an electric arc on the insulator

Table 2: Advantages and disadvantages of the introduced methods [33-35].

| Method | Advantage | Disadvantage |
|--------------------------|--|---|
| Finite difference method | <ul style="list-style-type: none"> • Understandable and simple • Fast calculations in simple problems • Can be used to solve ordinary and partial differential equations | <ul style="list-style-type: none"> • Low accuracy • Difficult to implement on problems with complex geometry • Reduced accuracy at boundary points |
| Finite element method | <ul style="list-style-type: none"> • Suitable for complex geometries and different boundary conditions • High accuracy of results with proper discretization • Usable for problems with variable material properties | <ul style="list-style-type: none"> • More complex to learn and implement • Requires long computation time • Requires the use of specialized software |
| Charge simulation method | <ul style="list-style-type: none"> • Easy to understand and use • Can be used for quick and approximate analyses | <ul style="list-style-type: none"> • Dependence of the accuracy of the results on the assumptions • Inability to solve problems with complex geometries |
| Boundary element method | <ul style="list-style-type: none"> • Reduces the dimensions of the problem because it only considers the boundaries • High accuracy in non-local problems with specific boundary conditions • Usable for problems with variable material properties | <ul style="list-style-type: none"> • Requires a deeper understanding of mathematics and physics • Difficult for complex and multidimensional geometries • Dependence of the accuracy of the results on the assumed boundary conditions |



Fig. 2: Type 1 insulator cap and pin model [36].

Table 3: Data of type 1 insulator [36].

| | |
|--------------------------------------|--------------|
| IEC Class | U120BS |
| Type | XP-120 |
| Porcelain Disc Diameter, D. mm | 245 |
| Unit Spacing, H. mm | 146 |
| Standard Coupling to IEC 120 | 16B/16A |
| Creepage Distance, mm | 320 |
| Combined M & E Strength, kN | 120 |
| Routine Test Load, kN | 48 |
| Power Frequency Flashover Voltage | Dry, kV 78 |
| | Wet, kV 45 |
| 50% Impulse Flashover Voltage | Pos., kV 120 |
| | Neg., kV 125 |
| Power Frequency Withstand Voltage | Dry, kV 70 |
| | Wet, kV 40 |
| Impulse Withstand Voltage, kV | 110 |
| Power Frequency Puncture Voltage, kV | 110 |

surface, and when the insulator surface is also covered with moisture in addition to dust, a path for the creation of an electric arc is created. This path is modeled as a conductive layer. As a result, to model the effect of dust on the insulator, a conductive layer with a thickness of 2 mm has been created on the insulator surface. Table 4 shows information related to the levels of contamination based on different standards. According to the IEC standard, if the level of contamination exceeds 0.6 mg/cm^2 , the contamination level will be very heavy.

Finite element method has been used to simulate and calculate electrostatic fields. To simulate dust on the insulator, an outer layer with a thickness of 2 mm is considered on the surface of the insulator. By changing the conductivity of the outer layer, the effect of different environmental conditions of humidity and pollution can be simulated on the surface of the insulator. Fig.3 shows the conductive layer created on the insulator, the conductivity of which is determined based on the data in Table 5.

The characteristics of the pollution layer change due to different pollution intensities. Table 5 typically presents the characteristics of different levels of pollution.

Therefore, by increasing the ESDD value in the present study, the effect of various pollutants such as industrial and marine pollution can be calculated in determining the probability of failure of electrical insulators located in the vicinity of these areas.

From (11) and (12), we have [31]:

$$\nabla \cdot \epsilon \nabla V = -\rho_s \Rightarrow \epsilon \nabla^2 V + \rho_s = 0 \quad (13)$$

In (13), ρ_s is the flux density and ϵ is the permeability coefficient; As a result, the voltage distribution in the presence of contamination will be as follows [31]:

$$(\sigma + j\omega\epsilon)\nabla^2 V + j\omega\rho_s = 0 \quad (14)$$

In (14), σ is the conductivity and ω is the angular frequency ($\omega = 2\pi f$). Since the surface charge density along the length of the insulator is zero ($\rho_s = 0$), equation (14) is rewritten as (15) [31]:

$$S_a = (5.7 \times 10^{-4} \times \sigma_{20})^{1.03} \quad (15)$$

S_a is the hardness of the solution in g/cm^3 and σ_{20} is the electrical conductivity of the solution in $\mu\text{S/cm}$ at a temperature of 20°C , V is the volume of the pollution solution in cm^3 , and A is the surface area of the insulator in cm^2 .

As a result, the pollution intensity index is extracted from (16) [7]:

$$ESDD = \frac{S_a \times V}{A} \quad (16)$$

Table 4: Different levels of pollution based on common standards [7].

| Pollution Level | IEC | IEEE | CIGRE |
|-----------------|-----------|-----------|------------|
| Very Light | - | 0-0.03 | 0.015-0.03 |
| Light | 0.03-0.06 | 0.03-0.06 | 0.03-0.06 |
| Medium | 0.1-0.2 | 0.06-0.1 | 0.06-0.12 |
| Heavy | 0.3-0.6 | >0.1 | 0.12-0.24 |
| Very Heavy | >0.06 | - | 0.24-0.48 |
| Special | - | - | >0.48 |

Table 5: Information about different pollution levels [18].

| Pollution Level | ESDD (mg/cm^2) | Conductivity (S/m) |
|-----------------|---------------------------|--------------------|
| Light | 0.035 | 1.4 |
| Medium | 0.1 | 4 |
| Heavy | 0.2 | 8 |
| Very Heavy | 0.4 | 16 |

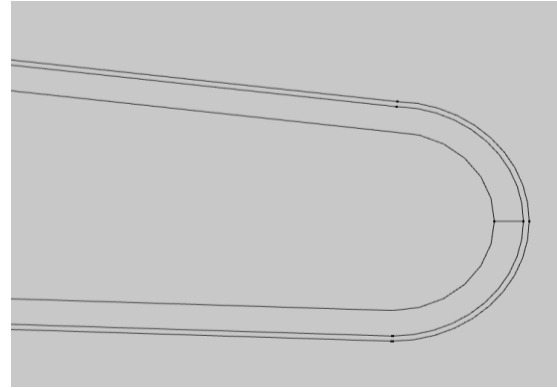


Fig. 3: Conductive layer created on the insulating shed to simulate dust.

2.4.3. Simulation of the Studied Insulator

At first, the studied insulator is designed in AutoCAD software. Fig.4 shows the pin and cap of the studied insulator in the AutoCAD Electrical software environment. Then we use Multiphysics 6.2 COMSOL program to simulate the pollution and moisture layer on the insulator. This program is one of the powerful tools for simulating physical and engineering phenomena. This software is especially used in the fields of electromagnetism, fluid mechanics, heat transfer and structural analysis. Fig.5 shows the electric potential distribution on the insulator designed in COMSOL software. Due to axial symmetry along the length of the insulator, two-dimensional modeling has been used for simulation. The electric field distribution on the studied insulator is shown in Fig.6.

In the next step, we determine the type of insulating material and the characteristics of the space around it. We put the material around the chain as air, cap and pin as iron, and silicon as the shackle. Table 6 shows the specifications of the materials used in the design of the insulator.

The boundary conditions of the problem are determined as the known potential of the high voltage electrode and the zero potential of the ground electrode. Fig.7 shows the meshing of the insulator and the space around it.

3. CALCULATING THE FLASHOVER PROBABILITY

Using the Finite Element Method (FEM), the electric field and potential distribution throughout the insulator is calculated. Complete electrical breakdown occurs when the average electric field between two points is greater than the critical value of electric field intensity (E_c), equation (17) shows this concept [16].

$$\Delta v(E) > E_c(H) \times d \quad (17)$$

To calculate the probability of electric arc jumping from one point to other points on the surface of the insulator, first the voltage difference between the desired point (such as point x) and its surrounding points should be calculated in

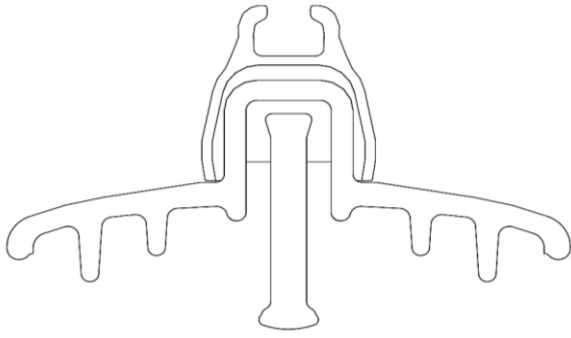


Fig. 4: Cap and pin modeling of type 1 insulator in AutoCAD software.

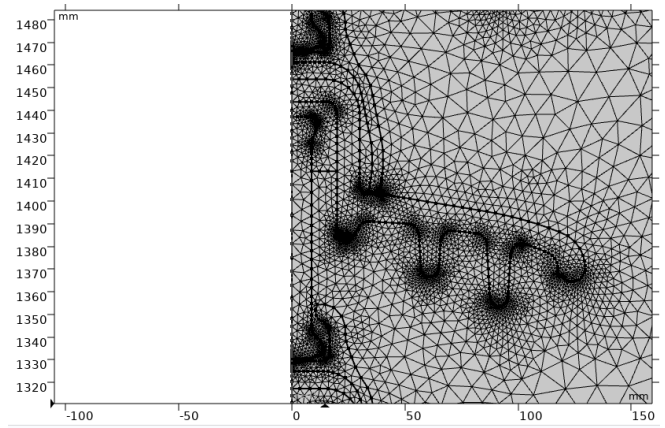


Fig. 7: Type 1 insulator meshing in COMSOL software.

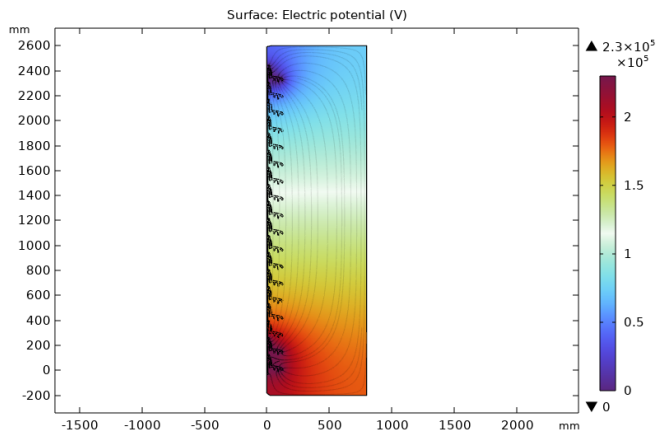


Fig. 5: Electric potential distribution on type 1 insulator in COMSOL software.

each step. Then, all the points whose voltage difference with the desired point is greater than the critical value are considered as possible points for electric arc jump [16]. Fig. 8 shows the process of selecting candidate points.

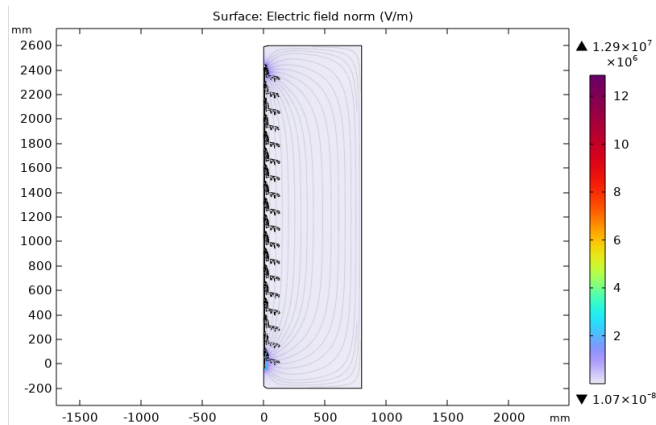


Fig. 6: Electric field distribution on type 1 insulator in COMSOL software.

Table 6: Characteristics of the materials used in the design of type 1 insulator [31].

| Material | Silicone rubber | Iron | Air |
|--------------------|---------------------|----------------------|-----|
| Conductivity (S/m) | 1×10^{-18} | 1.4×10^{-7} | 0 |
| Permittivity (F/m) | 3.6 | 100~500 | 1 |

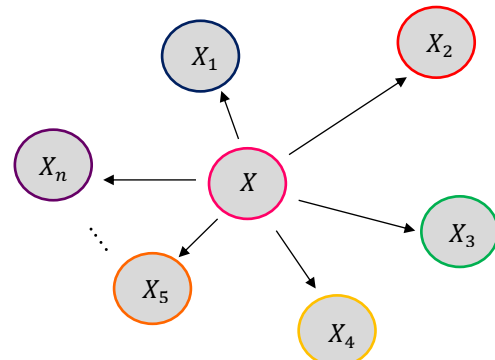


Fig. 8: Determining the initial point (X) and checking the probability of arc to each of the surrounding points.

The possible points for jumping the arc are placed randomly in a roulette wheel. The probability of arc jump depends on the intensity of the voltage difference and the distance between the points. Fig. 9 shows an example of the process of selecting the next candidate point to check the probability of arc.

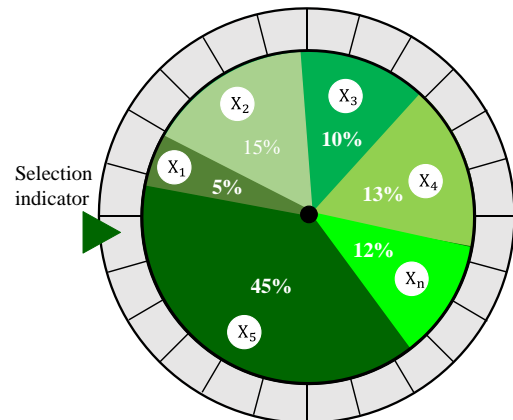


Fig. 9: Using the roulette wheel to determine the next point in consecutive arcs.

Finally, to calculate the flashover probability ($P_{Flashover}$), a certain number of arc jump processes must be repeated. Flashover probability is calculated using the ratio of the number of complete flashovers ($N_{Flashover}$) to the total number of flashovers (N_{All}).

$$P_{Flashover} = \frac{N_{Flashover}}{N_{All}} \quad (18)$$

In general, the relationship between AutoCAD, COMSOL and MATLAB software is shown in Fig.10. First, we design the insulator in AutoCAD Electrical software. From the Geometry section, using the Import option, we import the designed CAD file into the COMSOL software. Then, in the Materials section, enter the materials used in the insulation and apply the desired pollution and humidity in the Electric Current section. At the end, we extract the output text file in the Result section. By calling the text file in MATLAB software and using the procedure mentioned in Fig. 11, the probability of insulation failure is calculated. Fig.11 shows the process followed to calculate the probability of electrical breakdown in the insulator. We indicate the total number of iterations with N and set it equal to 100. At first, it is necessary to call the coordinates and voltage value of all the points in the text file taken from COMSOL software in MATLAB. Then, the point with the highest voltage is selected as the starting point for checking successive arcs. After finding this point using (17), the probability of arc occurrence is calculated for all the surrounding points. If the probability of arc occurrence to the surrounding points is equal to zero, we add one to the counter of no arc ($N_{No-Flashover}$) in this iteration. On the other hand, if the calculated probability is not equal to zero, that means the field difference between two points is greater than E_c (3 kV/mm), the next candidate point is selected using the roulette wheel, and this process continues until the voltage of the point where the arc is struck is equal to zero, in other words, the arc has reached the end point of the insulator. In this case, the flashover counter ($N_{Flashover}$) is incremented by one. Finally, if 100 repetitions for the insulator at a certain level of pollution and humidity are examined, the probability of failure will be calculated based on (18). To obtain the probability of failure in each level of humidity and different amounts of pollution in each step, the text output file taken from COMSOL software was called and the probability of failure for each level of humidity and pollution was calculated according to the flowchart in Fig.11.

4. NUMERICAL RESULTS

4.1. Model Validation

Most of the reviewed articles have considered the calculation of leakage current in different levels of dust and humidity. In articles [16] and [31], the probability of failure at different pollution levels and humidity of 80% has been investigated for 36 kV and 66 kV insulators. On the other hand, reference [37] have not mentioned the humidity level used for investigating the failure probability of 138 kV insulators. Given that the detailed data of the insulator model and humidity level in [31] and [37] are not provided, we have investigated the probability of failure of the silicone rubber insulator introduced in [16]. For this goal, we have modelled the insulator according to the explanations mentioned in the article. Subsequently, the failure curve was extracted for the modelled insulator. In Fig. 11, the curve reported in [16] and the curve that we extracted by simulation are compared.

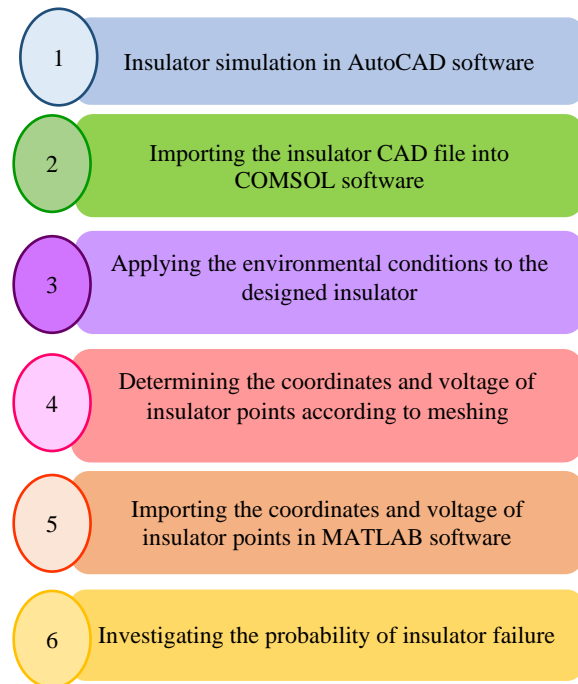


Fig. 10: Established links between software packages.

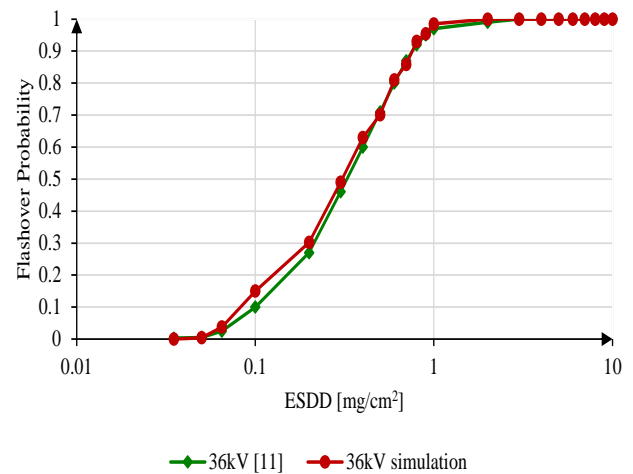


Fig. 11: Comparison of failure probability obtained from simulation and the curve reported in [11].

The results show that the obtained failure probability is in good agreement with the data in [11], and after validating the modelling process, we proceeded to examine the 230 kV insulator.

4.2. Calculation of Failure Probability in the Studied Insulator

In this section, we import the x and y values from the output of the text file taken from COMSOL software into MATLAB software. It is necessary to select insulator's high voltage point as the reference point to check possible arcs. In the insulator, electric breakdown occurs completely when these arcs start from the high voltage point and reach the point that has zero voltage (the bottom of the insulator). In this case, a complete arc occurs, but in some cases, the arc may advance to a certain point, but not reach the end of the insulator. In this case, we will not have a complete arc. Fig.12 shows examples

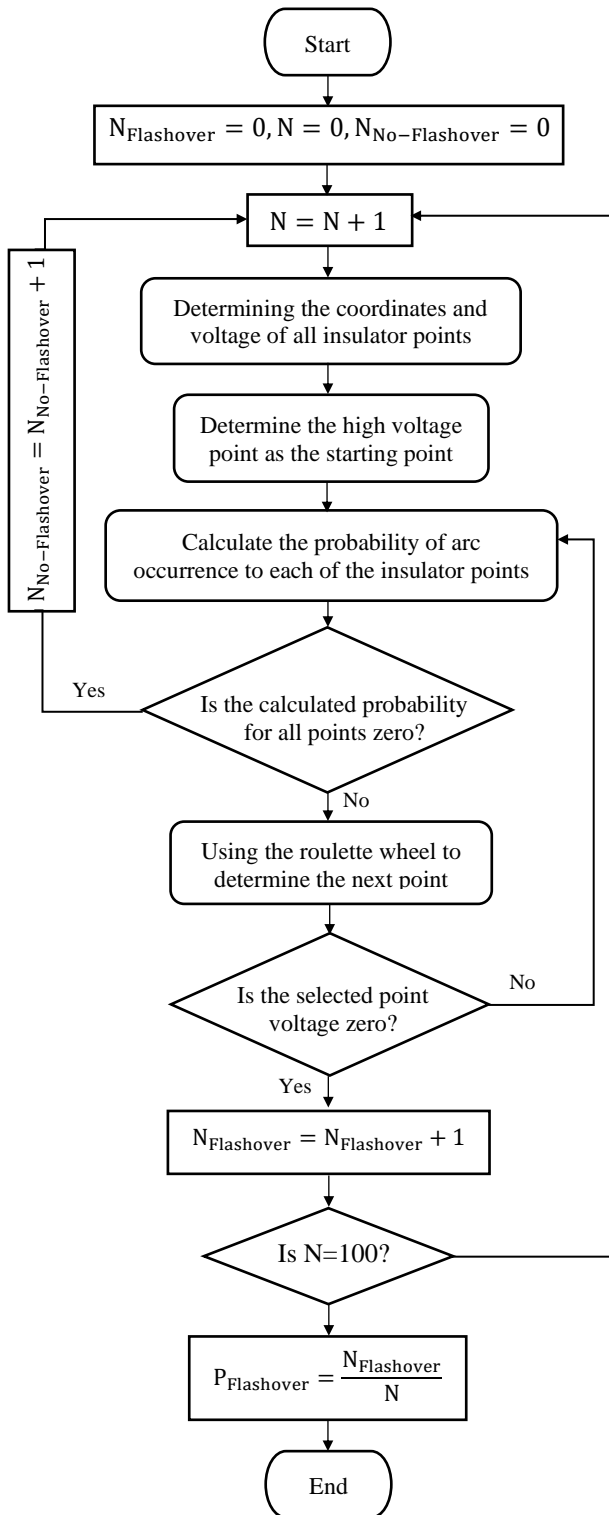


Fig. 11: Flashover probability calculation flowchart.

of complete and incomplete arc. Table 7 shows two examples of complete and incomplete arc processes that are determined based on (18). After going through the process mentioned for each of the data extracted at different levels of humidity and pollution, the probability curve of the insulation failure under study is shown in Fig. 13.

4.3. Sensitivity Analysis

4.3.1. Case study 1

Firstly, we want to investigate the effect of pollution on the

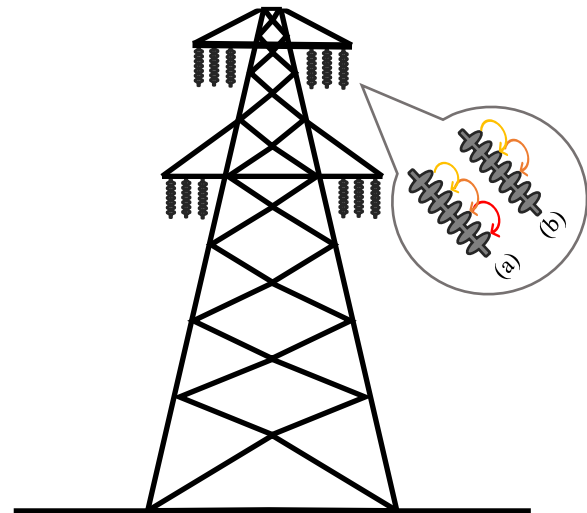


Fig. 2: (a) An example of a complete arc on an insulator surface, (b) An example of an incomplete arc on an insulator surface.

Table 7: Successive arcs in two complete and incomplete arc states for type 1 insulation in 65% humidity and ESDD of 0.2 (mg/cm²).

| Incomplete arc | | | |
|----------------|----------|----------------------|----------------------|
| j | X | Y | V(V) |
| 1 | 43.9163 | 47.2675 | 6.147×10^6 |
| 2 | 37.5892 | 90.9209 | 5.6652×10^6 |
| 3 | 93.4627 | 140.5593 | 4.5192×10^6 |
| 4 | 94.1069 | 192.20201 | 4.2863×10^6 |
| 5 | 154.2661 | 190.6057 | 4.1587×10^6 |
| 6 | 154.2661 | 190.6057 | 4.1587×10^6 |
| Complete arc | | | |
| j | X | Y | V(V) |
| 1 | 28.0634 | 2.3392×10^3 | 1.1104×10^6 |
| 2 | 22.6748 | 2.339×10^3 | 1.0908×10^6 |
| 3 | 22.7363 | 2.344×10^3 | 9.141×10^5 |
| 4 | 40.7162 | 2.3608×10^3 | 1.6772×10^5 |
| 5 | 37.9779 | 2.3581×10^3 | 8.0465×10^4 |
| 6 | 36.7238 | 2.359×10^3 | 0 |

probability of failure on the surface of the insulator at a constant level of humidity. According to the curve obtained in Fig.13, it can be concluded that for a constant humidity level such as 65%, with increasing pollution, the possibility of flash over in the insulator has increased. For example, the probability of electrical failure in ESDD of 0.1 is about 4%, while in ESDD of 0.5, the probability of failure is 32%. This point shows the effect of micro dust on power grid elements, especially high voltage insulators, which reduces the stability and reliability of the power system due to the occurrence of arcing in these insulators. Table 8 shows the probability of arc occurrence in 65% humidity for type 1 insulator at different pollution levels.

4.3.2. Case study 2

In this case, we intend to investigate the effect of humidity on the possibility of insulation failure in the presence of pollution. It was mentioned in the reviewed papers that the presence of fine dust alone does not cause

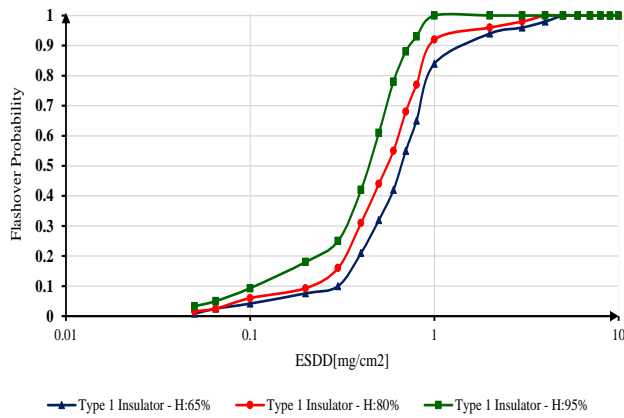


Fig. 13: Flashover probability of type 1 insulator at different levels of pollution and humidity.

Table 8: The flashover probability at 65% humidity for different amounts of pollution in type 1 insulator.

| Humidity (%) | ESDD (mg/cm ²) | Flashover Probability (%) |
|--------------|----------------------------|---------------------------|
| 65 | 0.1 | 4.2 |
| 65 | 0.5 | 32 |
| 65 | 1 | 84 |
| 65 | 5 | 100 |
| 65 | 10 | 100 |

arcing in insulators, and the presence of moisture along with fine dust creates the possibility of electrical breakdown in insulators. According to the results of Table 9, which are extracted from Fig. 13, we find that in a fixed level of pollution, by increasing the humidity, the probability of failure increases and this will affect the reliability of the power system.

4.3.3. Case study 3

In this section, we increase the number of discs from 18 to 23, and call it type 2 insulator. All the materials are similar to Table 6. We calculate the possibility of failure in 80 % humidity for different amounts of contamination for type 2 insulator. In Table 10, samples of complete and incomplete arc on type 2 insulator are provided. Fig. 14 compares the probability of type 1 and type 2 at humidity level of 80 %.

In Table 11, the probability of failure for type 1 and 2 insulators in 80% humidity and different levels of contamination is compared. As can be seen, with the increase in the number of disks and the increase in the creepage distance, the probability of electrical failure has decreased.

4.3.4. Case study 4

Among the ways to reduce the probability of arcing in power system insulators before natural disasters, predicting the probability of natural events [20], replacing worn-out elements of the network [2, 19], washing program of the insulators [8], using silicone rubber insulators [16], using organic paint coating to repair corrosion [29] and using insulators with more sheds [16]. As for the third study, we increase the number of sheds and set the type of insulating materials according to Table 12. The insulator studied in this section is called type 3 insulator. The potential distribution on the type 3 insulator in the COMSOL software environment is shown in Fig.15, and the electric field distribution on this

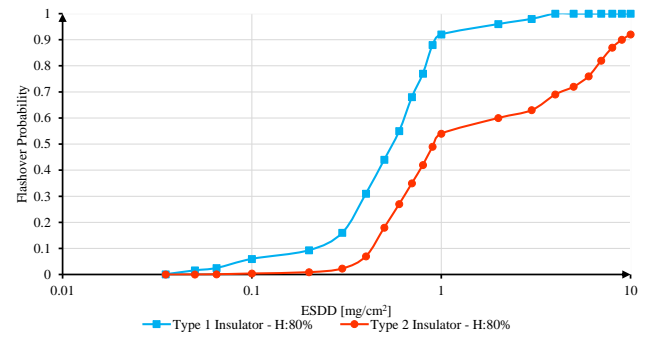


Fig. 14: Comparing the flashover probability of type 1 and type 2 insulators in 80% humidity for different amounts of pollution.

Table 9: The effect of humidity on the flashover probability of type 1 insulator.

| Humidity (%) | ESDD (mg/cm ²) | Flashover Probability (%) |
|--------------|----------------------------|---------------------------|
| 65 | 0.6 | 42 |
| 80 | 0.6 | 55 |
| 95 | 0.6 | 78 |

Table 10: Successive arcs in two complete and incomplete arc states for type 2 insulator in 80% humidity and ESDD of 0.3 (mg/cm²).

| Incomplete arc | | | |
|----------------|----------|----------------------|----------------------|
| j | X | Y | V(V) |
| 1 | 22.8496 | 1.3824×10^3 | 3.4535×10^5 |
| 2 | 43.4439 | 2.4347×10^3 | 2.5296×10^5 |
| 3 | 19.1831 | 2.3937×10^3 | 4.6612×10^3 |
| 4 | 19.1831 | 2.3937×10^3 | 4.6612×10^3 |
| Complete arc | | | |
| j | X | Y | V(V) |
| 1 | 9.7955 | 1.8878×10^3 | 2.148×10^6 |
| 2 | 9.6899 | 2.242×10^3 | 7.9706×10^5 |
| 3 | 130.659 | 2.3292×10^3 | 4.9211×10^4 |
| 4 | 12.3583 | 2.3273×10^3 | 7.5626×10^3 |
| 5 | 129.4585 | 2.328×10^3 | 0 |

Table 11: Comparing the probability of electrical breakdown of type 1 and 2 insulators for 80% humidity.

| Insulator Type | ESDD (mg/cm ²) | Flashover Probability (%) |
|----------------|----------------------------|---------------------------|
| 1 | 0.1 | 6 |
| 2 | | 0.4 |
| 1 | 0.5 | 44 |
| 2 | | 18 |
| 1 | 1 | 92 |
| 2 | | 54 |
| 1 | 10 | 100 |
| 2 | | 72 |

Table 12: The material used in the type 3 insulator [31].

| Material | Silicone rubber | Fiberglass | Metal fittings | Air |
|--------------------|---------------------|---------------------|---------------------|-----|
| Conductivity (S/m) | 1×10^{-18} | 1×10^{-18} | 3.774×10^4 | 0 |
| Permittivity (F/m) | 3.6 | 4.2 | 1 | 1 |

insulator is shown in Fig. 16. Fig.17 shows the meshing on the surface of the type 3 insulator in the COMSOL software

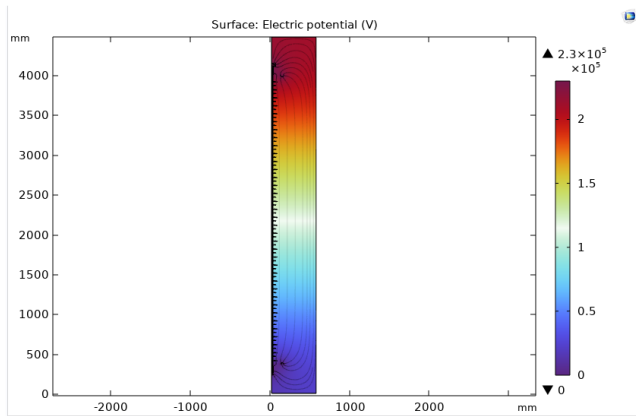


Fig. 15: Electric potential distribution on type 3 insulator in COMSOL software.

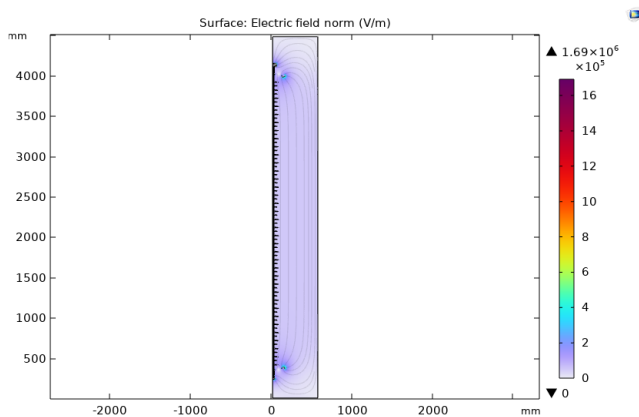


Fig. 16: Electric field distribution on type 3 insulator in COMSOL software.

Table 13: Specifications of type 3 insulator [38].

| | | |
|------------------------------------|----------|--------|
| Voltage Level | kV | 230 |
| Tensile Strength | kN | 160/80 |
| Creepage Distance, mm | mm | 11000 |
| Arcing Distance | mm | 2650 |
| Section Distance | mm | 2920 |
| Lighting Impulse Withstand Voltage | Pos., kV | 1050 |
| | Neg., kV | 1080 |
| Power Frequency Withstand Voltage | Dry, kV | 460 |
| | Wet, kV | 510 |

environment. The specifications of the type 3 insulator are reported in Table 13.

Fig. 18 compares the probability of failure of type 1 and type 3 insulators in 80% humidity. The effect of increasing the number of sheds as well as the materials used in insulation coating can be clearly seen in the probability of insulation failure. In type 1 insulator with ESDD of 1 and 80% humidity, the probability of electrical failure is more than 90%, while in type 3 insulator with the same pollution and humidity conditions, the probability of electrical failure is about 35%. Table 14 shows the probability of flashover for type 1 and 3 insulators for 80% humidity in different pollution levels.

4.3.5. Case study 5

In the following, different conductivity levels are applied to each of the 3 studied insulator types at 80% humidity. The

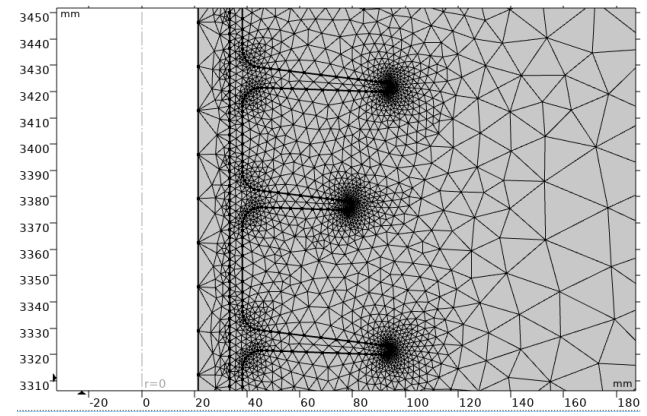


Fig. 17: Meshing on type 3 insulator in COMSOL software.

Table 14: Comparing the probability of electrical breakdown of type 1 and 3 insulators for 80% humidity.

| Insulation Type | ESDD (mg/cm ²) | Flashover Probability (%) |
|-----------------|----------------------------|---------------------------|
| 1 | 0.1 | 6 |
| 3 | | 0.025 |
| 1 | 0.5 | 44 |
| 3 | | 11 |
| 1 | 1 | 92 |
| 3 | | 35 |
| 1 | 10 | 100 |
| 3 | | 89 |

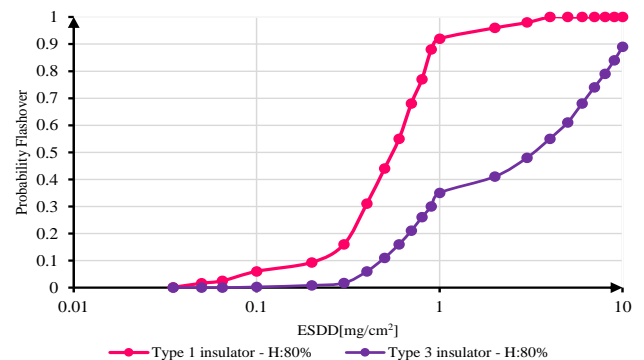


Fig. 18: Comparing the flashover probability of type 1 and type 3 insulators in 80% humidity for different amounts of pollution.

results in Fig. 19 show that by increasing the amount of ESDD, the conductivity also increases, resulting in a higher flashover probability. Moreover, the probability of failure at each humidity level is higher in type 1 insulator, while type 3 insulator has the lowest probability.

4.4. Curve Fitting Results

In order to use the obtained results more easily, using the curve fitting toolbox of MATLAB software, the equations of distribution probability function are obtained and reported in Table 15. In these equations, the probability of flashover is indicated by y and the value of ESDD is indicated by x. Fig. 20 shows an example of curve fitting in MATLAB software. In Fig. 20, the blue curve is the flashover curve of type 1 insulator at 65% humidity and the orange curve is the fitted probability distribution function.

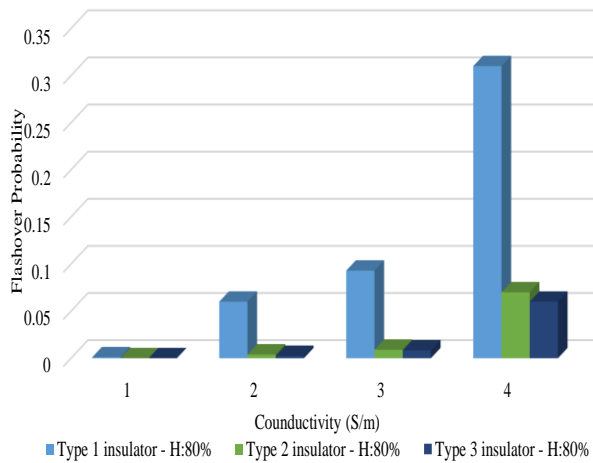


Fig. 19: Comparison of the failure probability of three types of insulators in different conductivities.

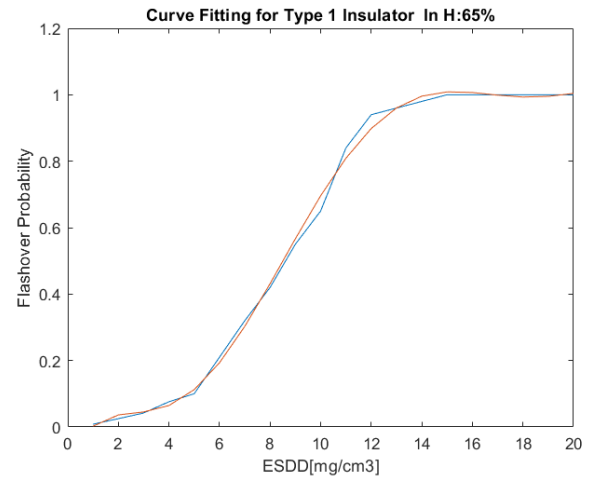


Fig. 20: Comparison of the flashover curve of type 1 insulator at 65% humidity with the fitted probability distribution function.

Table 15: Probability distribution function for the fragility curve of the studied insulator.

| Type of insulation | Probability Distribution Function |
|---------------------------|--|
| Type 1 insulator - H: 80% | $y = 2.7563 \times 10^{-4}(x^5) - 0.0083(x^4) + 0.095(x^3) - 0.5037(x^2) + 1.2275x - 0.1018$ |
| Type 1 insulator - H: 80% | $y = -4.7881 \times 10^{-5}(x^5) + 0.0018(x^4) + 0.0279(x^3) + 0.2121(x^2) - 0.8371x + 1.5931$ |
| Type 1 insulator - H: 80% | $y = -1.1648 \times 10^{-4}(x^5) + 0.004(x^4) - 0.0552(x^3) + 0.372(x^2) - 1.278x + 2.0473$ |
| Type 2 insulator - H: 80% | $y = 1.7018 \times 10^{-4}(x^4) - 0.0053(x^3) + 0.0615(x^2) - 0.3253x + 0.8041$ |
| Type 3 insulator - H: 80% | $y = 1.0215 \times 10^{-4}(x^4) - 0.0031(x^3) + 0.0343(x^2) - 0.1779x + 0.482$ |

5. CONCLUSION

The purpose of this article is to investigate the probability of failure of transmission network insulators in presence of micro dust phenomenon, as one of the adverse natural events that has become more intense in recent years due to climate changes. The presence of pollution alone does not cause arcing and electrical breakdown in insulators, whereas in the presence of humidity, the probability of electrical discharge increases. Failure of insulators affects the stability, reliability and resilience of the power system, and by reducing the probability of failure of insulators, the duration of blackout and the amount of unserved energy can be reduced. In this context, as the first step, type 1 insulator was investigated and it was shown that the probability of failure in the insulator increases with the increase in the amount of pollution at a certain level of humidity. Moreover, the results indicate that with the increase of humidity at a certain level of pollution, the probability of electrical discharge on the surface of the insulator has also increased. Finally, according to the proposed corrective measures, the number of discs has been increased, and a number of sheds have been placed among the discs, and the material used has also been changed to silicone rubber in order to investigate the possibility of insulation failure in this situation. The results show that by carrying out the above-mentioned corrective measures, the probability of electric failure in type 2 and 3 insulators has been greatly reduced, and this confirms the that replacement of grid insulators with silicon-rubber coated insulators, as well as the increasing their creepage distance, are effective solutions for improving the power system resilience against dust storms. Moreover, from the comparison of Fig. 7 and Fig. 17 in the

paper, which show the meshing on the sheds of the type 1 and 3 insulators, it can be seen that in the type 1 insulator, based on its cap model, a finer meshing was used with more points compared to type 3 insulator. This is due to the existence of sharp points, which justifies a finer meshing than other points where the electric field is more uniform.

CREDIT AUTHORSHIP CONTRIBUTION STATEMENT

Yasaman Abbasi Chahardah Cheriki: Data curation, Software, Visualization, Roles/Writing - original draft. **Hossein Farzin:** Conceptualization, Methodology, Validation, Writing - review & editing. **Elaheh Mashhour:** Validation, Writing - review & editing.

DECLARATION OF COMPETING INTEREST

The authors declare that they have no known competing financial interests or personal relationships that could have appeared to influence the work reported in this paper. The ethical issues; including plagiarism, informed consent, misconduct, data fabrication and/or falsification, double publication and/or submission, redundancy has been completely observed by the authors.

REFERENCES

- [1] R. Billinton and R. N. Allan, *Reliability evaluation of power system*, 1996.
- [2] M. Bhusal, M. Gautam, M. Abdelmalak, M. Benidris, "Modeling of natural disasters and extreme events for power system resilience enhancement and evaluation methods," in *2020 International Conference on*

- Probabilistic Methods Applied to Power Systems (PMAPS)*, 2020, pp. 1-6.
- [3] P. Mahzarnia, and P. Teimourzadeh Baboli, "A review of the measures to enhance power systems resilience," *IEEE System Journal*, vol. 14, no. 3, pp. 4059-4070, 2020.
 - [4] A. Roohinejad, and A. Ajili, "Evaluation of the effects of duststorm on vegetation (importance, consequences, solutions)", *National Conference on Agricultural Pollutants And Food Health, Challenges, Solutions, Impact Of Pollutants On Production And Performance*, 2013 (In Persian).
 - [5] R. Gharib Reza, and M. Lak, "Origin and geochemistry of fine dust in khuzestan province (Case Study: Dust Storm 2013)", *International Specialized Congress of Earth and Science*, 2014 (In Persian).
 - [6] M. Abdollahi, K. Madadi, and K. Ostad-Ali-Askari, "Monitoring and investigating dust phenomenon on using remote sensing science, geographical information system and statistical methods," *Applied Water Science*, vol. 11, no. 7, 2021.
 - [7] Habibian, *Effects of dust on the insulating surfaces of the Khuzestan power grid*, Tehran, Danesh Publications, 2019 (In Persian).
 - [8] R. Calle, J. Castillo, J. Soto Ortiz, J. Candelo-Becerra, and O. Oviedo-Trespacios, O., "A novel method for prediction of washing cycles of electrical insulators in high pollution environments," *International Journal of Electrical Power & Energy Systems*, vol. 130, p. 107026, 2021.
 - [9] M. Mohammadi Sawad Kohi, M. Mirzaei, and S. M. Seyed Barzegar, "Analysis of the effect of uniform and non-uniform pollution on the electric arc voltage of aged polymer insulators", *International Electricity Conference*, 2015 (In Persian).
 - [10] A. Talebi, A. Gholami, M. R. Shariati, and G. E. Alizadeh, "Technical and economic evaluation of the use of RTV silicone rubber coatings in high voltage substations in polluted areas," in *International Electricity Conference*, 2013 (In Persian).
 - [11] K. Mohammadnabi and K. H. Rahmani, "Investigation of leakage current and surface temperature of 230 kV composite insulator under the influence of moisture and contamination conditions," *Journal of Electrical Engineering and Computer Engineering of Iran*, vol. 19, no. 3, pp. 180-188, 2021.
 - [12] A. Sahib, A. A. Basiri, and D. Rahati, "Using hydrophobic and anti-dust nano materials in insulating coatings," *Nanotechnology Conference in the Electricity and Energy Industry*, 2012 (In Persian).
 - [13] M. Ghorbani and S. M. Seyyedbarzegar, "Flashover voltage assessment of polymeric insulators with different profiles under fan-shaped and longitudinal non-uniform pollutions and environment humidity effects," *Journal of Electrical Engineering and Computer Engineering of Iran*, vol. 18, no. 3, pp. 150-158, 2020.
 - [14] M. Ghanbarian, M. R. Shariati, and M. Mohamadi, "Industrial measuring of pollution effects on the operation of high voltage insulations," *Journal of Electrical Engineering Department (Electronics and Power)*, vol. 2, no. 2, pp. 231-30, 2010.
 - [15] M. Daha, M. E. Ibrahim, and M. A. Izzularab, "Effect of washing water flow rate and pollution level on leakage current of a fixed washed high voltage insulator," *International Middle East Power Systems Conference (MEPCON)*, 2016, pp. 234-239.
 - [16] R. Haghshenas, R.-A. Hooshmand, and M. Gholipour, "Power distribution system resilience enhancement planning against extreme dust storms via pre-and post-event actions considering uncertainties," *Sustainable Cities and Society*, vol. 78, 2022, pp. 103626.
 - [17] R. Shariati, M. A. Talebi, M. Rezaei, and D. Mohammadi, "Measurement of environmental pollution on isolation using directional pollution measuring devices in certain regions of the country", in *19th International Electricity Conference*, Tehran, 2004 (In Persian).
 - [18] Arshad, Nekahi, S. G. McMeekin, and M. Farzaneh, "Effect of pollution severity and dry band location on the flashover characteristics of silicone rubber surfaces," *Electrical Engineering*, vol. 99, pp.1053-1063, 2017.
 - [19] L. Ma, P. Bocchini, and V. Christou, "Fragility models of electrical conductors in power transmission networks subjected to hurricanes", *Structural Safety*, vol. 82, pp. 101890, 2020.
 - [20] B. Taheri, A. Safdarian, M. Moeini-Aghtaie, and M. Lehtonen, "Distribution systems resilience enhancement via pre-and post-event actions," *IET Smart Grid*, vol. 2, pp. 549-556, 2019.
 - [21] Zare-Bahramabadi, M. Ehsan, H. Farzin, "A risk-based dispatchable distributed generation unit and tie line planning framework to improve the resilience of distribution systems," *Sustainable Energy, Grids and Networks*, vol. 32, p. 100933, 2022.
 - [22] M. Zare-Bahramabadi, M. Ehsan, and H. Farzin, "A risk-based resilient distribution system planning model against extreme weather events.," *IET Renewable Power Generation*, vol. 16, pp. 2125-2135, 2022.
 - [23] X. Liu, K. Hou, H. Jia, J. Zhao, L. Mili, X. Jin, and D. Wang, "A planning-oriented resilience assessment framework for transmission systems under typhoon disasters," *IEEE Transactions on Smart Grid*, vol. 11, pp. 5431-5441, 2022.
 - [24] A. Ghaedi, and M. Mahmoudian, "Reliability evaluation of power systems including pumped-storage generation units," *Journal of Applied Research in Electrical Engineering*, vol. 3, no. 1, pp. 110-119, 2024.
 - [25] G. Li, Z. Huang, Z. Bie, Y. Lin, and Y. Huang, "Component importance assessment of power systems for improving resilience under wind storms," *Journal of Modern Power Systems and Clean Energy*, vol. 7, no. 4, pp. 676-687, 2019.

- [26] R. Safa, A. A. Ghadimi, and M. R. Miveh, "Assessing power system adequacy and generation expansion planning in the presence of wind power plants considering uncertainties in the DigSILENT software environment," *Journal of Applied Research in Electrical Engineering*, vol. 3, no. 1, pp. 99-109, 2024.
- [27] Y. Yang, W. Tang, Y. Liu, Y. Xin, W. Q. Wu, "Quantitative resilience assessment for power transmission systems under typhoon weather," *IEEE Access*, vol. 6, pp. 40747-40756, 2018.
- [28] R. Milani, Electricity distribution networks air lines, scientific-applied higher education institute of water and electricity industry, Tehran, 2002 (In Persian).
- [29] *IEEE Guide for the Installation and Maintenance of Overhead Electric Transmission and Distribution Systems*, IEEE Standard, November 1992.
- [30] Q. Mohammadi, *High voltage electric technology*, Farhang Publications, 1984 (In Persian).
- [31] R. Shariatinasab, S. Saghafi, M. Khorashadizadeh, and M. Ghayedi, "Probabilistic assessment of insulator failure under contaminated conditions," *IET Science, Measurement & Technology*, vol. 14, pp. 557-563, 2020.
- [32] Thaghafi, and R. Houshmand, *Insulations and high voltage*, Shahid Chamran University of Ahvaz, 2017. (In Persian).
- [33] T. Katsikadelis, *The boundary element method for engineers and scientists*, Academic Press, 2016.
- [34] C. Chapra, R. P. Canale, *Numerical methods for engineers*, Mc Graw Hill Education, 2015.
- [35] J. R. Hughes, *The finite element method: linear static and dynamic finite element analysis*, 2012.
- [36] Disc Insulator Manufacturer, Strain Clamp, Disc Insulator Supplier - Trigold Power Co., Ltd.
- [37] J. He, "Insulator flashover probability investigation based on numerical electric field calculation and random walk theory," PhD Thesis, Arizona State University, 2016.
- [38] Yaragh Avaran Pouya Company, [online]. Available: <https://www.yap-co.ir/>

BIOGRAPHIES



Yasaman Abbasi Chahardah Cheriki was born in Ahvaz, Iran, in 2000. She received the bachelor degree in electrical engineering from Shahid Chamran University of Ahvaz, Ahvaz, Iran, in 2022. She has been a Master's student in Electrical Engineering with a focus on Power Systems at the same university since 2022. Her

research interests are automation and smart grid technology, electricity markets, and the resilience and reliability of power systems.



Hossein Farzin received the BSc and PhD degrees in Electrical Engineering from Sharif University of Technology, Tehran, Iran, in 2011 and 2016, respectively. He was a postdoctoral researcher at Sharif University of Technology, from 2016 to 2017. He is currently an Associate Professor in the Electrical

Engineering Department, Shahid Chamran University of Ahvaz, Ahvaz, Iran. His research interests include microgrids design and optimization, integration of distributed energy resources and electric vehicles in smart grid, and power system reliability and resilience. Dr. Farzin ranked 2nd in Iran's nationwide universities entrance exam in 2007, and is ranked among the world's top 2% most cited researchers in 2021 and 2023. He has authored more than 60 journal and conference papers, and serves as an editor of the Scientia Iranica journal.



Elaheh Mashhour (M'08) was born in Tehran, Iran, in 1974. She received a Ph.D. degree in electrical engineering from K. N. Toosi University of Technology, Tehran, Iran, in 2010. She has worked in Khuzestan Electric Power Distribution Company for 15 years as the manager of network and load control office, the manager of power market office and head of DG participation unit. Now, she is an Associate Professor of the Department of Electrical Engineering, Shahid Chamran University of Ahvaz, Ahvaz, Iran, her workplace since 2011. Her research interests are distribution system automation and planning, power market, network resiliency and deep learning.

Copyrights

© 2025 Licensee Shahid Chamran University of Ahvaz, Ahvaz, Iran. This article is an open-access article distributed under the terms and conditions of the Creative Commons Attribution –NonCommercial 4.0 International (CC BY-NC 4.0) License (<http://creativecommons.org/licenses/by-nc/4.0/>).





Research Article

Improving the Performance Characteristics of Conventional Linear Switched Reluctance Motor by Eliminating Translator Yoke and Embedding Permanent Magnets in Stator Yoke

Milad Golzarzadeh^{1,*}, Hashem Oraee¹, and Babak Ganji²

¹ Department of Electrical Engineering, Sharif University of Technology, Tehran, Iran

² Faculty of Electrical and Computer Engineering, University of Kashan, Kashan, Iran

* Corresponding Author: milad.golzarzadeh@ee.sharif.edu

Abstract: In this paper, the Segmental Translator Permanent Magnet Linear Switched Reluctance Motor (STPMLSRM) has been introduced as a new type of improved Linear Switched Reluctance Motor (LSRM), which increases the flux density in the air-gap by using Permanent Magnets (PMs) in the stator yoke. Also, the moving part does not have a yoke, and discrete segments are used instead of the yoke, which reduces the volume of active magnetic materials. In order to better evaluate, the segmental translator permanent magnet linear switched reluctance motor is compared with the conventional linear switched reluctance motor and Segmental Translator Linear Switched Reluctance Motor (STLSRM) without permanent magnet, then their different aspects are discussed. In order to validate the introduced STPMLSRM, based on the Finite Element Method (FEM), the static and dynamic characteristics of linear motors including static flux-linkage, static force, co-energy, instantaneous current waveform, and instantaneous thrust waveform are predicted and compared. These comparisons show that the STPMLSRM has better performance characteristics than the conventional LSRM and STLSRM.

Keywords: Linear switched reluctance motor, segmental translator, permanent magnet, finite element method.

Article history

Received 10 March 2024; Revised 27 June 2024; Accepted 17 October 2024; Published online 20 April 2025.

© 2025 Published by Shahid Chamran University of Ahvaz & Iranian Association of Electrical and Electronics Engineers (IAEEE)

How to cite this article

M. Golzarzadeh, H. Oraee, and B. Ganji, "Improving the performance characteristics of conventional linear switched reluctance motor by eliminating translator yoke and embedding permanent magnets in stator yoke," *J. Appl. Res. Electr. Eng.*, vol. 3, no. 2, pp. 222-231, 2024. DOI: [10.22055/jaree.2024.46343.1111](https://doi.org/10.22055/jaree.2024.46343.1111)



1. INTRODUCTION

Switched Reluctance Motors (SRMs) have advantages such as simplicity of structure, robustness, no magnet or winding on one side and high fault tolerance, which makes them a suitable choice for many applications [1-3]. Linear switched reluctance motors have a structure similar to rotary SRMs, with the difference that the movement is linear instead of rotary and linear force is produced instead of torque. Therefore, they have all the advantages of SRM. These motors are widely used in applications such as transportation systems, home use, and etc. [4-6]. Electric trains and elevators are other applications of LSRMs [7, 8]. In these motors, both distributed windings and centralized windings are used, which can be mechanically and electrically isolated, so they have high reliability. These windings are placed in the stator or mover. Structures in which the winding is located on the translator produce more force than the structure in which the winding is located on the stator. In addition, the cost of mass production of these systems is lower [9-11].

In order to improve the performance of SRM and reduce its disadvantages, various structures have been presented, in most of which the structure complexity has increased and their production has also become more difficult. Considering that the principles and performance of LSRM are similar to the rotary SRM, the methods of improving the performance of rotary SRM can be used to improve the performance characteristics of LSRM. One of the ways to improve the performance of LSRM is to remove the yoke in stator or translator, where by using independent segments, the thrust force of new motor increases compared to conventional motors. This method is used both in rotary SRMs [12-14] and in linear SRMs [15-17], which significantly improves the performance characteristics of motor. Another way to improve the performance of LSRM is to use permanent magnet (PM) in the stator or translator, which creates a new structure. Choosing the right location for PMs in the motor is very important. By choosing an inappropriate location, some of the advantages of LSRM such as simplicity of structure,

reliability and endurance are lost [18-20]. In [21], by using the PM in structure of LSRM and linear flux switching motor, a comparison has been made between these two motors. This comparison shows that using the PM in the LSRM structure gives a better result. In [22], two improved double-sided LSRMs with PMs embedded in their structure are introduced. By comparing both structures, it is shown that using the PM in the structure of motors, the flux density in the air-gap has increased, which leads to a decrease in the magnetic saturation and an increase in the thrust force of the motor. In these two structures, due to the fact that PMs are located in the mover, the reliability of motors may decrease due to the movement of PMs.

The segmental translator linear switched reluctance motor (STLSRM) is one of the structures whose performance characteristics are improved compared to the conventional LSRM. Although the STLSRM has better performance than the conventional LSRM, few research has been carried out to introduce this motor. Also, in recent studies for the STLSRM, a model that uses the PM in its structure has not been presented. In [23], different structures of linear switched reluctance motor have been investigated and their static and dynamic characteristics have been compared based on the finite element method. In this paper, with the aim of improving the results presented in [23], changes including how to choose the right location for embedding permanent magnets in the motor structure, more detailed comparisons of the results, providing more details about the parameters and calculating specific parameters such as the average instantaneous power for different structures have been applied. Therefore, in this paper, in order to show the advantages of STPMLSRM compared to the conventional LSRM and STLSRM, firstly, a comparison is made between these motors, then, by placing PMs in the stator yoke of STLSTM, the segmental translator permanent magnet linear switched reluctance motor (STPMLSRM) is presented as a new structure. In order to show the effect of PMs on motors, the performance characteristics of STLSRM and STPMLSRM are predicted and compared. The novelties of this paper are the use of discrete segments instead of poles connected to the yoke in the moving part and adding PMs in the stator yoke. In this structure, compared to conventional LSRM, less magnetic material is used, and due to the presence of PMs, the flux density in the air-gap increases significantly, which causes more thrust force to be applied to the moving part. Based on this, modeling of motors and their comparison is carried out in Section 2 and the simulation results are presented in Section 3. Finally, the conclusion is given in Section 4.

2. DIFFERENT STRUCTURES OF LSRM

2.1. Conventional Linear Switched Reluctance Motor

The cross-section of a conventional LSRM is shown in Fig. 1. As it is clear from this figure, each stator slot is filled with the windings of two phases, and two windings that are connected in series form one phase. There are no coils or permanent magnets in the moving part (translator), which makes it electrically isolated and increases reliability. This motor (Fig. 1) is like a 6/4 rotary switched reluctance motor,

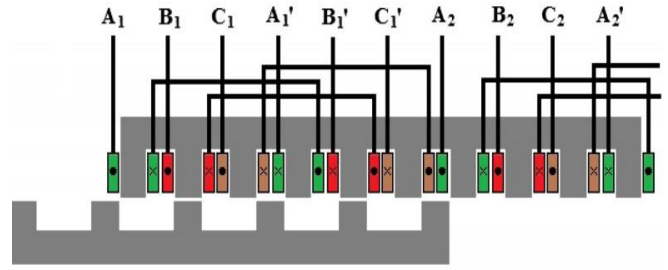


Fig. 1: 2-D geometry of conventional LSRM [15].

with extra poles in the stator and translator to reduce noise and end effect. These poles are connected by a yoke to create a flux path. The presence of a yoke in the motor body significantly increases the use of magnetic materials, which increases iron loss and reduces the force applied to translator [15].

2.2. Segmental Translator Linear Switched Reluctance Motor

The cross-section of a STLSRM is shown in Fig. 2. Each unit of this motor includes six poles and six slots in the stator and four segments in the translator. Therefore, in any length of this motor, the ratio of the number of stator poles to the translator segments is 3/2. To create a flux path in stator, the poles are connected by a yoke, while there is no yoke in the translator and instead of prominent poles, discrete segments are used. The segments are magnetically and mechanically independent from each other, and there is air or non-magnetic material between them. Since, the yoke has a considerable volume and weight of active magnetic materials, the use of magnetic materials in this motor is significantly reduced. The lack of yoke and special structure of translator makes the STLSRM produce more power than the conventional LSRM [16].

The STLSRM consists of three phases, each phase includes three stator poles. The current direction of coils enters from the first three slots and exits from the second three slots. According to Fig. 2, each phase occupies two slots of stator, and each slot of stator is filled only with the windings of one phase. Due to the type of placement of coils, the windings of different phases are mechanically independent from each other and no insulation is needed to separate the windings in the slots. Therefore, when one winding is damaged, the faulty winding can be replaced without damaging the other windings [17].

The prominent advantages of the STLSRM compared to the conventional LSRM are stated as follows:

- Only one coil is placed in each slot. Therefore, the use of insulating materials in the stator slot decreases and its space coefficient increases, which increases the output power.
- Optimum use of the stator slot surface and simplification of the manufacturing process due to the absence of an insulating separator in the stator slot.
- Due to the special structure of translator, the flux produced by each phase is independent from other phases.

- The translator does not have a yoke. Therefore, the use of magnetic materials is significantly reduced.
- Due to the fact that there is no pole or slot in the secondary, the windage loss in the translator is zero.
- Due to the absence of a yoke in the translator and the use of less iron, iron losses are reduced.

2.3. Segmental Translator Permanent Magnet Linear Switched Reluctance Motor

The use of PMs in the STLSRM makes a new structure that is effective in improving the performance of this motor. In recent studies for the STLSRM, a model that uses a PM in its structure has not been presented. Therefore, here by embedding the PMs in the motor body, the segmental translator permanent magnet linear switched reluctance motor (STPMLSRM) is presented as a new structure. The main role of the PM is to increase the flux density in air-gap, which reduces the magnetic saturation in the iron parts and the average current. Also, adding the PMs in the motor structure causes the motor produce more thrust force. For a better evaluation, the STLSRM of Fig. 2, is considered, in which there are no PMs in its structure and only phase (B) is excited. With simulation based on 3-D FEM and using ANSYS-Maxwell software, flux density distribution and magnetic flux path are obtained for the motor structure without PMs, which are shown in Fig. 3. In this case, by passing the magnetic flux through the teeth around the coil, air-gap, stator yoke and translator segments, the force is applied to the motor translator. The average static force for a current 10 A and different positions of the translator is equal to 108 N.

To investigate the effect of PMs on flux density distribution and magnetic flux path in the STPMLSRM, firstly, it is assumed that current of phase B is zero and only PMs create magnetic flux. For this purpose, PMs are placed in the stator yoke, then the motor is simulated and their results are discussed. Using modeling based on the FEM, flux density distribution and magnetic flux path are obtained according to Fig. 4. This figure shows that with the presence of PMs in the motor stator yoke and zero excitation current, a significant part of the magnetic flux lines produced by the PMs, close their path through the iron core with very low reluctance, the air-gap with high reluctance and the translator segments, which causes the force to be applied to translator.

Embedding PMs in the translator causes the PMs to move with the moving part, which challenges the outstanding advantages of the SRM by considering the mechanical factors. Therefore, PMs are embedded in the stator. The location of PMs in the stator should be in such a way that the flux produced by them and the flux produced by the coils are in the same direction to increase the flux density in the air-gap. In addition, the PMs should be placed in such a way that they completely cover the flux path produced by the coils. Therefore, the stator yoke section above the stator slot is a suitable location. Due to the fact that in this structure, the PM completely blocks the stator yoke, most of the flux produced by the PMs inevitably passes through the air-gap between the stator and translator, which increases the air-gap flux density. In the full load condition, where both the PMs and the winding of phase B generate magnetic flux, as shown in Fig. 5, the flux generated by PMs is in the same direction as the flux generated by phase B, which increases the flux density

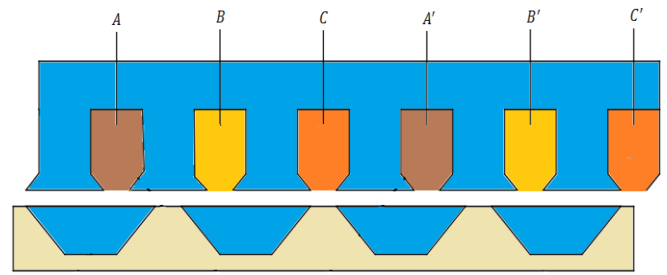


Fig. 2: Two-dimensional geometry of STLSRM.

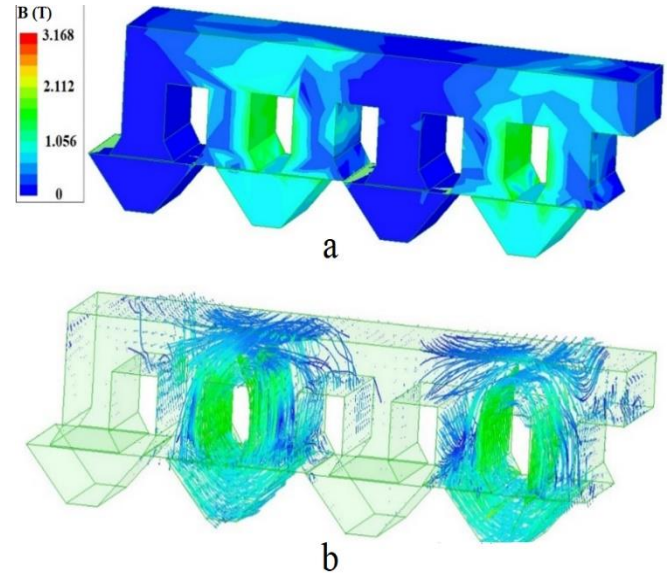


Fig. 3: Modeling of STLSRM without PM for current 10 A: (a) Flux density distribution, (b) Magnetic flux path.

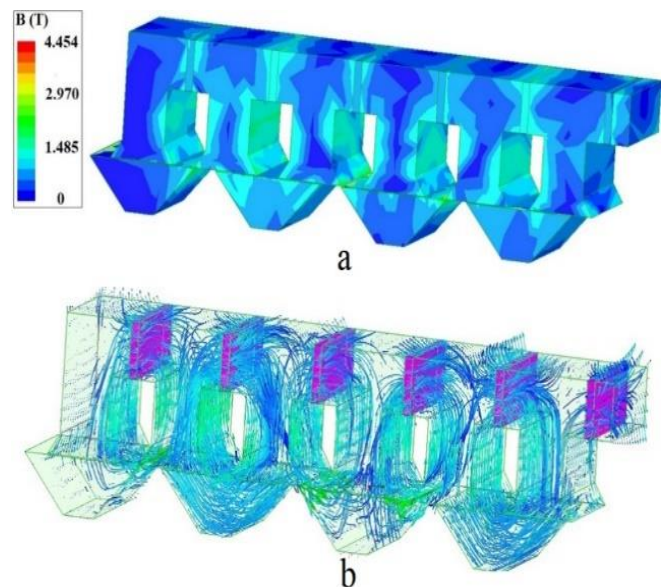


Fig. 4: Modeling of STLSRM by embedding PMs in the yoke and current 0 A: (a) Flux density distribution, (b) Magnetic flux path.

in air-gap, and in this case, the force applied to the translator is strengthened and the motor performance is improved. For different positions of translator (0 - 69 mm) and a current of 10 A, the average static force in the presence of PMs is equal to 195 N, which is more than the STLSRM without PM.

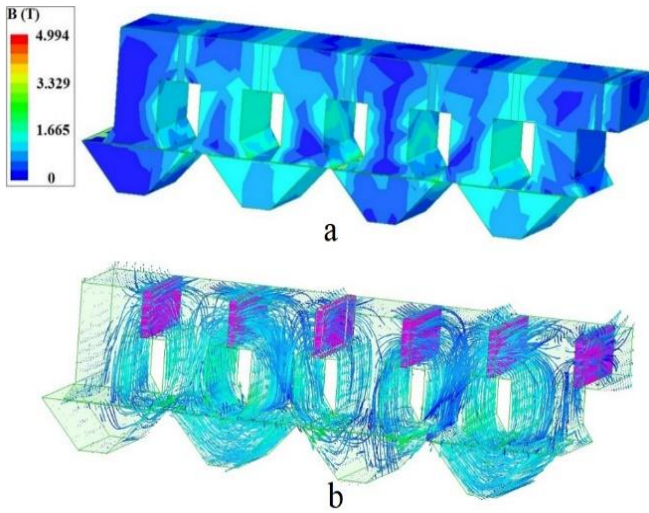


Fig. 5: Modeling of STL SRM by embedding PMs in the yoke and current 10 A: (a) Flux density distribution, (b) Magnetic flux path.

3. SIMULATION RESULTS

The simulation results for different topologies of linear switched reluctance motor based on the FEM are given here and compared. The specifications of motors are given in Tables 1 and 2, and the stator and translator core sheets are M800-50A with a thickness of 0.5 mm. The LSRMs generate thrust force by changing reluctance. The power produced of these motors is created by the co-energy difference between the fully aligned and fully unaligned positions. The flux path in two important positions for STL SRM and conventional LSRM are shown in Fig. 6 and Fig. 7, respectively. As can be seen in Fig. 6, in the aligned position, two poles adjacent in the stator pass the flux, while in the conventional LSRM as shown in Fig. 7, only one stator pole passes the flux. Therefore, it is clear that the proposed STL SRM can carry more flux.

Based on the 2-D FEM, the flux-linkage with a phase is calculated for the STL SRM and the conventional LSRM in different positions (0 - 69 mm) and shown in Fig. 8. For a better evaluation, the flux-linkage of STL SRM and the conventional LSRM are compared for two important positions including fully aligned and fully unaligned in Fig. 9 and Table 3. As can be seen in this figure, the co-energy difference between the two critical positions in the STL SRM is greater than that of the conventional LSRM.

Using the static characteristic of Flux-linkage, the co-energy characteristic is obtained from the following equation:

$$w_c(x, i) = \int \lambda(x, i) di \quad (1)$$

The co-energy characteristic in the current range of 0 to 20 A for two motors is shown in Fig. 10. This figure clearly shows that the co-energy difference in the STL SRM is higher than the conventional LSRM. Therefore, the STL SRM produces more static force at equal current.

The characteristic of static force ($F(x, i)$) is predicted from the following equation:

$$F(x, i) = \frac{\partial w_c(x, i)}{\partial x} \Big|_{i=\text{const}} \quad (2)$$

Table 1: Specifications of STL SRM.

| Parameter | Value |
|---------------------------|-------|
| Stator pole width [mm] | 46 |
| Stator slot width [mm] | 46 |
| Stator pole height [mm] | 67 |
| Stator core depth [mm] | 46 |
| Air-gap length [mm] | 1 |
| Segment width [mm] | 115 |
| Slot opening width [mm] | 23 |
| Segment height [mm] | 46 |
| Core stack thickness [mm] | 125 |
| Turns per phase | 160 |

Table 2: Specifications of conventional LSRM.

| Parameter | Value |
|-----------------------------|-------|
| Stator pole width [mm] | 46 |
| Stator slot width [mm] | 46 |
| Stator pole height [mm] | 67 |
| Stator yoke height [mm] | 46 |
| Air-gap length [mm] | 1 |
| Translator pole width [mm] | 49 |
| Translator slot width [mm] | 89 |
| Translator yoke height [mm] | 49 |
| Core stack thickness [mm] | 125 |
| Turns per phase | 160 |

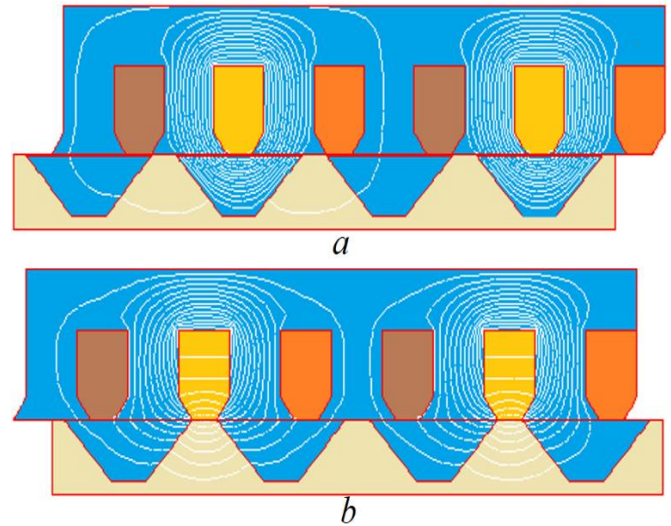


Fig. 6: Important positions for STL SRM (a) Aligned position, (b) Unaligned position.

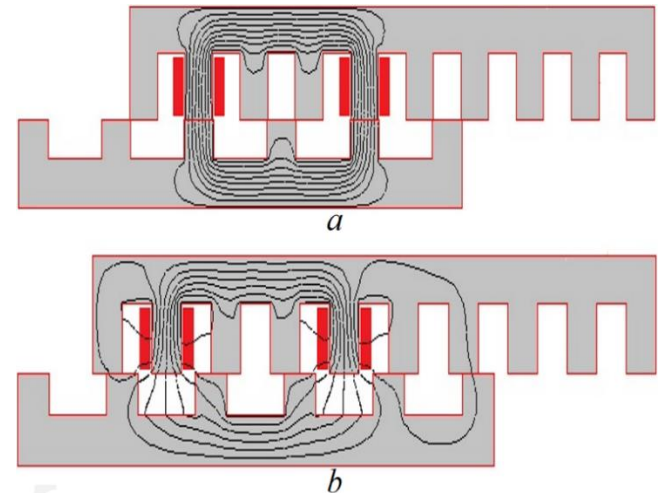


Fig. 7: Important positions for conventional LSRM, (a) Aligned position, (b) Unaligned position.

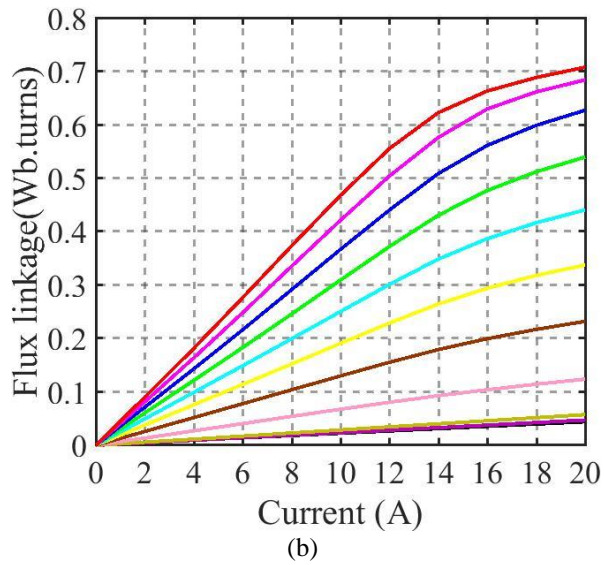
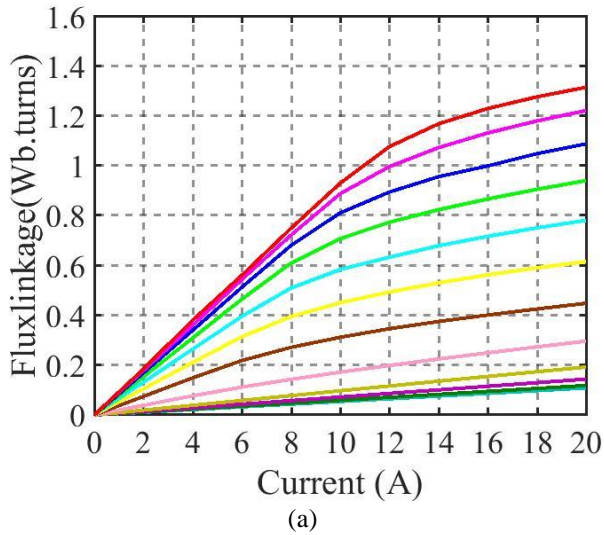


Fig. 8: Flux-linkage with a phase: (a) STLSRM, (b) conventional LSRM.

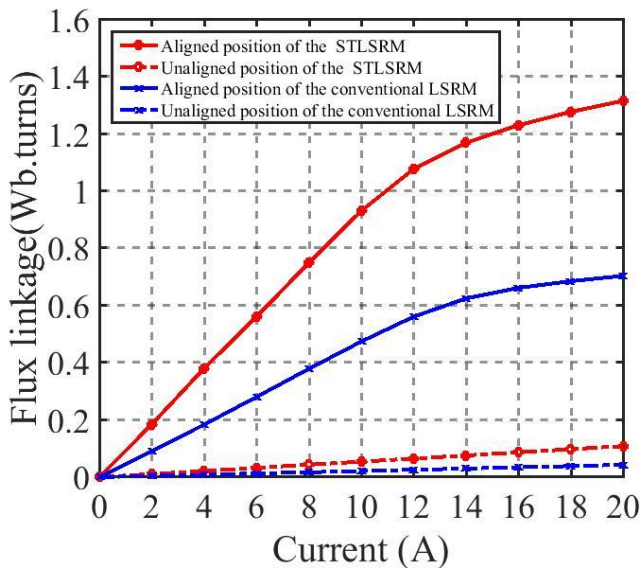


Fig. 9: Flux-linkage for two important positions.

Table 3: The values of flux-linkage (Wb.turns) predicted for two positions.

| Position | Motor type | Current (A) | | | |
|-----------|------------|-------------|-------|-------|-------|
| | | 2 | 6 | 10 | 14 |
| Unaligned | LSRM | 0.004 | 0.013 | 0.022 | 0.030 |
| | STLSRM | 0.011 | 0.033 | 0.054 | 0.076 |
| Aligned | LSRM | 0.091 | 0.280 | 0.474 | 0.625 |
| | STLSRM | 0.184 | 0.561 | 0.931 | 1.170 |

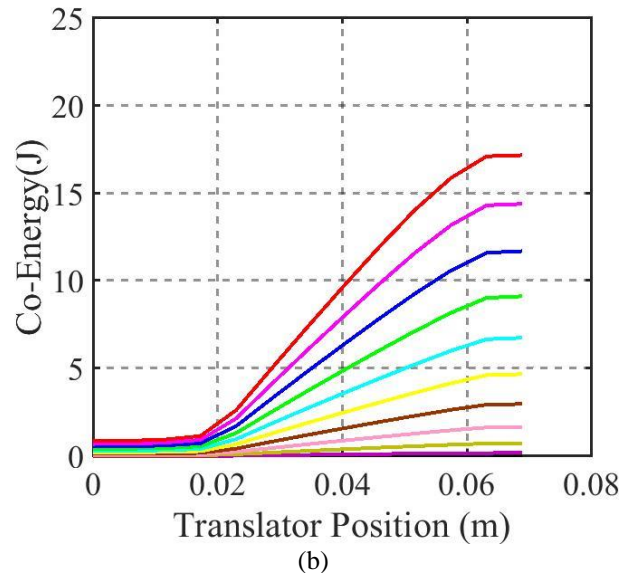
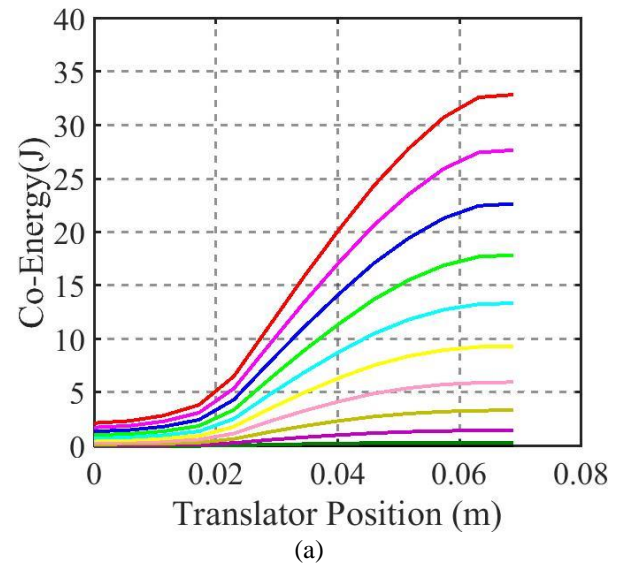


Fig. 10: The co-energy characteristic: (a) STLSRM, (b) conventional LSRM.

For STLSRM and conventional LSRM, the static force characteristics in terms of translator positions are obtained by solving (2) and shown in Fig. 11. For better evaluation, the average static force in terms of different currents for two motors are calculated and compared in Fig. 12 and Table 4,

which shows that the STL SRM produces more force than the conventional LSRM. For a better comparison of motors, instantaneous current ($i(x)$) and instantaneous thrust force ($F(x)$) can be used. The instantaneous current is predicted from the phase voltage equation of the SRM as follows:

$$V = Ri + \frac{d\lambda(x, i)}{dt} \quad (3)$$

where R is the resistance of the phase winding and V is the phase voltage. Having $i(x)$ and $F(x, i)$, $F(x)$ is calculated. Therefore, the dynamic characteristics of motors, including instantaneous current and instantaneous thrust force, for the working point: speed = 4 m/s, turn-on position = 15.8 (mm), turn-off position = 28.3 (mm) and the current regulation control mode when maximum current is 7 A, are predicted and compared in Fig. 13. It should be noted that in Fig. 10 and 11 obtained from equations (1) and (2), each color shows a current from 2 to 20 A.

The average instantaneous thrust force for STL SRM and conventional LSRM are 61.22 N and 32.18 N, respectively, while, the effective value of instantaneous phase current for STL SRM and conventional LSRM are 5.18 A and 7.28 A, respectively, which shows that with less effective current, more average thrust force is obtained for the STL SRM. The output power of the linear motor is calculated from $P_o = F_{tr} V_m$. In this equation, F_{tr} is the thrust force of translator and V_m is the linear velocity of translator. Therefore, using the dynamic characteristic of instantaneous thrust force (Fig. 13), the average instantaneous power for two motors is calculated. The average instantaneous power for STL SRM and the conventional LSRM are 244.4 W and 128.72 W, respectively, which shows that the average power for STL SRM is more than conventional LSRM.

In order to compare the performance of STL SRM and STPMLS RM, simulation results are given based on 3-D FEM and PMs are NdFeB35 with $\mu_r = 1.09$ and $B_r = 1.23$ T. The flux-linkage static characteristics of one phase for two motors are predicted and shown in Fig. 14. This figure has been obtained by applying currents of 0 to 16 A to the phase B and by moving from unaligned position to aligned position with a length of 69 mm. For a better evaluation, the flux-linkage of motors are compared for only two important positions including fully aligned and fully unaligned in Fig. 15 and Table 5. In this figure, the effect of PM is clearly visible. In the STL SRM, when there is no excitation current, the flux-linkage is zero both in the aligned and unaligned positions, but in the STPMLS RM with zero excitation current, the flux-linkage is greater than zero in all positions of translator. It should be noted that in Fig 8 and 14, which are the graphs of flux-linkage in terms of current, each color shows a position of the translator from the fully unaligned position to the fully aligned position.

The co-energy difference between the aligned and unaligned positions for the STPMLS RM is greater than the STL SRM, since the area between the flux-linkage in the aligned and unaligned positions is greater for the PM motor than for the motor without PM. Therefore, adding the PM in the motor structure increases the force applied to the translator. The average static force at different currents for two motors has been calculated using the static force characteristics, which are compared in Fig. 16 and Table 6.

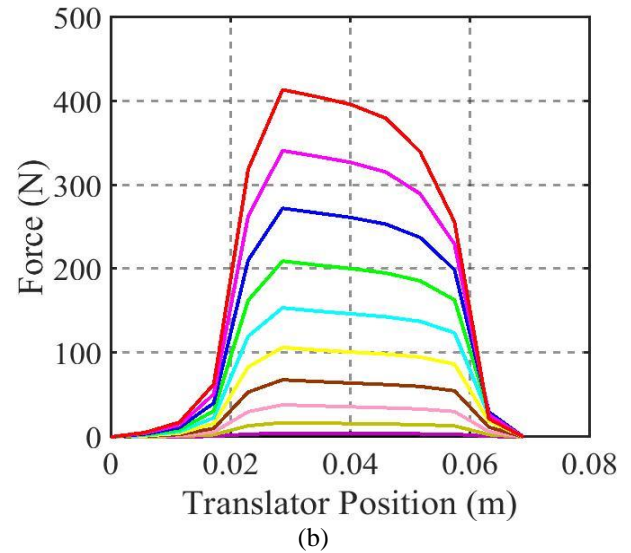
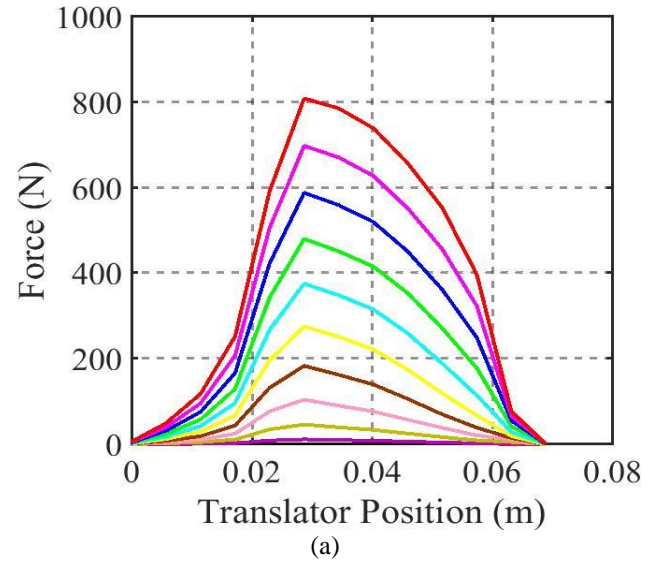


Fig. 11: The static force characteristics: (a) STL SRM, (b) conventional LSRM.

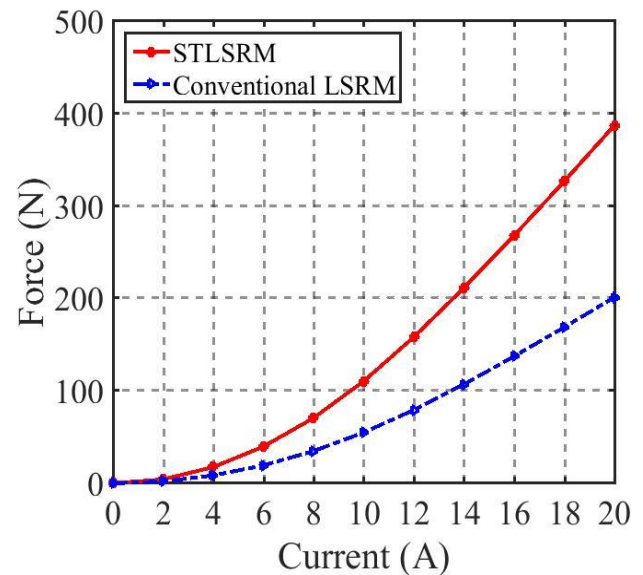


Fig. 12: Average static force for two linear motors.

Table 4: Average static force (N) of conventional LSRM and STL SRM for different currents.

| Current (A) | Average force for LSRM | Average force for STL SRM |
|-------------|------------------------|---------------------------|
| 2 | 2.1 | 4.3 |
| 4 | 8.6 | 17.6 |
| 6 | 19.5 | 39.7 |
| 8 | 34.9 | 70.7 |
| 10 | 55 | 110.5 |
| 12 | 79.3 | 158.2 |
| 14 | 107.2 | 211.5 |
| 16 | 137.4 | 268.1 |
| 18 | 168.9 | 326.8 |
| 20 | 201.3 | 387.2 |

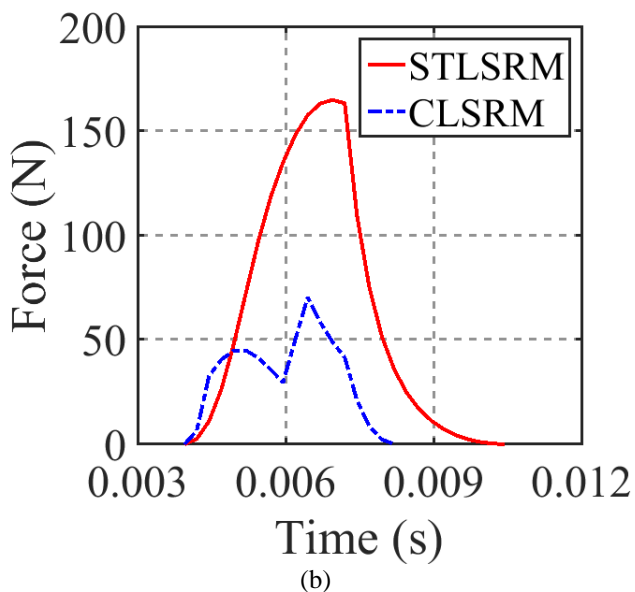
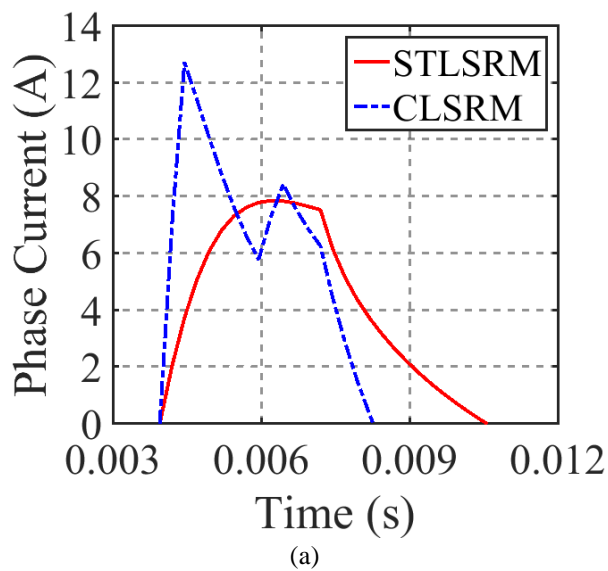
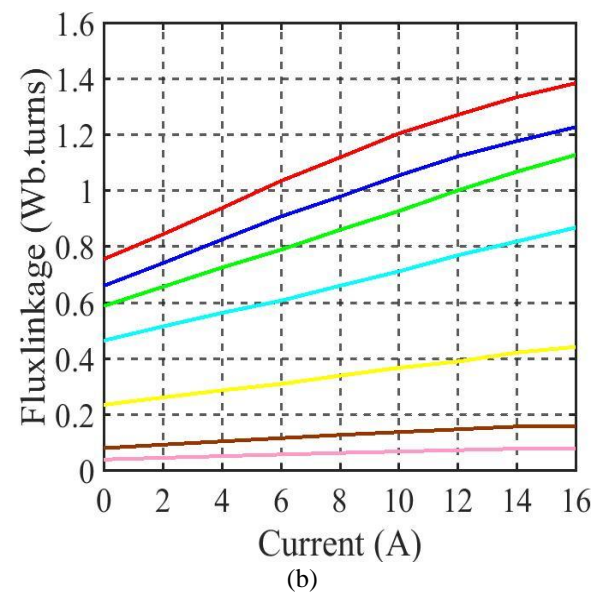
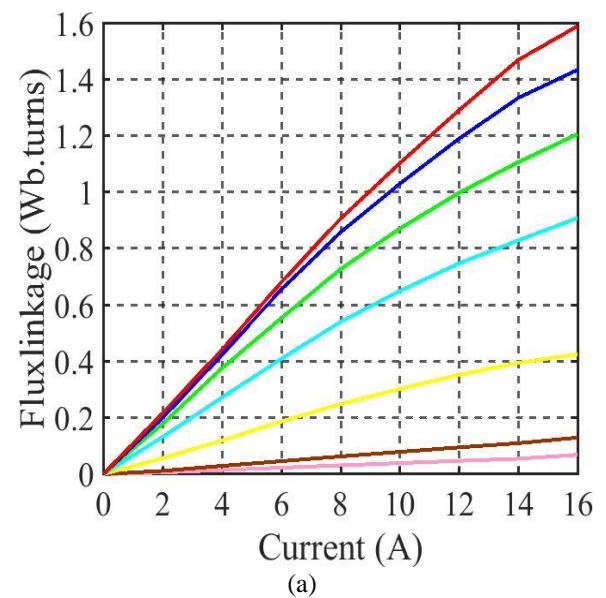
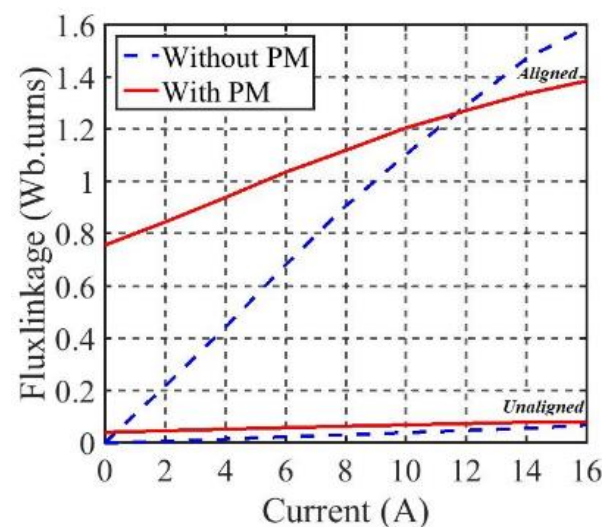
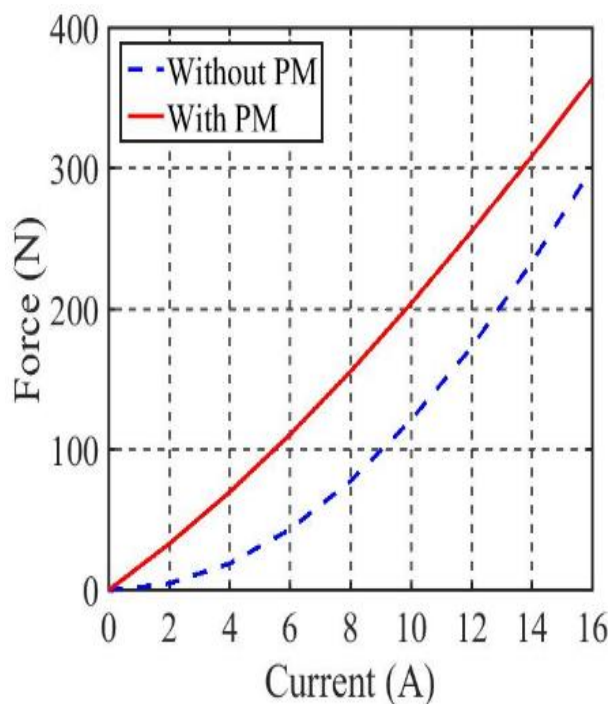
**Fig. 13:** Dynamic waveforms: (a) Instantaneous phase current, (b) Instantaneous thrust force.**Fig. 14:** 3-D Flux-linkage with a phase: (a) STL SRM, (b) STPML SRM.**Fig. 15:** Flux-linkage for positions of fully aligned and fully unaligned.

Table 5: The values of flux-linkage (Wb.turns) predicted for aligned and unaligned positions.

| Position | Motor type | Current (A) | | | |
|-----------|------------|-------------|-------|-------|-------|
| | | 2 | 6 | 10 | 14 |
| Unaligned | STPMLSRM | 0.047 | 0.059 | 0.069 | 0.079 |
| | STLSRM | 0.006 | 0.023 | 0.040 | 0.055 |
| Aligned | STPMLSRM | 0.846 | 1.036 | 1.206 | 1.337 |
| | STLSRM | 0.230 | 0.714 | 1.124 | 1.519 |

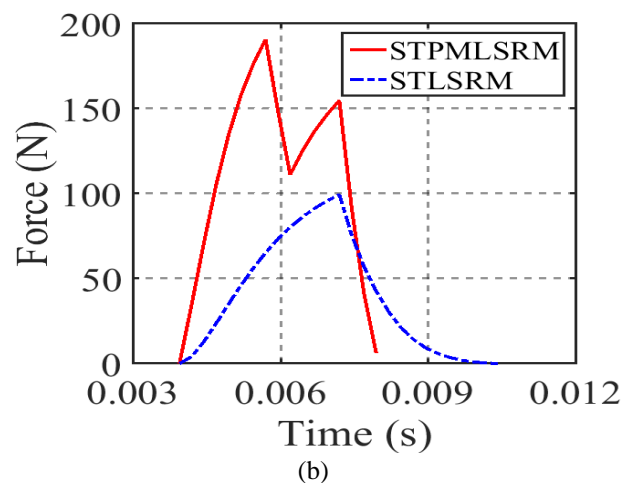
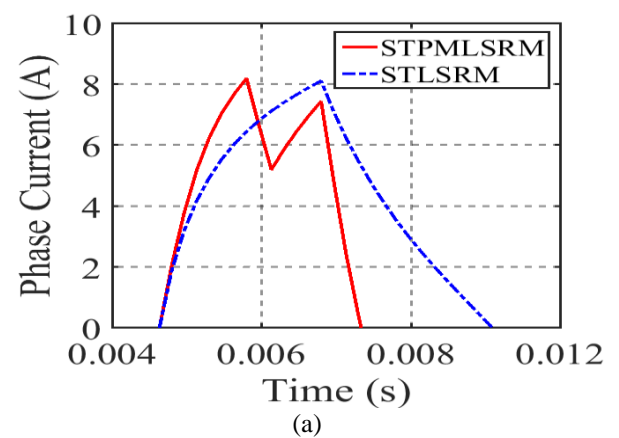
Table 6: Average static force (N) of STLSRM and STPMLSRM for different currents.

| Current (A) | Average force for STLSRM | Average force for STPMLSRM |
|-------------|--------------------------|----------------------------|
| 2 | 4.7 | 32.9 |
| 4 | 19 | 69.7 |
| 6 | 43.3 | 110.7 |
| 8 | 77.6 | 155.6 |
| 10 | 120.9 | 203.9 |
| 12 | 172.7 | 255.1 |
| 14 | 233.1 | 308.7 |
| 16 | 299.9 | 364.2 |

**Fig. 16:** Average static force for STLSRM and STPMLSRM.

This comparison shows that in all currents, the average static force has been increased by adding the PM in STLSRM structure. The dynamic characteristics of STLSRM and STPMLSRM, including instantaneous current and instantaneous thrust force, for the working point: speed = 4 m/s, turn-on position = 15.8 (mm), turn-off position = 28.3 (mm) and the current regulation control mode when maximum current is 7 A, are predicted and compared in Fig. 17.

The average instantaneous thrust force for STPMLSRM and conventional STLSRM are 82.26 N and 46.32 N, respectively, while, the effective current for STPMLSRM and conventional STLSRM are 4.41 A and 4.51 A, respectively. Therefore, adding the PM, increases the flux density in air-gap and the force applied to the translator. Using the dynamic characteristic of instantaneous thrust force (Fig. 17), the average instantaneous power for STPMLSRM and STLSRM are 329.04 W and 185.28 W, respectively, which shows that the average power for STPMLSRM is more than STLSRM.

**Fig. 17:** 3-D Dynamic characteristics: (a) Waveform of instantaneous phase current, (b) Waveform of instantaneous thrust force.

4. CONCLUSION

In this paper, a new type of segmental translator linear switched reluctance motor was introduced, and the performance characteristics were improved by placing permanent magnets in its structure, because, the presence of the permanent magnet has a significant effect on the air-gap flux density and increases the force applied to the moving part. The right position to place permanent magnets in the segmental translator linear switched reluctance motor is the

stator yoke, because it completely covers the flux passing surface and also strengthens the magnetic flux. To validate the introduced structure, based on the finite element method, comparisons were made between the introduced motors and their static and dynamic characteristics were compared. These comparisons showed that using discrete segments instead of continuous poles in the translator and placing permanent magnets in a suitable position in the motor structure improve the motor performance. Therefore, the average static force in different currents for the segmental translator permanent magnet linear switched reluctance motor is more than the segmental translator linear switched reluctance motor. The average instantaneous thrust force for STPMSRM and conventional STLSRM were 98.45 and 49.94 N, respectively, while, the effective current for STPMSRM and conventional STLSRM were 6.3 and 5.66 A, respectively. These comparisons clearly showed that adding the permanent magnet in the motor structure, increases the flux density in air-gap and the force applied to the translator.

CREDIT AUTHORSHIP CONTRIBUTION STATEMENT

Milad Golzarzadeh: Conceptualization, Data curation, Formal analysis, Investigation, Methodology, Project administration, Resources, Software, Validation, Roles/Writing - original draft, Writing - review & editing. **Hashem Oraee:** Conceptualization, Data curation, Methodology, Project administration, Validation, Roles/Writing - original draft, Writing - review & editing. **Babak Ganji:** Conceptualization, Data curation, Methodology, Project administration, Resources, Validation, Roles/Writing - original draft, Writing - review & editing.

DECLARATION OF COMPETING INTEREST

The authors declare that they have no known competing financial interests or personal relationships that could have appeared to influence the work reported in this paper. The ethical issues; including plagiarism, informed consent, misconduct, data fabrication and/or falsification, double publication and/or submission, redundancy has been completely observed by the authors. This paper is an extension of the authors' previous work [23] which was presented in the 2024 4th National Conference on Applied Research in Electrical Engineering (AREE2024), and selected as a top paper to be printed in this journal with some extensions.

REFERENCES

- [1] P. Upadhyay, and R. K., "Design of two-phase 4/6 switched reluctance motor for bidirectional starting in washing machine application," *IEEE Trans. Ind. App.*, vol. 59, pp. 1519-1529, 2023.
- [2] X. Sun et al., "Multiobjective and multiphysics design optimization of a switched reluctance motor for electric vehicle applications," *IEEE Trans. Energy Convers.* vol. 36, pp. 3294-3304, 2021.
- [3] P. Kumar, M. Israyelu, and S. Sashidhar, "A simple four-phase switched reluctance motor drive for ceiling fan applications," *IEEE Access*, vol. 11, pp. 7021-7030, 2023.
- [4] R. Nie et al. "Comparative researches on double-sided switched reluctance linear machines with different winding connections," *IET Electr. Power Appl.*, vol. 14, pp. 2082-2091, 2020.
- [5] D. Wang et al., "Comparative analysis of different topologies of linear switched reluctance motor with segmented secondary for vertical actuation systems," *IEEE Trans. Energy Convers.*, vol. 36, pp. 2634-2645, 2021.
- [6] H. Cheng, S. Liao, and W. Yan, "Development and performance analysis of segmented-double-stator switched reluctance machine," *IEEE Trans. Ind. Electron.*, vol. 69, pp. 1298-1309, 2022.
- [7] M. Lu, and R. Cao, "Comparative investigation of high temperature superconducting linear flux-switching motor and high temperature superconducting linear switched reluctance motor for urban railway transit," *IEEE Trans. Appl. Supercond.*, vol. 31, pp. 1-5, 2021.
- [8] S. Masoudi, H. Mehrjerdi, and A. Ghorbani, "New elevator system constructed by multi-translator linear switched reluctance motor with enhanced motion quality," *IET Electr. Power Appl.* vol. 14, pp. 1692-1701, 2020.
- [9] Z. Li et al., "Nonlinear analytical model of linear switched reluctance motor with segmented secondary considering iron saturation and end effect," *IEEE Access*, 11, pp. 132078-132087, 2023.
- [10] R. Nie et al., "Compensation analysis of longitudinal end effect in three-phase switched reluctance linear machines," *IET Electr. Power App.*, vol. 14, pp. 165-174, 2020.
- [11] D. Wang, X. Wang, and X. Du, "Design and comparison of a high force density dual-side linear switched reluctance motor for long rail propulsion application with low cost," *IEEE Trans. on Mag.*, vol. 53, pp. 1-4, 2017.
- [12] W. Sun, Q. Li, L. Sun, and L. Li, "Development and investigation of novel axial-field dual-rotor segmented switched reluctance machine," *IEEE Trans. Transport. Electrification*, vol. 7, pp. 754-765, 2021.
- [13] R. Madhavan, and B. G. Fernandes, "Axial flux segmented SRM with a higher number of rotor segments for electric vehicles", *IEEE Trans. Energy Convers.*, vol. 28, pp. 203-213, 2013.
- [14] R. Vandana, and B. G. Fernandes, "Design methodology for high-performance segmented rotor switched reluctance motors," *IEEE Trans. Energy Convers.*, vol. 30, pp. 11-21, 2015.
- [15] B. Ganji, and M. H. Askari, "Analysis and modeling of different topologies for linear switched reluctance motor using finite element method," *Alexandria Engineering Journal*, vol. 55, pp. 2531-2538, 2016.
- [16] M. Golzarzadeh, and B. Ganji, "Analytical modelling of the linear switched reluctance motor with segmental translator," *IET Electr. Power Appl.*, vol. 13, pp. 527-537, 2019.
- [17] M. Golzarzadeh, H. Oraee, and B. Ganji, "Lumped parameter thermal model for segmental translator linear switched reluctance motor," *IET Electr. Power Appl.* vol. 17, pp. 1548-1561, 2023.
- [18] M. A. J. Kondelaji, E. F. Farahani, and M. Mirsalim, "Performance analysis of a new switched reluctance motor with two sets of embedded permanent magnets," *IEEE Trans. Energy Convers.*, vol. 35, pp. 818-827, 2020.

- [19] M. Masoumi, and M. Mirsalim, "E-core hybrid reluctance motor with permanent magnets inside stator common poles," *IEEE Trans. Energy Convers.*, vol. 33, pp. 826–833, 2018.
- [20] M. M. Bouiabadi, A. D. Aliabad, S. M. Mousavi, and E. Amiri, "Design and analysis of e-core PM-assisted switched reluctance motor," *IET Electr. Power Appl.*, vol. 14, pp. 859–864, 2020.
- [21] R. Cao, E. Su, and M. Lu, "Comparative study of permanent magnet assisted linear switched reluctance motor and linear flux switching permanent magnet motor for railway transportation," *IEEE Trans. Appl. Supercond.*, vol. 30, pp. 1–5, 2020.
- [22] A. Ghaffarpour, M. Vatani, M. A. Jalali, and M. Mirsalim, "Analysis of linear permanent magnet switched reluctance motors with modular and segmental movers," *IET Electr. Power Appl.* vol. 17, pp. 756–772, 2023.
- [23] M. Golzarzadeh, H. Oraee, and B. Ganji, "Modeling and comparison of various structures for linear switched reluctance motor," in *4th Conference on Applied Research in Electrical Engineering*, Ahvaz, Iran, 2024.

BIOGRAPHY



Milad Golzarzadeh is currently a PhD candidate in electrical power engineering at Sharif University of Technology, Tehran, Iran. His research interests include modeling and design of electric machines, linear switched reluctance motors, thermal modeling of electric machines, permanent magnet motors and power electronics.



Hashem Oraee (Fellow of IET, Senior Member of IEEE) received the B.Eng. in electrical and electronic engineering from University of Wales, Cardiff, U.K., in 1980, and the Ph.D. degree in electrical machines from the University of Cambridge, Cambridge, U.K., in 1984. He is currently a Full Professor with the Department of Electrical Engineering, Sharif University of Technology, Tehran, Iran. His current research interests include renewable energies, electrical machines, and DFIGs.



Babak Ganji (Senior Member of IEEE) received the B.Sc. degree from Esfahan University of Technology, Iran in 2000, and M.Sc. and Ph.D. from the University of Tehran, Iran in 2002 and 2009 respectively, all in electrical power engineering. He is currently an Associate Professor with the Faculty of Electrical and Computer Engineering, University of Kashan, Kashan, Iran. His research interest is modeling and design of advanced electric machines, especially switched reluctance motor.

Copyrights

© 2025 Licensee Shahid Chamran University of Ahvaz, Ahvaz, Iran. This article is an open-access article distributed under the terms and conditions of the Creative Commons Attribution –NonCommercial 4.0 International (CC BY-NC 4.0) License (<http://creativecommons.org/licenses/by-nc/4.0/>).





Research Article

Investigating Robust Tracking of Type 1 Diabetes Control Using Model-Free Controllers

Peyman Vafadoost Sabzevar¹, Ahmad Hajipour^{1,*}, and Hamidreza Tavakoli²

¹ Biomedical Engineering Department, Electrical and Computer Faculty, Hakim Sabzevari University, Sabzevar, Iran

² Electronic Engineering Department, Electrical and Computer Faculty, Hakim Sabzevari University Sabzevar, Iran

* Corresponding Author: a.hajipour@hsu.ac.ir

Abstract: One of the main challenges in the field of control is the use of a stable controller and its lack of dependence on the system model and dynamics, so that the input signal is applied to the system based on the existing needs. One of the areas that needs controlling and applying the input signal is type 1 diabetes, where people with this disease need constant and regular insulin injections based on blood glucose concentration. Based on this, in this article, two free model methods called the Q-learning algorithm and PID have been used to determine insulin dose, and the results of insulin dose injection show the results and high performance of the Q-learning algorithm in determining insulin dose. This algorithm is one of the methods based on artificial intelligence that discovers the optimal policy based on trial and error. Finally, the Q-learning algorithm has been investigated in the presence of noise, and its stability has been proven to ensure the performance of the controller.

Keywords: Q-Learning, PID controller, model-free, injection insulin, tracking blood glucose.

Article history

Received 26 July 2024; Revised 15 October 2024; Accepted 17 October 2024; Published online 20 April 2025.

© 2025 Published by Shahid Chamran University of Ahvaz & Iranian Association of Electrical and Electronics Engineers (IAEEE)

How to cite this article

P. Vafadoost Sabzevar, A. Hajipour, and H. Tavakoli, "Investigating robust tracking of type 1 diabetes control using model-free controllers," *J. Appl. Res. Electr. Eng.*, vol. 3, no. 2, pp. 232-239, 2024.

DOI: 10.22055/jaree.2024.47542.1126



1. INTRODUCTION

The human body needs energy to perform daily activities, and the most important source of this energy is glucose, which enters the body through daily nutrition. Glucose provides the necessary energy for cells, making physical and mental activities possible. The concentration of glucose in the body must be maintained at a certain level. The pancreas secretes the hormones insulin and glucagon to regulate blood glucose (BG), as the functions of these two hormones complement each other. Insulin helps lower plasma glucose when it is high, and glucagon raises it when plasma glucose is low. Diabetes is one of the most common endocrine diseases that occurs due to damage to the beta cells in the pancreas, so insulin is not secreted in sufficient amounts to regulate BG. As a result, the patient's BG level increases from the normal range of 80-110 mg/dL. Hyperglycemia results from anomalies in either insulin secretion or insulin action or

both and manifests in a chronic and heterogeneous manner as carbohydrate, fat, and protein metabolic dysfunctions [1,2].

In general, diabetes is divided into two main types and several subtypes:

Type 1 diabetes (T1D), formerly known as juvenile-onset diabetes or insulin-dependent diabetes, in which the body's immune system mistakenly attacks and destroys beta cells in the pancreas, resulting in reduced insulin production, or it stops completely. People with this type of diabetes need insulin injections. Type 2 diabetes (T2D) is more common in adults. In this type of diabetes, the body does not use insulin effectively or does not produce enough insulin. The cause of this type of diabetes can be obesity, inactivity and improper diet and lifestyle. Gestational diabetes (GD) is a type of diabetes that occurs during pregnancy, and the hormones released during this period cause the body to resist insulin, which usually resolves after the birth of the baby. There are

other types of diabetes that are less often seen in people who have chemotherapy due to drug use [3].

T1D is the third most common chronic disease of childhood, affecting 1 in 300 children, and there is a consensus that its incidence is increasing [4]. Although significant progress has been made in the timeline of diagnosis, medical management and prevention and treatment of complications, T1D is still a disease with a significant burden with psychological, medical and financial damages for sufferers and their families [5]. Considering that in patients with diabetes, people with T1D require continuous insulin injections, this category of patients needs special attention. In T1D, the pancreas is unable to produce insulin or produces very little insulin, so these patients must inject insulin regularly to keep their BG levels within a normal range.

Many studies have been presented in the field of T1D control and optimal insulin injection.

Different controllers and methods have been used in different fields using machine learning techniques such as neural networks, deep learning and their combination. Also, in various studies, various types of traditional controllers have been used to determine the dose of insulin, and a number of mathematical models related to the diagnosis of diabetes have been reviewed and presented. Therefore, the collection of these models helps to determine the amount of insulin needed to control the disease. The goal of controllers should be to determine insulin dosage based on non-maximization of the model and achieve that goal through interaction with the desired model.

During their research, Babar *et al.* [9] designed an artificial pancreas using Bergman's minimal model and sliding mode control (SMC) and second-order sliding mode control (SOSMC) control techniques. In their results, the use of SOSMC led to better results and fewer complications than the SMC method. Matamoros-Alcivar *et al.* [10] used the model predictive control (MPC) controller and compared it with the proportional–integral–derivative (PID) controller in order to investigate and compare the effects of diets, disorders and other factors related to T1D patients. Single-network adaptive critical neural networks (SNAC), which are based on linear optimum control, were used in the research by Faruque and Padhi [11]. This article's main goal is to simulate how the human pancreas works, which is to continuously detect BG levels and then inject insulin in response to those findings. Tornese *et al.* [12] used a Hybrid Closed-Loop (HCL) programmed into an insulin pump to limit the spread of the coronavirus as well as the high vulnerability of people with T1D in this pandemic. In this method, insulin is injected automatically and semi-automatically based on the BG concentration measured by the sensors. The results of their research indicated that despite the quarantine, diabetes was controlled well and with acceptable results. Mosavi *et al.* [13] have presented a new approach in the control of T1D, which includes fuzzy logic and the modified Bergman model. They have used second type fuzzy logic system (T2FLS) to compensate the error and guarantee the stability. In this research, meal, patient activities and disorders are also considered to evaluate the stability of the controller. The results show that the BG level using this method, compared to other methods, returns to its base and reference value after

a short period of time. Nimri *et al.* [14] used a smart method to compare with doctor's prescriptions. The proposed method was to use decision support system (AI-DSS) and studies were conducted to determine whether frequent adjustments in this system are as effective as the doctor's prescription or not. During the six-month trial, different races and food styles were used on patients, the results of which indicated that during this research, severe complications of diabetes were reported by the doctor in three people, and no case was found in the proposed method. In conclusion, using an automated decision support tool to optimize insulin pump settings resulted in better outcomes than physician prescribing. For individuals with T1D, Patra *et al.* employed a continuous time model predictive controller (CMPC). They carried out a comparison analysis with H-infinity, a PID controller, a linear quadratic regulator (LQR/LQT), and linear quadratic Gaussian (LQG) control to support the efficacy of the controller. The correctness and robustness of the controllers' efficiency have been verified by simulation. The suggested controller's performance is described in terms of its capacity to monitor 81 mg/dL of BG in the presence of random and Gaussian noise [15]. Reference [16] addresses the problem of developing control algorithms for type 1 diabetic patients that provide an automatic connection between continuous glucose monitoring and insulin injection with model free adaptive controller. Reference [17] presents in-silico design and verification of an advanced multi-agent reinforcement learning (RL) strategy for personalized glucose regulation in individuals diagnosed with type 1 diabetes (T1D).

Complications of diabetes include two categories, acute and chronic. One of the acute complications of people with diabetes is diabetic ketoacidosis, which is caused by an increase in blood sugar concentration of more than 250 mg/dL and acidification of the blood, and the use of fat and protein by cells as an energy source leads to the release of acids. Free fat, cholesterol enters the bloodstream and can lead to coma and death. This complication occurs mainly in T1D and sometimes in T2D. Chronic complications can be kidney complications due to high BG and destruction of glomeruli as kidney purifiers. Also, diabetes can include severe complications such as blindness caused by retinal damage, heart diseases, digestive diseases, etc. [6-8].

It is evident from the literature review that different studies have employed different approaches to manage diabetes. Some of these techniques are based on the system model, which has drawbacks because of its unique structure and is unable to adequately take into account all the intricate details of managing diabetes. Linear models are typically utilized in other studies, however because of their lack of comprehensiveness, they are unable to account for all illnesses and variations in the patients' bodies. However, several studies have employed artificial intelligence techniques in place of conventional models. These techniques can handle massive volumes of data and offer more flexible and ideal diabetes management solutions. Artificial intelligence-based decision support systems, for instance, have improved the precision of BG control over conventional techniques by making necessary adjustments. All of these approaches have advantages and disadvantages, and the best approach will rely on the particular circumstances of the patients as well as the objectives of the researchers.

The main goal of this study is to improve and optimize the dose of injectable insulin for these patients. To achieve this goal, model free controller based on reinforcement learning (RL) method is used to calculate and adjust the appropriate dose of insulin by continuously monitoring the BG level and taking into account the daily activities, diet and individual needs of each patient.

According to the above mentions, in the following points, the contribution of this paper can be summarized as:

- Model free RL method has been used to adjust the dose of insulin.
- The performance of proposed method has been compared with performance of PID controller.
- The ability of the proposed controller in handling noise has been investigated

This paper is presented as follows: methodology is described in Section 2. Section 3 is presented the control methods. Simulations and results are presented in Section 4. Finally, Section 5 concludes the paper.

2. METHODOLOGY

According to the review of the literature and the methods used in the control of BG concentration in diabetic patients, in some cases controllers have been used that are dependent on the system model or they have used non-linear and non-comprehensive models in their studies that lead to gaps. In this regard, this paper uses two model-free methods based on classical PID controller, Q-learning algorithm as a sub-branch of machine learning. The desired process is done by measuring the BG concentration by the sensors and comparing it with the reference value, and then the difference value is delivered to the proposed controller and by applying insulin through the insulin pump to the diabetic patient, the BG concentration value until the time Its stability continues.

3. CONTROL METHODS

In this section, RL based on Q-Learning and PID controller methods, which are based on model-free controller, are presented.

3.1. Q-Learning

By examining and conducting studies on the behavior of living organisms, various algorithms and methods have been presented by modeling these systems. One of the desired algorithms used in this research is the Q-learning algorithm, which is presented as a sub-branch of RL. This algorithm optimally discovers its strategy independently of the environment and by interacting and receiving rewards or penalties. This policy is such that the bonus or penalty received reaches its maximum or minimum amount. Q-learning algorithm generally includes the following concepts [18]:

Agent: The agent performs various actions in the environment by using the stimuli defined in him and acts first as a learner and then as a decision maker in the environment after completing the learning.

State Space: The state space is a set of different states that the agent can be in. In this research, the state space depends on the patient's BG concentration. 144 states of the state space are defined in which the agent is placed in that state if the BG concentration falls within any given interval.

Action Space: The action space is called the set of actions of the agent in the state space. The dose of injectable insulin has been introduced as an action that can be performed by the agent, which can perform 120 different values from 0 to 12 μU .

Reward: Reward is one of the key and decisive components in the agent's performance. Reward as an immediate feedback signal that is presented to the agent and indicates the success rate of its performance in the environment. The amount of reward in this process is calculated based on the following formula, if there is a difference between the output and the reference signal, the agent receives a penalty:

$$R = -|G_{ref} - G| \quad (1)$$

Policy: Optimal policy as a situation where the agent in the desired state should perform an action. The optimal policy may be a function or a lookup table, and this concept is referred to as the core of RL algorithms.

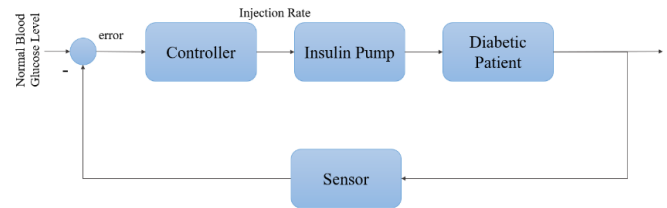


Fig. 1: Feedback regulation of BG.

| State | Glucose |
|-----------|---------------------------------|
| State 1 | $80 > \text{Glucose}$ |
| State 2 | $80 \leq \text{Glucose} < 81$ |
| State 3 | $82 \leq \text{Glucose} < 83$ |
| State 4 | $83 \leq \text{Glucose} < 84$ |
| . | . |
| . | . |
| . | . |
| State 142 | $219 \leq \text{Glucose} < 220$ |
| State 143 | $220 \leq \text{Glucose} < 221$ |
| State 144 | $\text{Glucose} \geq 221$ |

Fig. 2: State space.

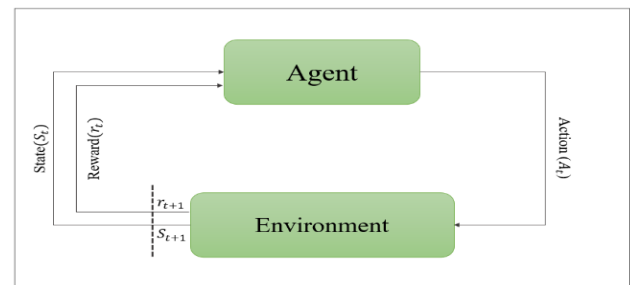


Fig. 3: Schematic of reinforcement learning operation.

Maximizing reward or penalty during the learning process is a primary objective of Q-learning, and it is characterized by the following formula:

$$G_t = \sum_{k=0}^{\infty} \gamma^k R_{t+k+1} = R_{t+1} + \gamma R_{t+2} + \dots \quad (2)$$

where γ is referred to as the discount factor, which is defined as a value between 0 and 1. The closer this value is to 1, the more important the factor is to long-term rewards, and conversely, the closer it is to 0, the more important short-term rewards are given. Considering that in this study it is necessary that the BG concentration of the patient has a higher stability in the long term, we use the value of 0.95.

To find the optimal policy in Q-learning, the state-action space function is defined, which indicates the value of the amount of action performed in that state, which is determined according to the following formula:

$$q_{\pi}(s, a) = E[G_t | S_t = s, A_t = a] \quad (3)$$

The value function of the optimal state-action in the presence of the optimal policy can be computed by replacing equation 2 in 3.

$$q_*(s, a) = \max_{\pi} q_{\pi}(s, a) \quad (4)$$

The optimal policy is defined based on value functions. When the state-action-value function is available, it selects the action factor that has the highest value among all states. The optimal policy is defined based on value functions according to the following formula:

$$\pi_*(s) = \operatorname{argmax}_a q_*(s, a) \quad (5)$$

Considering that at the beginning of learning, the agent does not understand the environment, it performs its actions based on the ϵ policy. This means that the action with the highest value is performed with a probability of $1 - \epsilon$, and an action is randomly selected and applied in the environment with a probability of ϵ . At the beginning of the process, due to the agent's lack of complete understanding of the environment, the value of ϵ is considered to be equal to 1 to search the environment based on random actions, and then with the completion of the learning process, its value is reduced using the following formula. It finds that its minimum value is considered equal to 0.01:

$$\epsilon = \min \epsilon + (\max \epsilon - \min \epsilon) e^{-0.01 * \text{episode}} \quad (6)$$

It is always possible to improve an existing policy, because a better policy leads to higher values. By determining the state-action value function relative to the initial policy, a better policy can be found. After determining the improved policy, the state-action value function is calculated and using this function, a better policy is created.

This process of evaluating and improving the policy is repeated until the optimal policy is reached. Any new policy is usually better than the previous policy unless the optimal policy is reached. Fig. 4 shows the performance of the Q-learning, which seeks to find the best solution by choosing different actions and receiving rewards for each action. Learning rate in the Q-learning algorithm is defined as alpha α . The amount that the new information replaces the old information is determined by this value. To put it another

way, α indicates the ratio of the algorithm's reliance on prior knowledge to that gained from new events. This value is used in this research based on trial and error based on 0.8. The important point is that all the parameters in the Q-learning algorithm have been evaluated through the process of trial and error. In this process, it has been tried to obtain the most optimal settings to improve the performance of the algorithm by checking and comparing the values of different parameters.

3.2. PID

PID is one of the most popular controllers in industrial systems because of its adaptability and simplicity; studies have shown that PID is successful and long-lasting [19]. This controller operates on closed loop control, which is composed of three basic components: proportional, integral, and derivative. It is independent of environmental conditions. The block diagram of this controller's overall operation is displayed in Fig. 5. The controller does the following tasks [20]:

Proportional controller: This type of controller has an output that is directly proportional to the current error. The controller's coefficient determines how strongly the controller reacts to the current error.

Integral controller: this component's output is based on the total amount of errors over time, which establishes how strongly the controller responds to previous errors.

Derivative controller: Its coefficient shows how the controller responds over time to changes in the system's error rate and is proportionate to the error change rate.

The control signal in this method is calculated according to the following formula:

| Q-Learning Algorithm | |
|----------------------|---|
| 1: | Set values learning rate $\alpha \in (0,1]$, discount factor $\gamma \in (0,1]$, $\epsilon > 0$, reward matrix R |
| 2: | Initialize $Q(s, a)$ to zeros |
| 3: | for each episode: do |
| 4: | Initialize s |
| 5: | for each step of episode: do |
| 6: | Choose a from using policy derived from $Q(e, g, \epsilon - greedy)$ |
| 7: | Take action, obtain reward r from R and next state s' |
| 8: | $Q(s, a) \leftarrow Q(s, a) + \alpha[r + \gamma \max_{a'} Q(s', a') - Q(s, a)]$ |
| 9: | $s \leftarrow s'$ |
| 10: | until s is terminal |
| 11: | end for |
| 12: | end for |

Fig. 4: Q-Learning algorithm.

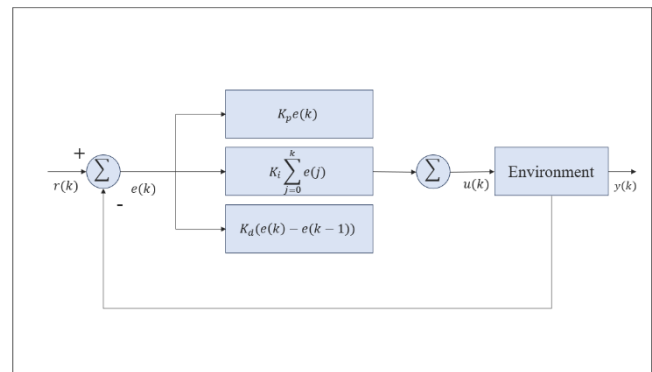


Fig. 5: PID control system's structure.

$$u(k) = K_p e(k) + K_i \sum_{j=0}^k e(j) + K_d (e(k) - e(k-1)) \quad (7)$$

The error considered in order to track the reference signal is calculated according to the following formula:

$$e(k) = r(k) - y(k) \quad (8)$$

The controller parameters of PID are set based on the studies done by Chengwei *et al*. PID parameters are $K_p = 0.09, K_i = 0, K_d = 0.04$ [21].

4. SIMULATIONS AND RESULTS

Considering that the two control methods are not dependent on the model and do not need to know the parameters of the system, therefore, in this research, due to the fact that the possibility and conditions of testing on the human biological system were not available, a non-linear comprehensive model called Bergman's minimal model was used in This research is used only to receive feedback and to apply insulin dosage, whose formula is as follows [22]:

$$\begin{aligned} \frac{dG}{dt}(t) &= -p_1[G(t) - G_b] - X(t)G(t) \\ \frac{dX}{dt}(t) &= -p_3[I(t) - I_b] - p_2X(t) \\ \frac{dI}{dt}(t) &= -n[I(t) - I_b] + \gamma[G(t) - h]^+ + u(t) \end{aligned} \quad (9)$$

The variables and parameters used in this model are thoroughly detailed and explained in Table 1. This table provides a comprehensive overview, listing each variable and parameter alongside its corresponding definition, unit of measurement used in the analysis. One of the most often used models for physiological study on the mechanism of glucose and insulin, which is used to characterize the concentration of blood glucose and insulin, is Bergman's minimum model. This model, which has two components to illustrate the behavior of glucose and insulin secretion following an intravenous injection of the sample, is called minimal because it uses the fewest parameters feasible to mimic diabetes individuals for the intravenous glucose tolerance. In equation 9, the sign "+" indicates the absorption of glucose by the body. When the value of $G(t)$ is higher than h , the desired relationship acts as a regulator in the body, which is not considered in insulin dynamics due to the lack of a regulator or its lack of influence in patients with diabetes.

For simulation purposes, MATLAB version 2021b software has been used to investigate the control of BG concentration in T1D patients. For this purpose, first, using the mathematical equations of Bergman's minimum model and the initial values of its parameters in Fig. 6, the changes in BG concentration for a healthy person and a T1D patient have been investigated. Fig. 7 shows that having an external injector is necessary for people with T1D.

Finally, based on the definitions in the problem description section, the insulin injection dose has been applied to the existing model by two controllers, and the reference signal is defined as follows in order to compare and improve the insulin injection:

$$G_{ref} = 80 + (200 - 80)e^{0.05t} \quad (10)$$

Fig. 8 depicts the outputs produced by two algorithms, namely the cue learning algorithm and the PID controller. This graph clearly shows that the Q-learning algorithm has a very strong and effective performance in tracking the reference signal compared to PID. Q-learning algorithm has been able to follow system changes well and achieve higher accuracy in setting control parameters.

The superior performance of the Q-learning algorithm is due to its ability to learn by interacting with the environment and continuously updating the Q-values, which leads to

| Parameters | Healthy | T1D |
|------------|-----------------------|-----------------------|
| $G(0)$ | 200 | 200 |
| $X(0)$ | 0 | 0 |
| $I(0)$ | 364.8 | 50 |
| G_b | 80 | 80 |
| I_b | 7 | 7 |
| p_1 | 0.0317 | 0.0 |
| p_2 | 0.123 | 0.0 |
| p_3 | 4.92×10^{-6} | 1.54×10^{-5} |
| n | 0.2655 | 0.2814 |
| h | 79.0353 | 79.0353 |
| γ | 0.0039 | 0 |

Fig. 6: Values of model parameters for a healthy person and a person with T1D [23].

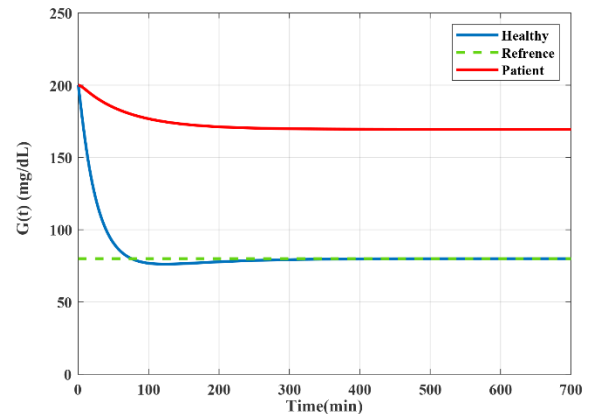


Fig. 7: Changes in BG concentration in healthy individuals and T1D patients.

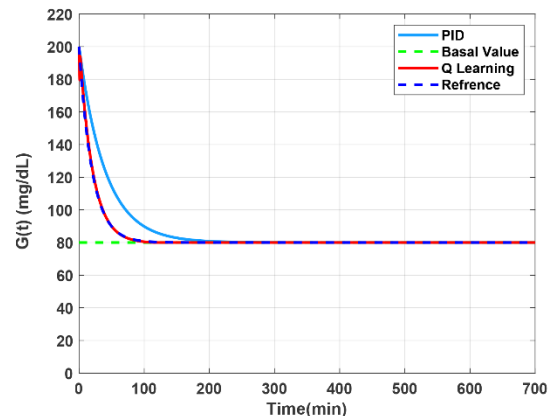


Fig. 8: BG concentration control using Q-learning and PID.

continuous improvement of decision making and control. This algorithm has been able to minimize system errors and create more stability in process control. The accuracy of the proposed algorithms is calculated according to the following formula:

$$\text{Accuracy (\%)} = \frac{\max |G(t) - G_{ref}(t)|}{G_{ref}(t)} \times 100 \quad (11)$$

According to (11), the accuracy of Q learning algorithm is 94.6% and PID is 74.3%.

To evaluate the robustness and stability of this algorithm, investigations have also been done by adding noise to the system. These noises have been applied in order to simulate more realistic conditions and evaluate the performance of the algorithm in the face of unexpected changes and environmental noises.

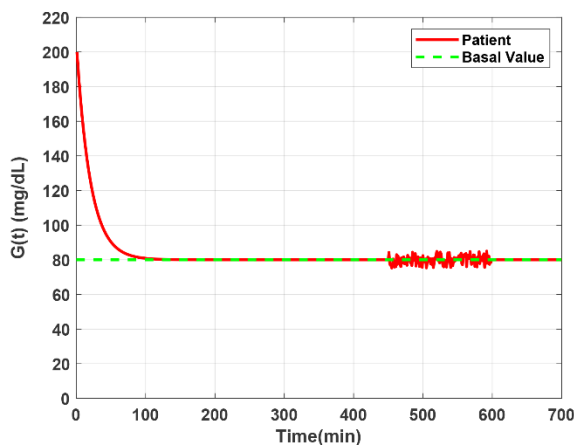


Fig. 9: Regulation of BG levels with Q-learning in noisy environments.

5. CONCLUSION

In this article, the application and efficiency of two control methods, one based on RL and the other PID, as model-free algorithms that do not depend on the system model, were investigated. One of the other primary goals of this article was to track the BG concentration of T1D patients. In particular, due to the lack of insulin secretion, this article focused on the parameters of T1D so that the BG concentration of these people is the same as that of healthy people. In the simulations and results, it was shown that the Q-learning algorithm, due to its continuous updating, had a

much higher and more acceptable accuracy in tracking and maintained its stability and resistance against abnormal conditions in the presence of noise. In the absence of inappropriate conditions in his biological system, the patient should not suffer from severe complications and a sudden drop or increase in BG concentration. One of the main advantages of this algorithm compared to PID is its compatibility with the environment, and if the appropriate reward is defined, the optimal policy can be converged to the desired problem. This adaptability makes them suitable for environments where traditional control methods may have difficulty finding a solution. Although the Q-learning algorithm has a high potential for optimizing the insulin dose, but due to these limitations, such as the fact that each person's body's response to insulin is complex and variable and various factors are involved, it requires a large set of different data. Also, during the process of learning and adjusting the parameters of the algorithm, there are health risks such as a severe drop in BG or an excessive increase in BG. These risks can threaten the patient's health during the implementation of an algorithm that is not yet optimized. Therefore, its use requires caution and the use of large data sets to be used in real environments with sufficient safety.

CREDIT AUTHORSHIP CONTRIBUTION STATEMENT

Peyman Vafadoost Sabzevar: Conceptualization, Data curation, Investigation, Methodology, Software, Validation, Writing - review & editing. **Ahmad Hajipour:** Conceptualization, Data curation, Formal analysis, Formal analysis, Funding acquisition, Investigation, Methodology, Project administration, Resources, Software, Supervision, Validation, Visualization, Writing - original draft, Writing - review & editing. **Hamidreza Tavakoli:** Formal analysis, Investigation, Software, Visualization, Writing - original draft, Writing - review & editing.

DECLARATION OF COMPETING INTEREST

The authors declare that they have no known competing financial interests or personal relationships that could have appeared to influence the work reported in this paper. The ethical issues; including plagiarism, informed consent, misconduct, data fabrication and/or falsification, double publication and/or submission, redundancy has been completely observed by the authors.

Table 1: Description of Bergman's minimal model parameters [22].

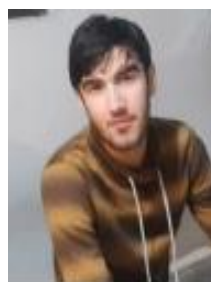
| Parameters | Description | Unit |
|------------|--|--|
| $G(t)$ | concentration of blood glucose in plasma at time t | [mg/dL] |
| $X(t)$ | the effect of insulin on the disappearance of glucose at time t | [1/min] |
| $I(t)$ | concentration of insulin in plasma at time t | [μU/mL] |
| G_b | basal value of glucose level | [mg/dL] |
| I_b | basal value of insulin level | [μU/mL] |
| p_1 | rate of glucose absorption in tissues independent of insulin | [1/min] |
| p_2 | rate of reduction of absorption ability Glucose in tissues | [1/min] |
| p_3 | rate of the ability of tissues | $I_b [(\frac{\mu U}{mL})^{-1} min^{-1}]$ |
| n | rate of insulin reduction | [1/min] |
| h | threshold value Glucose, insulin secretion if the glucose concentration exceeds | [mg/dL] |
| γ | rate of insulin secretion by beta cells when the blood glucose level exceeds the threshold value | $[(\mu/mL)(mg/dL)^{-1} min^{-2}]$ |

REFERENCES

- [1] American Diabetes Association, "Diagnosis and classification of diabetes mellitus," *Diabetes Care*, 2014, vol. 37, pp. S81-90.
- [2] American Diabetes Association, "Introduction: Standards of medical care in diabetes," *Diabetes Care*, 2018, vol. 41, pp. S1-2.
- [3] M. Z. Banday, S. S. Aga, and N. Saniya, "Pathophysiology of diabetes: An overview," *Avicenna Journal of Medicine*, vol. 10, no. 4, pp. 174-188, 2020.
- [4] C. C. Patterson et al., "Worldwide estimates of incidence, prevalence and mortality of type 1 diabetes in children and adolescents: Results from the international diabetes federation diabetes atlas." *Diabetes Research and Clinical Practice*, vol. 157, p. 107842, 2019.
- [5] T. Quattrin, L. D. Mastrandrea, and L. S. K. Walker, "Type 1 diabetes." *The Lancet*, vol. 401, no. 10394, pp. 2149-2162, 2023.
- [6] A/ H. A. Abu-Rmieleh, "Control and modeling techniques in biomedical engineering: the artificial pancreas for patients with type 1 diabetes," PhD Thesis, Universitat de Girona, 2013.
- [7] M. Bryer-Ash, *100 Questions & answers about diabetes*. Jones & Bartlett Publishers, 2009.
- [8] C. S. Marathe et al., "Gastrointestinal disorders in diabetes." [Online]. (2003), Available: <https://www.ncbi.nlm.nih.gov/books/NBK553219/>
- [9] S. A. Babar, A. Iftikhar, and I. S. Mughal, "Sliding - mode-based controllers for automation of blood glucose concentration for type 1 diabetes." *IET Systems Biology*, vol. 15, no. 2 pp. 72-82, 2021.
- [10] E. Matamoros-Alcivar, T. Ascencio-Lino, R. Fonseca, G. Villalba-Meneses, A. Tirado-Espín, L. Barona, and D. Almeida-Galárraga, "Implementation of MPC and PID control algorithms to the artificial pancreas for diabetes mellitus type 1," in *2021 IEEE International Conference on Machine Learning and Applied Network Technologies (ICMLANT)*, IEEE, 2021.
- [11] S. F. Ali, and R. Padhi. "Optimal blood glucose regulation of diabetic patients using single network adaptive critics," *Optimal Control Applications and Methods*, vol. 32, no. 2, pp. 196-214, 2011.
- [12] G. Tornese, V. Ceconi, L. Monasta, C. Carletti, E. Faleschini, and E. Barbi. "Glycemic control in type 1 diabetes mellitus during COVID-19 quarantine and the role of in-home physical activity." *Diabetes Technology & Therapeutics*, vol. 22, no. 6, pp. 462-467, 2020.
- [13] A. H. Mosavi et al., "Deep learning fuzzy immersion and invariance control for type-I diabetes," *Computers in Biology and Medicine*, vol. 149, p. 105975, 2022.
- [14] R. Nimri et al., "Insulin dose optimization using an automated artificial intelligence-based decision support system in youths with type 1 diabetes," *Nature Medicine*, vol. 26, no. 9, pp. 1380-1384, 2020.
- [15] A. K. Patra, and P. K. Rout. "Adaptive continuous-time model predictive controller for implantable insulin delivery system in Type I diabetic patient," *Optimal Control Applications and Methods*, vol. 38, no. 2, pp. 184-204, 2017.
- [16] B. Selma, H. Abouaïssa, S. Chouraqui, H. Kadem, D. Mehdeb, and M. Elaffifi, "Toward a model-free feedback control of blood glucose induced by meals for type-1 diabetics: in silico studies," *Iran Journal of Computer Science*, pp.1-11, 2024..
- [17] M. Jaloli, and M. Cescon, "Basal-bolus advisor for type 1 diabetes (T1D) patients using multi-agent reinforcement learning (RL) methodology," *Control Engineering Practice*, vol. 142, p.105762, 2024.
- [18] J. C. H. Christopher, "Watkins and peter dayan. Q-Learning." *Machine Learning*, vol. 8, no. 3, pp. 279-292, 1992.
- [19] K. H. Ang, G. Chong, and Y. Li. "PID control system analysis, design, and technology." *IEEE Transactions on Control Systems Technology*, vol. 13, no. 4, pp. 559-576, 2005.
- [20] M. A. Johnson, and M. H. Moradi, *PID control*. London, UK: Springer-Verlag London Limited, 2005.
- [21] C. Li, and R. Hu. "Simulation study on blood glucose control in diabetics," in *2007 1st International Conference on Bioinformatics and Biomedical Engineering*, pp. 1103-1106. IEEE, 2007.
- [22] K. E. Andersen, and M. Højbjerg, "A bayesian approach to bergman's minimal model," in *International Workshop on Artificial Intelligence and Statistics*, pp. 1-8, 2003.
- [23] P. S. Vafadoost, H. Sadrian, and A. Hajipour, "Tracking blood glucose concentration of type 1 diabetic patients using reinforcement learning," in *2023 9th International Conference on Control, Instrumentation and Automation (ICCIA)*, IEEE, 2023, pp. 1-6..

BIOGRAPHY

Peyman Vafadoost Sabzevar received his B.Sc. degree in Computer Engineering and his M.Sc. degree in Biomedical Engineering in 2020 and 2023 from Hakim Sabzevari University, Sabzevar, Iran, respectively. His research interests include internet of things and machine learning.



Ahmad Hajipour received the B.Sc. degree in control engineering from the Ferdowsi University of Mashhad, Iran, in 2002, and the M.Sc. and Ph.D. degrees in control engineering from the Shahrood University of Technology, Iran, in 2004 and 2009, respectively. Since 2011, he has been an Associate Professor with the Department of Electrical



Engineering, Hakim Sabzevari University. His research interests include fractional calculus, robotics, and machine learning.



Hamidreza Tavakoli received the B.Sc. degree in electronic engineering from the Ferdowsi University of Mashhad, in 2000, and the M.Sc. and Ph.D. degrees in electronic engineering from the Iran University of Science and Technology, in 2003 and 2014, respectively. Since 2015, he has been an Assistant Professor with the Department of Electrical

Engineering, Hakim Sabzevari University. His research interests include robotics, machine learning, and machine vision.

Copyrights

© 2025 Licensee Shahid Chamran University of Ahvaz, Ahvaz, Iran. This article is an open-access article distributed under the terms and conditions of the Creative Commons Attribution –NonCommercial 4.0 International (CC BY-NC 4.0) License (<http://creativecommons.org/licenses/by-nc/4.0/>).





Iranian Association of
Electrical and Electronics
Engineers

Journal of Applied Research in Electrical Engineering

E-ISSN: 2783-2864

P-ISSN: 2717-414X

Homepage: <https://jaree.scu.ac.ir/>



Research Article

IRS-Assisted Visible Light Communication for Improved Monitoring of Patient Vital Signals in Hospital Environment

Babak Sadeghi, and Seyed Mohammad Sajad Sadough*

Faculty of Electrical Engineering, Shahid Beheshti University, 1983969411 Tehran, Iran

* Corresponding Author: s_sadough@sbu.ac.ir

Abstract: This paper explores the integration of intelligent reflecting surfaces (IRS) with visible light communication (VLC) to enhance optical communication reliability and mitigate link blockage. We particularly focus on a patient vital signal monitoring system in a hospital, where a wireless optical device-to-device (D2D) unit transmits signals to a monitoring center. Our study highlights the benefits of using an IRS, demonstrating that a 35-unit IRS array can double the received optical power compared to traditional non-line-of-sight (NLOS) links. We also propose an optimal placement strategy for IRS on indoor area walls to maximize the signal-to-noise ratio (SNR) and minimize the bit error rate (BER), considering constraints specific to optical wireless communication. We formulate and solve an optimization problem to determine the best IRS location, aimed at achieving ubiquitous communication with minimal BER. Numerical results illustrate the system's effectiveness in enhancing optical link reliability for patient monitoring. The findings indicate that optimal IRS placement can result in a BER as low as 2.48×10^{-8} , and with adjustments to the photodetector orientation, an even lower BER of around 6.32×10^{-10} can be achieved without increasing transmitter power. This research underscores the potential of IRS in improving the performance of VLC systems, particularly in critical applications such as healthcare monitoring.

Keywords: Intelligent Reflecting Surface (IRS), Device-to-Device (D2D), Bit Error Rate (BER), Non-Line-Of-Sight (NLOS), vital signal monitoring system, Signal to Noise Ratio (SNR).

Article history

Received 16 August 2024; Revised 12 November 2024; Accepted 16 January 2025; Published online 20 April 2025.

© 2025 Published by Shahid Chamran University of Ahvaz & Iranian Association of Electrical and Electronics Engineers (IAEEE)

How to cite this article

B. Sadeghi, and S. M. Sajad Sadough, "IRS-Assisted visible light communication for improved monitoring of patient vital signals in hospital environment," *J. Appl. Res. Electr. Eng.*, vol. 3, no. 2, pp. 240-249, 2024.

DOI: 10.22055/jaree.2025.47734.1133



1. INTRODUCTION

1.1. Background

Device-to-device (D2D) communication enables communication devices to be directly linked with each other without the need for a central base station [1]. For instance, efficient data sharing, collaboration between devices, and improved reliability in dense network environments can be achieved with D2D. In 6G, D2D communication can be further improved by utilizing visible light communication (VLC) [1]. D2D communication through VLC can enable local, fast, and efficient data transfer, by reducing the load on the overall network. Therefore, VLC can be a good option for machine-type communications (MTC) in the hospital environment [1]. However, such a link can be blocked many

times by people and objects especially in dense hospital environments. As depicted in Fig. 1, intelligent reflecting surface (IRS) helps us to overcome the blockage of direct or line-of-sight (LOS) links as well as the random orientation of receiver/transmitter in VLC links by modifying the configuration of the optical channel. In the lack of a LoS path, the IRS link can provide a connection with higher quality-of-service (QoS), more reliability and higher flexibility compared to the classical non-line of sight (NLOS) link (from a wall, sofa, etc.) in an indoor hospital environment [2]. By finding the optimal location of IRS units, the benefits of IRS can be increased and the probability of outage in LOS links can be reduced.

Implementing intelligent reflecting surfaces (IRS) in a real-world hospital involves several technical issues such as

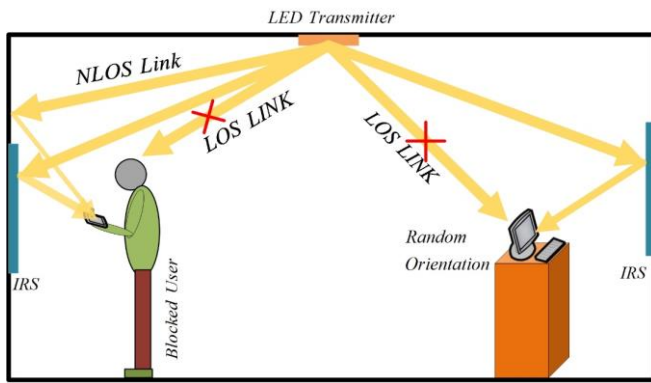


Fig. 1: Basic schematic of an IRS-assisted VLC system in overcoming the random orientation of the optical detector and link blockage.

[1-8]: **i)** site survey and assessment, to ensure optimal placement of IRS for effective coverage; **ii)** integration with existing infrastructure to avoid interference and ensure compatibility with existing wireless networks and medical devices; **iii)** accurate signal modeling is necessary due to the presence of walls, corridors, medical equipment, etc. that can attenuate the signal's strength; **iv)** staff training is crucial for successful deployment; **v)** signal quality index (SQI) should be considered as a metric to check the quality of the received signal, etc.

1.2. Related Works

Several studies have pointed out the pros and cons of combining IRS with indoor VLC communication (see for instance [4-10]).

The pioneering research in the field of using VLC as a transmission medium for monitoring the patient's vital signals was performed in [9, 10]. In these works, VLC is introduced as an emerging technology that can take over the role of radio frequency signals in hospital data transmission. These studies deal with general schematic of optical transmitters and receivers, but they do not mention the problems of applying visible light in transmitting and receiving data.

In [3], the authors have provided a depth literature survey of VLC-enabled patient monitoring systems and indoor localization where they present some of the major challenges and some of the open issues in the field of VLC-enabled healthcare.

In [4], the authors have compared meta-surface and mirror-type IRS where they have extracted the required phase changes of various reflecting surfaces for choosing an optimal power concentration method. However, in this study, the inherent constraints and required optimization of IRS are not addressed.

A framework for integrating IRS with indoor VLC systems is proposed in [5], where an overview of IRS and its advantages, different IRS types and its main applications in VLC systems are presented. Moreover, the authors have also investigated the capacity of IRS to overcome the effects of receiver's random orientation and blockage of optical links.

In [6], to tackle with receiver's random orientation, the authors have proposed an IRS-aided indoor VLC system with

an optimal irradiance angle guided toward the user subject, which can facilitate optimal orientation of the IRS element in order to maximize the received power at the user's location. Moreover, the closed-form expression for the obtained optimal irradiance angle is derived. However, the optimal location of IRS units to guarantee a ubiquitous coverage is not addressed.

One of the few studies in the field of IRS parameter optimization, is done in [7] where the authors propose optimizing the IRS-assisted VLC systems by controlling the IRS elements to maximize the network sum-rate while maintaining fairness in the user achievable throughput.

One of the most relevant study in the field of patient vital signs monitoring is that presented in [8], where SQI is used to evaluate the quality of the optical link.

In most of these studies in the field of VLC, the use of IRS has been mentioned in order to improve the optical link performance, but almost none of them have addressed the challenges and constraints of its use. These challenges are divided into three main categories: challenges caused by the optical transmitter, optical receiver, and also the restrictions caused by the IRS.

1.3. Main Contributions

The main purpose of this paper is to address the advantages brought by IRS deployment and optimization of IRS placement for increasing the received SNR and BER in the indoor VLC system inside a hospital environment for the critical application of healthcare monitoring system. In brief, our main contributions can be summarized as follows.

- We prove the superiority of the IRS-assisted VLC link over the classic NLOS VLC link in the hospital indoor environment, by comparing the received power at the receiver's location.
- We derive the inherent constraints for deploying IRS in indoor visible light D2D communication.
- We formulate and numerically solve the optimization problem to determine the optimal location of IRS deployment leading to the minimum BER at the location of the optical receiver in the considered area.
- Although the main aim of this article is to find the optimal location of the IRS in order to increase the SNR and reduce the BER, in this article we also show that fine-tuning the orientation of the optical detector (PD) of the receiver, can be very effective for improving these parameters.

1.4. Paper Organization

The rest of this paper is structured as follows. In [Section 2](#), we introduce the system model and the channel model of the IRS-assisted VLC healthcare monitoring system inside the considered hospital environment. In [Section 3](#), we derive the limitations and the constraints regarding optimal placement of IRS inside the indoor area. These constraints are divided into three general categories of receiver constraints, transmitter constraints and IRS application restrictions. In [Section 4](#), we consider the BER as the appropriate objective function that we minimize according to the constraints

derived in Section 3. In the rest of Section 4, we numerically solve the BER optimization problem to find the optimal placement of the IRS unit. Section 5 illustrates through simulations the superiority of the IRS-assisted VLC link over the classical NLOS link and also the advantages brought by optimizing the location of the IRS in terms of received SNR and BER. Finally, in Section 6, we draw our concluding remarks.

2. IRS-AIDED INDOOR VLC SYSTEM AND OPTICAL CHANNEL MODEL

Fig. 2 depicts the considered scenario of downlink VLC communication system. More precisely, we consider a non-coherent light-emitting diode (LED) access point (AP), oriented horizontally and installed on the platform of the room. The aim of the communication system is to measure vital signals of the patient located at height h_t in the hospital indoor environment of dimensions $L \times W \times H$. The receiver is a photodetector (PD) which is located at height h_r . In order to overcome blockage of the optical beam, an IRS array composed of N units is placed on the side wall, where angle diversity receiver (ADR) is also used. The location of AP and PD are assumed fixed, but their orientation can be changed. Fig. 3 implies the block diagram of the considered transmitter and receiver. As shown in Fig. 3, the intensity of the optical source is modulated with on-off keying (OOK) where the amplitude of symbols belongs to the set $\{0, A_{sym}\}$ and demodulation is performed by direct detection (IM/DD) of the optical beam and conversion to the photocurrent signal $y(t)$ by using a PD. We have:

$$y(t) = G_{oc} R x(t) \otimes h(t) + w(t), \quad (1)$$

where $x(t)$ is the radiated beam of the AP, generated from the modulated digital beam stream $S(t)$, G_{oc} is the gain of the optical concentrator, R is the responsivity of the optical detector, $h(t)$ is the baseband channel impulse response and $w(t)$ is the additive white Gaussian noise (AWGN) which is assumed independent from the data signal with probability density function $N(0, \sigma_r^2)$. Also, $h_m(t)$ is the matched filter impulse response, and $r(t)$ is the matched filter output, which is passed through the sampler working at nT_{sym} (T_{sym} is time of each symbol in OOK, $n \in \mathbb{N}$) to produce the discrete sequence r_n . According to (1) and the system model in Fig. 3, we have:

$$r(t) = [G_{oc} R x(t) \otimes h(t)] \otimes h_m(t) + w(t) \otimes h_m(t). \quad (2)$$

By defining $v(t) = w(t) \otimes h_m(t)$, we get:

$$r(t) = [G_{oc} R x(t) \otimes h(t)] \otimes h_m(t) + v(t). \quad (3)$$

The sampled symbol r_n at the output of the matched filter for the n -th bit can thus be expressed as follows:

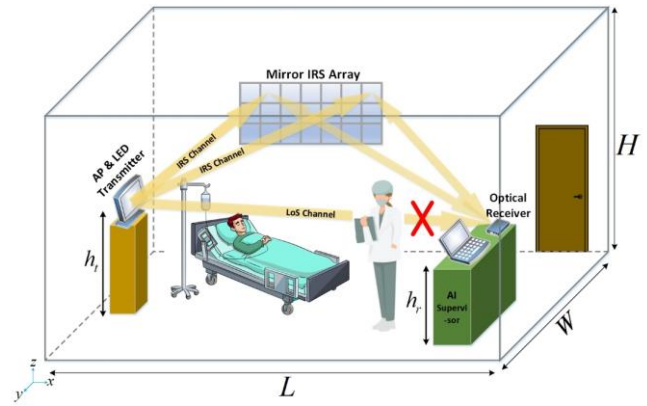


Fig. 2: Indoor hospital VLC system consisting of a transmitter and a receiver and an array of IRS.

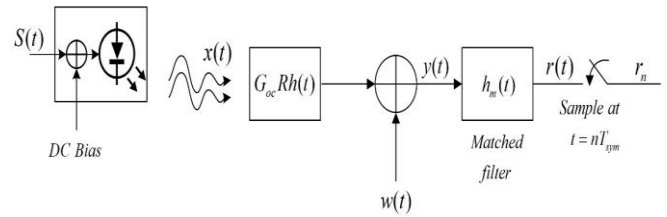


Fig. 3: Block diagram of an IM/DD transceiver.

$$r_n = \begin{cases} A_{sym} + v_n & ; \text{if 1 is sent} \\ v_n & ; \text{if 0 is sent} \end{cases}, \quad (4)$$

where v_n is the sampled noise which is a Gaussian random variable.

In IRS-assisted indoor VLC, the channel gain is composed as the sum of three terms: i) the LOS channel component, ii) the NLOS channel components due to reflections from wall and objects, and iii) reflections from the IRS units. So, the total IRS-assisted VLC channel DC gain can be expressed as [11, 12]:

$$H = H_{los} P_{out} + \sum_{k=1}^K H_{nlos,k} + \sum_{n=1}^N H_{irs,n}, \quad (5)$$

where H_{los} is the DC gain of the LOS channel, $H_{nlos,k}$ is the DC gain of the NLOS channel due to the k -th reflector ($k \in \{1, \dots, K\}$) and $H_{irs,n}$ is the DC gain of the IRS channel due to the n -th unit ($n \in \{1, \dots, N\}$). K and N are the number of reflectors in the room (wall, sofa, etc.) and the number of IRS elements, respectively. Moreover, in (2), we have assumed that the LOS link in the considered system model (hospital indoor environment) is blocked by humans (nurse, doctor, etc.) and/or objects, with a probability P_{out} .

2.1. LOS Channel Gain

The VLC channel DC gain corresponding the LOS component, is given as [2]:

$$H_{los} = \frac{A_{PD}(m_l + 1)}{2\pi d_{lr}^2} \cos^{m_l}(\phi) g(\psi) T(\psi) \cos(\psi), \quad (6)$$

where ϕ is the angle of irradiance, ψ is the angle of incidence, and $g(\psi)$ is a function of the refractive index and the semi-angle of the field-of-view ψ_{fov} ; A_{PD} , m_l , $T(\psi)$, and d_{tr} denote the PD area, the Lambertian order, the optical filter gain, and the distance between the transmitter and the receiver, respectively [2].

2.2. NLOS Channel Gain

In characterization of NLOS links, two general reflection model from the wall are commonly considered in the literature, namely the Lambertian model and the Phong model [4]. Here, to estimate the DC gain of the NLOS component, the Lambert's model is considered for reflection from the surfaces inside the room. The NLOS channel gain from the wall corresponding to the k -th reflector is defined as [2]:

$$H_{nlos,k} = \int_{A_{ref}} \frac{(m_l + 1)}{2\pi d_{ref}^2 d_{tr}^2} \rho_{ref} \cos^{m_l}(\phi) T(\psi) g(\psi) \cos(\theta_i) \times \cos(\theta_r) \cos(\psi) dA_{ref}, \quad (7)$$

where d_{tr} is the distance of the light source from the reflector, and d_{ref} is the distance between the reflector and the receiver. To increase the accuracy of NLOS channel DC gain estimation, we divide each reflector surface into small dA_{ref} surfaces with reflection coefficient ρ_{ref} ; θ_i and θ_r are the angles of incidence and reflection of the NLOS paths on the reflecting surfaces [13].

2.3. IRS Channel Gain

Let the effective area of each IRS unit be equal to ΔA_{irs} and the reflection coefficient for each unit ρ_i . The DC gain of the IRS channel with N serving units for one user, writes [14]:

$$H_{irs} = N \frac{A_{PD}(m_l + 1)}{2\pi d_{ii}^2 d_{ir}^2} \rho_i \Delta A_{irs} \cos^{m_l}(\phi) T(\psi) g(\psi) \times \cos(\theta_{iirs}) \cos(\theta_{rirs}) \cos(\psi), \quad (8)$$

where d_{ii} is the distance between the light source and the n -th IRS unit and d_{ir} is the distance between the n -th IRS unit and the optical receiver, θ_{iirs} and θ_{rirs} are the angle of incidence with the IRS surface and the angle of reflection from the IRS surface, respectively [14].

3. PRACTICAL CONSTRAINTS REGARDING IRS DEPLOYMENT

In what follows, we address the important constraints that should be considered at the transmitter, IRS and receiver sides in order to reduce the probability of link outage to ensure a ubiquitous communication. As can be seen from Fig. 4, these constraints lead to restrictions on the location of IRS deployment. As shown in Fig. 4, we assume a 3D Cartesian coordinate system where IRS units are deployed across the x -axis, where y is fixed (x and z are variable). The limitations

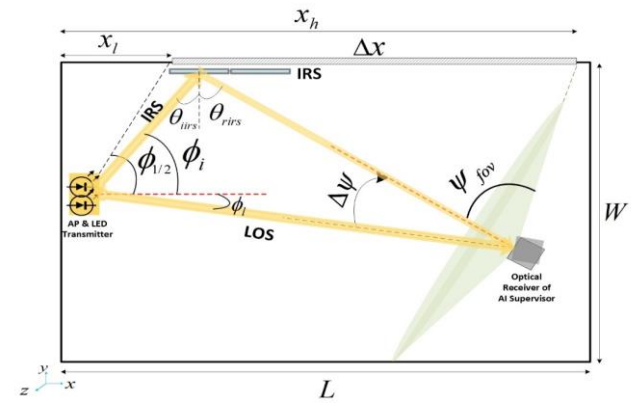


Fig. 4: Constraints affecting the placement of IRS in VLC communication (top view of the hospital room).

caused by AP will determine the lower limit on the x -axis, denoted by x_l , and the limitations caused by the photoreceptor and IRS can determine the upper limit of the use of IRS on the x -axis, that we denote by x_h .

3.1. Constraints Related to the Optical Transmitter

The first constraint is related to the optical transmitter i.e., the visible light source. Usually, in VLC systems, the Lambertian order (denoted m_l) of the source, which characterizes the directivity of the radiation beam, is one of the effective factors in determining the half-power angle ($\phi_{1/2}$), i.e., the illumination and communication coverage radius of the source [2].

As seen from Fig. 5, the increase of m_l causes the decrease of $\phi_{1/2}$. The decrease in $\phi_{1/2}$, in turn, narrows the width of the beam which causes the light beam to reach the walls at a larger vertical distance from the light source, which itself creates a lower limit for the placement of the IRS on the x -axis (see Fig. 4). Mathematically, for a light source of Lambertian order m_l , $\phi_{1/2}$ is expressed as [2]:

$$\phi_{1/2} = \cos^{-1} \left(\exp \left(-\frac{\ln 2}{m_l} \right) \right). \quad (9)$$

If an optical AP of Lambertian order m_l is located at the coordinate (x_T, y_T, z_T) , the first point on the wall that is within the teleradius of the source will be located at a longitudinal distance x_l from the origin [15].

More precisely, x_l is the lower limit allowed for the deployment of IRS, which is expressed as [13]:

$$x_l = x_T + \frac{|-w - y_T|}{\tan(\phi_{1/2})}. \quad (10)$$

It is worth mentioning that another important limiting factor related to the AP is its transmission power, which is usually limited by the sensitivity of human eyes and skin as well as hardware limitations of the transmitter [16].

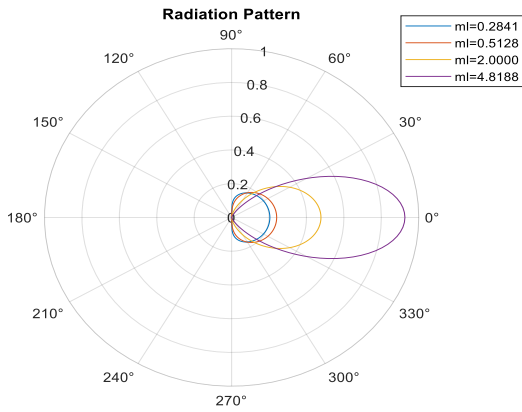


Fig. 5: Radiation pattern of the transmitter with different Lambertian order.

3.2. Constraints Related to the IRS

Since the function of mirror IRS is based on the formation of a virtual image (see Fig. 6), as a result, the IRS units must receive a light beam with an angle of incidence of less than 90 degrees from the light source. So, a limit should be considered for the allowed rotation of the IRS elements or equivalently the phase shift of the reflection beam, according to its location [17].

Let us assume that an IRS is located at coordinate (x_I, y_I, z_I) , then the maximum angle that the IRS can rotate around x and z axes can be expressed as [17]:

$$\begin{aligned} \theta_{\max} = \phi_{\text{rot}} &= \tan^{-1} \left(\frac{\sqrt{(z_I - z_T)^2 + (y_I - y_T)^2}}{(x_I - x_T)} \right) \\ &= \tan^{-1} \left(\frac{\sqrt{(z_I - h_I)^2 + (-w - y_r)^2}}{(x_I - x_T)} \right). \end{aligned} \quad (11)$$

By reducing $(x_I - x_T)$, i.e., the longitudinal distance between IRS and AP, IRS units are able to cover a wider area. Notice that since the minimum value of x_I is equal to x_I , this value is lower bounded by $(x_I - x_T)$.

3.3. Constraints Related to the PD

The field of view (FOV) of the optical detector (as well as its orientation) is the third limiting factor in deploying IRS in a VLC system. As can be seen from Fig. 7, according to the FOV of the detector and its orientation, the deployment location of the IRS is limited. As depicted in Fig. 7, by a counter-clockwise orientation, the length of the allowed IRS installation area on the wall is reduced by Δx_d , and in contrast, with a clockwise orientation, the length of the IRS installation area on the wall is increased by Δx_i . In practice, by adjusting the PD orientation, the SNR and as a result the length of the allowable area can be increased, but since in the usual case, the LOS link is responsible for the communication between the optical transmitter and the receiver, we will have a compromise in the PD orientation setting. So, in a way, the upper limit of the length of the allowed area for using IRS, i.e., x_h , and even the selection of the proper side wall for the

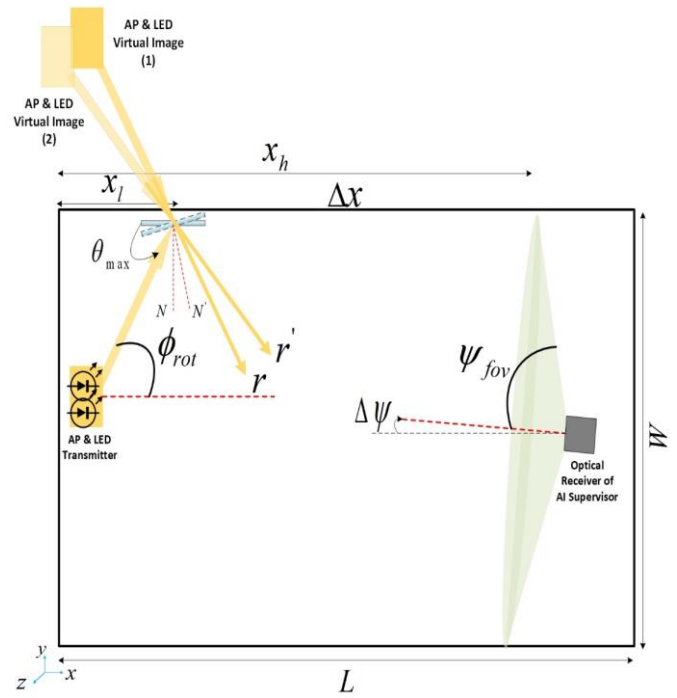


Fig. 6: Coverage profile of the optical transmitter, taking into account the geometry of the image formation and the constraints caused by it.

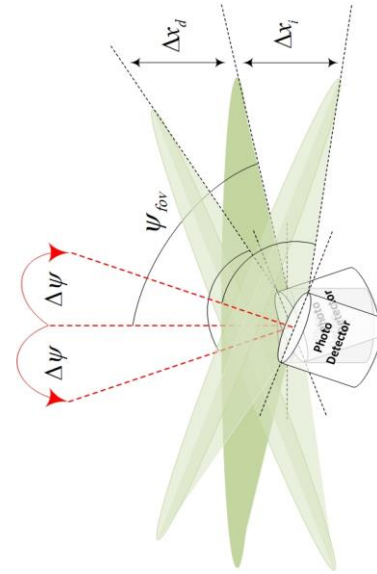


Fig. 7: Effect of FOV and PD orientation in determining the allowable area of IRS deployment.

purpose of engaging IRS is determined according to the orientation of PD.

In calculating the upper limit x_h , the deployment location of PD and its orientation play a role. Assuming that the location of the receiver is (x_r, y_r, z_r) and its initial random orientation is $\pm \Delta \psi$, we have:

$$x_h = x_{\text{ori}} = x_r - \frac{|-w - y_r|}{\tan(\psi_{\text{fov}} \pm \Delta \psi)}, \quad (12)$$

where x_{ori} is the limitation due to the orientation of the PD, ψ_{fov} is the FOV of the optical detector and $\Delta \psi$ is

considered positive in PD clockwise rotation and negative in counterclockwise rotation.

4. OPTIMIZATION OF IRS LOCATION

In this section, we propose to optimize the place of IRS inside the considered room so as to minimize the BER at the receiver by considering the constraints we discussed in

Section 3. According to the system model in Section 2, the probability of error at the receiver for OOK modulation, is expressed as [2]:

$$P(\text{error}) = P(0)P(\text{error}|0) + P(A_{\text{sym}})P(\text{error}|A_{\text{sym}}). \quad (13)$$

By assuming probability of each symbol $P(A_{\text{sym}}) = P(0) = P(1) = 0.5$, we get:

$$P(\text{error}) = \frac{1}{2}Q\left(\frac{A_{\text{sym}}}{\sigma_T}\right) + \frac{1}{2}Q\left(-\frac{A_{\text{sym}}}{\sigma_T}\right) = Q\left(\frac{A_{\text{sym}}}{\sigma_T}\right) = Q(\sqrt{\gamma}), \quad (14)$$

$$\gamma = \text{SNR} = \frac{A_{\text{sym}}^2}{\sigma_T^2} \quad Q(x) = \frac{1}{\sqrt{2\pi}} \int_x^\infty e^{-\lambda^2/2} d\lambda$$

where

Let us define $i_{ph} = i_{ph_{los}} + i_{ph_{nlos}} + i_{ph_{irs}}$ as the photocurrent caused by the received optical signal, which is the sum of three components: $i_{ph_{los}}$, $i_{ph_{nlos}}$, $i_{ph_{irs}}$ are the photocurrent caused by the LOS, NLOS and IRS links, respectively. We assume that the noise variance $\sigma_T^2 = \sigma_{sh}^2 + \sigma_{th}^2$ where σ_{sh}^2 and σ_{th}^2 are the shot noise variance and the thermal noise variance, respectively, that are assumed as the dominant noises in our scenario. The probability of error in (14) can be equivalently expressed as [2]:

$$P_{e_{ook}} = Q(\sqrt{\gamma}) = Q\left(\frac{G_{oc}RP_c}{\sigma_T}\right) = Q\left(\frac{i_{ph}}{\sigma_T}\right). \quad (15)$$

Since $y(t)$ in the system model is the photocurrent created in PD due to the received Power P_r , so its signal part i_{ph} corresponds to the transmitted symbol A_{sym} [2, 13], hence we will have:

$$P_{e_{ook}} = Q(\sqrt{\gamma}) = Q\left(\frac{i_{ph}}{\sigma_T}\right) = Q\left(\frac{i_{ph_{los}} + i_{ph_{nlos}} + i_{ph_{irs}}}{\sqrt{\sigma_{sh}^2 + \sigma_{th}^2}}\right). \quad (16)$$

Assuming that the impact of the NLOS link is negligible, $i_{ph_{nlos}}$ can be omitted. According to [2], the shot noise can be written as $2q(i_{ph_{los}} + i_{ph_{irs}})B_{\text{sys}}$ and the thermal noise as $4k_bTB_{\text{sys}}R_l^{-1}$, where q is the electric charge, B_{sys} is the bandwidth of the optical receiver, R_l is the load resistance, T is the absolute temperature, and k_b is the Boltzmann's constant. Equation (16) can thus be rewritten in an equivalent form as:

$$P_{e_{ook}} = Q\left(\frac{i_{ph_{los}} + i_{ph_{irs}}}{\sqrt{2q(i_{ph_{los}} + i_{ph_{irs}})B_{\text{sys}}} + 4k_bTB_{\text{sys}}R_l^{-1}}}\right). \quad (17)$$

Considering that the photocurrent is a function of the received power, since, the received power is a function of the transmitted power P_t [2], Eq. (17) can be written as follows:

$$P_{e_{ook}} = Q\left(\frac{G_{oc}RH_{los}P_t + G_{oc}RH_{irs}P_t}{\sqrt{2q(G_{oc}RH_{los}P_t + G_{oc}RH_{irs}P_t)B_{\text{sys}}} + 4k_bTB_{\text{sys}}R_l^{-1}}}\right). \quad (18)$$

As can be seen from (18), the photocurrent due to the NLOS link has been neglected. The numerical comparison results of IRS-based and NLOS-based VLC links are contrasted in the next section.

Now, to calculate the optimal location of the IRS, we formulate the following optimization problem:

$$\{\hat{x}_I, \hat{z}_I\} = \arg \min_{x_I \leq x_I \leq x_h, 0 \leq z_I \leq H} BER, \quad (19)$$

which can be expressed by using (18) as:

$$\{\hat{x}_I, \hat{z}_I\} = \arg \min_{x_I \leq x_I \leq x_h, 0 \leq z_I \leq H} Q\left(\frac{G_{oc}RH_{los}P_t + G_{oc}RH_{irs}P_t}{\sqrt{2q(G_{oc}RH_{los}P_t + G_{oc}RH_{irs}P_t)B_{\text{sys}}} + 4k_bTB_{\text{sys}}R_l^{-1}}}\right). \quad (20)$$

According to the basic properties of the Q -function, (20) can be rewritten in an equivalent form as:

$$\{\hat{x}_I, \hat{z}_I\} = \arg \max_{x_I \leq x_I \leq x_h, 0 \leq z_I \leq H} \left[\frac{G_{oc}RH_{los}P_t + G_{oc}RH_{irs}P_t}{\sqrt{2q(G_{oc}RH_{los}P_t + G_{oc}RH_{irs}P_t)B_{\text{sys}}} + 4k_bTB_{\text{sys}}R_l^{-1}} \right], \quad (21)$$

Finally, assuming that the LOS link is blocked ($H_{los} \simeq 0$) and the NLOS link is also not reliable due to the inability to control the reflection beam and choose the reflection model, we get:

$$\{\hat{x}_I, \hat{z}_I\} = \arg \max_{x_I \leq x_I \leq x_h, 0 \leq z_I \leq H} \left[\frac{G_{oc}RH_{irs}P_t}{\sqrt{2qG_{oc}RH_{irs}P_tB_{\text{sys}}} + 4k_bTB_{\text{sys}}R_l^{-1}} \right]. \quad (22)$$

Considering shot noise limited condition [2] (i.e., all other noises can be neglected except the shot noise), equation (22) can be written in an equivalent form as:

$$\{\hat{x}_I, \hat{z}_I\} = \arg \max_{x_I \leq x_I \leq x_h, 0 \leq z_I \leq H} \left[\frac{H_{irs}}{\sqrt{2qH_{irs}B_{\text{sys}}}} \right]. \quad (23)$$

In fact, the optimization problem (19) becomes equivalent to finding \hat{x}_I and \hat{z}_I by maximizing H_{irs} , because the noise parameters q and B_{sys} are almost constant values and the Eq. (23) is simplified to $\frac{H_{irs}}{\sqrt{H_{irs}}}$. So we can write:

$$\{\hat{x}_I, \hat{z}_I\} = \arg \max_{x_I \leq x_I \leq x_h, 0 \leq z_I \leq H} H_{irs}. \quad (24)$$

In (24), H_{irs} is a function of distances and angles (see Eq. (8)), which in turn are functions of x_I and z_I . Therefore,

H_{irs} will also be a function of x_I and z_I . If \hat{x}_I and \hat{z}_I maximize H_{irs} , then the following condition must hold:

$$H_{irs}(x_I, z_I) \leq H_{irs}(\hat{x}_I, \hat{z}_I), \quad (25)$$

where $x_I \leq x_h$, $0 \leq z_I \leq H$. For (25) to be satisfied, the directional derivative of H_{irs} , with respect to x and z , must be zero at \hat{x}_I and \hat{z}_I . That is why we can write:

$$(H_{irs x_I}(\hat{x}_I, \hat{z}_I), H_{irs z_I}(\hat{x}_I, \hat{z}_I)) = (0, 0). \quad (26)$$

where $H_{irs x_I}(\hat{x}_I, \hat{z}_I)$, $H_{irs z_I}(\hat{x}_I, \hat{z}_I)$ are the derivatives of H_{irs} with respect to x_I and z_I respectively. The values of x_I and z_I that maximize H_{irs} characterize the optimal location of IRS leading to minimization of the average BER at receiver that are obtained in the next section through numerical optimization.

5. NUMERICAL OPTIMIZATION AND SIMULATION RESULTS

Here, we propose to evaluate the performance of the considered IRS-assisted VLC system by particularly focusing on the effect of IRS placement. The simulation environment is graphically depicted in Fig. 2. The main values and assumptions considered throughout simulations are provided in Table 1.

In Table 2, we have gathered the limit of parameters related to IRS deployment on the side wall (by assuming $y_I = -5$), according to the constraints described in Section 3.

By evaluating the BER at different places of the allowed region, we place the IRS unit at coordinate where BER is minimal.

We focus on received power and BER at the receiver location achieved by using IRS in VLC link compared to classical NLOS, under practical constraints described in Section 3.

Fig. 8 depicts the received power when using the classical NLOS VLC link by considering the reflections from wall surface at different locations of the allowed region according to the Phong reflection model [18]. We can observe that as the reflector approaches the coordinate $(x_I, -W, z_T)$, the received power is increased up to about 5.85×10^{-9} watts. If we consider the entire allowed region can be dedicated as reflector, the received power is even increased up to 5.1245×10^{-4} watts.

Fig. 9 shows the received power at different locations of the considered area when a 35 unit array IRS is used (all 35 units serve the PD) at that location. We observe that, as the IRS approaches the location $(x_I, -W, z_T)$ which is the optimal point of IRS deployment, the received power increases (up to about watts). By comparing Figs. 8 and 9, we can see that the

Table 1: Parameters and assumptions.

| Parameter | Value | Description |
|-----------------------|------------------|---|
| $L \times W \times H$ | 5m×5m×3m | Room dimensions (Length, width, height) (m) |
| (x_T, y_T, z_T) | (0.5, -3.5, 1.5) | Coordinates of the transmitter's location (m) |
| (x_r, y_r, z_r) | (4, -1, 1.5) | Coordinates of the receiver's location (m) |
| m_l | 0.4 | Lambertian order of optical transmitter |
| ψ_{fov} | 80 | Field of view of the PD (degree) |
| $\phi_{1/2}$ | 80 | Half power angle (degree) |
| $\Delta\psi$ | 5 | PD orientation (degree) |
| A | 0.0004 | Effective area of the PD (m^2) |
| R | 1 | PD Responsivity |
| $T(\psi)$ | 1 | Optical filter gain |
| N | 35 | Number of IRS units |
| $a \times a$ | 0.1m×0.1m | Dimensions of IRS units (m^2) |
| n_i | 1.5 | Concentrator internal refractive index |
| R_b | 1 Gbps | Data rate (bps) |
| ρ_{ref} | 0.5 | Reflection coefficient of wall |
| ρ_i | 0.9 | Reflection coefficient of IRS units |
| P_t | 200 | Transmitted Power (Watts) |

Table 2: Calculated constraints regarding IRS installation.

| Parameter | Description | Value/unit |
|----------------|---|-----------------|
| x_l | Lower limit length of the allowed region for deployment of the IRS. | 1.1145 m |
| x_h | Upper limit length of the allowed region for deployment of the IRS. | 3.3 m |
| θ_{max} | Allowed rotation range of IRS units at the optimal deployment point (degree). | [30, 65] degree |

power received in the IRS link increases more than twice, i.e., about , compared to the classic NLOS link which proves the significant advantage of employing IRS in our system model (the entire allowed area of the reflector surface is taken into account).

Fig. 10 illustrates the BER comparison (plotted based on the theoretical BER of (15) and (18)) at the receiver in NLOS and IRS links. More precisely, in Fig. 10, by changing the transmitter power in the range $16 < P_t < 29$ dB, we get $-8 < SNR < 4.7$ dB at the receiver through NLOS link and $-4.7 < SNR < 8$ dB at the IRS-aided VLC link. These results confirm the superiority and also the reliability (in terms of

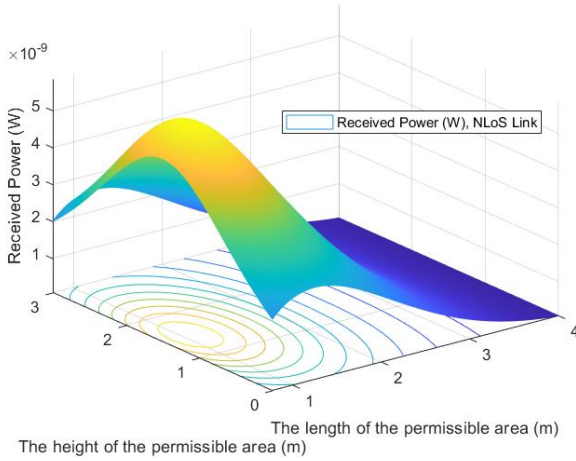


Fig. 8: The received power of the optical receiver considering the entire allowed area as reflective surface in the classical NLoS VLC link.

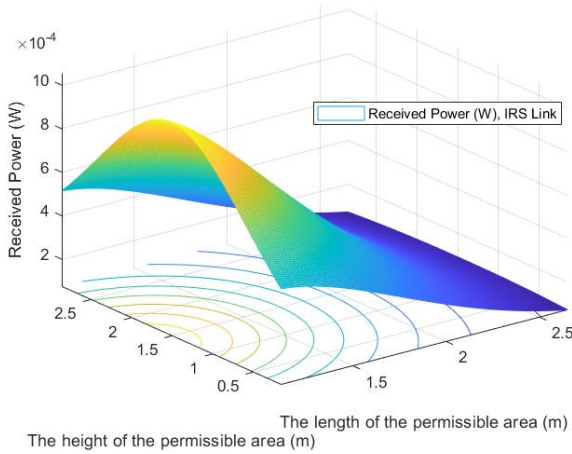


Fig. 9: The received power of the optical receiver at different locations of the considered area by using a 35 unit IRS.

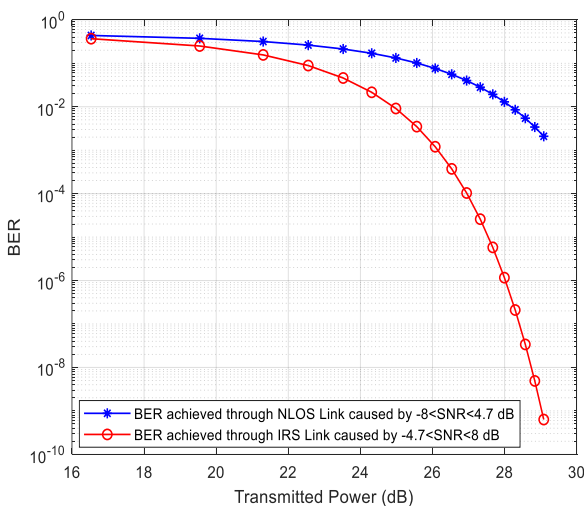


Fig. 10: Comparison of BER in IRS-based optical link and classic NLoS-based optical link according to the transmitted power.

QoS and SNR) [19] of IRS-aided VLC link compared to classic NLoS link in terms of BER.

Fig. 11 shows the BER variations versus location of the IRS for three different locations of the optical receiver. Notice that according to our system model, in the indoor hospital environment, the IRS cannot be placed across the y axis. So for each location of the receiver, the minimum of each curve is the optimal location of the IRS for its deployment in the allowed area. Considering these three curves, it can be concluded that the minimum BER values always occurs regardless of the location of the receiver when the IRS is located at the $(x_l, -W, z_T)$ coordinate, which is the optimal installation point.

Fig. 12 shows the BER variations for different PD orientations $\{-10^\circ, 0, +10^\circ\}$. We can particularly observe that when the transmit power changes in the range $16 < P_t < 29 \text{ dB}$, the BER can be reduced to a desired value by fine-tuning the PD orientation.

Finally, Fig. 13 plots the received SNR versus the Lambertian order of the source (m_l) in different lengths of the allowed area ($z_l = 1.5 \text{ m}$ & $y_l = -5 \text{ m}$). As can be seen, by increasing m_l , the length of the lower bound of the allowed area i.e., x_l which is the coordinate of the optimal place of IRS deployment, is increased (the length of the upper limit of the allowed area x_h is assumed fixed).

6. CONCLUSIONS

Optimal placement of IRS on the wall in order to minimize the BER at the receiver for an indoor VLC system was addressed. In this study, an optical AP and a photo-detector have been used to send and monitor the vital signals of a patient in a hospital environment. For the case where the LOS path is blocked in the VLC link, both the IRS directed link and the classical NLoS link have been considered. Comparative numerical results proved the superiority of the IRS-aided VLC link in terms of BER. Moreover, the power received through the IRS link is increased up to 2 times. Then, in order to have a reliable and ubiquitous connection, with the aim of minimizing the BER, the location of IRS installation was optimized. We also showed that by fine-tuning the PD orientation, even lower BER can be obtained. Finally, we showed that by increasing the Lambertian order, the optimal location of IRS deployment is shifted away from the source. The use of more complex optimization methods with multiple sources, multiple IRS arrays and fine tuning PD orientation can be considered as attractive future research directions in this field.

CREDIT AUTHORSHIP CONTRIBUTION STATEMENT

Babak Sadeghi: Conceptualization, Formal analysis, Investigation, Software, Roles/Writing - original draft. **Seyed Mohammad Sajad Sadough:** Project administration, Supervision, Writing - review & editing.

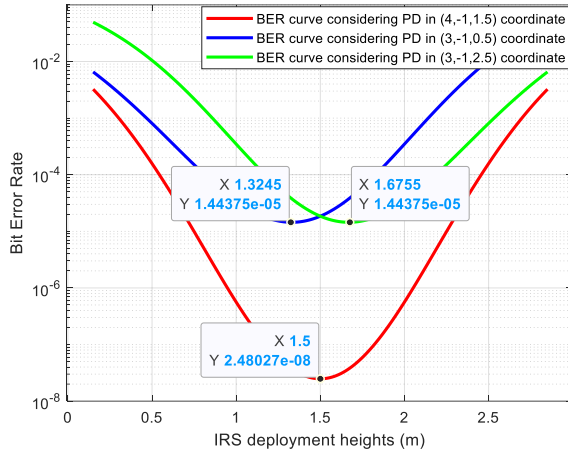


Fig. 11: BER curve resulting from variations in optical IRS location across the allowed region, considering three different locations for the optical receiver.

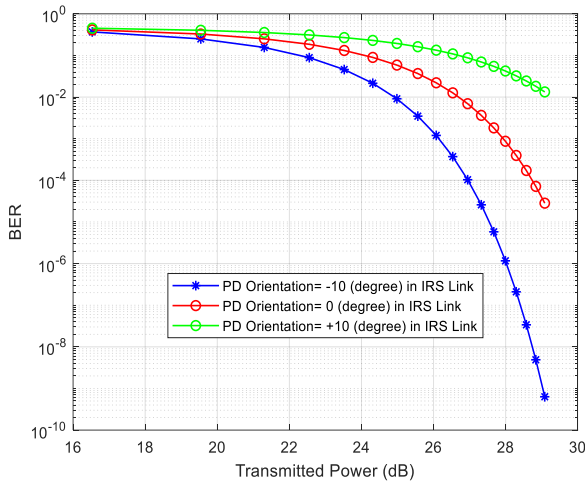


Fig. 12: The BER obtained in the receiver, caused by changes in the power of the optical transmitter as well as the different orientation of the PD, assuming that the noise power is constant.

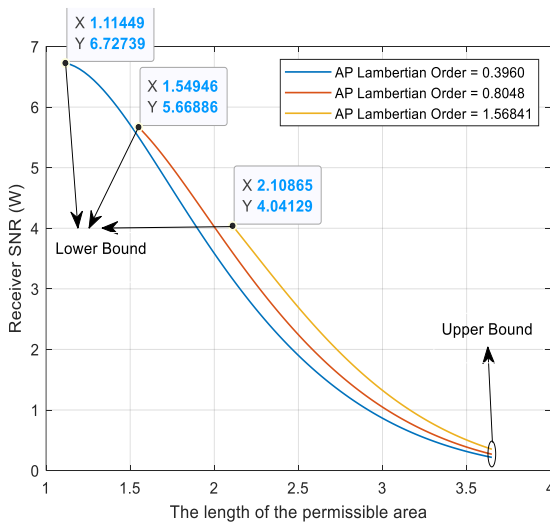


Fig. 13: Demonstration of the receiver SNR according to the location of the IRS in the allowed area, considering APs with three different Lambertian orders.

DECLARATION OF COMPETING INTEREST

The authors declare that they have no known competing financial interests or personal relationships that could have appeared to influence the work reported in this paper. The ethical issues; including plagiarism, informed consent, misconduct, data fabrication and/or falsification, double publication and/or submission, redundancy has been completely observed by the authors.

REFERENCES

- [1] H. Shah, A. K. Vyas, "A systematic review for 6G and beyond 6G enable IoT Network," in *IEEE 2024 2nd International Conference on Computer, Communication and Control*, 2024.
- [2] Z. Ghassemlooy, W. Popoola, and S. Rajbhandari, *Optical wireless communications: system and channel modelling with MATLAB®*. Taylor & Francis, 2012.
- [3] H. Kurunathan, R. Indhumathi, M. G. Gaitán, C. Taramasco, and E. Tovar, "VLC-enabled monitoring in a healthcare setting: Overview and Challenges," in *IEEE Conference on Visible Light Communications*, December 2023.
- [4] A. M. Abdelhady, A. K. Sultan, O. Amin, B. Shihada, and M. S. Alouini, "Visible light communications via intelligent reflecting surfaces: Metasurfaces vs mirror arrays," *IEEE Open Journal of the Communications Society*, Vol. 2, December 2020.
- [5] M. A. Arfaoui, A. Ghayeb, and C. Assi, "Integration of IRS in indoor VLC systems: Challenges, potential and promising solutions," *arXiv: 2101.05927 [eess.SP]*, January 2020.
- [6] M. Bhar, S. Kumar, and A. Singh, "On the optimal evaluation of the angle of irradiance and the orientation for an IRS-aided indoor VLC," *TechRxiv*, May 11, 2023.
- [7] S. Abdeljabar, M. W. Eltokhey, and M. S. Alouini, "Sum rate and fairness optimization in RIS-Assisted VLC systems," *IEEE Open Journal on the Communications Society*, vol. 5, pp. 2555 – 2566, April 2024.
- [8] A. Chehbani, S. Sahuguede, A. Julien-Vergonjanne, and O. Bernard, "Quality Indexes of the ECG Signal Transmitted Using Optical Wireless Link," *Sensors*, vol. 23, no. 9, p. 4522, May 2023.
- [9] K. Mahalakshmi, M. Sivaram, K. S. Kumari, D. Yuvaraj, and R. Keerthika, "Healthcare Visible Light Communication," *International Journal of Pure and Applied Mathematics*, vol. 118, no. 11, pp. 345-348, 2018.
- [10] A. Al-Qahtani et al., "A non-invasive remote health monitoring system using visible light communication," in *2015 2nd International Symposium on Future Information and Communication Technologies for Ubiquitous HealthCare (Ubi-HealthTech)*, Beijing, China, 2015, pp. 1-3.
- [11] Ö. Özdogan, E. Björnson, and E. Larsson, "Intelligent reflecting surfaces: physics, propagation, and pathloss

- modelling," *IEEE Wireless Communications Letters*, vol. 9, no. 5, pp. 581-585, May 2020,.
- [12] M. R. Cañizares, P. P. Játiva, J. Guaña-Moya, W. Villegas-Ch, and C. Azurdia-Meza, "On the performance of intelligent reconfigurable surfaces for 6G indoor visible light communications systems," *Photonics*, vol. 10, no. 10, p. 1117, 2023.
- [13] H. Haas, M. S. Islam, C. Chen, and H. Abumarshoud, *An introduction to optical wireless mobile communication*. Artech House, September 2021.
- [14] S. Sun, and T. Wang, "Intelligent reflecting surface-aided visible light communications: Potentials and challenges," *IEEE Vehicular Technology Magazine*, vol. 17, no. 1, pp. 47-56, March 2022.
- [15] M. Mohammadi, and S. M. S. Sadough, "Improved LED arrangement through outage probability minimization in LiFi communication systems," *The Institution of Engineering and Technology*, vol. 17, no.8, pp. 987-998, 2023.
- [16] A. Singh, H. B. Salameh, M. Ayyash, and H. Elgala, "Performance analysis of OIRS-Aided indoor VLC systems under dynamic human blockages and random UE orientation," *IEEE Internet of Things Journal*, vol. 11, no. 20, pp. 33110-33119, 2024.
- [17] Q. Wu, J. Zhang, and J.-N. Guo, "Position design for reconfigurable intelligent-surface-aided indoor visible light communication systems," *Electronics*, vol. 11, no. 19, p. 3076, 2022.
- [18] J. Burke, A. Pak, S. Höfer, M. Ziebarth, M. Roschani, and J. Beyerer, "Deflectometry for specular surfaces: An overview," *Advanced Optical Technologies*, vol. 12, July 2023.
- [19] Y. Zheng, P. He, Y. Cui, R. Wang, and D. Wu, "Reliability optimization in IRS-assisted UAV networks," *Vehicular Communications*, vol. 44, p. 100679, May 2023.

Copyrights

© 2025 Licensee Shahid Chamran University of Ahvaz, Ahvaz, Iran. This article is an open-access article distributed under the terms and conditions of the Creative Commons Attribution –NonCommercial 4.0 International (CC BY-NC 4.0) License (<http://creativecommons.org/licenses/by-nc/4.0/>).





Research Article

Reliability Modelling of Central Receiver Power Plants

Amir Ghaedi^{1,*} , and Mehrdad Mahmoudian² ¹ Department of Electrical Engineering, Dariun Branch, Islamic Azad University, Dariun, Iran² Department of Electrical Engineering, Apadana Institute of Higher Education, Shiraz, Iran* Corresponding Author: amir.ghaedi@miau.ac.ir

Abstract: In solar power towers or central receiver generation units, solar radiation is concentrated on a central receiver placed at the top of a tower through a heliostat field. The concentrated solar energy can generate superheated steam in a Rankine cycle to produce electricity. Since solar energy fluctuates, the output power of solar tower power plants changes frequently, and many aspects of power networks incorporating high-capacity solar tower power plants may be affected, which must be investigated. For this purpose, this paper presents a reliability model for solar power generation units based on the failure of component devices and changes in produced power. To determine the reliability of these plants, the effects of failures in their elements, including the heliostat field, central receiver, thermodynamic cycle components, generator, cable, electrical converter, and transformer, on the overall outage are considered. To decrease the number of states related to the reliability model of the solar power generation unit, the XB criterion is selected for calculation, and a fuzzy c-means clustering approach is used. The proposed multi-state reliability model is implemented to evaluate the adequacy assessment of RBTS and IEEE-RTS as two reliability test systems. Important reliability indices, including load and energy curtailed indices and those associated with the system's capability to supply the required load, are calculated.

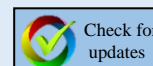
Keywords: Central receiver power plant, heliostat field, reliability, Rankine cycle, fuzzy c-means clustering, solar radiation.

Article history

Received 5 April 2024; Revised 19 October 2024; Accepted 18 January 2025; Published online 20 April 2025.

© 2025 Published by Shahid Chamran University of Ahvaz & Iranian Association of Electrical and Electronics Engineers (IAEEE)

How to cite this article

A. Ghaedi, and M. Mahmoudian, "Reliability modelling of central receiver power plants," *J. Appl. Res. Electr. Eng.*, vol. 3, no. 2, pp. 250-260, 2024. DOI: 10.22055/jaree.2025.46545.1114

1. INTRODUCTION

Renewable resources, especially solar and wind, generate clean and sustainable electric energy in power networks. Due to the clean nature and sustainability of renewable energies, renewable energy-based generation units are used to produce electricity in bulk power systems and microgrids for improving different aspects of these networks. In [1-2], resiliency and reliability of power systems are enhanced by integration of renewable generation units into the power systems. Sunlight energy received on Earth during one hour is more than the required energy for humans of the world during one year [3]. Due to the high potential of solar radiation around the world, large-scale solar power plants based on different technologies including photovoltaic farms, parabolic troughs, Fresnel troughs, parabolic dish systems, and tower collectors are installed in regions with high solar radiation levels for integration into bulk power systems. Among different kinds of solar generation units, solar towers

with high generated power can be connected to the power grid at the transmission level.

The 370MW Ivanpah Solar Electric Generating Station, the 200MW Bright Source Coyote Springs 1 and 2, the 200MW Bright Source PG&E 5, 6 and 7, the 245MW Gaskell Sun Tower, and the 150MW Rice Solar Energy Project are examples of large-scale central receiver power plants located in the USA [3]. Produced power of solar power towers is proportional to solar radiation. Due to wide variation in solar radiation, produced power of central receiver power plants changes a lot, and when the penetration level of renewable-based generation units in the power system is high, reliability and other aspects of the power network may be changed, which must be evaluated. To study the impact of solar towers on power systems, many researches have been carried out. In [4], the latest status of concentrating solar power towers is discussed, and the design and operating data of current central receiver power plants are examined. In this paper, new technologies are proposed to generate a better ratio of electric power to the power of heliostat field, better capacity factor,

better matching of generation and consumption, lower cost of power plant, enhancement of reliability, and improved life span of component parts. For this purpose, materials and manufacturing processes, design of heliostat field and central receiver, Rankine cycle components and working fluid, optimal operation scheduling of the power plant, and integration of the power plant with thermal desalination and combined cycle power plants can be utilized. In [5], different optimal schemes of heliostat fields in central receiver generation units are performed using the campo code. In this paper, a new code is proposed to calculate quickly and accurately factors related to shadowing and blocking of heliostats to find the optimum layout for the heliostat field and yield maximum annual energy. In [6], an analytical study is performed on the PS10 solar power tower located in Aswan, Egypt. In this paper, a comparison between the Aswan 11MW central receiver power plant and Mayor solar power tower based on the solar irradiance model, sunshine duration, optical and geometric analysis, annual average efficiency, and plant performance values is carried out.

In [7], different heliostat field layout methodologies are compared, and the effect of these layouts on solar power tower efficiency is investigated. In this paper, a detailed comparison of heliostat fields according to efficiency and energy yield is performed to determine the advantages and disadvantages of the algorithms used for optimization of heliostat layout designs. It is deduced from this paper that new biomimetic techniques are better than classic algorithm patterns with radial staggered approaches. In [8], the impact of a 200MW solar power tower on the steady-state and transient performances of Oman's transmission system is studied. In this research, a central receiver generation unit composed of a heliostat field, power tower, molten salt storage tank, heat exchangers, steam generator, turbine, generator, and transformer is considered for connection to the transmission network in two proposed locations. The transient response to three-phase faults, load flow analysis, and short circuit level calculations are performed to investigate the effect of adding the solar power tower to the transmission system.

In [9], modal analysis of a heliostat for central receiver power plants is performed. In this paper, an analytical and experimental program is proposed to improve the response of heliostat fields to wind loading on them. Based on these results, the structural models of the heliostats can be evaluated and improved to predict the deformations of the heliostats arising from gravitational and dynamic wind loadings. In [10], an optical study of central receiver power plants is performed. In this study, a mathematical model is suggested for analyzing optical efficiency of solar towers and studying the effect of different factors including shading and blocking losses, cosine effect, atmospheric attenuation, and spillage losses on optical efficiency. In [11], a heliostat field of a solar tower based on a 10MW peak power unfired closed Joule-Brayton cycle installed in Seville is studied. In this paper, a variable mass flow rate is achieved for constant-temperature operation of the turbine inlet using an auxiliary compressor and bleed valve. Thus, the number of installed heliostats is important for determining the rated thermal power of the plant. In [12], the effectiveness of a small-scale central receiver generation unit used in a residential application located in Italy is simulated. This generation unit

includes 48 heliostats with a total reflecting surface area of 8.7m² to generate 5kW of electricity. In this research, the design of the understudied solar tower is described, and the effect of different irradiance data on the performance of the system is evaluated.

In [13], optimal planning of a renewable energy-based microgrid considering the reliability cost is performed. In this paper, variable failure rates of component parts of renewable resources including wind turbines, current-type tidal turbines, and photovoltaic panels are used in the optimization algorithm. Paper [14] performs scheduling studies of the renewable energy-based microgrid considering the reliability effect. In this paper, different renewable resources including wind turbines, photovoltaic systems, wave energy converters, and stream-type tidal turbines are integrated into the system to reduce the reliability cost of the microgrid. In [15], reliability modeling of different types of wind turbines is carried out. In this paper, reliability assessments of various structures of wind turbines including doubly-fed induction generators, permanent magnet synchronous generators, wound rotor induction generators, brushless doubly-fed induction generators, and electrically excited synchronous generators are performed. Paper [16] studies the reliability of power systems containing ocean thermal energy conversion systems. In this research, variable failure rates of component parts of ocean thermal energy conversion systems considering variation in the outside temperature are determined.

In [17], the impact of different solar tracker systems on the reliability of photovoltaic power plants is studied. In this paper, a comparison from a reliability point of view among three photovoltaic power plants including fixed panel, PV systems equipped with single-axis trackers, and PV systems equipped with double-axis trackers is performed. Paper [18] studies the impact of variation in water flow rate on the failure rate of component parts of run-of-the-river power plants. Then, the obtained variable failure rate of run-of-the-river power plants is used for reliability assessment of the power system containing these renewable resources. In [19], reliability evaluation of power systems containing wave energy conversion systems is performed. In this paper, the reliability model of Pelamis as a large-scale wave power plant is determined considering both failure of component parts and variation in the generated power arising from variation in the height and period of the waves. In [20], reliability indices of the power system containing different types of renewable resources are calculated by Monte Carlo simulation technique. In this paper, various types of renewable resources including wind turbines, photovoltaic systems, tidal turbines, run-of-the-river power plants, and wave converters are integrated into the power system.

The current paper models the reliability performance of central receiver plants. The generated power of central receiver units is dependent on solar radiation. Solar radiation varies, and so, the generated power of solar power towers changes, too. Thus, similar to other renewable units, the uncertainty nature of central receiver plants affects many aspects of the power network. Due to the similarity between solar power towers and other renewable units such as wind turbines, photovoltaic systems, tidal stream turbines, tidal barrages, and run-of-the-river units, approaches developed to

Table 1: The comparison of the current research and reviewed references.

| References | Advantages | Drawback | | ocean thermal energy conversion systems is done. | plants are not considered |
|------------|---|---|---------|---|---|
| [1] | Resiliency of power hub is improved by integration of renewable resources. | Reliability of power hub is not studied. Central receiver power plant is not investigated. | [17] | The impact of different solar trackers on the reliability of PV systems is studied. | Reliability evaluation of thermal solar power plants is not performed. |
| [2] | Reliability evaluation of pumped storage power plant is studied. | Reliability evaluation of central receiver power plant is not performed. | [18-19] | Reliability assessment of power system including run of the river and wave power plants is performed. | Reliability analysis of central receiver solar power plants is not performed. |
| [3-4] | The current state of central receiver power plant is presented. | Reliability evaluation of central receiver power plant is not performed. | [20] | Reliability indices of the power system containing different types of renewable resources are calculated by Monte Carlo simulation technique. | In the understudied power system, central receiver power plants are not considered. |
| [5] | Different optimal schemes of heliostat field in central receiver generation units are performed using of the campo code. | Reliability assessment of heliostat power plant is not investigated. | [21-26] | The reliability modelling of wind turbines, photovoltaic farms, run-of-the-river units, ocean thermal energy conversion systems, current and barrage kind tidal generation units have been developed. | Reliability modelling of central receiver power plants is not performed. |
| [6] | A comparison between the Aswan 11MW central receiver power plant and Mayor solar power tower is carried out. | Reliability performance of two mentioned power plants is not compared. | | | |
| [7] | Different heliostat field layout methodologies are compared. | Reliability analysis of heliostat field is not carried out. | | | |
| [8] | The impact of solar power towers on the steady-state and transient performances of Oman transmission system is studied. | The impact of solar power towers on the reliability of Oman power system is not performed. | | | |
| [9] | An analytical and experimental program is proposed to improve the response of the heliostat fields to the wind loading on them. | Reliability analysis of heliostat field considering the wind loading on them is not carried out. | | | |
| [10] | An optical study of central receiver power plants is performed. | Reliability evaluation of central receiver power plant is not done. | | | |
| [11] | A heliostat field of solar tower based on 10MW peak power unfired closed Joule-Brayton cycle installed in Seville is studied. | Reliability assessment of solar towers is not performed. | | | |
| [12] | Effectiveness of small-scale central receiver generation unit used in residential application located in Italy is simulated. | Reliability studies of small-scale central receiver generation unit used in residential application located in Italy is not done. | | | |
| [13-14] | Optimal planning and scheduling of renewable energy-based micro grids considering reliability effect are done. | In the understudied micro grids, the central receiver power plants are not considered. | | | |
| [15-16] | Reliability evaluation of power system containing different wind turbines and | In the understudied power system, the central receiver power | | | |

consider the uncertainty nature of renewable resources in the associated reliability models can be utilized. The reliability modeling of wind turbines, photovoltaic farms, run-of-the-river units, ocean thermal energy conversion systems, and current and barrage-type tidal generation units has been developed in [21-26]. In Table 1, all reviewed references are compared with the present article.

To construct a reliability model of solar power towers, the current study is organized as follows. In the second section, solar power towers are described. The reliability modeling of this power plant is constructed in the third section. The adequacy performance technique considering solar power towers in reliability assessment of power systems is discussed in the fourth section. Numerical results related to adequacy assessment of RBTS and IEEE-RTS, as well-known reliability test systems, are given in the fifth section to examine the effect of solar power towers on power network reliability. The conclusion of the paper is given in the sixth section.

2. SOLAR POWER TOWERS

The share of solar generation units in electricity production is higher than other renewable energy sources. For conversion solar energy to the electricity, two technologies including solar photovoltaic and concentrated solar thermal systems are used. In photovoltaic systems, the energy of the sun is converted to the DC power through a p-n junction. In the second technology, i.e. concentrated solar thermal units; by using large number mirrors called reflectors with very high reflectivity, the direct sun radiation is concentrated onto a receiver. This radiation is absorbed through the receiver leads the receiver to heat. This heat is transferred to a suitable working fluid than can produce the steam in a heat exchanger

and generate electric power using steam turbines connected to generators. Several kinds of concentrated solar thermal units are parabolic trough, Fresnel mirror system, parabolic dishes and central receiver towers. In the parabolic trough reflectors, the sunlight is concentrated onto receiver tubes contain transfer fluid such as special oil. The fluid is circulated in the tubes through a pump and then enters a heat exchanger to produce superheated steam. The steam can generate electricity through steam turbine connected to the generator. In the linear concentrating Fresnel mirror system, the sunlight is reflected onto a stationary thermal receiver located at a common focal point of the reflectors with the operation temperature of 100-400°C. The concentrated energy is transferred to the thermal fluid through the absorber to produce the steam in the heat exchanger and generate the electricity. In the parabolic dish reflectors, like troughs the direct sunlight is concentrated to point focus of receiver, and heat the fluid inside this point to an operating temperature over 1000°C. This high temperature fluid can produce steam and consequently the electricity is generated. In the central receiver tower system, large mirrors equipped to two-axis sun tracker called heliostats are used for concentrating sunlight onto fixed receiver placed top of a tower. The concentrated energy in absorber is transferred to heat transfer fluid. The operating temperature of fluid would be over than 1000°C. This fluid can produce the steam through a heat exchanger and so the electricity is generated using of the steam turbine connected to the generator. The structure of a typical solar power tower and composed components are presented in Fig. 1.

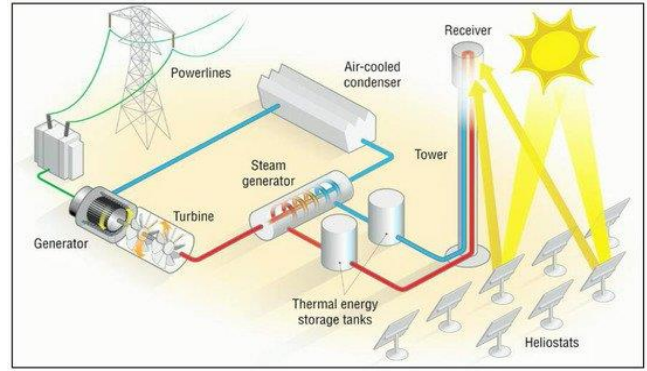


Fig. 1: Typical solar tower [27].

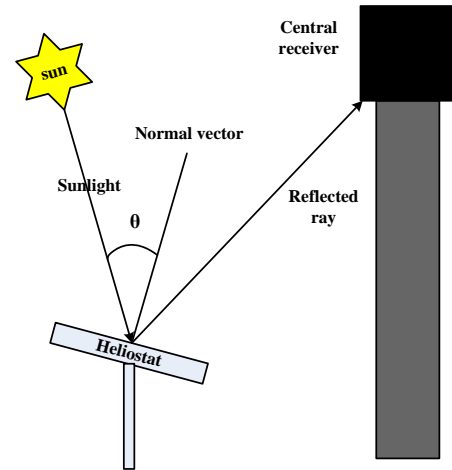


Fig. 2: The concept of cosine effect.

Heliostat fields play an important role in determining the performance and cost of solar power towers. Central receiver plant performance is defined as the ratio between net power captured by the receiver to normal radiation power shining on heliostats. Heliostat field optical losses are due to cosine effect, shading and blocking losses, imperfect mirror reflection coefficient, atmospheric attenuation, and spillage losses. Heliostat field losses are mainly due to the cosine effect, which is the cosine of the angle between sunlight and the normal vector on the surface of the heliostat. The cosine effect depends on the positions of the sun and heliostat and, based on Fig. 2, it can be calculated as $\cos(\theta)$. Due to the movement of Earth relative to the sun, the position of heliostats relative to the sun changes over time, and so the cosine effect changes too. The value of the cosine effect also depends on the layout of the heliostat field, and in a heliostat field, it may differ from one heliostat to another. A heliostat consists of optical sensors to sense the solar radiation on the heliostat, servomotors to track the sun and move the heliostat to reflect the sunlight onto the receiver, a control system, mirror, and the main structure. The concentrated energy can heat the receiver and the fluid inside it to temperatures above 1000°C. Water, based on the Rankine thermodynamic cycle, enters a heat exchanger called a steam generator where the heat transfer fluid can transfer heat to it and produce steam. Then, the steam is conducted to the turbine, and electricity is generated. In Fig. 3, the Rankine thermodynamic cycle is presented [28]. In state 1 of the Rankine cycle, water is pumped to the boiler or steam generator to reach state 2. The heat from the high-temperature fluid is transferred to the water, and steam is generated in state 3. Then, the steam enters the turbine and generates electricity. The low-pressure

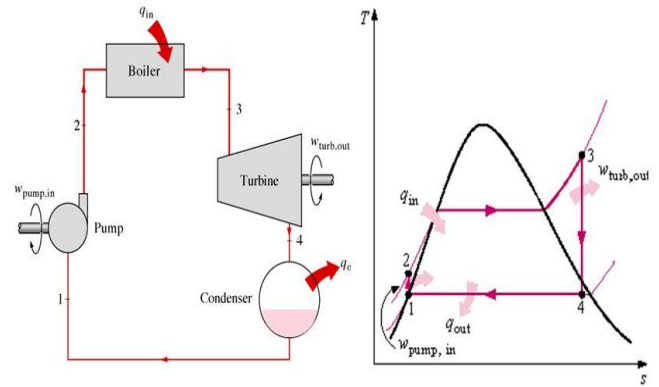


Fig. 3: The Rankine cycle.

steam of state 4 is condensed in the condenser, and the cycle is repeated.

The turbine work can be calculated as (1). In (1), h_3 and h_4 are the enthalpies of states 3 and 4, respectively. The work of pump can be determined as (2).

$$w_{\text{turbine}} = h_3 - h_4 \quad (1)$$

$$w_{\text{pump}} = V(P_2 - P_1) \quad (2)$$

where, P_2 and P_1 are respectively the pressure of boiler and condenser. The heat transferred from the heat transfer fluid to the boiler is calculated as (3):

$$q_{\text{in}} = h_3 - h_2 \quad (3)$$

where, h_3 and h_2 are, respectively the enthalpies of state 3 (high pressure steam) and 2 (high pressure water). The efficiency of the Rankine cycle can be determined as (4), [28]:

$$\eta = \frac{W_{turbine} - W_{pump}}{q_{in}} \quad (4)$$

To determine the generated power of solar power towers, based on the solar radiation, the area of the heliostats, the reflectivity of each heliostat, the number of heliostats and the reflection efficiency of the heliostats, the concentrated energy on the central receiver is calculated. According to heat transfer efficiency of understudied fluid and receiver concentrated thermal energy, the transferred heat to the boiler is determined. The thermal energy generated in the boiler is determined based on the boiler efficiency and the produced kinetic energy of the turbine is calculated by multiplying the generated thermal energy of boiler by the turbine efficiency. The generated electric power is obtained considering generator efficiency and produced kinetic energy. Thus, output power of central receiver unit is determined as (5):

$$P_{out} = sr \times n \times A \times R \eta_{atm} C \times CE \times SB \times \eta_{HTF} \eta_b \eta_T \eta_{ec} \eta_{tr} \quad (5)$$

where, P_{out} is plant produced power, sr is solar radiation (W/m^2), n is heliostats number, A is heliostat area (m^2), R is the reflectivity of the heliostats, η_{atm} is the atmosphere attenuation, C is the cleanliness of the mirrors, CE is the cosine effect, SB is the shading and blocking coefficient, η_{HTF} is heat transfer fluid efficiency, η_b is boiler efficiency, η_T is turbine efficiency, η_{ec} is the electrical converter efficiency and η_{tr} is the transformer efficiency.

3. RELIABILITY MODEL OF SOLAR POWER TOWERS

In this part, to develop multi-state reliability model for solar power towers, the effect of composed components failure and change in solar radiation are considered. Proposed model can be used to perform adequacy assessment related to the power networks with high-capacity central receiver units.

3.1. The Impact of Composed Components Failure

Main components of typical central receiver unit include heliostats, central receiver, thermodynamic cycle components including boiler, turbine, condenser and pump, generator, AC/AC converter, transformer and cable. To model each component of the solar power tower from reliability point of view, a Markov model with 2 states including up and down states is used. In this model, failure rate is transition rate from up to down state, and repair rate is transition rate from down to up state. In solar tower composed of n heliostats, failure of any heliostat results reduction in generated power by $(n-1)/n$ factor. The failure of other components, i.e. central receiver, thermodynamic cycle components, generator, electrical converter, transformer and cable, leads plant operation stops. In this circumstance, produced power of plant would be zero. Thus, reliability model of solar tower is as Fig. 4.

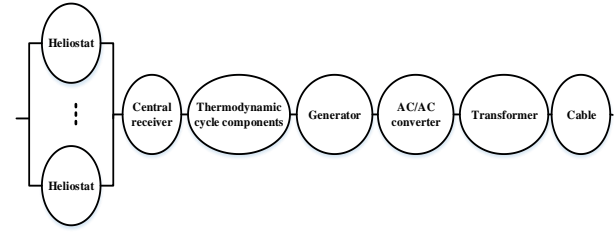


Fig. 4: Reliability model of solar tower considering components failure.

If a solar power tower composed of n heliostats, each with CMW nominal generation capacity, plant reliability model would be as Fig. 5.

The equivalent failure rate (λ) and repair rate (μ) associated to systems with series elements can be determined as (6) [29]:

$$\lambda = \sum \lambda_i, \quad \mu = \frac{\sum \lambda_i}{\sum (\lambda_i / \mu_i)} \quad (6)$$

In the reliability model of Fig. 5, λ_H and μ_H are heliostat failure and repair rates, λ_V and μ_V are equivalent failure and repair rate associated to a system composed of series connection of central receiver, thermodynamic cycle components, cable, generator, transformer and electrical converter.

3.2. Impact of change in solar radiation

In this part, the effect of variation in the solar radiation on plant reliability is investigated. Generated power of a solar tower is dependent on the solar radiation as (5). In Fig. 6, the hourly solar radiation in the Jask region in Iran during a year is presented. As can be seen in the figure, the solar radiation varies widely, and consequently generated power of solar plant changes. For integration solar tower in the analytical reliability analysis of power network, states number in the generated power of this plant must be reduced.

In this research, based on the XB index the appropriate reduced states number of produced power in solar tower is determined. Besides, to determine probability of reduces states, fuzzy c-means clustering algorithm is utilized. This clustering technique can categorize the objective data x including n various states to c clusters through minimizing objective function J as (7) [30]:

$$J = \sum_{i=1}^c \sum_{k=1}^n u_{ik}^m |s_k - z_i| \quad (7)$$

where, s_k is generated power of solar power tower in time k , z_i is center of i^{th} cluster, c is number of clusters or reduced states, n is number of input states, m is a real number (>1) associated to fuzzification (in the study it is 2), u_{ik} is fuzzy degree between s_k and i^{th} cluster. In the proposed clustering technique, number of reduced states as input date is required. To determine optimum number of reduced states, this paper proposes XB index. To calculate this index, equation (8) is used [31]. Based on the proposed method, XB index value at optimal condition is minimal. Thus, optimal state number is obtained.

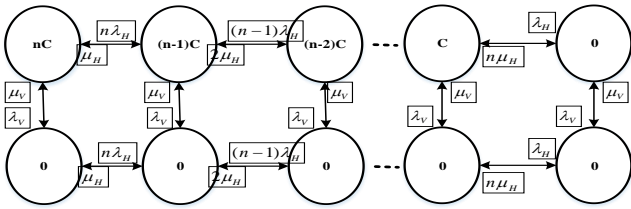


Fig. 5: The reliability model of solar power tower composed of n heliostats.

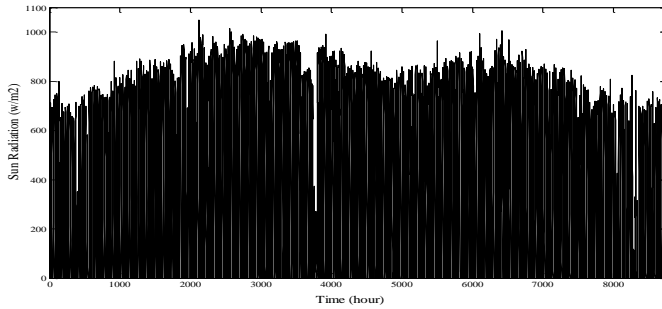


Fig. 6: The hourly solar radiation during a year.

$$XB = \frac{J_m(U, z)}{n \times \min_{i \neq j} \left(|z_i - z_j|^2 \right)} \quad (8)$$

3.3. Total Reliability Model of Solar Tower

For determination total reliability model of solar towers, plant reliability model related to components failure must combine with reliability model related to variation in plant power. The complete plant reliability model that resulted in h states by clustering method implementation with $P1$, $P2$, ..., Ph is presented in Fig. 7. In this model, the states with same capacity can be merged.

4. ADEQUACY PERFORMANCE OF POWER SYSTEMS WITH SOLAR TOWERS

Power network reliability defines as ability of power network for supplying required loads that is studied in two categories including security and adequacy. Adequacy requires sufficient devices for supplying required loads and security studies the ability of power network to response in occurrence of different disturbances such as power plant or transmission lines outage. Reliability studies of power network can be performed in three hierarchical levels. In the first level, only generation system is considered and transmission and distribution networks are neglected. Second level is composite power network that is composed of generation and transmission sections. In the third level, all power system elements in generation, transmission and distribution sections are taken into account. For evaluation adequacy of power networks incorporating high-capacity solar towers, all generation units, i.e. conventional and central receiver power plants and also system load are connected to common bus as can be seen in the Fig. 8. Capacity outage probability table (COPT) is a table containing state capacity and probability is developed for each generation units. The total COPT can be determined by combining the COPT of all generation units. With convolving generation system model, i.e. total COPT and load model, reliability indices such as loss of load expectation (LOLE), expected energy not supplied

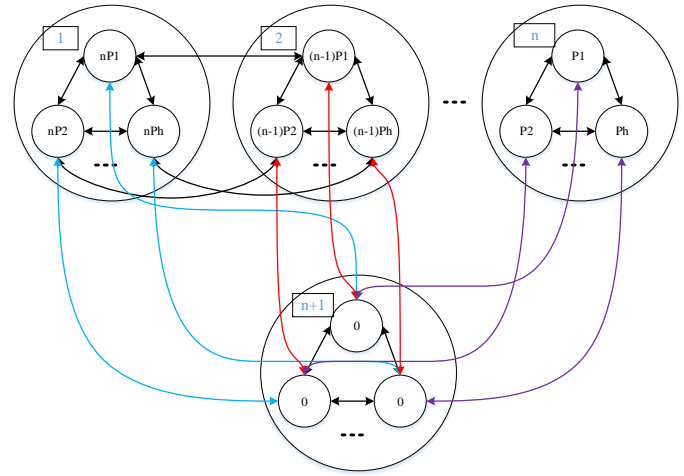


Fig. 7: The complete reliability model of solar power tower composed of n heliostats.

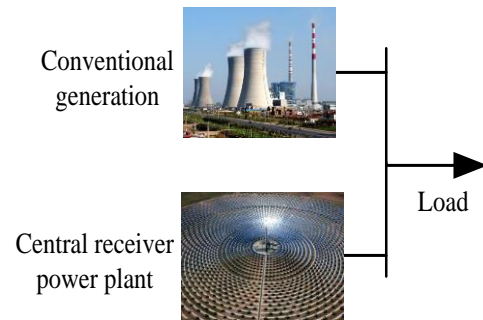


Fig. 8: Adequacy assessment technique.

(EENS), peak load carrying capability (PLCC) and increase in peak load carrying capability (IPLCC) are calculated.

5. NUMERICAL RESULTS

In this part, reliability model of central receiver plant is obtained. Solar radiation data associated to Jask region in Iran is utilized for simulation. Proposed multi-state reliability model is used for adequacy assessment performance of well-known reliability test networks, i.e. RBTS and IEEE-RTS that are integrated into central receiver power plant.

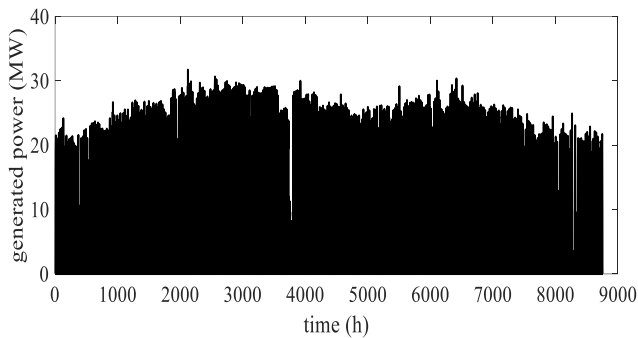
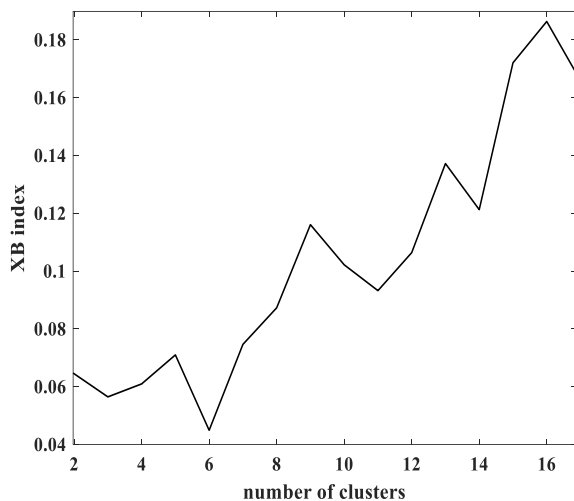
5.1. Reliability Modelling of the Understudied Solar Power Tower

In this part, a 30MW solar power tower composed of 3750 heliostats, each with 36-m² area is installed in Jask. Characteristic of understudied plant is assumed so that the performance parameters of the plant would be as presented in Table 2. The heliostats are equipped to the two-axis sun tracker that leads the reflected sunlight is concentrated on the central receiver.

Based on the (5), hourly solar radiation and the parameters presented in Table 2, the hourly generated power of the understudied solar power tower during a year is calculated and presented in Fig. 9. According to proposed approach, value of XB index considering number of clusters is calculated and illustrated in Fig. 10. It is seen from the figure that when cluster number is six, XB index is minimal, and so, six clusters as shown in Table 3 can be used to model

Table 2: The parameters of the understudied solar power tower.

| | |
|------------------------------------|------|
| Reflectivity | 0.94 |
| Atmosphere attenuation coefficient | 0.95 |
| Cleanliness of the mirrors | 0.85 |
| Cosine effect | 0.93 |
| Shading and blocking coefficient | 1 |
| Heat transfer fluid efficiency | 0.85 |
| Boiler efficiency | 0.89 |
| Turbine efficiency | 0.45 |
| Generator efficiency | 0.97 |
| Electrical converter efficiency | 0.98 |
| Transformer efficiency | 0.98 |

**Fig. 9:** Hourly produced power of understudied solar tower.**Fig. 10:** Value of XB index versus cluster number.

variation in output power of understudied solar power tower in term of reliability.

To obtain the complete reliability model of central receiver power plant, the Markov model of the plant developed in section 3-1 should be combined with the model determined Table 3. In this power plant, the number of heliostats is high and if one or several heliostats are failed the reduction in the generated power is not significant. Thus, with good accuracy, it can be neglected from heliostats failure in solar tower reliability model. Based on this assumption, a two-state Markov model considered the failure of main components can be developed to model the understudied central receiver power plant. Then, the obtained model should be combined with the model determined in Table 3. Solar tower failure and repair rates are 1.39 and 90.5 occurrence in year, respectively, and so, plant availability is 0.98. With combining two-state reliability model obtained due to failure of components and 6-state reliability model obtained due to

variation in solar radiation, the total reliability model of understudied plant is determined and illustrated in Table 5. The resulted model is used to evaluate adequacy performance of RBTS and IEEE-RTS integrated to the solar power tower.

The reliability parameters of the composed components of the understudied solar power tower including failure rate and repair time are presented in Table 4.

5.2. RBTS

Adequacy studies of RBTS is performed for evaluation effect of integration of solar towers on reliability indices of power networks. The RBTS has 11 power plants with 240MW installed capacity. Characteristic of RBTS power plants is given in [32]. In this study, load duration curve is a straight line that extends from yearly peak load to 60% of yearly peak load. To evaluate effect of solar tower on system reliability indices, three cases are studied that includes: original RBTS as case I, RBTS with 30MW conventional unit with availability of 0.98 as case II and RBTS integrated to understudied solar tower as case III. The value of LOLE and EENS of these cases considering different loads are determined and illustrated in Figs. 11 and 12, respectively. These figures present that reliability of power network gets worse when system peak load increases. Thus, in power network planning, new generation units must be added to the system when the load is grown. Besides, the figures present that addition of new power plants results in reliability indices improvements. However, conventional generation units have improved the reliability indices more than the solar power tower.

In this stage, the peak load carrying capability (PLCC) index associated with these cases is determined. To calculate PLCC, an increase in system peak load is performed. PLCC is the maximum peak load that satisfies the reliability criterion. If the peak load increases more than the PLCC, the risk criterion is not satisfied. The PLCC index of these cases for different reliability criteria is determined and illustrated in Table 6. In this research, three reliability criteria based on the Expected Energy Not Supplied (EENS) index are considered. The table shows that the capability of the power network to supply the required load improves with the addition of a new power plant. However, conventional units improve the capability of the power network in supplying the required load more than solar power towers. The increase in peak load carrying capability of RBTS with the new power plant is calculated and presented in Table 7. The table shows that the system peak load can be increased when either conventional units or solar power towers are integrated into the network. However, conventional units improve the peak load carrying capability of the system more than solar power towers.

5.3. IEEE-RTS

Characteristics of power plants installed in IEEE-RTS as high-capacity reliability test network are illustrated in [33]. For study solar tower effect on reliability indices of IEEE-RTS, three cases are simulated as below: original IEEE-RTS as case I, IEEE-RTS with 30MW conventional power plant with unavailability 0.02 as case II and IEEE-RTS integrated to the understudied central receiver power plant as case III. The LOLE and EENS indices for three cases are determined and illustrated in Figs. 13 and 14, respectively. Besides, PLCC and IPLCC associated to understudied cases for three

Table 3: Clustering results.

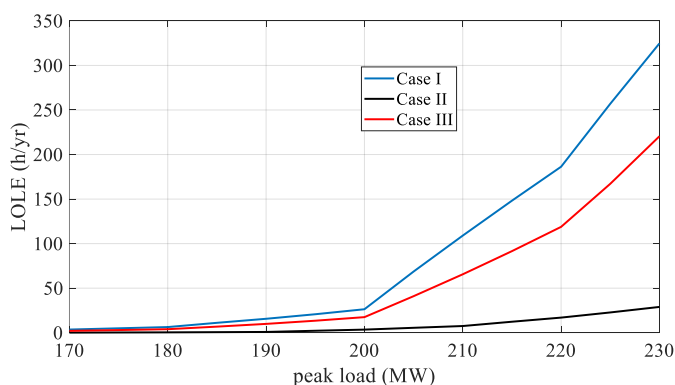
| Capacity (in MW) | Probability |
|------------------|-------------|
| 0 | 0.5096 |
| 5.8 | 0.0533 |
| 11.3 | 0.0634 |
| 17.8 | 0.0880 |
| 22.4 | 0.1550 |
| 26.4 | 0.1307 |

Table 4: Reliability parameters of solar tower.

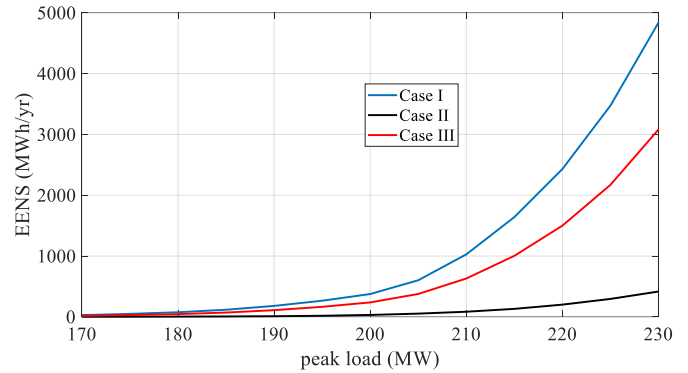
| Elements | Failure rate (number per year) | Repair time (hour) |
|-----------------------------------|--------------------------------------|-----------------------|
| Heliostat | 0.1 | 50 |
| Central receiver | 0.1 | 100 |
| Thermodynamic cycle components | 1 | 100 |
| Generator transformer | 0.1 0.05 | 100 50 |
| Electrical converter | 0.04 | 50 |
| Cable | 0.1 | 100 |

Table 5: The complete reliability model of understudied solar power tower.

| Capacity (in MW) | Probability |
|------------------|-------------|
| 0 | 0.5195 |
| 5.8 | 0.0522 |
| 11.3 | 0.0621 |
| 17.8 | 0.0862 |
| 22.4 | 0.1519 |
| 26.4 | 0.1281 |

**Fig. 11:** The LOLE index in different peak loads.

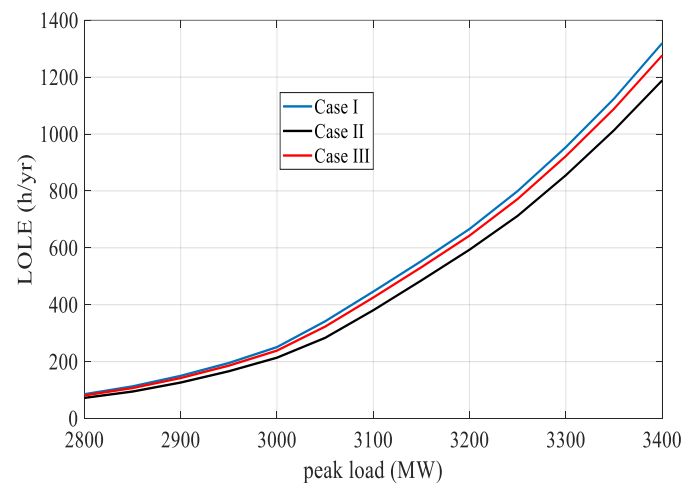
reliability criteria including EENS of 20, 50 and 100 GWh/yr are calculated and presented in Table 8 and 9, respectively.

**Fig. 12:** The EENS index in different peak loads.**Table 6:** The PLCC.

| Cases | 100 MWh/yr | 200 MWh/yr | 300 MWh/yr |
|----------|------------|------------|------------|
| Case I | 183 | 191 | 196 |
| Case II | 211 | 219 | 225 |
| Case III | 188 | 197 | 202 |

Table 7: The PLCC.

| Cases | 100 MWh/yr | 200 MWh/yr | 300 MWh/yr |
|----------|------------|------------|------------|
| Case II | 28 | 28 | 29 |
| Case III | 5 | 6 | 6 |

**Fig. 13:** The LOLE index in different peak loads.

Numerical results present central receiver power units improve reliability indices of IEEE-RTS. However, effect of central receiver power plant on the reliability enhancement is less than conventional power plants with same size.

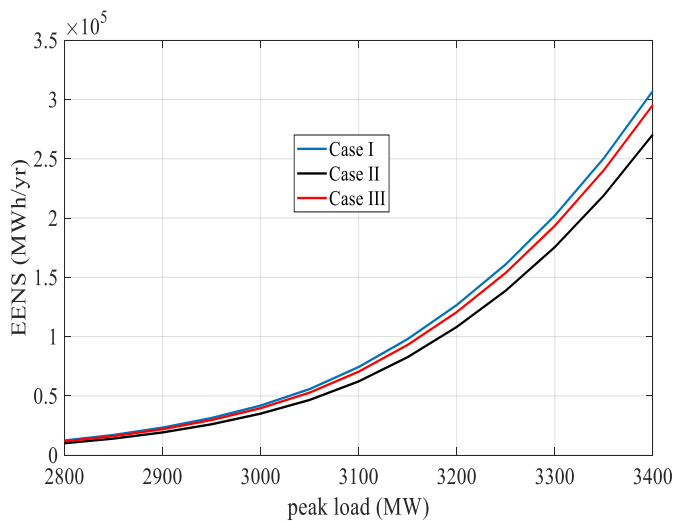


Fig. 14: The EENS index in different peak loads.

Table 8: PLCC

| Cases | 20 GWh in year | 50 GWh in year | 100 GWh in year |
|----------|-------------------|-------------------|--------------------|
| Case I | 2875 | 3031 | 3153 |
| Case II | 2904 | 3060 | 3181 |
| Case III | 2885 | 3040 | 3163 |

Table 9: IPLCC

| Cases | 20 GWh in year | 50 GWh in year | 100 GWh in year |
|----------|-------------------|-------------------|--------------------|
| Case II | 29 | 29 | 28 |
| Case III | 10 | 9 | 10 |

6. CONCLUSION

In this research, among different kinds of solar generation units, central receiver power plants that can be constructed with high generation capacity and connected to the bulk power system are considered to evaluate their effect on the adequacy of power systems. In this regard, a multi-state reliability model is introduced for this power plant that takes into account both changes in plant power arising from changes in solar radiation and component failures. The main components affecting the performance of a solar tower are heliostats, central receiver, thermodynamic cycle, generator, power electronic converter, cable, and transformer. To model each component of the solar power tower from a reliability point of view, a Markov model with two states, including up and down states, is used. In a solar tower composed of n heliostats, failure of any heliostat results in a reduction of generated power by a factor of $(n-1)/n$. The failure of other components, i.e., central receiver, thermodynamic cycle components, generator, electrical converter, transformer, and cable, leads to plant operation stoppage. In this circumstance, the produced power of the plant would be zero. In the Markov model, it is assumed that only one failure may occur at a time. Because there are a large number of heliostats in the power plants, the reduction of plant produced power due to the failure of one or several heliostats is insignificant and is therefore neglected in the reliability model. A two-state model can present an equivalent reliability model of the plant that considers the failure of component parts. The variation in solar radiation leads to many power states existing in the

reliability model of the plant, making analytical reliability assessment of the power network difficult. Thus, this research proposes a fuzzy c-means clustering method for reducing the number of power states. Additionally, the XB index is selected to determine the optimal number of power states in the model. The optimum number of states is determined when the XB index is minimal. The complete plant reliability model is obtained by combining the reliability model related to the failure of component elements and the reliability model related to the uncertainty nature of produced power arising from variation in solar radiation. The proposed multi-state reliability model related to a 30MW solar tower is obtained to evaluate the impact of central receiver generation units on the adequacy performance of RBTS and IEEE-RTS. Numerical results show that integration of central receiver plants into the power network leads to improved reliability indices. However, the produced power of central receiver plants is dependent on solar radiation. Since wide variation occurs in solar radiation, the output power of solar towers changes significantly, and the produced power of central receiver generation units is less than nominal capacity most of the time. Thus, central receiver power plants improve power network reliability indices less than conventional power plants with the same capacity.

CREDIT AUTHORSHIP CONTRIBUTION STATEMENT

Amir Ghaedi: Conceptualization, Investigation, Methodology, Software, Supervision, Validation. **Mehrdad Mahmoudian:** Data curation, Formal analysis, Resources, Writing - review & editing.

DECLARATION OF COMPETING INTEREST

The authors declare that they have no known competing financial interests or personal relationships that could have appeared to influence the work reported in this paper. The ethical issues; including plagiarism, informed consent, misconduct, data fabrication and/or falsification, double publication and/or submission, redundancy has been completely observed by the authors.

REFERENCES

- [1] S. Rezaei, and A. Ghasemi. "Optimal day-ahead scheduling of a CHP and renewable resources-based energy hub with the aim of improving resiliency during input energy carriers' outage," *Journal of Applied Research in Electrical Engineering*, Vol. 1, no. 1, pp. 93-111, 2022.
- [2] A. Ghaedi, and M. Mahmoudian, "Reliability evaluation of power systems including pumped-storage generation units," *Journal of Applied Research in Electrical Engineering*, vol. 3, no. 1, pp. 110-119, 2024.
- [3] H. L. Zhang, J. Baeyens, J. Degève, and G. Cacères, "Concentrated solar power plants: Review and design methodology," *Renewable and Sustainable Energy Reviews*, vol. 22, pp. 466-481, 2013.
- [4] A. Boretti, S. Castelletto, and S. Al-Zubaidy, "Concentrating solar power tower: Latest status report and survey of development trends," 2017. [Online]. Available: <https://doi.org/10.20944/preprints201710.0027.v2>.

- [5] F. J. Collado, and J. Guallar, "A review of optimized design layouts for solar power tower plants with campo code," *Renewable and Sustainable Energy Reviews*, vol. 20, pp. 142-154, 2013.
- [6] M. A. Mustafa, S. Abdelhady, and A. A. Elweteedy, "Analytical study of an innovated solar power tower (PS10) in Aswan," *International Journal of Energy Engineering*, vol. 2, no. 6, pp. 273-278, 2012.
- [7] A. Mutuberria, J. Pascual, M. V. Guisado, F. Mallor, "Comparison of heliostat field layout design methodologies and impact on power plant efficiency," *Energy Procedia*, vol. 69, pp. 1360-1370, 2015.
- [8] O. H. Abdalla, R. Al-Badwawi, H. Al-Hadi, H. Al-Riyami, and A. Al-Nadabi, "Impact of a 200 MW concentrated receiver solar power plant on steady-state and transient performances of Oman transmission system," in *2012 IEEE International Power Engineering and Optimization Conference*, Malaysia, IEEE, 2012, pp. 401-406.
- [9] D. T. Griffith, C. K. Ho, P. S. Hunter, J. Sment, A. C. Moya, and A. R. Menicucci, "Modal analysis of a heliostat for concentrating solar power," in *Topics in Modal Analysis I*, Vol. 5, pp. 415-423, New York, NY, 2012.
- [10] F. Eddhibi, M. B. Amara, M. Balghouthi, and A. Guizani, "Optical study of solar tower power plants," *Journal of Physics: Conference Series*, vol. 596, no. 1, p. 012018, IOP Publishing, 2015.
- [11] M. Amelio, P. Beraldi, V. Ferraro, M. Scornaienchi, and F. Rovense, "Optimization of heliostat field in a thermal solar power plant with an unfired closed Joule-Brayton cycle," *Energy Procedia*, vol. 101, pp. 472-479, 2016.
- [12] M. Renzik, L. Egidib, L. Cioccolantic, and G. Comodib, "Performance simulation of a small-scale heliostat CSP system: Case studies in Italy," *Energy Procedia*, vol. 105, pp. 367-372, 2017.
- [13] A. Nargeszar, A. Ghaedi, M. Nafar, and M. Simab, "Optimal planning of renewable energy-based micro grids considering the reliability cost," *Journal of Operation and Automation in Power Engineering*, In press.
- [14] A. Ghaedi, R. Sedaghati, and M. Mahmoudian. "Optimal scheduling of a renewable-based micro grid considering reliability effect," *Signal Processing and Renewable Energy*, vol. 8, no. 1, 2024.
- [15] A. Ghaedi, R. Sedaghati, and M. Mahmoudian. "Reliability modeling of various type of wind turbines," *AUT Journal of Electrical Engineering*, vol. 56, no. 2, 2024.
- [16] A. Ghaedi et al., "Reliability assessment of the ocean thermal energy conversion systems through Monte Carlo simulation considering outside temperature variation," *Journal of Marine Science and Technology*, vol. 29, no.1, pp. 36-52, 2024.
- [17] A. Ghaedi, M. Mahmoudian, and R. Sedaghati, "The impact of different solar tracker systems on reliability of photovoltaic farms," *Journal of Energy Management and Technology*, vol. 8, no.1, vol. 68-77, 2024.
- [18] A. Ghaedi, R. Sedaghati, and M. Mahmoudian, "The impact of variation in water flow rate and temperature on reliability analysis of run of the river power plants," *IET Renewable Power Generation*, vol. 18, no.6, pp. 929-940, 2024.
- [19] A. Ghaedi, et al., "Reliability modeling of wave energy converters based on pelamis technology," *Electric Power Systems Research*, vol. 227, p. 109977, 2024.
- [20] A. Ghaedi, R. Sedaghati, and M. Mahmoudian, "Adequacy studies of different renewable resources using Monte Carlo simulation method," *International Journal of Smart Electrical Engineering*, vol. 4, no.4 2024.
- [21] A. Ghaedi, A. Abbaspour, M. Fotuhi-Firuzabad, and M. Moeini-Aghtaie, "Toward a comprehensive model of large-scale DFIG-based wind farms in adequacy assessment of power systems," *IEEE Transactions on Sustainable Energy*, vol. 5, no. 1, pp. 55-63, 2013.
- [22] A. Ghaedi, A. Abbaspour, M. Fotuhi-Firuzabad, and M. Parvania, "Incorporating large photovoltaic farms in power generation system adequacy assessment," *Scientia Iranica*, vol. 21, no. 3, pp. 924-934, 2014.
- [23] E. Khalilzadeh, M. Fotuhi-Firuzabad, F. Aminifar, and A. Ghaedi, "Reliability modeling of run-of-the-river power plants in power system adequacy studies," *IEEE Transactions on Sustainable Energy*, vol. 5, no. 4, pp. 1278-1286, 2014.
- [24] A. Ghaedi, K. Nasiriani, and M. Nafar, "Spinning reserve scheduling in a power system containing OTEC power plants," *International Journal of Industrial Electronics, Control and Optimization*, vol. 3, no. 3, pp. 379-391, 2020.
- [25] M. Mirzadeh, M., Simab, and A. Ghaedi, "Reliability evaluation of power systems containing tidal power plant," *Journal of Energy Management and Technology*, vol. 4, no. 2, pp. 28-38, 2020.
- [26] M. Mirzadeh, M. Simab, and A. Ghaedi, "Adequacy studies of power systems with barrage-type tidal power plants," *IET Renewable Power Generation*, vol. 13, no. 14, pp. 2612-2622, 2019.
- [27] R.P. Praveen, "Performance analysis and optimization of central receiver solar thermal power plants for utility scale power generation," *Sustainability*, vol. 12, no. 1, pp. 1-16, 2019.
- [28] N.B. Desai, and S. Bandyopadhyay, "Thermo-economic comparisons between solar steam Rankine and organic Rankine cycles," *Applied Thermal Engineering*, vol. 105, pp. 862-875, 2016.
- [29] R. Billinton, R. N. Allan, *Reliability evaluation of power systems*, 2nd edition. New York, NY, USA and London, U.K.: Plenum, 1994.
- [30] R. L. Cannon, V. D. Jitendra, and J. C. Bezdek, "Efficient implementation of the fuzzy c-means clustering algorithms," *IEEE Trans. Pattern Analysis and Machine Intelligence*, vol. PAMI-8, no. 2, pp. 248-255, March

1986.

- [31] M. Chen, and S. A. Ludwig, "Particle swarm optimization based fuzzy clustering approach to identify optimal number of clusters," *Journal of Artificial Intelligence and Soft Computing Research*, vol. 4, no. 1, pp.43– 56, 2014.
- [32] R. Billinton, and S. Jonnavithula, "A test system for teaching overall power system reliability assessment," *IEEE Transactions on Power Systems*, vol. 11, no. 4, pp.1670-1676, 1996.
- [33] C. Grigg *et al.*, "The IEEE reliability test system-1996. A report prepared by the reliability test system task force of the application of probability methods subcommittee," *IEEE Transactions on power systems*, vol. 14, no. 3, pp. 1010-1020, 1999.

BIOGRAPHY



Amir Ghaedi was born in 1984 in Kheirabad, a village of Shiraz, and received the M.Sc., and Ph.D. degrees in electrical engineering, power field, from Sharif University of Technology, Tehran, Iran, in 2008, and 2013, respectively. He is currently associate professor in Department of Electrical Engineering,

Dariun Branch, Islamic Azad University, Dariun, Iran. His main research interests are the power quality, power system reliability, smart grids, renewable resources and high voltage engineering.



Mehrdad Mahmoudian was born in Iran, in 1990. He received the B.Sc. degree in Electrical Engineering from Shahid Bahonar University, Kerman, Iran, and M.S. degree in Electrical Engineering from Iran University of Science and Technology (IUST), Tehran Iran, in 2012 and 2014 respectively. His research interests include DC/DC Converters, Energy Conversion and Photovoltaic Power System.

Copyrights

© 2025 Licensee Shahid Chamran University of Ahvaz, Ahvaz, Iran. This article is an open-access article distributed under the terms and conditions of the Creative Commons Attribution –NonCommercial 4.0 International (CC BY-NC 4.0) License (<http://creativecommons.org/licenses/by-nc/4.0/>).



| | |
|--|-----|
| Wide Area Robust Controller Design for SSSC to Improve the Oscillations Caused by the Time Delay of Remote Signals Babak Keshavarz Zahed, Mohammad Hassan Moradi | 120 |
| Network Virtualization Utilizing Blockchain: A Review Patikiri Arachchige Don Shehan Nilmantha Wijesekara | 136 |
| Voltage Regulation in Low Voltage Distribution Networks Using Reactive Power Capability of Photovoltaic Inverters (PV) and PID Consensus Algorithm Iman Ali Hassanvand, Javad Ebrahimi, Mahyar Abasi | 159 |
| Optimization of PSS and UPFC Controllers to Enhance Stability by Using a Combination of Fuzzy Algorithm and Shuffled Frog Leaping Algorithm Mohammad Abedini, Mahyar Abasi | 168 |
| Economic Analysis of Photovoltaic Systems During Peak Load of the Electric Power Distribution System in the Presence of Electric Vehicles Musa Khosravi, Saeed Hasanvand, Mahyar Abasi, Mohammad Esmaeil Hassanzadeh | 177 |
| Improving Power Quality Using a Fuzzy Inference System-Based Variable Forgetting Factor Recursive Least Error Square Control Scheme of DSTATCOM Arash Rohani, Javad Ebrahimi, Shirin Besati | 185 |
| Comparative Analysis of Lithium-ion Battery for Long and Short Pulse Discharge Experiments in State-of-Charge Estimation with Extended Kalman Filter Behnam Ersi Alambaz, Mohsen Ghalehnoie, Hamid Reza Moazami | 200 |
| Investigating the Flashover Probability of Transmission Network Insulators During Dust Storms Yasaman Abbasi Chahardah Cheriki, Hossein Farzin, Elaheh Mashhour | 207 |
| Improving the Performance Characteristics of Conventional Linear Switched Reluctance Motor by Eliminating Translator Yoke and Embedding Permanent Magnets in Stator Yoke Milad Golzarzadeh, Hashem Oraee, Babak Ganji | 222 |
| Investigating Robust Tracking of Type 1 Diabetes Control Using Model-Free Controllers Peyman Vafadoost Sabzevar, Ahmad Hajipour, Hamidreza Tavakoli | 232 |
| IRS-Assisted Visible Light Communication for Improved Monitoring of Patient Vital Signals in Hospital Environment Babak Sadeghi, Seyed Mohammad Sajad Sadough | 240 |
| Reliability Modelling of Central Receiver Power Plants Amir Ghaedi, Mehrdad Mahmoudian | 250 |

